Mechanics and thermodynamics of suspended two-dimensional membranes

Liu, Hanqing

Important note
To cite this publication, please use the final published version (if applicable).
Please check the document version above.

MECHANICS AND THERMODYNAMICS OF SUSPENDED TWO-DIMENSIONAL MEMBRANES

MECHANICS AND THERMODYNAMICS OF SUSPENDED TWO-DIMENSIONAL MEMBRANES

Dissertation

for the purpose of obtaining the degree of doctor
at Delft University of Technology
by the authority of the Rector Magnificus, prof. dr. ir. T.H.J.J. van der Hagen,
chair of the Board for Doctorates
to be defended publicly on Monday 16 October 2023 at 15:00 o'clock

by

Hanqing LIU

Master of Engineering in Electronic Science and Technology,
National University of Defense Technology,
born in Shandong, China.

This dissertation has been approved by the promotors

promotor: prof. dr. P. G. Steeneken
copromotor: dr. G. J. Verbiest

Composition of the doctoral committee:

Rector Magnificus,	chairperson
Prof. dr. P. G. Steeneken,	Delft University of Technology, promotor
Dr. G. J. Verbiest,	Delft University of Technology, copromotor

Independent members:

Prof. dr. ir. H. S. J. van der Zant,	Delft University of Technology
Prof. dr. Y. M. Blanter,	Delft University of Technology
Prof. dr. S. Lodha,	Indian Institute of Technology Bombay, India
Prof. dr. A. A. Bol,	University of Michigan, United States of America
Prof. dr. K. I. Bolotin,	Free University of Berlin, Germany, reserve member

An electronic version of this dissertation is available at
http://repository.tudelft.nl/.

Never be over thrilled or over depressed by external environment and personal gains.

Zhongyan Fan, AD 1044, China (Song Dynasty)

Contents

SUMMARY

This thesis provides a comprehensive research of both the mechanics and thermodynamics of suspended two-dimensional (2D) membranes, such as tunable mechanical resonance, membrane deformation, heat transport, phonon scattering, and energy dissipation. These characteristics make nanomechanical resonators, made of a suspended 2D membrane, promising candidates for both fundamental studies and engineering applications. This thesis is composed of eight chapters in total.

In Chapter 1, we give an overview of the fields of 2D materials and nanomechanical resonators. We emphasize the significant benefits of using 2D materials for more sensitive and accurate nano- devices and systems, thus to interpret our motivation for investigating the mechanics and thermodynamics of suspended 2D membranes in this thesis.

In Chapter 2, we first introduce the method for suspending 2D membranes over cavities in a substrate to fabricate nanomechanical resonators. Afterwards, we present the typical techniques to characterize the basic properties of the fabricated devices, such as Atomic Force Microscope and Raman Microscope. Optomechanical measurement, achieved by a laser interferometry setup, is highlighted, which allows us to measure the resonance frequency, quality factor, thermal time constant and thermal expansion amplitude of 2D nanomechanical resonators.

The following Chapter 3 to Chapter 7 are the primary research contents of this thesis. Chapter 3 and Chapter 4 mainly focus on the mechanics of suspended 2D membranes. We propose a novel fabricating route for 2D heterostructure resonators based on Atomic Layer Deposition (ALD) technique in Chapter 3. The fabricated ALD MoS_2/Graphene devices hold comparable mechanical performance to their exfoliated counterparts, while showing a lower interface dissipation. Chapter 4 deals with the effect of thermally-induced buckling on the mechanical behaviours of 2D resonators, including the turning of resonance frequency and the enhancement of photothermal response at buckling bifurcation point.

Chapter 5 and Chapter 6 move onto the thermodynamics of suspended 2D membranes. Chapter 5 provides an optomechanical approach for characterizing the heat thermal properties of the membrane, including thermal expansion coefficient, specific heat and in-plane thermal conductivity. However, this given methodology cannot explain the experimentally observed two orders-of-magnitude larger than expected thermal time constant in graphene resonators. To solve this, we introduce a phononic scattering model is built in Chapter 6, where we attribute the larger thermal time constant to the strong scattering of flexural acoustic phonons at the boundary of graphene membrane between its suspended and supported regions. We induce surface tension in graphene resonator by electrostatic deflection to validate the model experimentally and realize a substantial tuning on the thermal transport.

Chapter 7 gives an outlook to our on-going work which could potentially have a significant impact in the domains of 2D mechanics and thermodynamics. We characterize the thermal interface conductance in a $FePS_3/WSe_2$ heterostructure resonator by combining optomechanical measurements with COMSOL simulations. Finally, we conclude with Chapter 8 which summarizes all findings in this thesis.

SAMENVATTING

Deze scriptie biedt een uitgebreid onderzoek naar zowel de mechanica als de thermodynamica van gesuspendeerde tweedimensionale (2D) membranen, zoals regelbare mechanische resonantie, membraandeformatie, warmtetransport, fononverstrooiing en energiedissipatie. Deze kenmerken maken nanomechanische resonatoren, gemaakt van een hangend 2D-membraan, veelbelovende kandidaten voor zowel fundamentele studies als technische toepassingen. Deze scriptie bestaat in totaal uit acht hoofdstukken.

In Hoofdstuk 1 geven we een overzicht van het vakgebied van 2D-materialen en nanomechanische resonatoren. We benadrukken de aanzienlijke voordelen van het gebruik van 2D-materialen bij de productie van nanodevices en -systemen, en zo interpreteren we onze motivatie om de mechanica en thermodynamica van zwevende 2D-membranen in deze scriptie te onderzoeken.

In Hoofdstuk 2 introduceren we eerst de methode om 2D-membranen over holtes in een substraat te spannen om Nano mechanische resonatoren te fabriceren. Vervolgens presenteren we de gebruikelijke technieken om de basiskenmerken van de gefabriceerde apparaten te karakteriseren, zoals de Atomaire kracht microscoop en de Raman microscoop. Er word vooral gefocust op optomechanische metingen, uitgevoerd met een laser interferentie opstelling, waarmee we de resonantiefrequentie, kwaliteitsfactor, thermische tijdsconstante en thermische uitzettingsamplitude van 2D-nanomechanische resonatoren kunnen meten.

De daaropvolgende hoofdstukken 3 tot en met 7 vormen Het hoofd onderzoeksonderwerp van deze scriptie. Hoofdstuk 3 en hoofdstuk 4 richten zich voornamelijk op de mechanica van gesuspendeerde 2D-membranen. In hoofdstuk 3 stellen we een nieuwe fabricage methode voor 2D-heterostructuurresonatoren voor op basis van de Atomic Layer Deposition (ALD) techniek. De gefabriceerde ALD MoS_2/Graphene-preparaten laten vergelijkbare mechanische eigenschappen zien als hun geëxfolieerde tegenhangers, met een lagere interface-dissipatie . Hoofdstuk 4 behandelt het effect van thermisch geïnduceerde opbolling op het mechanisch gedrag van 2D-resonatoren, inclusief de verandering in resonantiefrequentie en de verbetering van de fotothermische respons op het bifurcatiepunt van de opbolling.

Hoofdstuk 5 en Hoofdstuk 6 gaan over de thermodynamica van gesuspendeerde 2D-membranen. Hoofdstuk 5 biedt een optomechanische methode om de thermische eigenschappen van het membraan te karakteriseren, waaronder de thermische uitzettingscoëfficiënt, specifieke warmte en thermische geleidbaarheid. Deze gegeven methodologie kan echter de experimenteel waargenomen thermische tijdsconstante die twee ordes van grootte meer is dan verwacht in grafeen resonatoren niet verklaren. Om dit op te lossen, introduceren we in Hoofdstuk 6 een fononisch verstrooiingsmodel , waarbij we de grotere thermische tijdsconstante toeschrijven aan de sterke verstrooiing van

flexurale akoestische fononen aan de rand van het grafenmembraan tussen zijn gesus-
pendeerde en ondersteunde regio's. We veroorzaken oppervlaktespanning in de grafeen
resonator door het membraan te buigen door er elektrostatisch aan te trekken, om het
model experimenteel te valideren en een aanzienlijke afstembaarheid op het warmte-
transport te realiseren.

Hoofdstuk 7 werpt een blik op ons lopende werk dat mogelijk een aanzienlijke im-
pact zou kunnen hebben op de domeinen van 2D-mechanica en thermodynamica.
We karakteriseren de warmtegeleiding door het interface in een FePS3/WSe2 hetero-
structuurresonator door optomechanische metingen te combineren met een COMSOL-
simulatie. Tot slot sluiten we af met Hoofdstuk 8, waarin we alle bevindingen in deze
scriptie samenvatten.

1

1

INTRODUCTION

In this chapter, we give a overview of background and current status of two-dimensional (2D) materials and nanomechanical resonators. We provide a motivation for investigating mechanics and thermodynamics of suspended 2D membranes in this thesis.

1
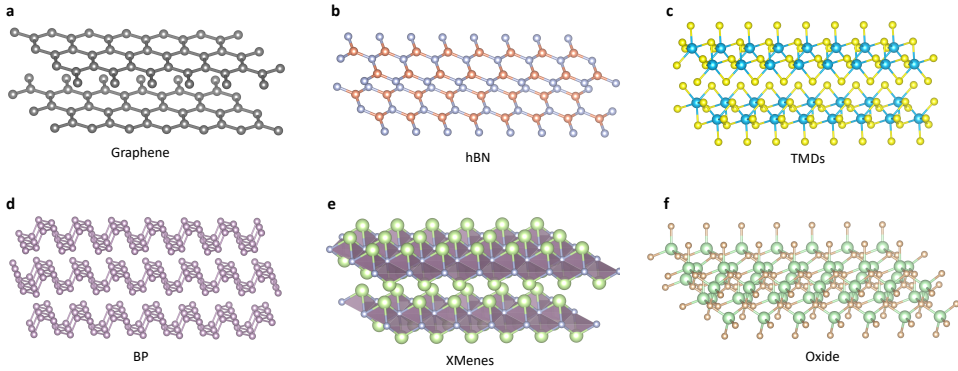
Figure 1.1: Atomic structure of types of 2D materials. **a** Graphene. **b** Hexagonal-Boron Nitride (hBN). **c** Transition metal dichalcogenides (TMDs). **d** Black phosphorus (BP). **e** MXenes; **f** Transition metal oxides.

O VER the past century, the aim of ever-smaller devices and systems with high-power integration has motivated substantial research efforts, produced significant breakthroughs, and drove scientists into hitherto uncharted fields. Moore's law, which states that the number of transistors per square inch will double approximately every 18 months, has continued to set the pace for the semiconductor industry since it was put forward in the 1970s [1]. Owe to the flourishing multidisciplinary field of low-dimensional nanomaterials, including one-dimensional (1D) nanowires and nanotubes, as well as two-dimensional (2D) atomic layers such as graphene, growing interests and consistent effort have been devoted to device technology toward the ultimate limit of miniaturization-genuinely down to the atomic scale [2, 3]. Nanodevices, in particular nanomechanical resonators that exploit the vibratory motion in these 1D and 2D nanoscale structures, offer exceptional device-level properties like ultralow mass, ultrawide frequency tuning range, and ultralow power consumption, thus holding strong potential for both fundamental studies and engineering applications [4, 5].

1.1. TWO-DIMENSIONAL MATERIALS

2D materials have attracted extensive attentions due to their unique crystal structure and excellent performance in various aspects. Encouraged by the first exfoliated graphene in 2004, numerous 2D materials have been successfully found and synthesized, such as hexagonal-Boron Nitride (hBN), transition metal dichalcogenides (TMDs), monochalcogenides (MNs), black phosphorus (BP), transition metal oxides, MXenes and 2D organic crystals, and polymers. Fig. 1.1 shows the atomic structure of several typical 2D materials. The exceptional mechanical, thermal, magnetic, electrical, optical and optoelectronic properties of 2D materials are highly enhanced as the surface to volume ratio increases, resulting from the transition of atomic structure from bulk to the few- to mono- layer limit. Such unique attributes brought great revolution in the fields of semiconductor industry [6], nanoelectronics [7], biomedicine [8], photoelectricity [9], advanced sensing technology [4] and quantum nanoscience [10].
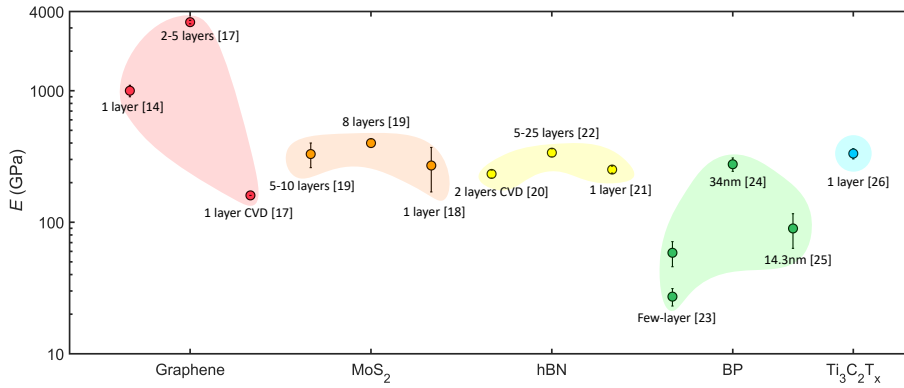
Figure 1.2: Wide range of Young's modulus of 2D materials obtained from experimental studies.

1.1.1. Mechanics

Due to the atomic thickness and high aspect-ratio, 2D materials are exceedingly flexible out-of-plane in comparison to their bulk counterparts. However, the in-plane mechanical response is quite stiff as a consequence of their high Young's modulus and strength. These special properties make 2D materials as the most promising candidates for flexible and transparent electronics and composite applications [11]. The mechanics of freely suspended 2D membranes has also been explored in dynamic experiments in which the 2D materials were used as mechanical resonators. With superior mechanical strength and toughness, such resonators are ideal for ultra-sensitive applications such as force sensors and functional switches [12]. On the other hand, the mechanics of 2D materials is also strongly related to the defects, wrinkles and interface interactions like friction and adhesion, which play significant roles in 2D applications such as nanoelectronics, nanoelectromechanical systems (NEMS), and nano-composites [13].

A direct measurement of mechanical properties of 2D materials was first reported by Lee et al. [14], where suspended monolayer graphene membranes are indented by atomic force microscope (AFM) tapping mode. The indentation force–displacement behavior was interpreted as a result of the nonlinear elastic properties of graphene, with a ultra-high Young's modulus about 1000 GPa. Besides AFM indentation, MEMS-based mechanical testing [15], in situ TEM observation [16], and shearing tests [13] by probe tip are commonly utilized for mechanical characterization. Using these methods, the Young's modulus of different types of discovered 2D materials have been experimentally studied [14, 17–26], showing a wide range from ∼ 20 GPa to almost 4000 GPa (see Fig. 1.2).

1.1.2. Thermodynamics

2D materials also provides exciting opportunities for studying the phononic transport behaviours at nanoscale. Impressively, 2D materials have been demonstrated to exhibit superior lattice thermal conductivity, e.g., suspended monolayer graphene has a thermal conductivity between 4800 and 5300 $Wm^{-1}K^{-1}$ at room temperature, exceeding its bulk counterpart graphite [27]. This inspires many studies aiming at both understanding its

1
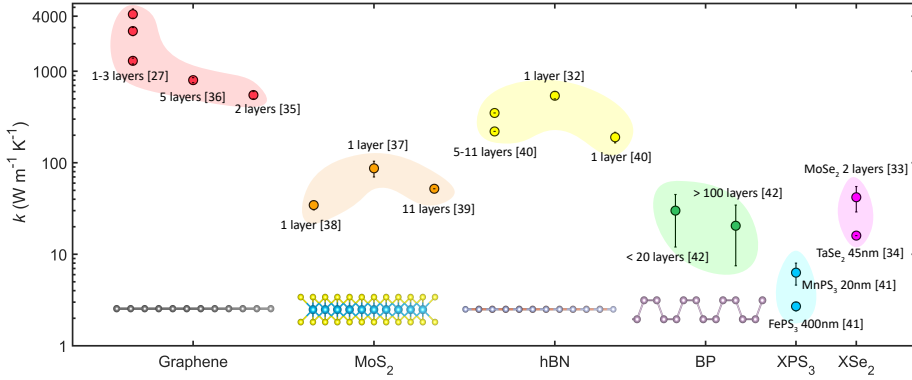
Figure 1.3: Lattice thermal conductivity k of 2D materials at room temperature, which are experimentally obtained by Raman microscopy measurements. Bottom insert: monolayer atomic structures (side view) of graphene, MoS_2, hBN and black phosphorus.

underlying physics and exploring potential applications for thermal managements. The control of the thermal properties of 2D materials could enable new generations of thermoelectric materials, thermal insulators, and even phononic computing devices. Additionally, 2D materials may present a novel platform to realize phonon thermal diodes, phonon transistors, topological phonon insulators, and quantum memories [28].

Various methods based on electrical or optical readouts have been developed for nanoscale thermal measurements, of which the most commonly utilized is optothermal method using Raman microscopy [29, 30]. Typically, Raman laser irradiates in the center of 2D materials and generates heat flux, causing a radial temperature gradient in a basal plane. Since the peak shifts in Raman spectrum is proportional to the temperature variation, one can connect the temperature rise with the laser heating power, thus to extract the thermal conductivity of the tested 2D materials. Figure. 1.3 shows the thermal conductivity of types of 2D materials obtained from experiments at room temperature [27, 31–42]. It is of interest to see that the thermal conductivity of graphene and hBN, with planar crystal structures, are larger than that of MoS_2 with trilayer symmetric crystal structure and BP with asymmetric structure. This can be explained by the scattering of acoustic phonons in 2D materials that is remarkably influenced by the crystal structures (see insert in Fig. 1.3).

Regarded as the dominant heat carriers in 2D materials, acoustic phonons have been theoretically investigated through various approaches, including molecular dynamics simulations [43], non-equilibrium Green function method [44] and Boltzmann transport equation [45]. Depending on the polarization, acoustic phonons can be divided into in-plane longitudinal (LA) and transverse (TA) phonons, as well as out-of-plane flexural (ZA) phonons. The dispersion relations of LA and TA phonons are related to the elastic modulus, while that of ZA phonons is determined by the bending rigidity and surface strain [46–48]. Particularly, it has been demonstrated that ZA phonon with a long mean free path (> 10 μm) dominates the heat transport in monolayer graphene [49], leading to its ultra-large thermal conductivity.

1.2. Two-dimensional nanomechanical resonators

Intriguing mechanical properties together with atomic thickness makes 2D materials highly suit for a new class of nanoscale resonators, especially nanoelectromechanical systems (NEMS). Resonant 2D devices show high fundamental frequencies, outstanding tunability and broad dynamic range due to the ultrahigh strength, ultralow mass density and ultrahigh tensile strength. Through coupling electrostatic, optical, thermal, and magnetic excitation to the membrane vibration, numerous cutting-edge applications have been made possible by 2D nanomechanical resonators [2]. Further, the compact size and high stiffness of these devices also possess the potential of greatly increased sensitivity for detecting a variety of physical stresses [50].

The key procedure for fabricating 2D nanomechanical resonators is suspending 2D membranes over cavities. To achieve this, 2D nanoflakes are mechanically exfoliated (similar to the first graphene devices made in 2004) or synthesized through chemical vapor deposition (CVD), and then transferred onto the target substrate with etched cavities [51, 52]. For 2D NEMS, a further configuration of top/bottom gate electrodes is needed [53]. After fabrication, the next challenge is how to actuate and detect the mechanical vibration of 2D resonators. For this, optothermal [12] and electrostatic [54] excitations are commonly utilized. Figure 1.4a gives the illustration of optothermal excitation: a blue laser with modulated intensity drives the membrane via periodic thermal expansion, while a fixed red laser is employed for detection since its reflected intensity depends on the membrane motion. This method not only provides a efficient drive for mechanical measurement, but also allows to investigate the phononic thermal transport in 2D membranes. With regards to electrostatic excitation, the cavity gap between the membrane and the substrate forms an electrical capacitor, thus by applying the gate voltage on top and bottom electrodes, time-dependent electrostatic force is generated to drive the membrane vibrating periodically. For large-scale resonators with a radius more than 100 μm, we adopt a laser Doppler vibrometer with piezoresistive transduction to achieve the actuation [55, 56].

1.2.1. Resonant dynamics

Frequency tuning

The capability of tuning the fundamental resonant frequency, f_0, is crucial for 2D nanomechanical resonators using as voltage-controlled oscillators, tunable RF filters, and advanced sensing [2]. The strong dependence of f_0 on the effective spring constant, more specifically, the surface tension of the membrane enables a wide-range tuning on its resonance. For instance, using Joule heating, the tunability of resonance frequency, $\Delta f_0 / f_0$, can reach up to $\sim 1300\%$ for few-layer graphene resonators [57]. In addition, MEMS comb-drive stretching [58] and electrostatic gate [59] are also efficient ways for realizing large $\Delta f_0 / f_0$.

Quality factor

Quality factor Q of the resonance (see Fig. 1.4b), a dimensionless metric defined as the ratio of the peak energy stored in an oscillation cycle to the energy lost each cycle, is a essential indicator in the design of 2D nanomechanical resonators. A less damped resonator has an intrinsically high Q meaning that larger resonance peak can be ob-

1
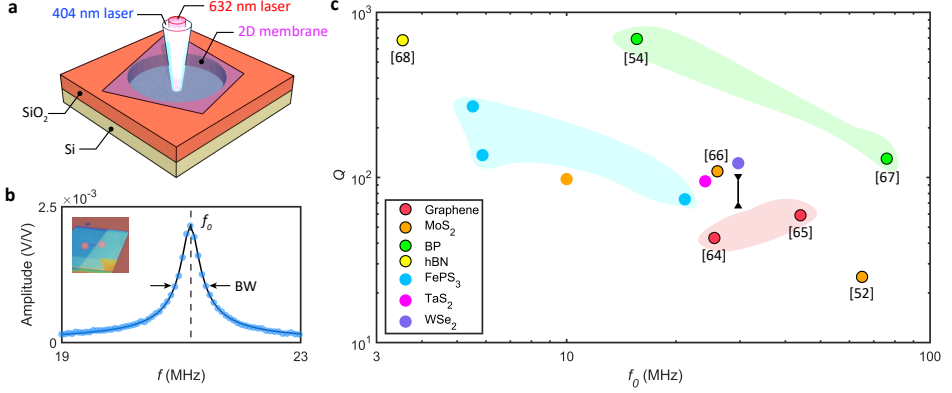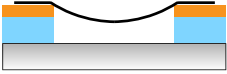
Figure 1.4: Optothermal excitation on 2D nanomechanical resonators. **a** Schematic diagram. The device is composed of suspended 2D membrane on a circular cavity. **b** Resonance peak of a FePS$_3$ resonator. Insert, optical image of the measured FePS$_3$ resonator. **c** Resonance frequency f_0 and quality factor Q for different types of 2D nanomechanical resonators, measured at room temperature and in vacuum. The dots without frame are obtained from our measurements.

tained. Q is dominated by the intrinsic dissipation mechanisms of the resonator, such as materials-defect-induced loss [60], interlayer coupling [54, 61] and thermoelastic damping [62, 63]. These need to be optimized to produce high-Q resonators, so as to increase the frequency sensitivity as well as to reduce the power required to maintain the oscillation. Figure. 1.4c shows the reported results of f_0 and Q for types of 2D nanomechanical resonators [52, 54, 64–68]. In general, we find a decrease of Q as f_0 increases in most cases, which is in line with the reported observations [69]. Also, compared to graphene resonators, the product $f_0 \times Q$ for MoS$_2$, TaS$_2$ and WSe$_2$ resonators are larger because TMDs exhibit lower intrinsic energy dissipation than graphene [70].

STIFFNESS AND DEFLECTION SHAPE

Attributed to the high ratio of surface area to volume of 2D materials coupled with large out-of-plane vibration amplitudes, 2D nanomechanical resonators perform a variety of nonlinear dynamic behaviors [71]. Under nonlinear driven, the large amplitude of membrane vibration induces an enlarged radial in-plane tension, leading to the frequency response of the device to extend beyond its linear case, known as hardening or softening [54, 72, 73]. These phenomenons can be described by a Duffing equation to characterize the nonlinear dynamic parameters in 2D nanomechanical resonators [74]. The linear and nonlinear stiffness, k_1 and k_3, are highly dependent upon the deflection shape of the membrane. Table 1.1 summarizes the stiffness parameters and the corresponding deflection shape under three different cases [75]. We see that the linear stiffness is dominated by surface pretension n_0 of the membrane, while the nonlinear stiffness is related to the Young's modulus E, Poisson ratio v, thickness t and radius r of the membrane. In this thesis, the cases of AFM indentation and bulge test have been widely used to characterize the mechanically static and dynamic behaviours of 2D nanomechanical resonators.

Table 1.1: Summary of stiffness of 2D membranes under different deflection shapes, adapted from [75]. k_1, linear stiffness; k_3, nonlinear stiffness; n_0, pretension; t, thickness; E, Young's modulus; r, radius; v, Poisson ratio.

	k_1	k_3	Deflection shape
AFM indentation [76]	πn_0	$\frac{1}{(1.05 - 0.15v - 0.16v^2)}\frac{Et}{r^2}$	
Bulge test [77]	$4\pi n_0$	$\frac{8\pi Et}{3r^2(1-v)}$	
Nonlinear dynamics [75]	$1.56\pi n_0$	$\frac{\pi Et}{r^2(1.27 - 0.97v - 0.27v^2)}$	

1.2.2. APPLICATIONS

Considering the wide new and abundant range of dynamics brought from 2D nanomechanical resonators, they have the potential to be used in many applicable fields. Their atomic thickness and high aspect-ratio make them ideal candidates for straintronics and twistronics nanodevices [78, 79]. The out-of-plane flexibility and in-plane stiffness of suspended 2D membranes increase the tunable capability on resonance frequency yielding high-performance sensing applications for probing force [80], pressure [81], mass [4] and temperature [82]. In addition, the ability of 2D nanomechanical resonators to survive harsh environments involving temperature and pressure makes them well suited for space applications [83]. Moreover, due to their superior thermal conductivity, suspended 2D materials are promising for thermal managements in next-generation flexible electronic devices [84]. Recently, 2D nanomechanical resonators also show impressive potentials in the fields of biological nanotechnology, quantum transport and computing, as well as RF signal processing [2, 5, 85, 86].

1.3. FRAMEWORK OF THIS THESIS

In this thesis, we focus on the mechanics and thermodynamics of suspended 2D membranes, of which the main research concern for each chapter is listed in Table 1.2. In Chapter 2, we introduce the fabrication of 2D nanomechanical resonators, where the dry and wet transfer methods are utilized to suspend 2D flakes on the etched SiO_2/Si substrate. We then characterize the structural and static properties of the fabricated devices, such as the thickness and Young's modulus, which are taken as the basic parameters in the following analysis. Optomechanical measurement is further introduced in details, to explain how we detect the dynamic resonance and phononic thermal transport of 2D nanomechanical resonators in this thesis.

In Chapter 3, we propose a new technical route for fabricating 2D heterostructure resonators. This is achieved by growing MoS_2 layer on top of suspended graphene membrane through atomic layer deposition (ALD). The fabricated devices show the compa-

Table 1.2: Research concern of each chapter in this thesis.

	Key word	Device	Property
Chapter 1	Introduction		
Chapter 2	Methodology		
Chapter 3	ALD	MoS_2/Graphene heterostructure	Mechanics
Chapter 4	Buckling	$FePS_3$	Mechanics
Chapter 5	Heat transport	$2H-TaS_2$, Poly Si, $FePS_3$, ...	Thermodynamics
Chapter 6	Tunability	Graphene	Thermodynamics
Chapter 7	Interface	WSe_2/$FePS_3$ heterostructure	Thermodynamics
Chapter 8	Conclusion		

rable static and dynamic properties, while surprisingly, a lower interlayer energy dissipation, compared to their exfoliated counterparts, which verifies the feasibility of ALD technique for designing high-performance 2D resonators.

In Chapter 4, we look at the mechanical buckling bifurcation in 2D nanomechanical resonators. By heating up the devices, boundary compression is applied on the membrane, resulting in a vertical deformation of the membrane due to the buckling. We build a mechanical buckling model for clamped circular plate, which well describes the turning of temperature-dependent resonance frequency at the buckling location. In particular, we also observe an enhanced amplitude of resonance peak attributed to the low out-of-plane stiffness of the membrane near buckling bifurcation.

We then turn our attention more to the thermodynamic properties of suspended 2D membranes. In Chapter 5, we measure the resonance frequency and thermal time constant of 2D nanomechanical resonators as the function of temperature, respectively, so as to extract the thermal conductivity using a thermodynamic relation. However, this presented approach cannot be used to explain the heat transport in graphene, where the experimentally observed thermal time constant is about 100 times larger than theoretical estimation. As a result, in Chapter 6, we attribute this to a strong scattering of acoustic phonons, especially flexural phonon at the boundary between the suspended and supported region of graphene membrane. By applying in-plane tension in the membrane through electrostatic deflection, we modulate the transmission possibility of phonons at the boundary, thus to achieve an effective tuning on heat transport.

We further show our unpublished work that also brings exciting results for better understanding nano-scale mechanics and thermodynamics. In Chapter 7, we fabricate a double-layered $FePS_3$/WSe_2 heterostructure device, and use optomechanical measurement and COMSOL simulation to extract the thermal conductance at the interface. Finally, we give a summary of all works we have done in Chapter 8 and provide an outlook for future directions.

BIBLIOGRAPHY

[1]M.-Y. Li, S.-K. Su, H.-S. P. Wong, and L.-J. Li, "How 2d semiconductors could extend moore's law", Nature **567**, 169–170 (2019).

[2] B. Xu, P. Zhang, J. Zhu, Z. Liu, A. Eichler, X.-Q. Zheng, J. Lee, A. Dash, S. More, S. Wu, et al., "Nanomechanical resonators: toward atomic scale", Acs Nano **16**, 15545–15585 (2022).

[3] R. Frisenda, E. Navarro-Moratalla, P. Gant, D. P. De Lara, P. Jarillo-Herrero, R. V. Gorbachev, and A. Castellanos-Gomez, "Recent progress in the assembly of nanodevices and van der waals heterostructures by deterministic placement of 2d materials", Chemical Society Reviews **47**, 53–68 (2018).

[4] M. C. Lemme, S. Wagner, K. Lee, X. Fan, G. J. Verbiest, S. Wittmann, S. Lukas, R. J. Dolleman, F. Niklaus, H. S. van der Zant, et al., "Nanoelectromechanical sensors based on suspended 2d materials", Research **2020** (2020).

[5] K.-M. Hu, P. Bo, X.-Y. Li, Y.-H. Xin, X.-R. Bai, L. Li, and W.-M. Zhang, "Resonant nano-electromechanical systems from 2d materials", Europhysics Letters **131**, 58001 (2020).

[6] D. Chi, K. J. Goh, and A. T. Wee, *2d semiconductor materials and devices* (Elsevier, 2019).

[7] M. Dragoman, A. Dinescu, and D. Dragoman, "2d materials nanoelectronics: new concepts, fabrication, characterization from microwaves up to optical spectrum", physica status solidi (a) **216**, 1800724 (2019).

[8] Y. Qiu, "Two-dimensional materials beyond graphene: emerging opportunities for biomedicine", Nano Life **6**, 1642008 (2016).

[9] C. Hu, X. Wang, and B. Song, "High-performance position-sensitive detector based on the lateral photoelectrical effect of two-dimensional materials", Light: Science & Applications **9**, 88 (2020).

[10] S. A. Iyengar, A. B. Puthirath, and V. Swaminathan, "Realizing quantum technologies in nanomaterials and nanoscience", Advanced Materials, 2107839 (2022).

[11] V. Shanmugam, R. A. Mensah, K. Babu, S. Gawusu, A. Chanda, Y. Tu, R. E. Neisiany, M. Försth, G. Sas, and O. Das, "A review of the synthesis, properties, and applications of 2d materials", Particle & Particle Systems Characterization **39**, 2200031 (2022).

[12] P. G. Steeneken, R. J. Dolleman, D. Davidovikj, F. Alijani, and H. S. Van der Zant, "Dynamics of 2d material membranes", 2D Materials **8**, 042001 (2021).

[13] X. Li, M. Sun, C. Shan, Q. Chen, and X. Wei, "Mechanical properties of 2d materials studied by in situ microscopy techniques", Advanced Materials Interfaces **5**, 1701246 (2018).

[14] C. Lee, X. Wei, J. W. Kysar, and J. Hone, "Measurement of the elastic properties and intrinsic strength of monolayer graphene", science **321**, 385–388 (2008).

[15] N. M. Kommanaboina, M. F. Pantano, and A. Bagolini, "Optimization of an amplification mechanism enabling large displacements in mems-based nanomaterial testing devices", Micro and Nano Engineering **15**, 100131 (2022).

[16] L. Fei, S. Lei, W.-B. Zhang, W. Lu, Z. Lin, C. H. Lam, Y. Chai, and Y. Wang, "Direct tem observations of growth mechanisms of two-dimensional mos2 flakes", Nature communications **7**, 12206 (2016).

1

[17] Y. Li, S. Huang, C. Wei, C. Wu, and V. N. Mochalin, "Adhesion of two-dimensional titanium carbides (mxenes) and graphene to silicon", Nature communications **10**, 3014 (2019).

[18] J. Zhang, N. Kong, S. Uzun, A. Levitt, S. Seyedin, P. A. Lynch, S. Qin, M. Han, W. Yang, J. Liu, et al., "Scalable manufacturing of free-standing, strong ti3c2tx mxene films with outstanding conductivity", Advanced Materials **32**, 2001093 (2020).

[19] K. Liu, C.-L. Hsin, D. Fu, J. Suh, S. Tongay, M. Chen, Y. Sun, A. Yan, J. Park, K. M. Yu, et al., "Self-passivation of defects: effects of high-energy particle irradiation on the elastic modulus of multilayer graphene", Advanced Materials **27**, 6841–6847 (2015).

[20] S. Bertolazzi, J. Brivio, and A. Kis, "Stretching and breaking of ultrathin mos2", ACS nano **5**, 9703–9709 (2011).

[21] A. Castellanos-Gomez, V. Singh, H. S. van der Zant, and G. A. Steele, "Mechanics of freely-suspended ultrathin layered materials", Annalen der Physik **527**, 27–44 (2015).

[22] L. Song, L. Ci, H. Lu, P. B. Sorokin, C. Jin, J. Ni, A. G. Kvashnin, D. G. Kvashnin, J. Lou, B. I. Yakobson, et al., "Large scale growth and characterization of atomic hexagonal boron nitride layers", Nano letters **10**, 3209–3215 (2010).

[23] C. Li, Y. Bando, C. Zhi, Y. Huang, and D. Golberg, "Thickness-dependent bending modulus of hexagonal boron nitride nanosheets", Nanotechnology **20**, 385707 (2009).

[24] M. Moreno-Moreno, G. Lopez-Polin, A. Castellanos-Gomez, C. Gomez-Navarro, and J. Gomez-Herrero, "Environmental effects in mechanical properties of few-layer black phosphorus", 2D Materials **3**, 031007 (2016).

[25] J.-W. Jiang, T. Rabczuk, and H. S. Park, "A stillinger–weber potential for single-layered black phosphorus, and the importance of cross-pucker interactions for a negative poisson's ratio and edge stress-induced bending", Nanoscale **7**, 6059–6068 (2015).

[26] J.-Y. Wang, Y. Li, Z.-Y. Zhan, T. Li, L. Zhen, and C.-Y. Xu, "Elastic properties of suspended black phosphorus nanosheets", Applied Physics Letters **108**, 013104 (2016).

[27] A. A. Balandin, S. Ghosh, W. Bao, I. Calizo, D. Teweldebrhan, F. Miao, and C. N. Lau, "Superior thermal conductivity of single-layer graphene", Nano letters **8**, 902–907 (2008).

[28] X. Gu, Y. Wei, X. Yin, B. Li, and R. Yang, "Colloquium: phononic thermal properties of two-dimensional materials", Reviews of Modern Physics **90**, 041002 (2018).

[29] S. Chen, Q. Wu, C. Mishra, J. Kang, H. Zhang, K. Cho, W. Cai, A. A. Balandin, and R. S. Ruoff, "Thermal conductivity of isotopically modified graphene", Nature materials **11**, 203–207 (2012).

[30] A. A. Balandin, "Thermal properties of graphene and nanostructured carbon materials", Nature materials **10**, 569–581 (2011).

[31] H. Jang, J. D. Wood, C. R. Ryder, M. C. Hersam, and D. G. Cahill, "Anisotropic thermal conductivity of exfoliated black phosphorus", arXiv preprint arXiv:1510.00051 (2015).

[32] L. Lindsay and D. Broido, "Enhanced thermal conductivity and isotope effect in single-layer hexagonal boron nitride", Physical Review B **84**, 155421 (2011).

[33] X. Zhang, D. Sun, Y. Li, G.-H. Lee, X. Cui, D. Chenet, Y. You, T. F. Heinz, and J. C. Hone, "Measurement of lateral and interfacial thermal conductivity of single-and bilayer mos2 and mose2 using refined optothermal raman technique", ACS applied materials & interfaces **7**, 25923–25929 (2015).

[34] Z. Yan, C. Jiang, T. Pope, C. Tsang, J. Stickney, P. Goli, J. Renteria, T. Salguero, and A. Balandin, "Phonon and thermal properties of exfoliated tase2 thin films", Journal of Applied Physics **114**, 204301 (2013).

[35] S. Ghosh, W. Bao, D. L. Nika, S. Subrina, E. P. Pokatilov, C. N. Lau, and A. A. Balandin, "Dimensional crossover of thermal transport in few-layer graphene", Nature materials **9**, 555–558 (2010).

[36] Z. Wei, Z. Ni, K. Bi, M. Chen, and Y. Chen, "In-plane lattice thermal conductivities of multilayer graphene films", Carbon **49**, 2653–2658 (2011).

[37] R. Yan, J. R. Simpson, S. Bertolazzi, J. Brivio, M. Watson, X. Wu, A. Kis, T. Luo, A. R. Hight Walker, and H. G. Xing, "Thermal conductivity of monolayer molybdenum disulfide obtained from temperature-dependent raman spectroscopy", ACS nano **8**, 986–993 (2014).

[38] X. Gu, B. Li, and R. Yang, "Layer thickness-dependent phonon properties and thermal conductivity of mos2", Journal of Applied Physics **119**, 085106 (2016).

[39] S. Sahoo, A. P. Gaur, M. Ahmadi, M. J.-F. Guinel, and R. S. Katiyar, "Temperature-dependent raman studies and thermal conductivity of few-layer mos2", The Journal of Physical Chemistry C **117**, 9042–9047 (2013).

[40] I. Jo, M. T. Pettes, J. Kim, K. Watanabe, T. Taniguchi, Z. Yao, and L. Shi, "Thermal conductivity and phonon transport in suspended few-layer hexagonal boron nitride", Nano letters **13**, 550–554 (2013).

[41] F. Kargar, E. A. Coleman, S. Ghosh, J. Lee, M. J. Gomez, Y. Liu, A. S. Magana, Z. Barani, A. Mohammadzadeh, B. Debnath, et al., "Phonon and thermal properties of quasi-two-dimensional feps3 and mnps3 antiferromagnetic semiconductors", ACS nano **14**, 2424–2435 (2020).

[42] S. Lee, F. Yang, J. Suh, S. Yang, Y. Lee, G. Li, H. Sung Choe, A. Suslu, Y. Chen, C. Ko, et al., "Anisotropic in-plane thermal conductivity of black phosphorus nanoribbons at temperatures higher than 100 k", Nature communications **6**, 1–7 (2015).

[43] A. Bagri, S.-P. Kim, R. S. Ruoff, and V. B. Shenoy, "Thermal transport across twin grain boundaries in polycrystalline graphene from nonequilibrium molecular dynamics simulations", Nano letters **11**, 3917–3921 (2011).

[44] M. Pourfath, *The non-equilibrium green's function method for nanoscale device simulation*, Vol. 3 (Springer, 2014).

[45] G. Xie, Y. Shen, X. Wei, L. Yang, H. Xiao, J. Zhong, and G. Zhang, "A bond-order theory on the phonon scattering by vacancies in two-dimensional materials", Scientific reports **4**, 5085 (2014).

[46] Y. Kuang, L. Lindsay, S. Shi, X. Wang, and B. Huang, "Thermal conductivity of graphene mediated by strain and size", International Journal of Heat and Mass Transfer **101**, 772–778 (2016).

1

[47] N. Bonini, J. Garg, and N. Marzari, "Acoustic phonon lifetimes and thermal transport in free-standing and strained graphene", Nano letters **12**, 2673–2678 (2012).

[48] Y. Kuang, L. Lindsay, and B. Huang, "Unusual enhancement in intrinsic thermal conductivity of multilayer graphene by tensile strains", Nano letters **15**, 6121–6127 (2015).

[49] L. Lindsay, D. Broido, and N. Mingo, "Flexural phonons and thermal transport in graphene", Physical Review B **82**, 115427 (2010).

[50] Y. Xiao, F. Luo, Y. Zhang, F. Hu, M. Zhu, and S. Qin, "A review on graphene-based nano-electromechanical resonators: fabrication, performance, and applications", Micromachines **13**, 215 (2022).

[51] J. Lee and P. X.-L. Feng, "High frequency graphene nanomechanical resonators and transducers", in 2012 ieee international frequency control symposium proceedings (IEEE, 2012), pp. 1–7.

[52] J. Lee, Z. Wang, K. He, J. Shan, and P. X.-L. Feng, "High frequency mos2 nanomechanical resonators", ACS nano **7**, 6086–6091 (2013).

[53] F. Ye, A. Islam, T. Zhang, and P. X.-L. Feng, "Ultrawide frequency tuning of atomic layer van der waals heterostructure electromechanical resonators", Nano Letters **21**, 5508–5515 (2021).

[54] S. Kim, J. Yu, and A. M. Van Der Zande, "Nano-electromechanical drumhead resonators from two-dimensional material bimorphs", Nano letters **18**, 6686–6695 (2018).

[55] Z. Li, M. Xu, R. A. Norte, A. M. Aragón, F. Van Keulen, F. Alijani, and P. G. Steeneken, "Tuning the q-factor of nanomechanical string resonators by torsion support design", Applied Physics Letters **122**, 013501 (2023).

[56] R. Pezone, G. Baglioni, P. M. Sarro, P. G. Steeneken, and S. Vollebregt, "Sensitive transfer-free wafer-scale graphene microphones", ACS Applied Materials & Interfaces **14**, 21705–21712 (2022).

[57] F. Ye, J. Lee, and P. X.-L. Feng, "Electrothermally tunable graphene resonators operating at very high temperature up to 1200 k", Nano Letters **18**, 1678–1685 (2018).

[58] G. Verbiest, D. Xu, M. Goldsche, T. Khodkov, S. Barzanjeh, N. Von Den Driesch, D. Buca, and C. Stampfer, "Tunable mechanical coupling between driven microelectromechanical resonators", Applied Physics Letters **109**, 143507 (2016).

[59] A. Keskekler, H. Arjmandi-Tash, P. G. Steeneken, and F. Alijani, "Symmetry-breaking-induced frequency combs in graphene resonators", Nano letters **22**, 6048–6054 (2022).

[60] J. A. Henry, Y. Wang, D. Sengupta, and M. A. Hines, "Understanding the effects of surface chemistry on q: mechanical energy dissipation in alkyl-terminated (c1- c18) micromechanical silicon resonators", The Journal of Physical Chemistry B **111**, 88–94 (2007).

[61] P. F. Ferrari, S. Kim, and A. M. Van Der Zande, "Dissipation from interlayer friction in graphene nanoelectromechanical resonators", Nano letters **21**, 8058–8065 (2021).

[62] M. Will, M. Hamer, M. Muller, A. Noury, P. Weber, A. Bachtold, R. V. Gorbachev, C. Stampfer, and J. Guttinger, "High quality factor graphene-based two-dimensional heterostructure mechanical resonator", Nano letters **17**, 5950–5955 (2017).

[63] B. Witkamp, M. Poot, and H. S. van der Zant, "Bending-mode vibration of a suspended nanotube resonator", Nano letters **6**, 2904–2908 (2006).

[64] A. M. v. d. Zande, R. A. Barton, J. S. Alden, C. S. Ruiz-Vargas, W. S. Whitney, P. H. Pham, J. Park, J. M. Parpia, H. G. Craighead, and P. L. McEuen, "Large-scale arrays of single-layer graphene resonators", Nano letters **10**, 4869–4873 (2010).

[65] C. Chen, S. Rosenblatt, K. I. Bolotin, W. Kalb, P. Kim, I. Kymissis, H. L. Stormer, T. F. Heinz, and J. Hone, "Performance of monolayer graphene nanomechanical resonators with electrical readout", Nature nanotechnology **4**, 861–867 (2009).

[66] A. Castellanos-Gomez, R. van Leeuwen, M. Buscema, H. S. van der Zant, G. A. Steele, and W. J. Venstra, "Single-layer mos2 mechanical resonators", Advanced Materials **25**, 6719–6723 (2013).

[67] Z. Wang, H. Jia, X. Zheng, R. Yang, Z. Wang, G. Ye, X. Chen, J. Shan, and P. X.-L. Feng, "Black phosphorus nanoelectromechanical resonators vibrating at very high frequencies", Nanoscale **7**, 877–884 (2015).

[68] X.-Q. Zheng, J. Lee, and P. X.-L. Feng, "Hexagonal boron nitride nanomechanical resonators with spatially visualized motion", Microsystems & Nanoengineering **3**, 1–8 (2017).

[69] R. A. Barton, B. Ilic, A. M. Van Der Zande, W. S. Whitney, P. L. McEuen, J. M. Parpia, and H. G. Craighead, "High, size-dependent quality factor in an array of graphene mechanical resonators", Nano letters **11**, 1232–1236 (2011).

[70] J.-W. Jiang, H. S. Park, and T. Rabczuk, "Mos 2 nanoresonators: intrinsically better than graphene?", Nanoscale **6**, 3618–3625 (2014).

[71] A. Keşkekler, O. Shoshani, M. Lee, H. S. van der Zant, P. G. Steeneken, and F. Alijani, "Tuning nonlinear damping in graphene nanoresonators by parametric–direct internal resonance", Nature communications **12**, 1099 (2021).

[72] R. Mestrom, R. Fey, K. Phan, and H. Nijmeijer, "Simulations and experiments of hardening and softening resonances in a clamped–clamped beam mems resonator", Sensors and Actuators A: Physical **162**, 225–234 (2010).

[73] X. Zhang, K. Makles, L. Colombier, D. Metten, H. Majjad, P. Verlot, and S. Berciaud, "Dynamically-enhanced strain in atomically thin resonators", Nature Communications **11**, 5526 (2020).

[74] T. Inoue, Y. Anno, Y. Imakita, K. Takei, T. Arie, and S. Akita, "Resonance control of a graphene drum resonator in a nonlinear regime by a standing wave of light", ACS omega **2**, 5792–5797 (2017).

[75] D. Davidovikj, F. Alijani, S. J. Cartamil-Bueno, H. S. van der Zant, M. Amabili, and P. G. Steeneken, "Nonlinear dynamic characterization of two-dimensional materials", Nature Communications **8**, 1253 (2017).

[76] A. Castellanos-Gomez, M. Poot, G. A. Steele, H. S. Van Der Zant, N. Agraıt, and G. Rubio-Bollinger, "Elastic properties of freely suspended mos2 nanosheets", Advanced materials **24**, 772–775 (2012).

[77] P. Zhang, Y. Jia, M. Xie, Z. Liu, S. Shen, J. Wei, and R. Yang, "Strain-modulated dissipation in two-dimensional molybdenum disulfide nanoelectromechanical resonators", ACS nano **16**, 2261–2270 (2022).

[78] O. Çakıroğlu, J. O. Island, Y. Xie, R. Frisenda, and A. Castellanos-Gomez, "An automated system for strain engineering and straintronics of 2d materials", Advanced Materials Technologies **8**, 2201091 (2023).

[79] Z. Hennighausen and S. Kar, "Twistronics: a turning point in 2d quantum materials", Electronic Structure **3**, 014004 (2021).

[80] M. Hempel, D. Nezich, J. Kong, and M. Hofmann, "A novel class of strain gauges based on layered percolative films of 2d materials", Nano letters **12**, 5714–5718 (2012).

[81] E. Kramer, J. Van Dorp, R. Van Leeuwen, and W. Venstra, "Strain-dependent damping in nanomechanical resonators from thin mos2 crystals", Applied Physics Letters **107**, 091903 (2015).

[82] R. Wu, L. Ma, C. Hou, Z. Meng, W. Guo, W. Yu, R. Yu, F. Hu, and X. Y. Liu, "Silk composite electronic textile sensor for high space precision 2d combo temperature–pressure sensing", Small **15**, 1901558 (2019).

[83] T. Yildirim, L. Zhang, G. P. Neupane, S. Chen, J. Zhang, H. Yan, M. M. Hasan, G. Yoshikawa, and Y. Lu, "Towards future physics and applications via two-dimensional material nems resonators", Nanoscale **12**, 22366–22385 (2020).

[84] H. Song, J. Liu, B. Liu, J. Wu, H.-M. Cheng, and F. Kang, "Two-dimensional materials for thermal management applications", Joule **2**, 442–463 (2018).

[85] G. P. Neupane, W. Ma, T. Yildirim, Y. Tang, L. Zhang, and Y. Lu, "2d organic semiconductors, the future of green nanotechnology", Nano Materials Science **1**, 246–259 (2019).

[86] M. C. Lemme, D. Akinwande, C. Huyghebaert, and C. Stampfer, "2d materials for future heterogeneous electronics", Nature communications **13**, 1392 (2022).

2

2

METHODOLOGY

In this chapter, we introduce the production, transfer, and processing procedures of 2D nanomechanical resonators, as well as the fundamental testing approaches and the used experimental setups of this thesis. These ensure the accurate and reliable experimental outcomes.

2
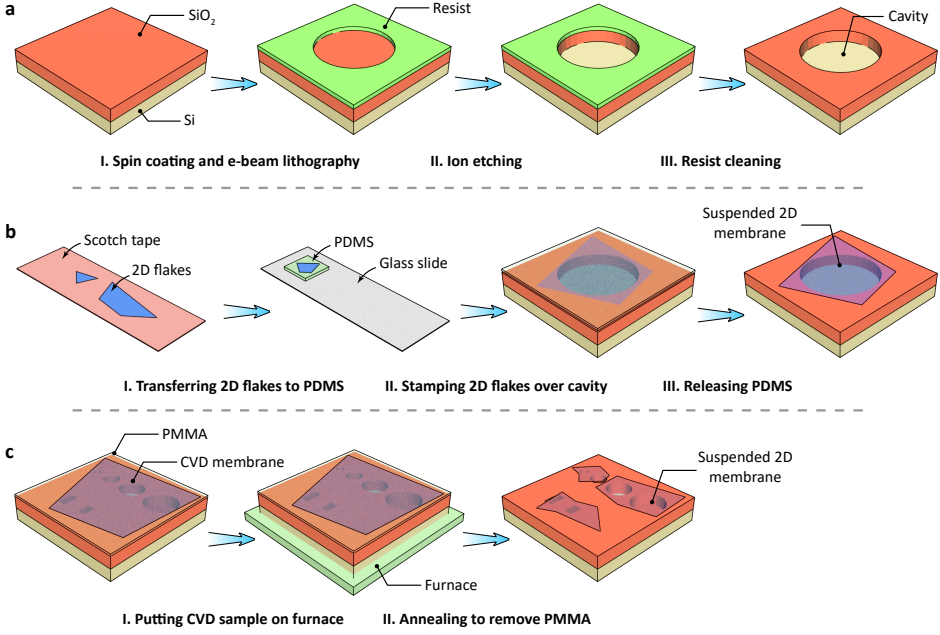
Figure 2.1: Recipes for suspending 2D nanosheets over SiO_2/Si substrate. **a** Preparation of substrate with etched circular cavities. A layer of electron beam resist is spin-coated and developed on the substrate **b** Mechanical exfoliation transfer method. **c** CVD transfer method.

2.1. FABRICATION

2.1.1. MECHANICAL EXFOLIATION TRANSFER

Suspended 2D membranes are extremely flexible out-of-plane as a consequence of their atomic thickness, yet very stiff within the plane due to their high Young's modulus [1, 2]. To peel off 2D sheets and make them free-standing, we begin by creating patterned cavities in the substrate. As illustrated in Fig. 2.1a, a layer of silicon dioxide (SiO_2) layer with a thickness of 285 nm is grown on the silicon wafer. To create circular cavities, the wafer is spin-coated with a positive resist and exposed by electron beam (e-beam) lithography. Afterwards, SiO_2 layer without protection is completely etched using CHF_3 and Ar plasma in a reactive ion etcher. This dry etching process results in cavities after the removal of resist, with high aspect ratios and well-defined dimensions examined by AFM and scanning electron microscopy (SEM).

Mechanical exfoliation of 2D crystals is a powerful and simple tool to create atomically thin membranes for research purposes. As shown in Fig. 2.1b, using Scotch tape, we exfoliate thin pieces of 2D sheets from natural crystal. These pieces are transferred to a optically transparent Polydimethylsiloxane (PDMS) stamp, where one sheet with suitable thickness and size is selected under optical microscopy. We then flip the stamp upside-down and clamp it above the SiO_2/Si substrate fixed on the XYZ stage. Using optical microscopy, we align the position of the stamp, making it exactly on top of the circular

Figure 2.2: Optical images (top view) of 2D nanomechanical resonators fabricated by exfoliation transfer method. **a** FePS$_3$. **b** 2H-TaS$_2$. **c** MoS$_2$. **d** WSe$_2$. Black error bar: 10 μm.
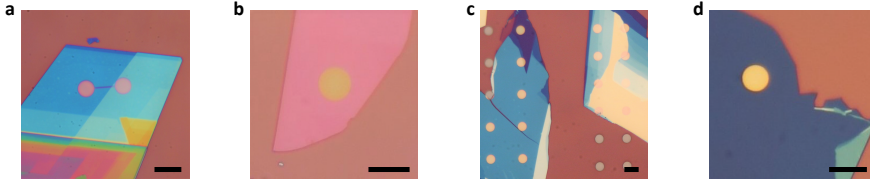
cavity. Afterwards, the stamp is brought into contact with the substrate and then slowly released. Due to a stronger adhesion of 2D materials on SiO$_2$ compared to PDMS, the release of stamp will leave the sheet on the substrate, forming a suspended 2D membrane over the cavity. Using the introduced approach, different types of 2D nanomechanical resonators have been fabricated in this thesis, of which several devices are shown in Figs. 2.2a to 2.2d. Here, the observed color difference under microscopy allows us to primarily evaluate the thickness of the transferred membranes, from monolayer to bulk.

2.1.2. CHEMICAL VAPOR DEPOSITION (CVD) TRANSFER

Mechanical exfoliation is a time-consuming process that yields relatively small or single samples. Thus, it is unable to fulfill the requirement for mass fabrication of large-area uniform 2D membranes. Chemical vapor deposition (CVD) has been demonstrated to provide large-area coverage [3]. Reliable transfer of large-area 2D membranes onto arbitrary substrates is a critical step in the use of CVD-grown 2D materials for most practical applications. In Chapter 6, the bilayer graphene devices are fabricated by directly transferring CVD graphene/polymethyl methacrylate (PMMA) over the cavities (see Fig. 2.1c). The PMMA is then removed by annealing the chip inside a furnace. However, we find that CVD graphene is usually broken into small pieces during the annealing.

Here, we introduce a novel and feasible pathway for suspending ultra-large CVD graphene membranes, as depicted in Fig. 2.3. First, multi-layer graphene was deposited using CVD on a thin-film Mo catalyst (Fig. 2.3a). For this, 50 nm of Mo was sputter coated on a 100 mm Si (100) wafer with 600 nm of thermal oxide. The CVD deposition was performed at a substrate temperature of 915 °C using 960/40/25 of, receptively, Ar/H$_2$/CH$_4$ at a pressure of 25 mbar. The growth time was set to 60 minutes, after which the wafer was cooled down in an Ar ambient. The frames to fabricate the drums were manufactured using deep reactive ion etching (DRIE) of a 100 mm Si (100) wafer (Fig. 2.3b). As hard mask, 6 μm of SiO$_2$ was deposited on both side of the wafer using plasma-enhanced CVD. Holes in the hard mask were subsequently patterned using optical lithography and reactive ion etching, which was followed by DRIE till the SiO$_2$ hard mask at the bottom of the hole was reached. Next, Teflon residues from the DRIE were stripped and the SiO$_2$ hard mask was completely removed using wet etching in BHF(1:7). Finally, a 300 nm thermal oxide was grown on the wafer by wet oxidation.

Next, the graphene was transferred from the growth substrate to the target substrate with a wet transfer process (Fig. 2.3c). Individual die of graphene on wafer were im-

2
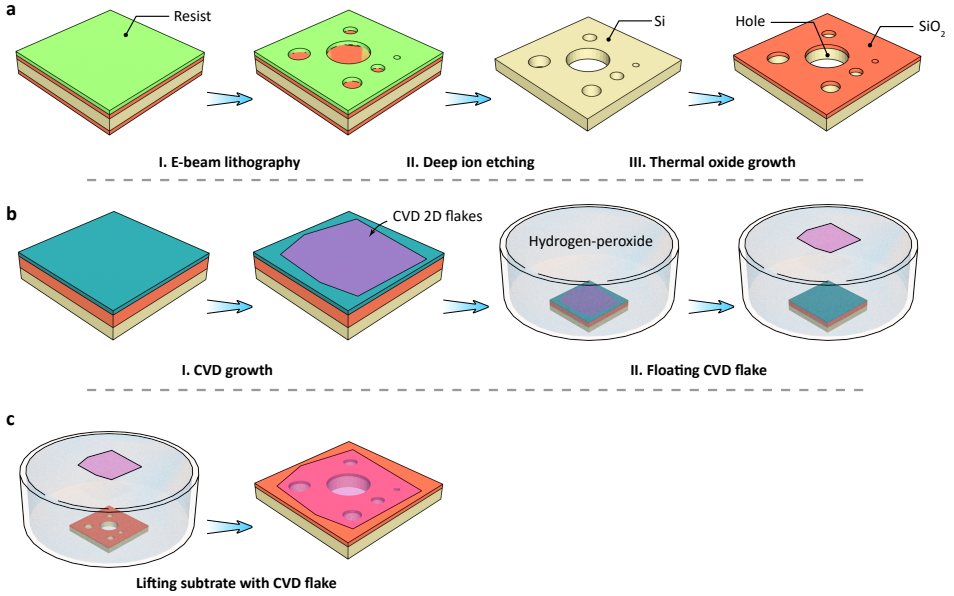
Figure 2.3: Wet CVD transfer method to fabricate ultra-large graphene resonators. **a** Recipe of SiO$_2$/Si substrate with circular holes. **b** Preparation for CVD graphene membrane. **c** Transfer process.

mersed separately in 30% hydrogen-peroxide for 25 mins. Hydrogen peroxide etches away the Mo underneath the graphene layer, so that the graphene is released, floating on the surface of the hydrogen peroxide solution. Hydrogen peroxide was exchanged with deionized (DI) water. The DI water was then replaced twice more to ensure the removal of peroxide. Subsequently, 1.5 ml of detergent solution (1 drop of Triton ×100 in 150 ml of DI water) was dissolved in the water to reduce the surface tension and improve membrane formation yield. Graphene was then carefully picked up onto the substrate with holes. Graphene membranes were formed over the holes. The sample was dried at room temperature for 25 mins, and was put under a glass bell for the next 24 hours to dry completely.

Figure 2.4 shows the suspended graphene resonators through wet CVD transfer method, with the radius varies from < 100 μm to > 1000 μm. Since graphene is an atomically thin membrane, boundary deformation caused by the irregular distribution of tension between graphene and substrate happens inevitably during transfer, results in the visible wrinkles and crumples. These kinds of structural defects will play a role on graphene resonators with respect to their mechanical properties. This CVD transfer method has also been used to fabricate high-performance graphene microphones in recent studies [4, 5].

2.2. CHARACTERIZATION

After the 2D nanomechanical resonator is fabricated, we characterize its fundamental properties, such as thickness, Young's modulus, Raman spectrum and structural defor-
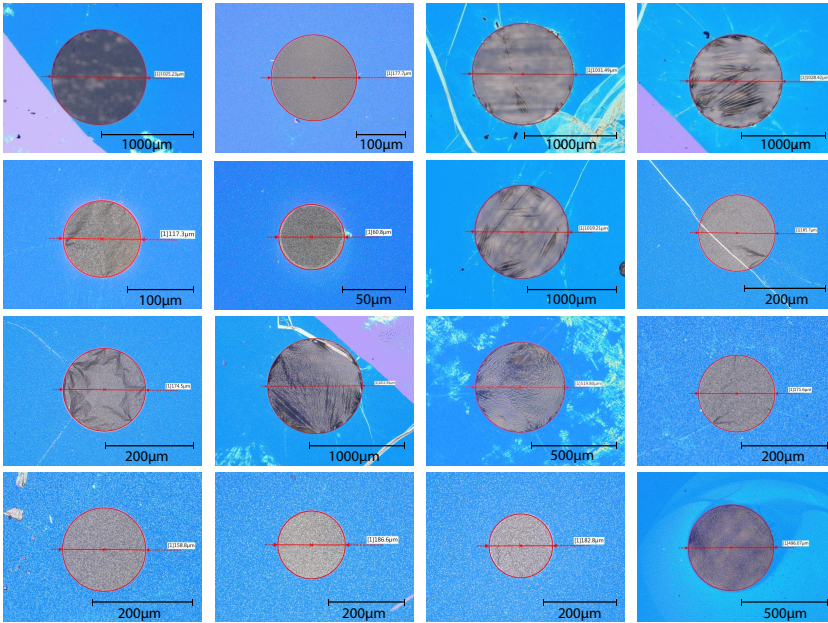
Figure 2.4: Optical images of suspended graphene membranes fabricated by wet CVD transfer method.

mation, so as to confirm its quality on the substrate. More importantly, these predetermined parameters are highly required in the following, in order to determine the mechanical tuning and phononic thermal transport of the fabricated devices.

2.2.1. ATOMIC FORCE MICROSCOPE (AFM)

Atomic Force Microscopy (AFM) works on the principle of surface sensing by using a very sharp tip attached to the silicon cantilever. The tip can be used to image the surface features of a sample with atomic resolution or indent the sample depending on the mode of usage. When the cantilever tip comes in contact with the sample during the measurements, the cantilever bends. This cantilever bending is detected using a laser diode and a photodetector. AFM is generally used to capture maps of modulus, adhesion, deformation, conductivity, surface potential, permittivity, and optical absorption of the sample. All these capabilities contained within one single instrument makes AFM a versatile platform for investigating highly multidisciplinary research. Therefore, AFM stands out among other techniques for the characterization of 2D materials.

MEMBRANE THICKNESS

AFM tapping mode is typically used to determine the thickness of 2D membranes. We scan the edge of the supported part of the membrane, as illustrated in Fig. 2.5a (black frame). Along with the scanning profile, the height increases from 16.3 nm to 23.8 nm, indicating a thickness of the membrane about 7.5 nm (see Figs. 2.5b and 2.5c). However, since graphene membrane is bumpy with bulges and collapses, it is not fairly accurate to
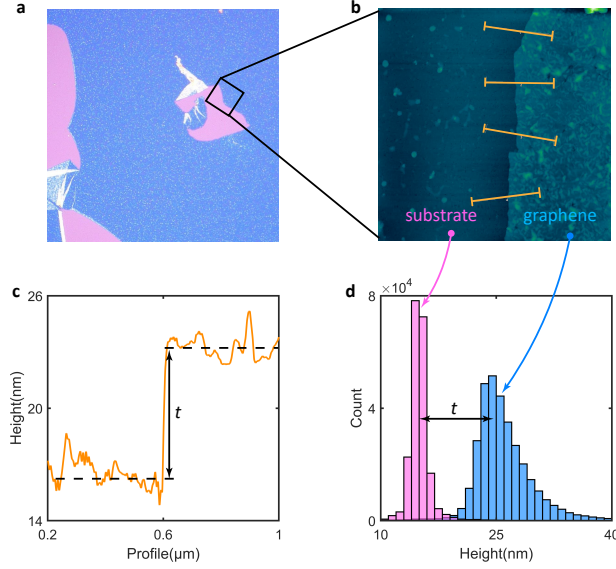
Figure 2.5: Measurement of membrane thickness t using AFM tapping mode. **a** Optical image of graphene membrane (supported part). Black square is the selected area for AFM scanning. **b** Obtained scanning graph, where the left and right regions are substrate and graphene, respectively. **c** Measured height profile follows the orange line in **b**. **d** Height histograms of substrate (cyan) and graphene membrane (blue).

extract the realistic thickness from only a few scanning profiles. Therefore, we count the height of the entire region which contains thousands of points, as plotted in Fig. 2.5d. The mean height of both substrate and graphene membrane are thus calculated by the statistics, so as to obtain the mean thickness of the membrane about 9.6 nm.

YOUNG'S MODULUS

Force-indentation AFM method is a reliable mechanical probe of 2D material membrane defection in response to a force applied at its center by an AFM cantilever tip, as illustrated in Fig. 2.6a. We first image the fabricated membrane using AFM tapping/AC mode and thus to align the tip exactly above the center of the membrane (see insert in Fig. 2.6b). Then the membrane is indented with a preset value of maximum force to obtain its corresponding deflection behaviour. The actual deflection, δ, of the membrane is accounted for by by subtracting the cantilever deflection Δz_c from the Z-scanner(piezo) readout Δz as $\delta = \Delta z_c - \Delta z$. We use AFM cantilevers of typical stiffness k_c ranging from $10-46$ N/m in the force-indentation experiments.

We extract the pretension n_0 and Young's modulus E of the membrane from the obtained force-deflection curve, as shown in Fig. 2.6b. Small applied force F causes the linearly proportional membrane deflection δ, thus the linear spring constant of the membrane k_1 is related to both its pretension n_0 and bending rigidity. However, at large F range, we find F is cubic in δ. The tip radius of $7-10$ nm, confirmed by scanning electron microscope imaging, is far smaller than the equivalent radius of the membrane. Therefore, the force-deflection responses of AFM indentation (Fig. 2.6b), corresponding

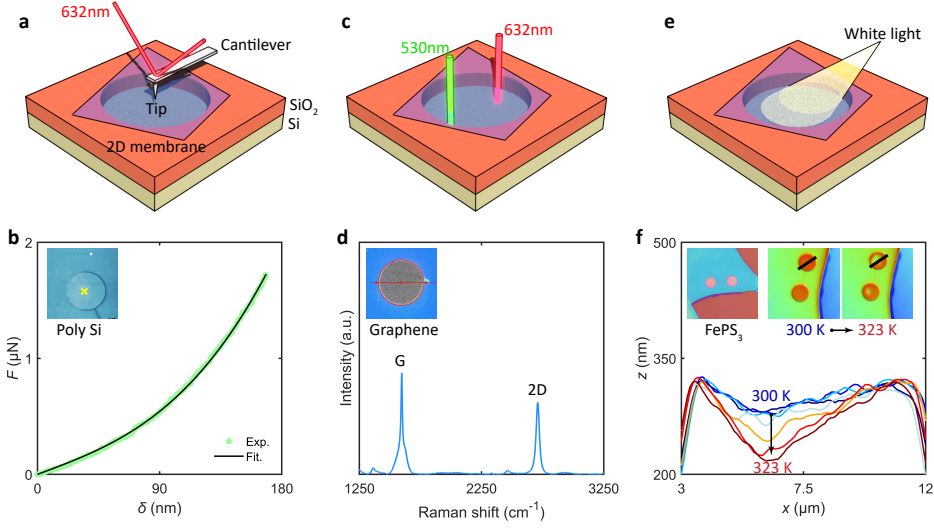Figure 2.6: Characterizations on suspended 2D membrane. **a** Schematic of AFM nanoindentation. **b** Indentation curve of force F versus deflection δ for a polycrystalline silicon membrane, which is fitted with Eq. 2.1 to extract the Young's modulus of the membrane. Δz is the motion of piezoelectric-actuated cantilever in vertical direction. Insert, optical image of polycrystalline silicon membrane. **c** Schematic of Raman microscope. **d** Measured Raman spectrum of the suspended CVD graphene membrane. Insert, optical image of the measured device. **e** Schematic of white light interferometry. **f** Heating-induced membrane deflection in FePS$_3$ resonator measured by white light interferometry. Inserts, optical and height profile images of the measured device.

to the deflection shape in Table 1.1, can be described by [6]:

$$F = (\frac{16\pi D}{r^2}\delta) + n_0\pi\delta + Etq^3(\frac{\delta^3}{r^2}), \tag{2.1}$$

where $D = Et^3/(12(1-v^2))$ is the bending rigidity of the membrane which can be ignored if t is small enough, v is Poisson ratio, $n_0 = Et\epsilon_0/(1-v)$ is the pretension, ϵ_0 is the built-in strain, and $q = 1/(1.05 - 0.15v - 0.16v^2)$ is the geometry-related parameter. Note that the cubic term of F versus δ is only determined by E while independent to n_0, thus generally in our experiments, we adopt a large enough force to trigger the nonlinear indentation. This allows us to extract the accurate E of the membrane from Eq. 2.1, with the measured r and t from AFM tapping mode and the value of v taken from literature

2.2.2. RAMAN MICROSCOPY

Raman spectroscopy is a fast, non-destructive, and high-resolution tool for investigating layered materials. Attributed to Raman scattering, the frequency of light will shift when it passes through a medium. This shift is related to the modes of molecular vibration or rotation, means that each molecule has its own characteristic Raman spectrum. As a result, Raman has the capability of characterizing the structural properties of 2D materials, as well as detecting the layer thickness, band structures, doping type, concentration, electron–phonon coupling, and interlayer coupling [7, 8]. Figure 2.6c shows the schematic

illustration of Raman measurement. We used a Horiba Raman Spectroscopy that provides two kinds of optical wavelengths: 532 nm (green) and 633 nm (red) lasers. We fix our sample on xy piezoelectric positioning stage, thus to obtain the Raman spectrum anywhere in the membrane. As shown in Fig. 2.6d, through the measured amplitude ratio between G peak at 1596 cm^{-1} and 2D peak at 2709 cm^{-1} [9], we determine that our fabricated CVD graphene is multilayer.

2.2.3. WHITE LIGHT INTERFEROMETRY

As shown in Figs. 2.6e and 2.6f, we use scanning white light interferometry to characterize the structural deformation of the suspended 2D membrane. The white light from a source is reflected at a beam splitter and passes into a Michelson infinite conjugate interferometric objective, where it is split into a reference beam and a sample beam [10]. The two beams interfere and produce patterns of bright and dark fringes that depend upon the path length difference between the reference and sample beams. The fringe pattern is detected with a camera as a piezo actuator displaces the interference objective to produce a series of data, which is digitally processed to yield a 3D image of the surface. This technique is mainly utilized in Chapter 4 to check the downward deformation of 2D membranes due to mechanical buckling.

2.3. OPTOMECHANICAL MEASUREMENT

2.3.1. LASER INTERFEROMETRY AND RESONANT MEMBRANE MOTION

With the fabrication of 2D nanomechanical resonators complete, an experimental setup is required to actuate and detect their motion. To this end, we fix the sample onto a laser interferometry system, as depicted in Figs. 2.7a and 2.7b. An alternating current is used to adjust the intensity of diode laser ($\lambda = 404$ sinm), which produces a periodically-changing heat flux and actuate the membrane moving due to thermal expansion. On the other hand, a helium-neon laser ($\lambda = 632$ nm) is employed for the readout of motion. This is performed using Fabry-Perot interferometry, in which the substrate and the membrane act as a fixed back mirror and a moving mirror, respectively (Fig. 2.7a, bottom). The resulting optical cavity makes it possible to probe the membrane motion, since the reflected light intensity is a clear function of the membranes location along the horizontal direction.

The transmission from the diode laser modulation to the signal detected by the photodiode is then handled by a vector network analyzer (VNA). This gives the amplitude and phase of the signal as function of frequency. The sample is mounted on a xyz piezopositioning stage inside a vacuum chamber. The laser spot irradiated on the membrane is in the order of ~$1-2$ μm, allowing to measure membranes > 2 μm in lateral size. The whole operation is done under a high vacuum of 10^{-6} mbar.

Using the laser interferometry technique, we acquire the amplitude $|A_f|$ of the frequency response for a 2H-TaS$_2$ resonator over the frequency ranging from 10 kHz to 100 MHz, as plotted in Fig. 2.7c. Near the fundamental resonance peak (see Fig. 2.7d),
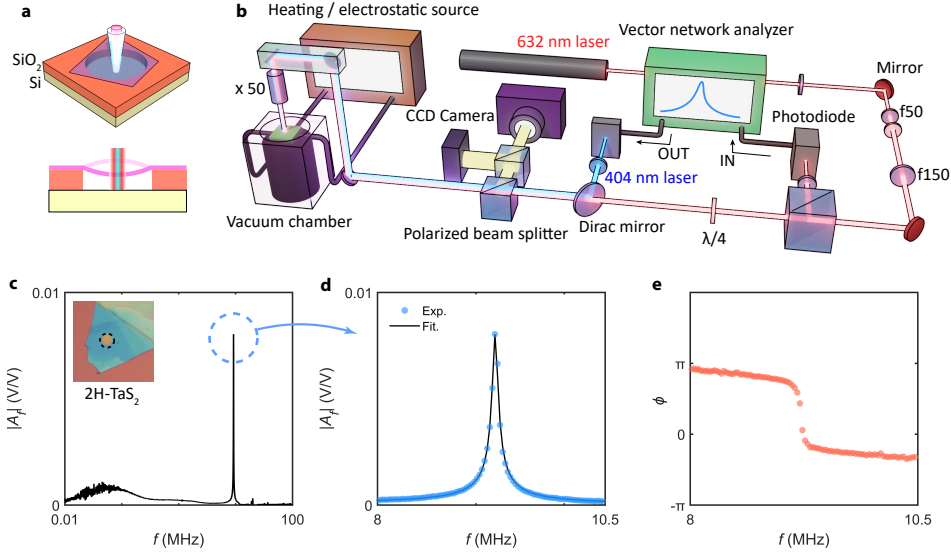
Figure 2.7: Detection on resonant membrane motion. **a** Schematic of 2D nanomechanical resonator under optomechanical drive. **b** Schematic of the laser interferometry setup. **c** Amplitude $|A_f|$ of frequency response for a 2H-TaS$_2$ resonator. Insert, optical image of the measured device. **d** $|A_f|$ of fundamental resonance frequency peak, which is fitted with Eq. 2.2 to extract the resonance frequency f_0 and its quality factor Q. **e** Corresponding phase ϕ of the resonance peak.

$|A_f|$ can be described by a linear harmonic oscillating model [11] given by:

$$|A_f| = \frac{A/m}{\sqrt{\left(\omega_0^2 - \omega^2\right)^2 + \left(\frac{\omega_0\omega}{Q}\right)^2}}, \tag{2.2}$$

where A is amplitude of driven force, m is the effective mass of the membrane, $\omega = 2\pi f$, $\omega_0 = 2\pi f_0$, and Q is the quality factor for a membrane in motion that indicates the energy dissipation together with the mechanical oscillation. The phase ϕ of the vibration, with a shift of 180° near f_0 (see Fig. 2.7e), is given by:

$$\phi_f = -\arctan\left(\frac{\omega_0\omega}{Q\left(\omega_0^2 - \omega^2\right)}\right). \tag{2.3}$$

Here, by fitting Eq. 2.2 to the measured $|A_f|$ in Fig. 2.7d, we extract $f_0 = 9.21$ MHz and $Q = 153.5$ for 2H-TaS$_2$ resonator.

For vibration of clamped circular resonator, the fundamental resonance frequency f_0 is determined by both the bending rigidity D and pretension n_0 of the resonator [11, 12]:

$$f_0 \approx \sqrt{f_{\text{membrane}}^2 + f_{\text{plate}}^2} = \sqrt{\left(\frac{2.4}{\pi d}\right)^2 \frac{n_0}{\rho t} + \left(\frac{5.1}{\pi d^2}\right)^2 \frac{D}{\rho t}}, \tag{2.4}$$

where $d = 2r$ is the diameter of the resonator and $D = \frac{Et^3}{12(1-v^2)}$. Note that the constants 2.4 and 5.1 in Eq. 2.4 are determined by assuming a specific mode shape of the resonator [13]. Eq. 2.4 is appropriate for estimating the resonance of the exfoliated few-layer 2D samples, as commonly used in this thesis. While for thin membrane-like resonators, such as the double-layer CVD graphene resonators, $n_0 r^2/D \rightarrow \infty$, thus $f_0 \approx f_{\text{membrane}}$ and the contribution from the flexural rigidity can be negligible.

2.3.2. TUNING RESONANCE FREQUENCY

The resonant tunability of 2D nanomechanical resonator make it promising for ultra-sensitive sensing designs. In this thesis, we mainly utilize the electrostatic deflection or temperature changing to modulate the in-plane surface tension in 2D resonators, so as to achieve an effective modulation of their resonance frequency.

ELECTROSTATIC METHOD

For electrostatic method, as illustrated in Fig. 2.8a, the suspended membrane forms a capacity C_g with a bottom Si gate electrode underneath. The gate voltage V_g change leads to an electrostatic force on the membrane and pull it downwards, resulting in the enhanced tensile stress in the membrane. This tuning approach was firstly studied by Chen C. in graphene drumheads [14, 15]. According to a continuum mechanics model that analyses the minimum of total energy in a circular membrane under electrostatic loading, the tuned f_0 can be expressed as:

$$f_0(V_g) = \frac{1}{2\pi}\sqrt{\frac{1}{m_{\text{eff}}}\left(\frac{2\pi Et\epsilon_0}{1-v^2} + \frac{8\pi Et}{(1-v^2)r^2}z_g^2 - \frac{1}{2}\frac{\partial^2 C_g}{\partial z_g^2}V_g^2\right)}, \tag{2.5}$$

where $m_{\text{eff}} = 0.271\pi r^2 \rho t$ is the effective mass, $\frac{\partial^2 C_g}{\partial z_g^2} \approx \frac{0.542\epsilon_0 \pi r^2}{g_0^3}$ is the second derivative of capacitance, g_0 is the depth of capacitor between membrane and Si substrate, ε_0 is the permittivity of vacuum, $z_g \approx \frac{\epsilon_0 r^2(1-v)V_g^2}{8g_0^2 Et\epsilon_0}$ is the deflection of membrane [16]. Notice that in Eq. 2.5 the contribution from bending rigidity is already ignored. Assume $t = 1$ nm, $r = 4$ μm, $v = 0.16$, $\rho = 2330$ kg/m^3, $\epsilon_0 = 1 \times 10^{-4}$, and $E = 200$ GPa for a graphene resonator, we estimate f_0 as the function of V_g using Eq. 2.5, as plotted in Fig. 2.8a. We see f_0 first decreases and then increases again as $|V_g|$ increases, attributed to the electrostatic softening (related to $\frac{\partial^2 C_g}{\partial z_g^2}$) and the enhanced deflection z_g of the membrane, correspondingly. This kind of W-shape $f_0(V_g)$ is typically observed in previous studies on the gate-tuning 2D NEMS [17, 18], as well as the double-layer graphene resonators studied in Chapter 6.

THERMAL METHOD

For thermal method, surface strain in the membrane is controlled through temperature change (Fig. 2.8b). Ye, F. [19] has reported on the first experimental demonstration of electrothermally tuned graphene NEMS resonators operating in the high frequency band. Owe to the unique negative thermal expansion coefficient (TEC) of graphene,
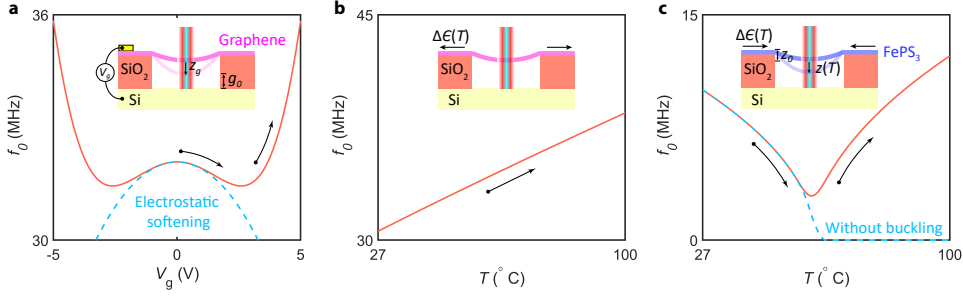
Figure 2.8: Tuning resonance frequency f_0 in 2D nanomechanical resonators. **a** Electrostatic tuning on graphene resonator. **b** Thermal tuning on graphene resonator. **c** Thermal tuning on 2D resonators with positive thermal expansion coefficient.

temperature rise from heating causes a tensile strain in the membrane, leading to an enhancement of resonance frequency. This variation can be expressed by:

$$f_0(T) = \frac{2.4}{2\pi r} \sqrt{\frac{E}{\rho(1-\nu)}(\epsilon_0 + \Delta\epsilon(T))}, \tag{2.6}$$

where the thermally-induced strain is $\Delta\epsilon(T) = \int_{T_0}^{T}(\alpha_g - \alpha_{Si})\,dT$, T_0 is the initial temperature, α_g and α_{Si} are the TECs of graphene and substrate, respectively. Because $\alpha_{SiO_2} \ll \alpha_{Si}$, the effect of the thin SiO_2 layer in the substrate can be neglected. Assume $\alpha_g = -3 \times 10^{-6}$ K^{-1} and $\alpha_{Si} = 2.63 \times 10^{-6}$ K^{-1}, we estimate f_0 as the function T for graphene resonator by Eq. 2.6, as shown in Fig. 2.8b. It should be noticed that the TEC of 2D materials, α_m, is a T-dependent parameter, thus the slope of $\frac{df_0}{dT}$ is not always a constant, especially at high T range. The direct connection between f_0 and α_m opens up the prospect of studying condensed matter physics based on 2D nanomechanical resonators. In addition, according to the thermodynamic relation, the thermal expansion coefficient is proportional to a fundamental material parameter of the materials - the specific heat [16, 20]. This allows to further investigate the thermal properties and phononic transport of 2D membranes, as we discuss in Chapter 5.

Opposite to graphene, the TECs for most 2D materials, such TMDs like MoS$_2$, are positive and much larger than α_{Si}. Temperature rise generates compressive stress in the membrane, resulting in a decrease of f_0. However, this reduction will not end up to a zero f_0. Actually, f_0 of 2D resonators first decreases, while as T further increases, f_0 levels off and then starts increasing with T, as observed before in 1D-beam resonators [21, 22]. This increase in f_0 arises from the thermally-induced buckling of the membrane when the internal thermal stress exceeds the critical load. Following our derivation in Chapter 4, f_0 for a clamped circular plate under buckling is found as:

$$f_0(T) = \frac{10.33t}{\pi d^2} \sqrt{\frac{E}{3\rho(1-\nu^2)}(1 + \beta(1-\nu^2)\frac{3z^2 - z_{free}^2}{t^2} + \frac{3}{8}(1+\nu)\frac{U(T)d}{t^2}},\tag{2.7}$$

where $U(T)$ is the thermally induced in-plane displacement of the plate, ρ is the mass density, $d = 2r$ is the diameter, $z(T)$ is the central deflection of the membrane, z_{free} is
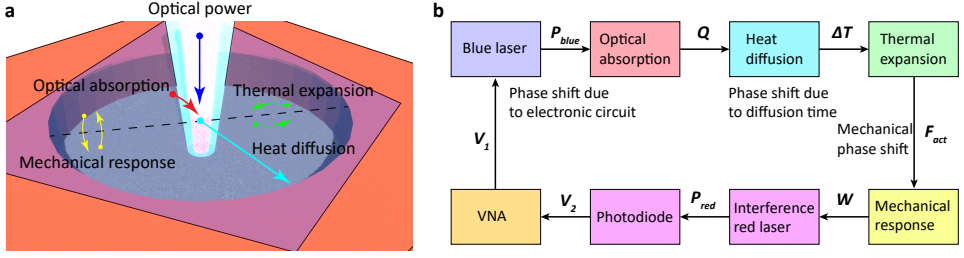
Figure 2.9: Measurement method to characterize the heat transport in suspended 2D membrane. **a** Illustration to depict how the optical power is transduced into mechanical motion of the membrane. **b** Corresponding block diagram that describe how deflection signal readout from the optothermal actuation, adapted from [23].

the central deflection of free plate without loading (when $U = 0$), and β is a fitting factor which is related to v (see Chapter 4). The expression of z is:

$$\frac{32}{3}\left(1 - \frac{z_{free}}{z}\right) - 10.7\beta(1-v^2)\left(\frac{z_{free}^2 - z^2}{t^2}\right) + 4(1+v)\frac{Ud}{t^2} = 0. \tag{2.8}$$

We adopt Eq. 2.8 to plot f_0 as a function of T for buckled 2D material resonators. For practical reasons, we use materials parameters $t = 30$ nm, $r = 4$ μm, $v = 0.304$, $\rho = 3375$ kg/m^3, $\epsilon_0 = 5.8 \times 10^{-4}$, $\alpha_m = 2.5 \times 10^{-5}$ and $E = 70$ GPa, that are close to that of FePS$_3$, which is used in Chapter 4 to Chapter 7. As shown in Fig. 2.8c, f_0 first decreases and then starts increasing with T, which is attributed to the increase of $z(T)$ once the buckling happens.

2.3.3. OPTOMECHANICAL DELAY

It is discovered that, in relation to the intensity modulation of the laser that opto-thermally actuates a circular membrane, its mechanical motion is delayed by a typical thermal time constant τ [23]. This is attributed to the time required for heat flux to diffuse through the system. Therefore, the optomechanics offers a tool for researching the dynamic thermal characteristics of 2D materials. Details of the physical mecha-nism for optomechanics in the membrane can be found in Fig. 2.9. The diode (blue) laser with modulated intensity P_{blue} is absorbed by 2D membrane through photon-electron-phonon couplings [24, 25], generating a virtually instantaneous heat flux Q in the center. This heat will raise the membrane's temperature and flow in-plane to-ward the substrate, leading to the temperature increase ΔT of the membrane. This results in a time-dependent thermal expansion force F_{act} that actuates the motion of the membrane, which is in-phase at the range far below resonance frequency. Finally, the intensity modulation P_{red} of the red laser due to the interference effect is used to detect the motion and generate the entire spectrum.

Since the coupling of photoexcited carriers in 2D membrane and the detection of red laser are instantaneous with timescales of a few picoseconds, we thus conclude that the time delay in optothermal drive of the membrane is nearly arisen from the delay that the heat flux requires to diffuse through the membrane to increase the temperature.
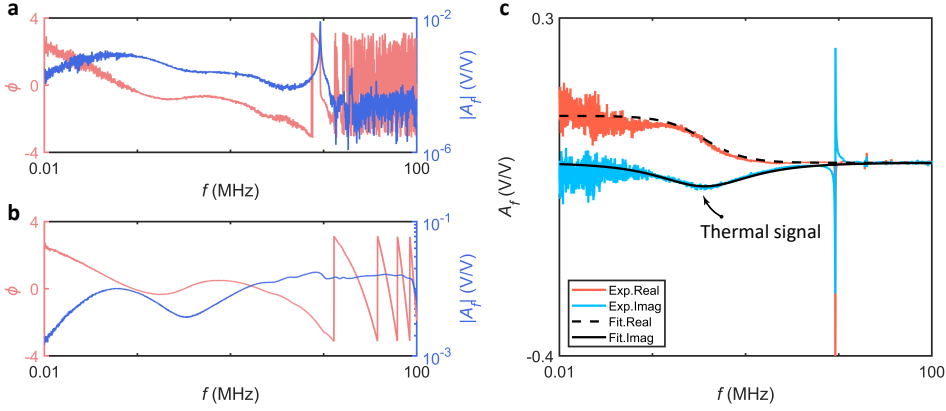
Figure 2.10: Determining thermal time constant τ of suspended 2D membrane under optothermal actuation. **a** Amplitude $|A_f|$ (blue) and phase ϕ (red) of the measured frequency response for 2H-TaS$_2$ resonator. **b** Background signals of laser interferometry system, which is obtained by directly irradiating blue laser on the photo diode. **c** Calibrated signals A_f of the amplitude, of which the imaginary part (blue) is fitted with Eq. 2.9 to extract τ of the membrane.

Following a thermal model that describes the heat equation in a circular thin plate [23], the motion of the membrane A_f at the frequencies far below resonance is given by:

$$A_f = \frac{A_{\text{th}}}{i2\pi f\tau + 1}, \tag{2.9}$$

where A_{th} is the thermal expansion amplitude. We still use the experimental data of 2H-TaS$_2$ device (the same one in Fig. 2.7c), $|A_{f1}|$ and ϕ_{f1}, as shown in Fig. 2.10a. In order to correct the intrinsic phase shifts in the laser interferometry setup, the blue laser is directly irradiated to photodiode to obtain the calibration curves, $|A_{f2}|$ and ϕ_{f2}, for the system (Fig. 2.10b). This is done by the deconvolution given as $|A_f| = \frac{|A_{f1}|}{|A_{f2}|}$ and $\phi_f = \phi_{f1} - \phi_{f2}$. In Fig. 2.10c, we fit Eq. 2.9 to the deconvoluted imaginary part of A_f (drawn solid line). Here, the thermal signal in the imaginary part of A_f is located at around 362.87 kHz, corresponding to $\tau = (2\pi \times 362.87 \text{ kHz})^{-1} = 438.58$ ns.

2.4. COMSOL SIMULATION

The "heat transport in thin shells" module of COMSOL Multiphysics allows us to simulate the thermal transport in suspended 2D membranes. We build a simple circular domain as illustrated in Fig. 2.11a, where a point heat source of radius r_0 is set in the center of the membrane. We define thermal insulation condition on the edge of the entire system, with a initial temperature $T_0 = 273.15$ K. The mesh size is using "Extra fine" to ensure the simulation accuracy of thermal transport (see the insert in Fig. 2.11b).

The simulated temperature distribution of the built model in COMSOL is shown in Fig. 2.11b. Here, we adopt $r_0 = 0.5$ μm which is equal to the realistic size of laser spot in our optomechanical measurements, the membrane radius $r = 4$ μm, specific heat $c_p = 700$ J/kgK, mass density $\rho = 3375$ kg/m^3, and thermal conductivity $k = 5$ W/mK. We
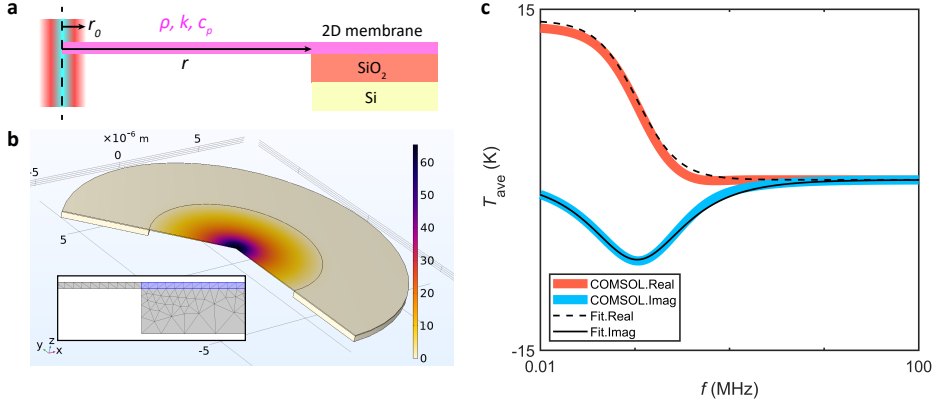
Figure 2.11: COMSOL simulation of thermal transport in suspended 2D membrane. **a** Schematic diagram (cross-section view) of COMSOL model. **b** Temperature distribution of the membrane. Insert, mesh setting in COMSOL software. **c** Simulation results of average temperature T_{ave} versus heating frequency f, which are fitted with Eq. 2.9 to extract thermal time constant τ of the membrane.

further define a harmonic perturbation of heating with a frequency varies from 10 kHz to 100 MHz, and thus to obtain the average temperature T_{ave} of the membrane as a function of heating frequency f, as shown in Fig. 2.11c. By fitting Eq. 2.9 to the simulated T_{ave} versus f, we extract the thermal time constant $\tau = 1506.9$ ns.

From literature [26], we know that the in-plane thermal time constant τ of 2D membrane is related to its thermal characteristics give by:

$$\tau = \frac{r^2 c_p \rho}{\mu^2 k},\tag{2.10}$$

where μ^2 is the thermal diffusive constant. By substituting r, c_p, ρ and k, as well as the simulated τ into Eq. 2.10, we extract $\mu^2 \approx 5.02$. In comparison, we obtain a larger result of $\mu^2 = 5.78$ from analytical model in Chapter 5. Considering the small size of laser spot as well as the influence of Si substrate, the analysis via COMSOL simulation is reliable to the realistic case. In Chapter 7, we use COSMOL model to study the thermal transport in 2D heterostructure, providing us a more convenient pathway compared to analytical solution.

Bibliography

[1] P. G. Steeneken, R. J. Dolleman, D. Davidovikj, F. Alijani, and H. S. Van der Zant, "Dynamics of 2d material membranes", 2D Materials **8**, 042001 (2021).

[2] C. Lee, X. Wei, J. W. Kysar, and J. Hone, "Measurement of the elastic properties and intrinsic strength of monolayer graphene", science **321**, 385–388 (2008).

[3] J. W. Suk, A. Kitt, C. W. Magnuson, Y. Hao, S. Ahmed, J. An, A. K. Swan, B. B. Goldberg, and R. S. Ruoff, "Transfer of cvd-grown monolayer graphene onto arbitrary substrates", ACS nano **5**, 6916–6924 (2011).

[4]G. Baglioni, R. Pezone, S. Vollebregt, K. C. Zobenica, M. Spasenović, D. Todorović, H. Liu, G. J. Verbiest, H. S. van der Zant, and P. G. Steeneken, "Ultra-sensitive graphene membranes for microphone applications", Nanoscale **15**, 6343–6352 (2023).

[5]R. Pezone, G. Baglioni, P. M. Sarro, P. G. Steeneken, and S. Vollebregt, "Sensitive transfer-free wafer-scale graphene microphones", ACS Applied Materials & Interfaces **14**, 21705–21712 (2022).

[6]A. Castellanos-Gomez, M. Poot, G. A. Steele, H. S. Van Der Zant, N. Agraıt, and G. Rubio-Bollinger, "Elastic properties of freely suspended mos2 nanosheets", Advanced materials **24**, 772–775 (2012).

[7]M. Paillet, R. Parret, J.-L. Sauvajol, and P. Colomban, "Graphene and related 2d materials: an overview of the raman studies", Journal of Raman Spectroscopy **49**, 8–12 (2018).

[8]F. Liang, H. Xu, X. Wu, C. Wang, C. Luo, and J. Zhang, "Raman spectroscopy characterization of two-dimensional materials", Chinese Physics B **27**, 037802 (2018).

[9]A. C. Ferrari, J. C. Meyer, V. Scardaci, C. Casiraghi, M. Lazzeri, F. Mauri, S. Piscanec, D. Jiang, K. S. Novoselov, S. Roth, et al., "Raman spectrum of graphene and graphene layers", Physical review letters **97**, 187401 (2006).

[10]R. R. Vallance, C. J. Morgan, S. M. Shreve, and E. R. Marsh, "Micro-tool characterization using scanning white light interferometry", Journal of micromechanics and microengineering **14**, 1234 (2004).

[11]J. Lee, Z. Wang, K. He, J. Shan, and P. X.-L. Feng, "High frequency mos2 nanomechanical resonators", ACS nano **7**, 6086–6091 (2013).

[12]A. Castellanos-Gomez, R. van Leeuwen, M. Buscema, H. S. van der Zant, G. A. Steele, and W. J. Venstra, "Single-layer mos2 mechanical resonators", Advanced Materials **25**, 6719–6723 (2013).

[13]M. Will, M. Hamer, M. Muller, A. Noury, P. Weber, A. Bachtold, R. V. Gorbachev, C. Stampfer, and J. Guttinger, "High quality factor graphene-based two-dimensional heterostructure mechanical resonator", Nano letters **17**, 5950–5955 (2017).

[14]C. Chen, S. Lee, V. V. Deshpande, G.-H. Lee, M. Lekas, K. Shepard, and J. Hone, "Graphene mechanical oscillators with tunable frequency", Nature nanotechnology **8**, 923–927 (2013).

[15]C. Chen, S. Rosenblatt, K. I. Bolotin, W. Kalb, P. Kim, I. Kymissis, H. L. Stormer, T. F. Heinz, and J. Hone, "Performance of monolayer graphene nanomechanical resonators with electrical readout", Nature nanotechnology **4**, 861–867 (2009).

[16]M. Šiškins, M. Lee, S. Mañas-Valero, E. Coronado, Y. M. Blanter, H. S. van der Zant, and P. G. Steeneken, "Magnetic and electronic phase transitions probed by nanomechanical resonators", Nature communications **11**, 2698 (2020).

[17]F. Ye, A. Islam, T. Zhang, and P. X.-L. Feng, "Ultrawide frequency tuning of atomic layer van der waals heterostructure electromechanical resonators", Nano Letters **21**, 5508–5515 (2021).

[18]J. Lee, Z. Wang, K. He, R. Yang, J. Shan, and P. X.-L. Feng, "Electrically tunable single-and few-layer mos2 nanoelectromechanical systems with broad dynamic range", Science advances **4**, eaao6653 (2018).

[19]F. Ye, J. Lee, and P. X.-L. Feng, "Electrothermally tunable graphene resonators operating at very high temperature up to 1200 k", Nano Letters **18**, 1678–1685 (2018).

[20]M. Lee, M. Šiškins, S. Mañas-Valero, E. Coronado, P. G. Steeneken, and H. S. van der Zant, "Study of charge density waves in suspended 2h-tas2 and 2h-tase2 by nanomechanical resonance", Applied Physics Letters **118**, 193105 (2021).

[21]E. Kramer, J. Van Dorp, R. Van Leeuwen, and W. Venstra, "Strain-dependent damping in nanomechanical resonators from thin mos2 crystals", Applied Physics Letters **107**, 091903 (2015).

[22]S. Rechnitz, T. Tabachnik, M. Shlafman, S. Shlafman, and Y. E. Yaish, "Mode coupling bi-stability and spectral broadening in buckled carbon nanotube mechanical resonators", Nature Communications **13**, 5900 (2022).

[23]R. J. Dolleman, S. Houri, D. Davidovikj, S. J. Cartamil-Bueno, Y. M. Blanter, H. S. Van Der Zant, and P. G. Steeneken, "Optomechanics for thermal characterization of suspended graphene", Physical Review B **96**, 165421 (2017).

[24]H. Zobeiri, N. Hunter, R. Wang, T. Wang, and X. Wang, "Direct characterization of thermal nonequilibrium between optical and acoustic phonons in graphene paper under photon excitation", Advanced Science **8**, 2004712 (2021).

[25]H. Liu, J. Wang, Y. Liu, Y. Wang, L. Xu, L. Huang, D. Liu, and J. Luo, "Visualizing ultrafast defect-controlled interlayer electron–phonon coupling in van der waals heterostructures", Advanced Materials **34**, 2106955 (2022).

[26]R. J. Dolleman, D. Lloyd, M. Lee, J. S. Bunch, H. S. Van Der Zant, and P. G. Steeneken, "Transient thermal characterization of suspended monolayer mos 2", Physical Review Materials **2**, 114008 (2018).

3

3

NANOMECHANICAL RESONATORS FABRICATED BY ATOMIC LAYER DEPOSITION ON SUSPENDED 2D MATERIALS

Atomic layer deposition (ALD), a layer-by-layer controlled method to synthesize ultra-thin materials, provides various merits over other techniques such as precise thickness control, large area scalability and excellent conformality. In this chapter, we demonstrate the possibility of using ALD growth on top of suspended 2D materials to fabricate nanomechanical resonators. We fabricate ALD nanomechanical resonators consisting of a graphene/MoS_2 heterostructure. Using AFM indentation and optothermal drive, we measure their mechanical properties including Young's modulus, resonance frequency and quality factor, showing a lower energy dissipation compared to their exfoliated counterparts. We also demonstrate the fabrication of nanomechanical resonators by exfoliating an ALD grown NbS_2 layer. This study exemplifies the potential of ALD techniques to produce high-quality suspended nanomechanical membranes, providing a promising route towards high-volume fabrication of future multilayer nanodevices and nanoelectromechanical systems.

3.1. Introduction

The properties of 2D materials, in particular their ultralow weight and ultrahigh mechanical flexibility, provides them with an excellent sensitivity to external forces [1–3]. Hence, resonators from 2D materials have become a popular choice for the next generation of nanoelectromechanical systems (NEMS) [4, 5]. Recently, there is surge towards stacking different 2D materials into heterostructures often exhibiting better sensing properties. Such heterostructures are used for tunable resonators and oscillators [6], and can potentially lead to better sensors in microphone and pressure sensing applications [5].

To achieve high-performance nanomechanical resonators, clean interfaces between different 2D materials are important [7]. Therefore, bottom-up synthesis methods were developed, of which chemical vapor deposition (CVD) is the most attractive due to its large-scale and high-quality growth. The main shortcoming of CVD, however, is the difficulty to accurately control the thickness and morphology of grown 2D materials. Atomic layer deposition (ALD), a vapor phase thin film deposition technique based on self-limiting surface reactions, inherently yields atomic-scale thickness control, excellent uniformity, and conformality [8]. ALD processes exists for a large variety of materials ranging from pure elements to metal oxides and chalcogenides [9]. In terms of 2D materials, ALD was applied to fabricate 2D-based field effect transistors, p-n diode devices, solar cells and photodetectors, displaying high electrical and optical uniformities [10]. Since experimental research of ALD materials for nanomechancial resonators is unexplored territory, it is of interest to study the potential of such devices and evaluate their mechanical performance.

In this chapter, we show two types of nanomechancial resonators fabricated using ALD: one consists of a heterostructure made from exfoliated graphene (bottom layer) and ALD MoS_2 (top layer) and the other is ALD NbS_2. We use atomic force microscope (AFM) indentation to determine their Young's moduli and use an optomechanical method to study their resonance frequency and corresponding quality factor in vacuum conditions. The extracted parameters from our measurements agree well with literature values for 2D exfoliated or CVD resonators. Furthermore, by fitting a relation between the quality factors before and after ALD, we verify a low-level dissipation induced by ALD MoS_2. This work indicates the potential of ALD fabrication techniques for realizing multilayer nanomechanical membranes and resonators with enhanced functionality and thickness control.

3.2. Results and discussion

3.2.1. Fabrication

The ALD layers are deposited (see Figs. 3.1a and 3.1b) by plasma-enhanced atomic layer deposition (PE-ALD) technique using an Oxford Instruments Plasma Technology FlexAL ALD reactor. The base pressure of the system is 10^{-6} Torr. The metal-organic precursors bis(tert-butylimido)-bis(dimethylamido) molybdenum (STREM Chemical, Inc., 98%) and (tert-butylimido)-tris-(diethylamino)-niobium (STREM Chemical, Inc., 98%) are used for MoO_x and NbO_x growth, respectively [9, 11]. The Mo and Nb precursors are kept in stainless steel bubblers at 50 °C and 65 °C, respectively and are bubbled using Ar as the carrier gas. In both the processes, O_2 plasma is used as the coreactant. The
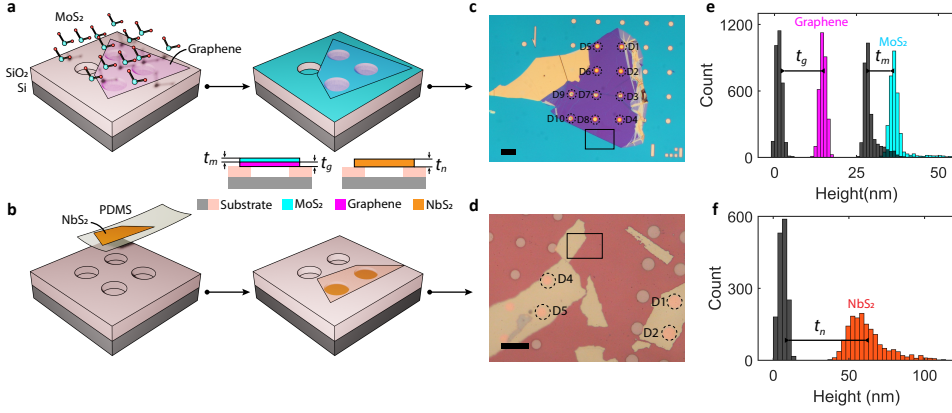
Figure 3.1: Fabrication of the ALD nanomechanical resonators measured in this work. **a** Fabrication process of exfoliated graphene/ALD MoS_2 heterostructure resonators. MoS_2 is directly deposited onto the suspended graphene membrane. **b** Fabrication process of ALD NbS_2 resonators. ALD NbS_2 flake is exfoliated from glassy carbon using PDMS, and then transferred on top of a prepatterned Si/SiO_2 substrate with circular cavities. Inserts between **a** and **b** are the cross-section views of the heterostructure and NbS_2 resonators, respectively. **c** and **d** Optical images of our fabricated heterostructure and NbS_2 devices, respectively, where the black scale bars are $20\,\mu m$. Note that the heterostructure devices D3 and D9 were broken during deposition. **e** and **f**, Height histograms of SiO_2/Si substrate (black), graphene (pink) and MoS_2 (blue) measured by AFM scanning, allow us to extract the thicknesses $t_g = 13.3\,nm$, $t_m = 7.8\,nm$, and $t_n = 56.1\,nm$. The scanning areas for fixing t_g and t_n are the black frames in **c** and **d**, respectively, while that for fixing t_m is the scratch on MoS_2 layer after deposition. We observe that the thickness distribution of ALD MoS2 is satisfyingly as uniform as the exfoliated graphene, while the surface of thick ALD NbS_2 is rugged.

MoO_x and NbO_x films are deposited at $100\,°C$ and $150\,°C$, respectively. More details on the PE-ALD recipes can be found in Appendix section 1.

Both the MoS_2 and NbS_2 films are synthesized by a two step approach. As the first step, metal oxide (MoO_x or NbO_x) film is deposited by PE-ALD technique. Next, the metal oxide film is sulfurized at $900\,°C$ in H_2S environment (10% H_2S and 90% Ar) to form metal sulfide film (MoS_2 or NbS_2). As shown in Figs. 3.1a and 3.1c, the MoS_2 film is synthesized by PE-ALD on top of suspended graphene drums, resulting in 10 resonators with a radius $r = 4\,\mu m$. Note that device D3 and D9 broke (buckled, Fig. 3.1c) during fabrication and will not be considered further. On the other hand, NbS_2 film is synthesized by growing NbO_x on glassy carbon followed by sulfurization at $900\,°C$. Then, we fabricate the NbS_2 resonators by transferring the NbS_2 films from glassy carbon substrate over circular cavities in a SiO_2/Si substrate to form suspended drums using the Scotch tape method [5] (see Fig. 3.1b). We tested the transfer of ALD nanoflakes with different thicknesses grown on different susbtrates and found that only the transfer of thick NbS_2 films from glassy carbon to the substrate with cavities was possible (see table 3.1). The cavities have a depth of 285 nm and were fabricated by reactive ion etching [4]. The fabricated NbS_2 resonators, shown in Fig. 3.1d, have a radius of $r = 4\,\mu m$ (devices D1 and D2) or $r = 3\,\mu m$ (devices D4 and D5). We use AFM (tapping mode) to scan the surface of our fabricated samples, to determine the thickness of the 2D materials. By calculating the height difference between the membranes and substrate (see the statistics in Figs. 3.1e

and 3.1f), we extract the mean thickness of the graphene t_g = 13.3 nm (40 layers), MoS$_2$ t_m = 7.8 nm (12 layers) and NbS$_2$ t_n = 56.1 nm (92 layers), respectively. The total thickness of the heterostructure is thus $t_h = t_m + t_g$ = 21.1 nm.

Raman spectra of both ALD heterostructures and NbS$_2$ devices, obtained with a 515 nm green laser at room temperature (see Appendix section 1), clearly show the expected Raman modes and thereby verify the quality of fabricated devices after the high-temperature ALD synthesis processes. We also measure and theoretically analyse the Raman intensity ratio between the Si peak of suspended MoS$_2$/graphene membrane and that of substrate (see Fig. 3.4), from which we conclude that ALD MoS$_2$ layer is only deposited on top (but not on bottom) of the exfoliated graphene membrane in the fabricated heterostructure devices.

3.2.2. AFM INDENTATION AND STATIC MECHANICS

After fabrication, we determine the Young's modulus of the ALD devices by indenting with an AFM (contact mode) cantilever at the centre of the suspended area (see Fig. 3.2a, insert). Following literature [12], the applied vertical force F versus membrane deflection δ for a circular membrane (composed of single material), as depicted in Fig. 3.2a, is given by

$$F = \left(\frac{16\pi D}{r^2}\right)\delta + n_0\pi\delta + Etq^3\left(\frac{\delta^3}{r^2}\right), \tag{3.1}$$

where $D = \gamma E t^3/(12(1-v^2))$ is bending rigidity, E is Young's modulus, v is the Poisson ratio, n_0 is pretension, $q = 1/(1.05-0.15v-0.16v^2)$, and γ is a factor that quantifies the effect of interlayer shear interactions on D in multilayer 2D materials [13]. The first two terms in Eq. 3.1 scale linearly with δ ($F \sim \delta$) and are set by D and n_0; while the third cubic term ($F \sim \delta^3$) is due to the geometric nonlinearity of the membrane, which lead to an increase in the in-plane stress that depends on its Young's modulus E. Note that Eq. 3.1 is suitable for NbS$_2$, while for heterostructures, it contains contributions from graphene and MoS$_2$ layers (see Eq. 3.6). We use the bulk Poisson ratios v_g = 0.165, v_m = 0.25 and v_n = 0.28 of graphene, MoS$_2$ and NbS$_2$, respectively, in further analysis. In addition, considering the measured layer numbers of graphene, MoS$_2$ and NbS$_2$ membranes, we use the factors γ_g = 0.1 and γ_m = 0.4 from literature [13] and assume $\gamma_n = \gamma_m$.

We extract E_h and E_n by the fitting the measured F versus δ with Eq. 3.6 and Eq. 3.1, respectively, which nicely describe the experimental data for the NbS$_2$ device D1 (pink points) and the heterostructure device D2 (green points) as shown in Fig. 3.2a. The extracted statistics of effective Young's moduli for heterostructure devices (E_h) and Young's moduli (E_n) for NbS$_2$ devices give the mean values of E_h = 952± 161 GPa and E_n = 101± 13 GPa, respectively. In Fig. 3.2b, we compare E_h and E_n with values reported in the literature: E_n shows a good agreement with the reported values of 75± 35 GPa [14–16]; E_h is between the reported values for MoS$_2$ 250 ± 120 GPa and graphene membranes 1025 ± 125 GPa [12, 17–20], but higher than the reported values for similar fully exfoliated heterostructures 461 ± 43 GPa [17, 21, 22]. The larger E_h might be caused by the stronger interlayer adhesion or the larger intrinsic Young's modulus of ALD MoS$_2$. The standard deviations in extracted Young's moduli, ±13 GPa and ±161 GPa for NbS$_2$ and heterostructure resonators, respectively, are comparable to the ones reported in literature for exfoliated materials. This illustrates the high homogeneity of ALD materials.
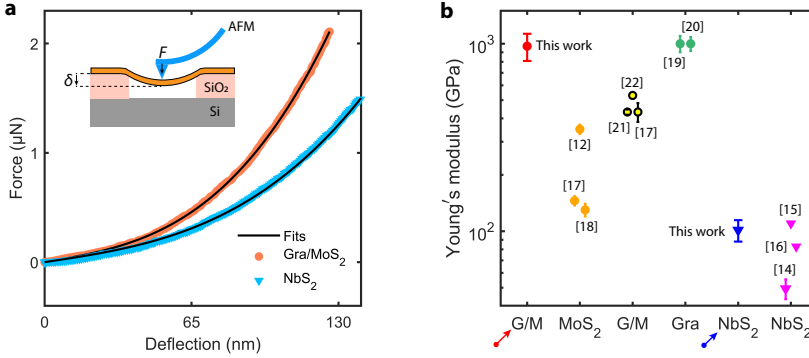
Figure 3.2: Static characterization of the fabricated ALD nanomechanical resonators. **a** Typical force-deflection curve obtained by AFM indentation onto the suspended part of heterostructure (green points) and NbS$_2$ (pink points) resonators. The solid lines show fits using the model from Eq. 3.1, gives the pretension and Young's modulus of the membranes. Insert: schematic of AFM indentation. Statistics over all devices give the mean values of E_h = 952 GPa (heterostructure) and E_n = 101 GPa (NbS$_2$). **b** Comparison of Young's modulus between this work (errorbars, marked with arrows in x-axis) and previous studies (bars and points). The numbers in brackets give the citations we select in **b**.

In addition to the Young's modulus, we also extract the pretension n_0 for each device. Tables 3.2 and 3.3 in Appendix show a complete overview of the obtained parameters from the fitting to Eq. 3.1. The extracted n_0 ranges from 0.45 to 1.55 N/m for all heterostructure and NbS$_2$ resonators, which are similar to values reported in the literature for resonators made by exfoliation and CVD methods [4, 21, 23].

3.2.3. DYNAMICS OF ALD RESONATORS

Let us now focus on the dynamics of the ALD resonators. We measured the dynamic response of the membranes with a laser interferometer [23] (see Fig. 3.3a, bottom). A power modulated blue diode laser (λ = 405 nm) photothermally actuates the resonator, while the refection of a continuous-wave red He-Ne laser (λ = 632 nm) is sensitive to the time-dependent position of membrane. A vector network analyzer (VNA) provides a signal at drive frequency f (OUT port) that modulates the blue laser intensity while the intensity of the red laser recorded by a fast photodiode is connected to the IN port. The VNA thus measures a signal z_f that is proportional to the ratio of the membrane amplitude and actuation force. By sweeping the drive frequency f, we locate the resonance peak in the range from 100 kHz to 100 MHz. Laser intensities are set to 0.3 mW (blue) and 1.1 mW (red), respectively. These intensities are low enough for the resonator to vibrate in the linear regime. All measurements were performed at room temperature in vacuum at a pressure of 10^{-5} mbar.

Figure 3.3a (top inserts) shows the measured signal z_f of NbS$_2$ device D6, at around the fundamental and second resonance frequency, respectively. By fitting z_f to the response function of a harmonic oscillator, we extract f_0 = 16.0 MHz with Q = 28.9 and f_1 = 25.3 MHz with Q = 34.4. For vibrations of clamped drums, we can compute the
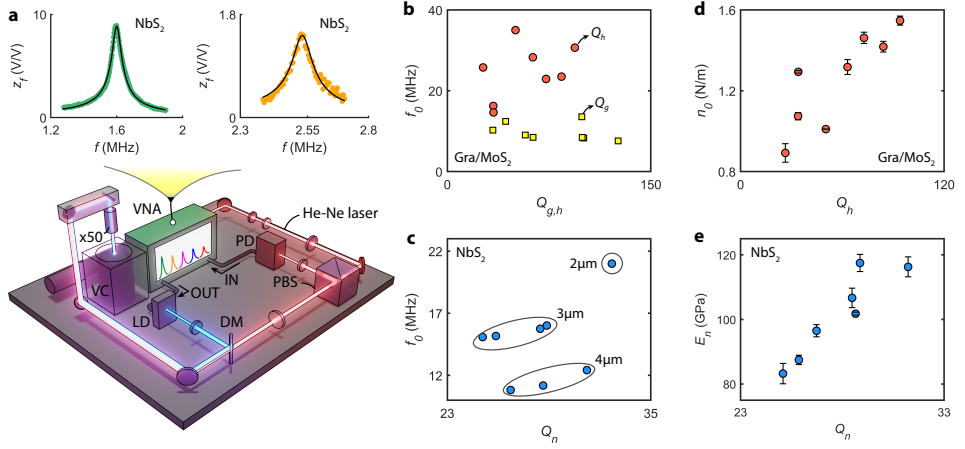
Figure 3.3: Dynamic characterization of the fabricated ALD nanomechanical resonators. **a** Top, the measured amplitude z_f (points) of NbS$_2$ device D6, around the fundamental and second resonance, respectively; z_f is fitted by a harmonic oscillator model (black lines) to extract resonance frequency and corresponding quality factor. Bottom, interferometry setup. ALD device is placed inside the vacuum chamber (VC). The diode laser (LD) is modulated by a vector network analyzer (VNA) to actuate the resonator, while intensity variations of the reflected He-Ne laser caused by resonator motion, are measured by photodiode (PD) and recorded with the VNA. PBS: polarized beam splitter; DM: dichroic mirror; x50: 50-fold objective. **b** The measured Q versus f_0 for graphene resonators before ALD (Q_g, yellow points) and for heterostructure resonators after ALD (Q_h, red points). **c** The measured Q_n versus f_0 for NbS$_2$ resonators. **d** Q_h versus the extracted pretension n_0. **e** Q_n versus the extracted Young's modulus E_n.

resonance frequencies f_i using [3]

$$f_i = \left(\frac{\mu_i}{2\pi}\right)\sqrt{\frac{D}{\sigma r^4}\left[\mu_i^2 + \frac{n_0 r^2}{D}\right]}, i = 0, 1, ..., \tag{3.2}$$

where $\sigma = \eta \rho t$ is the areal mass density, η is a correction factor of mass considering the contaminations on resonators, and μ_i is a mode-specific factor. We have $\mu_1 = 2.4048$ for the fundamental mode and $\mu_2 = 3.8317$ for the second mode. For an ideal membrane, in which $n_0 r^2$ is much larger than the flexural rigidity D and thus $n_0 r^2/D \rightarrow \infty$, we have $f_1/f_0 = \mu_1/\mu_0 = 1.59$; while for an ideal plate where D is much larger than $n_0 r^2$, we have $n_0 r^2/D \rightarrow 0$ and thus $f_1/f_0 = (\mu_1/\mu_0)^2 = 2.54$. The measured f_1/f_0 are 1.595 ± 0.167 and 1.959 ± 0.642 for heterostructure and NbS$_2$ devices, respectively (see tables 3.2 and 3.3), suggesting that the modes of heterostructure resonators are near the membrane limit, while the modes of NbS$_2$ resonators are in between the membrane and plate limit. We plot the extracted Q versus f_0 for all heterostructure resonators (Q_h) and NbS$_2$ resonators (Q_n) in Figs. 3.3b and 3.3c, respectively, including the quality factor Q_g of the exfoliated graphene membranes before ALD. As expected from Eq. 3.2, f_0 decreases with increasing r for the NbS$_2$ resonators, while f_0^h for heterostructure resonators varies widely from 14.6 to 30.7 MHz. This is attributed to the inhomogenieties like wrinkles and crumples in the heterostructures (see images in Fig. 3.8) and large differences in pretension. All measured resonance frequencies are comparable to those in literature reported for similar devices [3, 12].
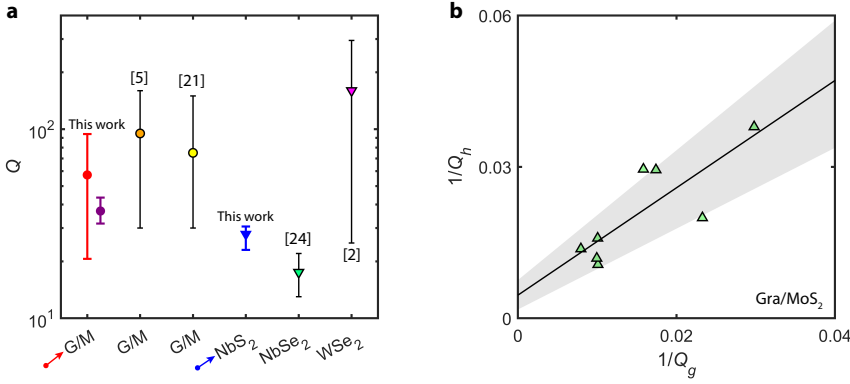
Figure 3.4: **a** Comparison of Q between this work (errorbars, marked with arrows in x-axis) and previous studies (bars). Purple errorbar shows the measured Q of purely exfoliated heterostructure devices, as introduced in Appendix. **b** The measured results of Q_h^{-1} versus Q_g^{-1} (green points) with a linear fit by Eq. 3.3 (black line). Gray shadow represents the fitting error bar.

The extracted values of Q_n and Q_h are also comparable to values of previously studied resonators made by exfoliation and CVD [2, 6, 21, 24], as illustrated in Fig. 3.3f. To gain insight into the damping, we plot Q_h versus n_0 for heterostructure resonators and Q_n versus E_n for NbS$_2$ resonators, respectively, as plotted in Figs. 3.3d and 3.3e. For both cases, we observe a linear relation, indicating that pretension plays a more important role on damping than bending rigidity for heterostructure resonators, while it is on the other way around for NbS$_2$ resonators. This is exactly as expected based on the ratio f_1/f_0. On the other hand, we do not see clear relations of Q_h versus E_h and Q_n versus n_0 as plotted in Figs. 3.9a and 3.9b, respectively.

Concerning the effective masses, we determine the correction factors η_h and η_n by substituting the measured f_0, and the extracted n_0 and E into Eq. 3.2 (see values in tables 3.2 and 3.3). We obtain $\eta_h = 1.34 \pm 0.92$ and $\eta_n = 2.87 \pm 0.83$, respectively. The high η_n of NbS$_2$ devices is attributed to the contaminations from the PDMS stamping. The values η_h for the heterostructure are surprisingly close or even below 1. This suggests the absence of any residues and possibly even the thinning of the graphene membrane during the ALD process, while the ALD MoS$_2$ layer is mainly deposited on top of the suspended graphene membrane instead of bottom.

We also observe a general decrease of quality factor in heterostructure resonators after ALD ($Q_h < Q_g$), as shown in Fig. 3.3b. Considering the dissipation mechanism for two parallel membranes, the overall Q_h can be modeled as

$$1/Q_h = \alpha/Q_g + 1/Q_m, \tag{3.3}$$

where α can be different than 1 on account of structural changes in the graphene because of the ALD process, and Q_m^{-1} is a fit parameter that represents the damping in the heterostructure originating from the ALD MoS$_2$. We fit the measured Q_h^{-1} versus Q_g^{-1} with Eq. 3.3 (see Fig. 3.3g) and extract $\alpha = 1.1 \pm 0.1$ and $1/Q_m = 4.7 \pm 3.1 \times 10^{-3}$. The fact that the obtained α (within errors) is close to 1, provides evidence that there little

to none increase of the dissipation in the graphene during the ALD process. A control experiment has been done with purely exfoliated graphene/MoS$_2$ heterostructures (see Fig. 3.10), giving us $\alpha = 1.1 \pm 0.2$ and $1/Q_m = 17.6 \times 10^{-3}$. The lower $1/Q_m$ of ALD heterostructure compared to exfoliated layers can be attributed to a better conformality of the ALD layer and the absence of contamination by transfer polymers.

Compared with PE-CVD method that grows 2D materials under a temperature more than 400 °C, the reaction temperature window for ALD here is much lower (100 °C for MoO$_x$ deposition), which significantly improve the survival rate of suspended graphene membranes. Therefore, PE-ALD is a safer and more efficient method for fabricating high-performance 2D heterostructure resonators. In addition, although ALD is known to be capable of wafer-scale synthesis, the dimensions of our fabricated devices are still quite small due to the use of exfoliation in the fabricating process. A strategy could be to grow transferless suspended CVD 2D material membranes like graphene [25], and subsequently grow ALD material heterostructures from them. In addition, ALD could benefit from a method to precisely control the flatness, so as to avoid the cragged surfaces of nanoscale devices as illustrated in Figs. 3.8a and 3.8b.

3.3. CONCLUSIONS

In conclusion, we presented the fabrication and mechanical characterization of ALD-based nanomechanical resonators. We developed two PEALD based approaches to suspend ALD flakes on a patterned Si/SiO$_2$ substrate: one is dry transfer using PDMS (exfoliate ALD Nb$_2$ flakes from glassy carbon); the other is ALD deposition of MoS$_2$ on mechanically exfoliated suspended graphene drums. AFM indentation allows us to determine their Young's moduli as 101.4 ± 13.3 GPa and 951.7 ± 161.0 GPa. Using an optomechanical method, we extracted their resonance frequencies and the corresponding quality factors. All of the above parameters are well comparable to the reported values of exfoliated and CVD resonators. We found experimental indications that the dissipation of ALD MoS$_2$ membranes in heterostructures is roughly 3.7 times lower than that of purely exfoliated MoS$_2$ membranes, which is promising for high-performance 2D heterostructure resonators. Our results show possibilities toward exploiting ALD technique for nanomechancial resonators in explorations on atomically thin tunable resonators and 2D sensors. Further work could focus on the thickness control of ALD resonators, which can bring significant improvements in device performance and lead to new functionalities.

3.4. METHODS

A Si wafer with 285 nm dry SiO$_2$ is spin coated with positive e-beam resist and exposed by electron-beam lithography. Afterwards, the SiO$_2$ layer without protection is completely etched using CHF$_3$ and Ar plasma in a reactive ion etcher. More details on the fabrication of substrate can be found in Appendix section 1. The edges of cavities are examined to be well-defined by scanning electron microscopy (SEM) and AFM (see Figs. S2a and S2b). After resist removal, few-layer graphene and ALD NbS$_2$ nanoflakes are exfoliated by Scotch tape, and then separately transferred onto the substrate at room temperature through a deterministic dry stamping technique.

We use an interferometer setup to measure the resonance frequency and Q factor of the fabricated resonators. An intensity-modulated blue laser ($\lambda = 405$ nm) irradiates the membrane resulting in a periodic heat flux to actuate it, while a intensity-fixed red laser ($\lambda = 633$ nm) is utilized to detect the motion. The heat flux results in a motion of the drum due to the thermal expansion force. All measurements are performed at room temperature inside a vacuum chamber at 10^{-6} mbar. A vector network analyzer (VNA) modulates the intensity of a blue laser at frequency ω to optothermally actuate a resonator while it analyzes the resulting intensity modulation of the red laser caused by the mechanical response of the same resonator. The red and blue laser powers used are 1.20 and 0.13 mW respectively, where the resonators vibrate in the linear regime and the temperature increase due to self-heating was negligible.

3.5. APPENDIX

3.5.1. SAMPLE FABRICATION

Our starting substrates are 4 inch wafers of dry low pressure chemical vapour deposition (LP-CVD) SiO_2 grown on doped Si commercially available. The thickness of SiO_2 layer is 285 nm. Pre-cleaning were done in advance before the spin coating: we placed the wafer in the beaker with HNO_3, and then placed the beaker into the sonicator and start sonicating (7 minutes, 27 °C with power 9); afterwards, we prepared 2 DI beakers with water, and then removed the wafer from the acid and rinsed in each DI beakers for 30 seconds; finally, we set down the wafer on the wet bench and blew dry it.

In order to etch cavities in wafer, we did the spin coating with a positive e-beam resist AR-P 6200, which has a high dry etching resistance compared to PMMA. To ensure the wafer is clean enough before spin coating, we whirled the wafer in Acetone for 30 seconds and then in IPA for another 30 seconds, and finally blew dry. The resist was spun at a speed of 6000 rpm, resulting in a 650 nm thick layer. After spin coating, we put the wafer on a hot plate and baked the AR-P 6200 at 150 °C for 3 minutes. The cavity design was exposed using e-beam lithography EBPG-5000+ and then developed in pentyl acetate for 60 seconds, MIBK:IPA (1:1) for 60 seconds, rinsed in pure IPA for 60 seconds and finally blow-dried. The exposure beam current is set as 32 nA.

We then used Sentech Etchlab to etch exposed SiO_2 all the way to the Si layer. The exposed substrate areas were etched with CHF_3 (500 sccm) and Ar (2.5 sccm). The chamber pressure was set to 0.01 mbar. An RF power of 55 W was applied and the resulting DC bias voltage was measured at -225 V. Finally, the remnant resist was removed in a warm bath of PRS-3000, rinsed in DI water, blow-dried and plasma cleaned in a Tepla 300 oxygen plasma asher. After RIE etching, the wafer was spin coated with S1813 (for the protection of the high quality oxide during dicing) and diced using Disco dicer into 6 mm × 6 mm small squared substrates, which were then plasma-cleaned in O_2 barrel asher and prepared for 2D material resonators in the following. Figures. 3.5a and 3.5b give the AFM scanning results of the etched circular cavities, showing a good quality of the edge definition of the substrate.

For PE-ALD process, we adopted the same recipes for MoO_x and NbO_x as we have reported in previous works [9, 11]. PE-ALD is done in two half-reactions: the metal precursors ($(N^tBu)_2(NMe_2)_2Mo$ precursor to grow MoO_x and $^tBuN=Nb(NEt_2)_3$ precursor to
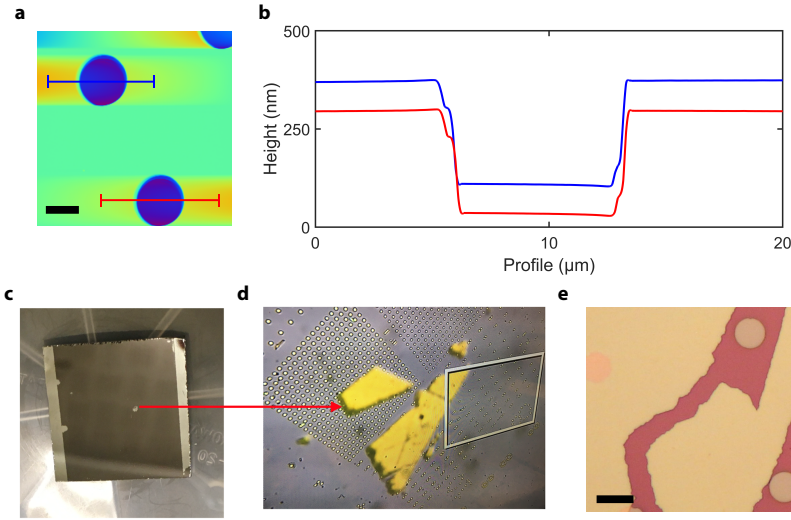
Figure 3.5: **a** AFM image of the fabricated substrate with etched circular cavities. Scale bar: 5 μm. **b** Height curve of the cavities along with the red and blue profiles in (a), showing good quality of the edge definition of the substrate. **c** and **d** Large-scale ALD NbS$_2$ nanoflakes on glassy carbon substrate and on PDMS, respectively. **e** ALD NbS$_2$ nanoflakes on SiO$_2$ substrate, which are broken to small pieces after stamping.

grow NbO$_x$ in this work) is first adsorbed on the deposition substrate and the reactants (O$_2$ plasma) then react with the adsorbed precursors to produce the target metal oxide film (MoO$_x$ and NbO$_x$). ALD method has a better uniformity than PE-CVD, additionally also offers higher thickness control on both planar and high-aspect ratio 3D surfaces.

Here we introduce the PE-ALD and sulfurization processes of MoS$_2$ as an example. MoO$_x$ films were deposited in a home-built ALD reactor, consisting of a vacuum chamber connected to an inductively coupled plasma source and a pump unit. The liquid ((N^{t}Bu)$_2$(NMe$_2$)$_2$Mo precursor was contained in a bubbler at 50 °C, at which it is reported to have a vapor pressure of 0.13 Torr. The standard ALD recipe consists of precursor dosing for 6 s in the first half of the ALD cycle. Ar gas is used as a carrier gas during the precursor dose, resulting in a chamber pressure of 7.5 mTorr. Subsequently, the reactor is purged with Ar for 3 s and pumped down for 3 s. The second half cycle consists of O$_2$ plasma exposure with a plasma power of 100 W at a chamber pressure 5.1 mTorr for 4 s [9]. Afterwards, MoO$_x$ thin films were sulfurized in a tube furnace at 900 °C under atmospheric pressure. A combination of H$_2$S + Ar gas (10 % H$_2$S) was used as sulfurization gas. Corresponding process details for fabricating NbS$_2$ can be found in [11].

The thickness of MoS$_2$ layers is controlled by controlling the thicknesses of the initial ALD grown MoO$_x$ films. The thickness of the ALD grown MoO$_x$ layers are controlled by the number of ALD cycles, as growth per ALD cycle is around 0.06 nm. Based on this growth per cycle, a MoO$_x$ thickness range of 0.6 to 12.4 nm was obtained for 10 to 160 ALD number of cycles. The relation between the MoO$_x$ thickness and the final MoO$_x$ thickness is also detailed in [9]. Overall, the final MoS$_2$ films were thinner than the initial MoO$_x$ counter-parts. This is most likely due to the MoO$_x$ sublimation that can occur
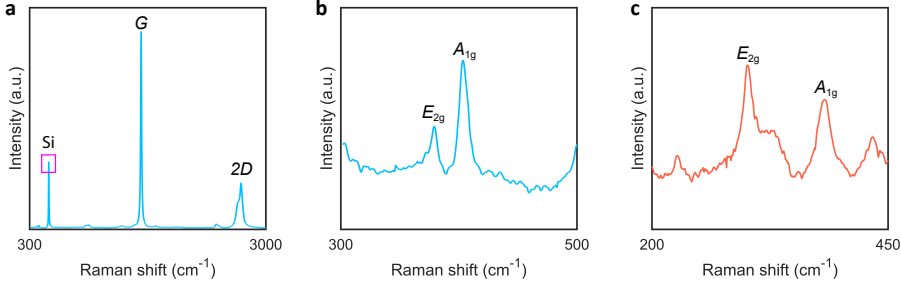
Figure 3.6: Raman measurements of fabricated ALD devices using 514.5 nm laser line. **a** Entire Raman spectra of ALD heterostructure device D1. **b** Raman spectra of MoS$_2$ for device D1, which is the zoom-in graph of carmine frame in **a**. **c** Raman spectra of NbS$_2$ for ALD NbS$_2$ device D1.

during the sulfurization process at elevated temperatures.

3.5.2. RAMAN MICROSCOPE MEASUREMENTS ON ALD RESONATORS

We measure the Raman spectrum of the fabricated ALD devices using 514 nm green laser at room temperature. As shown in Figs. 3.6a and 3.6b, E_{2g} (~383 cm^{-1} for MoS$_2$), A_{1g} (~407 cm^{-1} for MoS$_2$), G (~1579 cm^{-1} for graphene) and $2D$ (~2723 cm^{-1} for graphene) modes are observed in ALD graphene/MoS$_2$ heterostructure device D1. This means the ALD heterostructures still has good physical and chemicall properties after the high-temperature ALD synthesis process for the MoS$_2$ layer. As depicted in Fig. 3.6c, we also measure the Raman spectrum of ALD NbS$_2$ and observe its E_{2g} (~301 cm^{-1}) and A_{1g} (~382 cm^{-1}) modes. The Raman shift of all the measured modes above are exactly where we expect them based on values reported in the literature at room temperature [26–28].

In order to determine whether the ALD MoS2 layer is deposited on top or bottom (or on both sides) of the exfoliated graphene layer, we extract the Raman intensity ratio, I_1/I_2, between the Si peak (~520 cm^{-1} in Fig. 3.6a) from the suspended devices (region 1, Fig. 3.7a) and that from the substrate (region 2, Fig. 3.7a). As depicted in Fig. 3.7b, assume MoS$_2$ is deposited on both sides of graphene, the multilayer structure is made of air, MoS$_2$ (top layer) with thickness d_1, graphene with thickness $d_2 = t_g = 13.3$ nm (t_g is measured by AFM in the main text), MoS$_2$ (bottom layer) with thickness d_3, air with thickness $d_4 = 285$ nm (cavity depth) and Si from top to bottom. We number each material as the i-th layer ($i = 0,...6$) of heterostructure. The thickness of ALD MOS$_2$ on Si substrate is $t_m = 7.8$ nm as measured by AFM, thus we have the geometrical relation $t_m = d_1 + d_3$.

For a four-layer structure, Wang et al.[29] used Fresnel's equations to solve the transmitted and reflected amplitudes of light between different layers. Here, we extend this approach to our six-layer structure (Fig. 3.7b, region 1), and thus the normalized Raman intensity of Si peak is given by

$$I = \int_0^\infty \left| T_{05} e^{-i\frac{2\pi \tilde{n}_5 y}{\lambda}} e^{\beta_5 y} T_{50} e^{-i\frac{2\pi \tilde{n}_5 y}{\lambda}} e^{e^{\beta_5 y}} \right|^2 dy, \tag{3.4}$$

where T_{05} is the total transmitted amplitude of light from the air into the Si substrate

and T_{50} is the one from the Si substrate into the air, $\beta_5 = -\frac{2\pi k_5}{\lambda}$, $\tilde{n}_5$ is the complex refractive index of Si, $\lambda = 514.5$ nm is the wavelength of Raman laser, and k_5 is the extinction coefficient of Si. The expressions of T_{05} and T_{50} are given by

$$T_{05} = \frac{T_{04} \cdot T_{45} \cdot e^{-\mathrm{i}f_4} \cdot e^{\beta_4 d_4}}{1 + R_{04} \cdot R_{45} \cdot e^{-2\mathrm{i}f_4} \cdot e^{2\beta_4 d_4}}, \quad \text{and} \quad T_{50} = \frac{T_{54} \cdot T_{40} \cdot e^{-\mathrm{i}f_4} \cdot e^{\beta_4 d_4}}{1 + R_{54} \cdot R_{40} \cdot e^{-2\mathrm{i}f_4} \cdot e^{2\beta_4 d_4}},$$

where $\beta_4 = -\frac{2\pi k_4}{\lambda}$, and $f_4 = \frac{2\pi \tilde{n}_4 \cdot d_4}{\lambda}$ is the phase difference for light passing through the 5-th media (air). R represents the reflected amplitude of light, e.g., R_{45} is the reflected amplitude of light from 4-th media (MoS_2) to 5-th media (air). To determine T_{05} and T_{50}, the expression of T_{ij} and R_{ij} on different interfaces (i-th/i-th) are

$$\begin{cases} R_{ij} = \frac{\tilde{n}_i - \tilde{n}_j}{\tilde{n}_i + \tilde{n}_j}, \quad R_{ji} = -R_{ij}, \quad T_{ij} = \frac{2\tilde{n}_i}{\tilde{n}_i + \tilde{n}_j}, \quad T_{ji} = \frac{1 - R_{ij}^2}{T_{ij}}, \quad \text{when} \quad i = j - 1, \\ R_{04} = \frac{R_{03} + R_{34} \cdot e^{-2\mathrm{i}f_3} \cdot e^{2\beta_3 d_3}}{1 + R_{03} \cdot R_{34} e^{-2\mathrm{i}f_3} \cdot e^{2\beta_3 d_3}}, \quad R_{40} = \frac{R_{43} + R_{30} \cdot e^{-2\mathrm{i}f_3} \cdot e^{2\beta_3 d_3}}{1 + R_{30} \cdot R_{43} e^{-2\mathrm{i}f_3} \cdot e^{2\beta_3 d_3}}, \quad T_{04} = \frac{T_{03} T_{34} \cdot e^{-\mathrm{i}f_3} \cdot e^{\beta_3 d_3}}{1 + R_{03} \cdot R_{34} e^{-2\mathrm{i}f_3} \cdot e^{2\beta_3 d_3}}, \\ T_{40} = \frac{T_{43} T_{30} \cdot e^{-\mathrm{i}f_3} \cdot e^{\beta_3 d_3}}{1 + R_{43} \cdot R_{30} e^{-2\mathrm{i}f_3} \cdot e^{2\beta_3 d_3}}, \quad R_{03} = \frac{R_{02} + R_{23} \cdot e^{-2\mathrm{i}f_2} \cdot e^{2\beta_2 d_2}}{1 + R_{02} \cdot R_{23} e^{-2\mathrm{i}f_2} \cdot e^{2\beta_2 d_2}}, \quad R_{30} = \frac{R_{32} + R_{20} \cdot e^{-2\mathrm{i}f_2} \cdot e^{2\beta_2 d_2}}{1 + R_{32} \cdot R_{30} e^{-2\mathrm{i}f_2} \cdot e^{2\beta_2 d_2}}, \\ T_{03} = \frac{T_{02} T_{23} e^{-\mathrm{i}f_2} \cdot e^{\beta_2 d_2}}{1 + R_{02} \cdot R_{23} e^{-2\mathrm{i}f_2} \cdot e^{2\beta_2 d_2}}, \quad T_{30} = \frac{T_{32} T_{20} \cdot e^{-\mathrm{i}f_2} \cdot e^{\beta_2 d_2}}{1 + R_{32} \cdot R_{20} e^{-2\mathrm{i}f_2} \cdot e^{2\beta_2 d_2}}, \quad R_{02} = \frac{R_{01} + R_{12} \cdot e^{-2\mathrm{i}f_1} \cdot e^{2\beta_1 d_1}}{1 + R_{01} \cdot R_{12} e^{-2\mathrm{i}f_1} \cdot e^{2\beta_1 d_1}}, \\ R_{20} = \frac{R_{21} + R_{10} \cdot e^{-2\mathrm{i}f_1} \cdot e^{2\beta_1 d_1}}{1 + R_{21} \cdot R_{10} e^{-2\mathrm{i}f_1} \cdot e^{2\beta_1 d_1}}, \quad T_{02} = \frac{T_{01} T_{12} \cdot e^{-\mathrm{i}f_1} \cdot e^{\beta_1 d_1}}{1 + R_{01} \cdot R_{12} e^{-2\mathrm{i}f_1} \cdot e^{2\beta_1 d_1}}, \quad T_{20} = \frac{T_{21} T_{10} \cdot e^{-\mathrm{i}f_1} \cdot e^{\beta_1 d_1}}{1 + R_{21} \cdot R_{10} e^{-2\mathrm{i}f_1} \cdot e^{2\beta_1 d_1}}, \end{cases}$$

where $\beta_i = -\frac{2\pi k_i}{\lambda}$ and $f_i = \frac{2\pi \tilde{n}_i \cdot d_i}{\lambda}$ ($1 \le i \le 4$).

Using Eq. 3.4, we calculate the normalized Raman intensity I_1 of the suspended membrane (region 1) using the complex refractive index $\tilde{n}_0 = \tilde{n}_4 = 1$ (air), $\tilde{n}_1 = \tilde{n}_3 = 4.47 - 0.7i$ (MoS_2), $\tilde{n}_2 = 2.6 - 1.1i$ (graphene) and $\tilde{n}_5 = 4.21 - 0.06i$ (Si). We compute the normalized Raman intensity I_2 of the supported region (region 2) using $d_2 = 0$ (without graphene) and $\tilde{n}_4 = 1.47$ for SiO_2. In Fig. 3.7d (blue line), we obtain I_1/I_2 as a function of the layer number L_{top} of the top ALD MoS_2 ($d_1 = L_{\text{top}} \cdot 0.65$ nm). It shows that I_1/I_2 gradually enhances as L_{top} increases from 0 to 12.

Fig. 3.7c shows the measured amplitude of I_1 and I_2 using Raman spectroscope, where we separately tested four suspended devices (D1, D2, D5 and D6) and four different spots on the substrate. The mean value of the measured I_1/I_2 is 0.406. When comparing this ratio to the one expected for a given thickness, see Fig. 3.7d, we find that the layer number L_{top} of top ALD MoS_2 should be equal to 12 and thus 7.8 nm (see intersection of orange and blue line). As this is exactly equal to the total thickness t_m measured with the AFM (see Fig. 3.1), we conclude that ALD MoS_2 layer is only deposited on top (but not on bottom) of the exfoliated graphene membrane in the fabricated heterostructure devices.

3.5.3. AFM INDENTATION MEASUREMENTS ON ALD RESONATORS

We fit the measured curves of F versus δ to extract the pretension n_0 and Young's modulus E of the fabricated resonators. The applied force F equals the product of the cantilever stiffness k_c and its deflection Δz_c. We use a cantilever with $k_c = 53.7 \pm 0.1$ N/m, and repeat the indentation measurement three times for each device.

The classical relation for the bending rigidity, $D = Et^3/(12(1-\nu^2))$, in general, is not valid for multilayer 2D materials, where the interlayer shear interactions are weak and

3
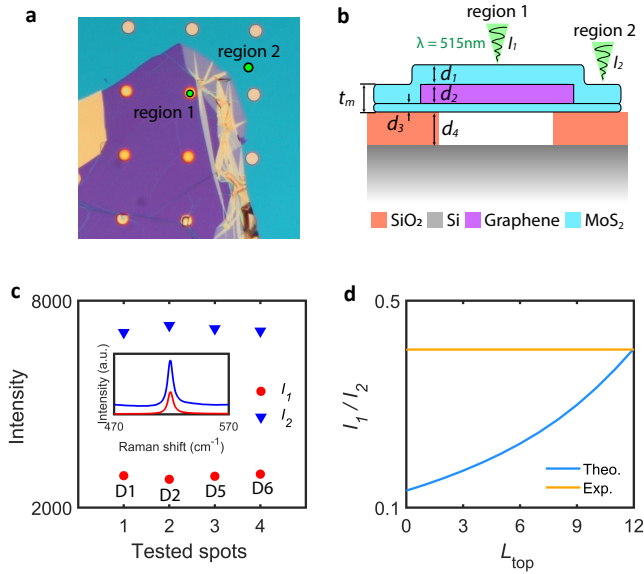
Figure 3.7: Characterizing hierarchical medias of ALD heterostructure devices by Raman methodology. **a** Experimental positions, including suspended (region 1) and supported (region 2) parts. **b** Illustration of heterostructure device (cross-section view). **c** Raman intensity I_1 (red) and I_2 (blue) of Si peak measured on region 1 and 2, respectively. Four heterostructure devices (D1, D2, D5 and D6) and four different spots on substrate are tested in total. Insert, measured Raman spectra of Si peak from region 1 and 2. **d** Ratio I_1/I_2 versus top layer number L_{top} of ALD MoS$_2$. The intersection between experiment (orange line) and calculation (blue line) verify that ALD MoS$_2$ is deposited on top of the exfoliated graphene.

Table 3.1: Transfer of exfoliated ALD NbS$_2$ and MoS$_2$ nanoflakes.

	$t = 5$ nm	$t = 15$ nm	$t = 30$ nm	$t > 50$ nm
MoS$_2$ on Scotch tape	No			No
NbS$_2$ on Scotch tape	No			No
MoS$_2$ on Si wafer	No	No	No	
NbS$_2$ on Si wafer	No			No
MoS$_2$ on Glassy carbon	No	No	No	Yes

Table 3.2: Nanomechanical properties of graphene/MoS$_2$(ALD) heterostructure resonators, including Young's modulus E (GPa), pretension n_0 (N/m), resonance frequency f_0^g (MHz) and its Q factor Q for pure graphene, correspondingly f_0^h (MHz) and Q for graphene/MoS$_2$, ratio f_1^h/f_0^h, and effective layer number η.

Device	E	n_0	f_0^g	Q_g	f_0^h	Q_h	f_1^h/f_0^h	η
D1	951.7	1.418	8.3	100.6	23.5	84.2	1.41	1.16
D2	771.4	1.547	13.6	99.1	30.7	94.0	1.49	0.61
D4	825.5	1.074	8.5	63.2	16.2	33.9	1.58	2.03
D5	1095.7	1.293	9.0	57.5	14.6	34.0	1.71	3.23
D6	1182.6	1.462	7.6	125.9	22.9	72.8	1.53	1.44
D7	950.7	1.318	8.4	99.4	28.3	63.0	1.67	0.78
D8	1162.9	0.892	10.2	33.6	25.8	26.4	1.92	1.01
D10	820.9	1.010	12.4	43.0	35.0	50.3	1.45	0.43

slippage is inevitable. As a result, a calibration factor γ is induced to describe this interaction, giving the formula as $D = \gamma E t^3/(12(1-v^2))$. Since the layers number of graphene and MoS$_2$ in the fabricated heterostructures are 40 and 13 roughly, we adopt $\gamma_g = 0.1$ and $\gamma_m = 0.4$ from literature [13], respectively. We also assume $\gamma_n = \gamma_m$ due to their similar lattice structures. For NbS$_2$ resonators, we can directly fit the measured F versus δ to Eq. 1 to obtain n_0 and E_n. However, for heterostructure resonators, considering the different mechanical properties of graphene and MoS$_2$ layers, their effective Young's modulus E_h and effective bending rigidity D_h are given by [21, 23]

$$E_h t_h = E_g t_g + E_m t_m \quad \text{and} \quad D_h t_h = D_g t_g + D_m t_m, \tag{3.5}$$

respectively, where $t_h = t_m + t_g$. As a result, the relation of F versus δ for heterostructure resonators is expressed as

$$F = \left[\frac{4\pi}{3r^2} \cdot \left(\frac{\gamma_g E_g t_g^4}{1-v_g^2} \cdot \frac{1}{t_h} + \frac{\gamma_m E_m t_m^4}{1-v_m^2} \cdot \frac{1}{t_h} \right) \right] \delta + n_0 \pi \delta + (E_g t_g + E_m t_m) q^3 \left(\frac{\delta^3}{r^2} \right). \tag{3.6}$$

Using the values of $t_g = 13.3$ nm, $t_m = 7.8$ nm, $v_g = 0.165$, $v_m = 0.25$, $\gamma_g = 0.1$ and $\gamma_m = 0.4$, the part inside parenthesis of the first term in Eq. 3.6 can be rewritten as $(E_g t_g \cdot 11.46 + E_m t_m \cdot 9.60) \times 10^{-18}$. This part is then replaced by $E_h t_h \cdot 9.60 \times 10^{-18}$ and $E_h t_h \cdot 11.46 \times 10^{-18}$ separately in the fit, causing only a deviation $< 0.7\%$ to the extracted n_0.

3.5.4. Nanomechanical characteristics for all fabricated ALD resonators

As shown in Table 3.1, we tested directly exfoliating ALD nanoflakes from the grown substrate to fabricate the ALD resonators, including different thicknesses of ALD MoS$_2$ and NbS$_2$ flakes on different substrates. The only successful way is thick NbS2 films (with a thickness of 56.1 nm) grown on glassy carbon, where the adhesion between NbS$_2$ and SiO$_2$/Si is weak enough, thus allows us to use Scotch tape and PDMS to suspend ALD NbS$_2$ on the cavities. Therefore, compared to the exfoliation transfer method, growing ALD films on top of the suspended 2D membranes is more effective for enabling ALD nanomechanical resonators.

Table 3.3: Nanomechanical properties of ALD NbS_2 resonators.

Device	r	E_n	n_0	f_0	Q_n	f_1/f_0	η
D1	4	116.3	0.899	12.4	31.2	1.81	2.05
D2	4	101.8	0.447	11.2	28.6	2.26	2.12
D3	4	96.5	0.593	10.8	26.7	1.58	2.20
D4	3	87.5	1.320	15.2	25.9	1.67	3.30
D5	3	106.7	1.077	15.8	28.5	1.72	3.60
D6	3	117.5	1.005	16.0	28.9	1.57	3.79
D7	3	83.2	0.797	15.1	25.1	3.10	3.05
D8	2	–	–	21.0	32.7	–	–

3

Table 3.2 gives the measured parameters of all ALD heterostructure devices, including radius r of drums, Young's modulus E_h, pretension n_0, fundamental resonance frequency f_0^h and f_0^g (corresponding to the graphene membrane before ALD), quality factor Q_h and Q_g, modes ratio f_1^h/f_0^h, and the calibration factor η with respect to the mass of membrane. Table 3.3 gives the measured parameters of all ALD NbS_2 devices. We cannot extract a precise value of E_n for device D8 due to its small size, which needs a quite large loading F to achieve the effective indentation with cubic regime. The second resonance frequency f_1 of device D8 is missed as well, since we use a low pass filter (up to 60 MHz) on VNA during the dynamic measurements.

Note that in the calculation of η for heterostructure resonators, we have already used the relation $\sigma = \eta(\rho_g t_g + \rho_m t_m)$, where the thickness t_m of ALD MoS_2 is determined by scanning the scratch of MoS_2 layer on Si/Si_2 substrate. We assume that ALD MoS_2 mainly grows on top of the graphene membrane, since the average value of η in Table 3.2 is close to 1, indicating that the thickness of ALD MoS_2 layer in heterostructure is roughly equal to that on substrate. For heterostructure devices D4 and D5, η is larger than 1, which might result from a small quantity of ALD MoS_2 deposited on the bottom of graphene.

Figure 3.8 shows the AFM scanning images of ALD NbS_2 device D1 and D2, as well as all ALD heterostructure devices. We can observe the visible polymer residues, crumples and wrinkles on these devices, which significantly affect their static and dynamic properties. More details about the TEM images of ALD MoS_2 can be found in our previous work [30]. In addition, we also observe that the ALD MoS_2 layer on the substrate, as well as the surface of heterostructure devices are uniform as we expect (see Figs. 3.8i and 3.8m), indicating the good qualities of our fabricated resonators.

Figures 3.9a and 3.9b give the obtained E_h versus Q_h for heterostructure resonators and n_0 versus Q_n for NbS_2 resonators, respectively. Unlike the proportional relations shown in Fig. 3b and 3c in the main text, we see E_h versus Q_h and n_0 versus Q_n are irregular here.

3.5.5. QUALITY FACTORS FOR PURELY EXFOLIATED GRAPHENE/MoS_2 RESONATORS

To shed light on the energy dissipation Q_m^{-1} of MoS_2 layer in the heterostructure, purely exfoliated graphene/MoS_2 heterostructure devices are fabricated (Fig. 3.10a) and mea-

3
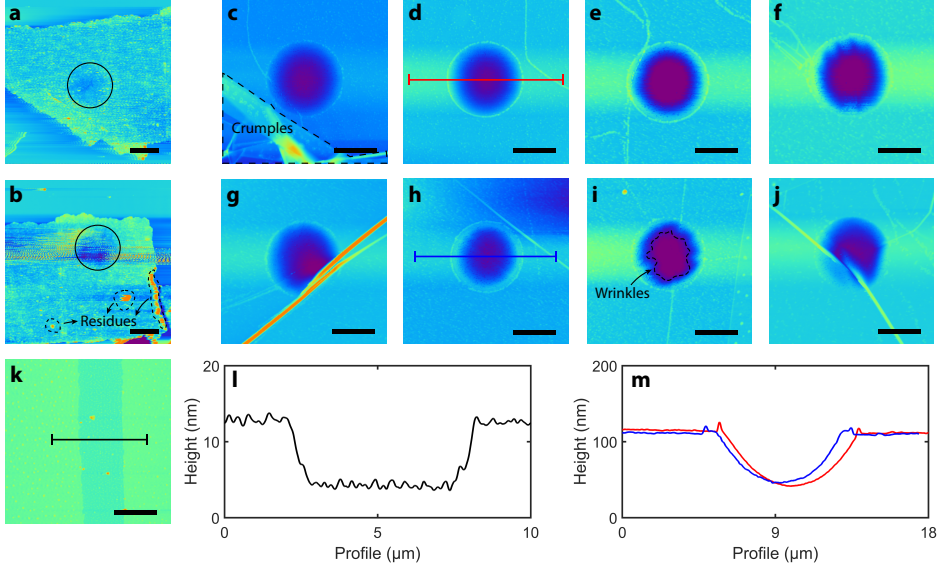
Figure 3.8: AFM scanning results of our fabricated ALD devices. **a** and **b** ALD NbS$_2$ device D1 and D2, respectively. **c−j** All measured ALD heterostructure devices D1 to D10, except the broken ones D3 and D9. **k** ALD MoS$_2$ on the substrate which is scratched by tweezers. Scale bar is 5 μm. **l** Height profile of ALD MoS$_2$ layer along with the black line in **k**. **m** Height profiles of heterostructure devices along with the red and blue lines in **m** and **h**, respectively.

Figure 3.9: Discussion on mechanical properties of fabricated ALD devices. **a** Effective Young's modulus E_h versus quality factor Q_h for heterostructure resonators. **b** Pretension n_0 versus quality factor Q_n for NbS$_2$ resonators.

Figure 3.10: Discussion on the dissipation of MoS_2 layer in purely exfoliated graphene/MoS_2 heterostructure resonators. **a** Optical images of partial fabricated devices (marked by dotted circles), where the red and blue frames represent graphene (bo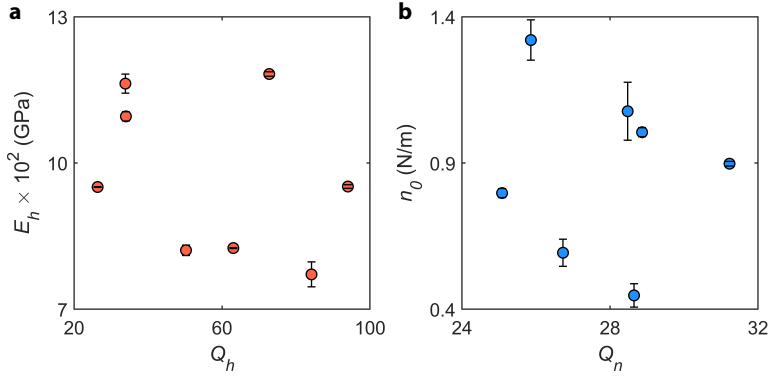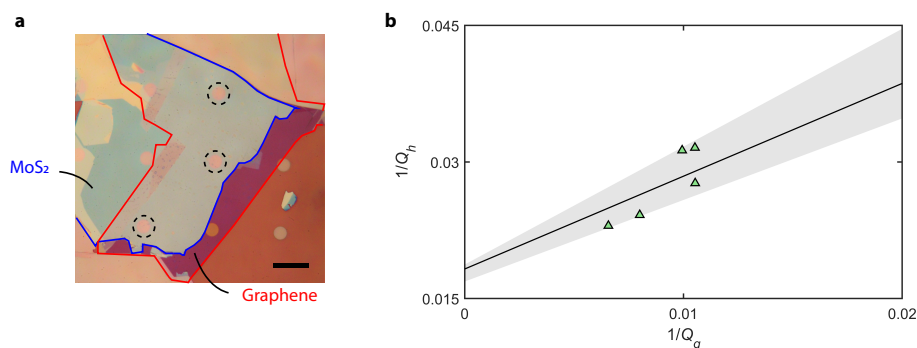ttom) and MoS_2 (top) flakes, respectively. Scale bar is 20 μm. **b** The measured results of Q_h^{-1} versus Q_g^{-1} (green points) and its fitting with Eq. 3.3 (black line and shadow).

sured in interferometry setup. As plotted in Fig. 3.10b, the measured Q_h^{-1} versus Q_g^{-1} is fitted with Eq. 3 and thus extract $\alpha = 1.1 \pm 0.2$ and $1/Q_m = 17.6 \pm 1.9 \times 10^{-3}$.

BIBLIOGRAPHY

[1] R. A. Barton, B. Ilic, A. M. Van Der Zande, W. S. Whitney, P. L. McEuen, J. M. Parpia, and H. G. Craighead, "High, size-dependent quality factor in an array of graphene mechanical resonators", Nano letters **11**, 1232–1236 (2011).

[2] J. Zhu, B. Xu, F. Xiao, Y. Liang, C. Jiao, J. Li, Q. Deng, S. Wu, T. Wen, S. Pei, et al., "Frequency Scaling, Elastic Transition, and Broad-Range Frequency Tuning in WSe2 Nanomechanical Resonators", Nano Letters **22**, 5107–5113 (2022).

[3] J. Lee, Z. Wang, K. He, J. Shan, and P. X.-L. Feng, "High frequency mos2 nanomechanical resonators", ACS nano **7**, 6086–6091 (2013).

[4] P. G. Steeneken, R. J. Dolleman, D. Davidovikj, F. Alijani, and H. S. Van der Zant, "Dynamics of 2d material membranes", 2D Materials **8**, 042001 (2021).

[5] M. C. Lemme, S. Wagner, K. Lee, X. Fan, G. J. Verbiest, S. Wittmann, S. Lukas, R. J. Dolleman, F. Niklaus, H. S. van der Zant, et al., "Nanoelectromechanical sensors based on suspended 2d materials", Research **2020** (2020).

[6] F. Ye, A. Islam, T. Zhang, and P. X.-L. Feng, "Ultrawide frequency tuning of atomic layer van der waals heterostructure electromechanical resonators", Nano Letters **21**, 5508–5515 (2021).

[7] A. Mackus, A. Bol, and W. Kessels, "The use of atomic layer deposition in advanced nanopatterning", Nanoscale **6**, 10941–10960 (2014).

[8] A. Sharma, M. A. Verheijen, L. Wu, S. Karwal, V. Vandalon, H. C. Knoops, R. S. Sundaram, J. P. Hofmann, W. E. Kessels, and A. A. Bol, "Low-temperature plasma-enhanced atomic layer deposition of 2-D MoS2: Large area, thickness control and tuneable morphology", Nanoscale **10**, 8615–8627 (2018).

[9] M. F. Vos, B. Macco, N. F. Thissen, A. A. Bol, and W. Kessels, "Atomic layer deposition of molybdenum oxide from (NtBu)2(NMe2)2Mo and O2 plasma", Journal of Vacuum Science & Technology A: Vacuum, Surfaces, and Films **34**, 01A103 (2016).

[10] W. Hao, C. Marichy, and C. Journet, "Atomic layer deposition of stable 2D materials", 2D Materials **6**, 012001 (2018).

[11] S. B. Basuvalingam, B. Macco, H. C. Knoops, J. Melskens, W. M. Kessels, and A. A. Bol, "Comparison of thermal and plasma-enhanced atomic layer deposition of niobium oxide thin films", Journal of Vacuum Science & Technology A: Vacuum, Surfaces, and Films **36**, 041503 (2018).

[12] A. Castellanos-Gomez, M. Poot, G. A. Steele, H. S. Van Der Zant, N. Agraït, and G. Rubio-Bollinger, "Elastic properties of freely suspended mos2 nanosheets", Advanced materials **24**, 772–775 (2012).

[13] G. Wang, Z. Dai, J. Xiao, S. Feng, C. Weng, L. Liu, Z. Xu, R. Huang, and Z. Zhang, "Bending of multilayer van der Waals materials", Physical Review Letters **123**, 116101 (2019).

[14] A. Sheraz, N. Mehmood, M. M. Çiçek, I. Ergun, H. R. Rasouli, E. Durgun, and T. S. Kasırga, "High elasticity and strength of ultra-thin metallic transition metal dichalcogenides", Nanoscale Advances **3**, 3894–3899 (2021).

[15] H. Sun, P. Agrawal, and C. V. Singh, "A first-principles study of the relationship between modulus and ideal strength of single-layer, transition metal dichalcogenides", Materials Advances **2**, 6631–6640 (2021).

[16] Y. Sun, Z. Zhuo, and X. Wu, "Bipolar magnetism in a two-dimensional NbS2 semiconductor with high Curie temperature", Journal of Materials Chemistry C **6**, 11401–11406 (2018).

[17] R. M. Elder, M. R. Neupane, and T. L. Chantawansri, "Stacking order dependent mechanical properties of graphene/MoS2 bilayer and trilayer heterostructures", Applied Physics Letters **107**, 073101 (2015).

[18] S. Bertolazzi, J. Brivio, and A. Kis, "Stretching and breaking of ultrathin mos2", ACS nano **5**, 9703–9709 (2011).

[19] G. Lopez-Polın, C. Gomez-Navarro, V. Parente, F. Guinea, M. I. Katsnelson, F. Perez-Murano, and J. Gomez-Herrero, "Increasing the elastic modulus of graphene by controlled defect creation", Nature Physics **11**, 26–31 (2015).

[20] C. Lee, X. Wei, J. W. Kysar, and J. Hone, "Measurement of the elastic properties and intrinsic strength of monolayer graphene", science **321**, 385–388 (2008).

[21] F. Ye, J. Lee, and P. X.-L. Feng, "Atomic layer MoS2-graphene van der Waals heterostructure nanomechanical resonators", Nanoscale **9**, 18208–18215 (2017).

[22] K. Liu, Q. Yan, M. Chen, W. Fan, Y. Sun, J. Suh, D. Fu, S. Lee, J. Zhou, S. Tongay, et al., "Elastic properties of chemical-vapor-deposited monolayer MoS2, WS2, and their bilayer heterostructures", Nano letters **14**, 5097–5103 (2014).

[23] M. Šiškins, S. Kurdi, M. Lee, B. J. Slotboom, W. Xing, S. Mañas-Valero, E. Coronado, S. Jia, W. Han, T. van der Sar, et al., "Nanomechanical probing and strain tuning of the Curie temperature in suspended Cr2Ge2Te6-based heterostructures", npj 2D Materials and Applications **6**, 1–8 (2022).

[24]M. A. C. Aguila, J. C. Esmenda, J.-Y. Wang, T.-H. Lee, C.-Y. Yang, K.-H. Lin, K.-S. Chang-Liao, S. Kafanov, Y. A. Pashkin, and C.-D. Chen, "Fabry–Perot interferometric calibration of van der Waals material-based nanomechanical resonators", Nanoscale Advances **4**, 502–509 (2022).

[25]R. Pezone, G. Baglioni, P. M. Sarro, P. G. Steeneken, and S. Vollebregt, "Sensitive transfer-free wafer-scale graphene microphones", ACS Applied Materials & Interfaces **14**, 21705–21712 (2022).

[26]H. Li, Q. Zhang, C. C. R. Yap, B. K. Tay, T. H. T. Edwin, A. Olivier, and D. Baillargeat, "From bulk to monolayer MoS2: evolution of Raman scattering", Advanced Functional Materials **22**, 1385–1390 (2012).

[27]A. C. Ferrari, J. C. Meyer, V. Scardaci, C. Casiraghi, M. Lazzeri, F. Mauri, S. Piscanec, D. Jiang, K. S. Novoselov, S. Roth, et al., "Raman spectrum of graphene and graphene layers", Physical review letters **97**, 187401 (2006).

[28]X. Song, Y. Wang, F. Zhao, Q. Li, H. Q. Ta, M. H. Rummeli, C. G. Tully, Z. Li, W.-J. Yin, L. Yang, et al., "Plasmon-free surface-enhanced Raman spectroscopy using metallic 2D materials", ACS nano **13**, 8312–8319 (2019).

[29]Y. Y. Wang, A. Z. Li, Y. H. Wang, Y. Liang, J. Jiang, H. Y. Nan, Z. H. Ni, D. Wang, B. Zhong, and G. W. Wen, "Determination of the thickness of two-dimensional transition-metal dichalcogenide by the Raman intensity of the substrate", Materials Research Express **3**, 025007 (2016).

[30]A. Sharma, R. Mahlouji, L. Wu, M. A. Verheijen, V. Vandalon, S. Balasubramanyam, J. P. Hofmann, W. E. Kessels, and A. A. Bol, "Large area, patterned growth of 2D MoS2 and lateral MoS2–WS2 heterostructures for nano-and opto-electronic applications", Nanotechnology **31**, 255603 (2020).

3

4

4

ENHANCED SENSITIVITY AND TUNABILITY OF THERMOMECHANICAL RESONANCE NEAR THE BUCKLING BIFURCATION

The high susceptibility of ultrathin two-dimensional (2D) material resonators to force and temperature makes them ideal systems for sensing applications and exploring thermomechanical coupling. Although the dynamics of these systems at high stress has been thoroughly investigated, their behaviour near the buckling transition has received less attention. Here, we demonstrate that the force sensitivity and frequency tunability of 2D material resonators are significantly enhanced near the buckling bifurcation. This bifurcation is triggered by compressive stress that we induce via thermal expansion of the devices, while measuring their dynamics via an optomechanical technique. We understand the frequency tuning of the devices through a mechanical buckling model, which allows to extract the pre-strain, central deflection and boundary compressive stress of the membrane. Surprisingly, we obtain a remarkable enhancement of up to 14× the vibration amplitude attributed to a very low stiffness of the membrane at the buckling transition, as well as a high frequency tunability by temperature of more than 4.02 % K^{-1}. The presented results provide insights into the effects of buckling on the dynamics of free-standing 2D materials and thereby open up opportunities for the realization of 2D resonant sensors with buckling-enhanced sensitivity.

4.1. Introduction

A flat mechanical plate subjected to a sufficiently high in-plane compressive stress becomes unstable, as its out-of-plane stiffness gradually reduces to zero [1]. When this happens, the plate experiences a buckling bifurcation. Even the slightest imperfection in the device, like a very small initial deformation, can determine whether the plate buckles up or downward. This high sensitivity to initial conditions offers exciting prospects, both for studying material properties [2, 3] and for realizing new sensing applications [4]. Therefore there has been a growing interest for buckling in nano-electromechanical systems (NEMS) and resonators such as phononic waveguides [5], carbon nanotubes [6] and SiN$_x$ drumheads [7], showing reversible control of signal transmission, high sensitive switching, as well as remarkable nonlinear effects and high tunability of resonance frequencies. These properties of buckled resonators make them very suitable for applications as actuators, sensors, and energy harvesters [8, 9].

Nanomechanical resonators made of free-standing 2D materials are stiff within the plane, due to their high Young's modulus, but extremely flexible out-of-plane due to their atomic thickness[10–12]. As a result, free-standing 2D materials buckle at relatively low compressive stress values and thereby present an ideal platform for studying the buckling bifurcation in nanoscale systems. In fact, the buckling bifurcation provides a sensitive method to determine the bending rigidity of 2D materials [2, 13]. However, most of the work on 2D NEMS resonators has focused on flat 2D mechanical resonators under tensile stress, because these can be more reproducibly fabricated [14, 15]. Moreover, the experimental detection of the buckling bifurcation in 2D NEMS remains difficult, as it requires a methodology to induce symmetric in-plane compression in suspended 2D materials while measuring their mechanical motion with high spatial resolution.

In this chapter, we study the effect of the buckling bifurcation on the dynamics of optothermally driven nanomechanical resonators made of FePS$_3$ membranes. By varying temperature, the membranes expand, causing a compressive stress that triggers the membranes to deflect out-of-plane. Interestingly, this buckling bifurcation does not only cause a large change in the temperature-dependent resonance frequency, but also gives rise to a significant enhancement of vibration amplitude of the resonators when driven on-resonance. To account for these observations and relate them to the device parameters, we fit a mechanical buckling model to the experiments that quantifies prestrain, central membrane deflection, and boundary compressive stress of the membrane. Based on the model we attribute the force response to a significantly reduced out-of-plane stiffness at buckling transition. The large frequency tuning and high responsivity to forces of 2D resonators near the buckling bifurcation might be utilized to enhance sensitivity in future designs of 2D NEMS devices like microphones and pressure sensors.

4.2. Fabrication and methodology

We fabricated 2D nanomechanical resonators by transferring exfoliated 2D flakes over etched circular cavities with a depth of $d_p = 285$ nm and varying radius R in a Si/SiO$_2$ substrate (Methods). In total, we made three FePS$_3$ devices D1−D3. Figure 4.1a shows a schematic cross-section and a top view (optical microscope) of the fabricated devices

Table 4.1: Characteristics of the fabricated devices including radius R, thickness h, Young's modulus E, Poisson ratio v, mass density ρ, initial resonance frequency $f_0(T_0)$, temperature at turning point T_t, resonance frequency at turning point f_t, central deflection without boundary displacement loading z_{free}, initial displacement U_0, and pre-strain ϵ_0. D1 and D2 are from the same nanoflake (see Fig. 4.1a).

	R (μm)	h (nm)	E (GPa)	$f_0(T_0)$ (MHz)	T_t (K)
D1	4	33.9	69.9	5.89	302.0
D2	4	33.9	70.3	5.52	303.0
D3	3	34.5	93.1	11.18	307.5

	f_t (MHz)	z_{free} (nm)	U_0 (nm)	$\epsilon_0 \times 10^{-5}$
D1	5.53	20.6	0.08	1.84
D2	3.97	6.2	0.08	1.99
D3	6.89	4.3	0.04	1.32

D1 and D2 with $R = 4\,\mu$m. Using tapping mode atomic force microscopy (AFM), we measure the height difference between the membrane and the Si/SiO_2 substrate. As Fig. 4.1b shows, we find a membrane thickness h of 33.9 nm for devices D1 and D2. To determine the Young's modulus E of the resonators, we indent the membrane centre by an AFM cantilever while measuring its deflection [16]. We fit the applied force F versus indentation δ, as depicted in Fig. 4.1c (orange points), to a model for point-force loading of a circular plate given by $F = (\frac{16\pi D}{R^2}\delta) + n_0\pi\delta + Ehq^3(\frac{\delta^3}{R^2})$, where $D = Eh^3/(12(1-v^2))$ is the bending rigidity of the membrane, v is Poisson ratio, $n_0 = Eh\epsilon_0/(1-v)$ is the pre-tension in the membrane, and ϵ_0 is the built-in strain. From the fit (black line, Fig. 4.1c) we extract $E = 69.9$ GPa for device D1. The AFM measurements on devices D2 and D3 can be found in Appendix section 2. The extracted Young's moduli of all devices are listed in Table 4.1 and are similar to values reported in the literature [17].

To probe the thermodynamic properties of the fabricated devices, we use a laser interferometer (see Methods)[18, 19]. As shown in Fig. 4.1d, we place the samples in a vacuum chamber with a pressure below 10^{-5} mbar during the measurements. A power-modulated diode laser ($\lambda = 405$ nm) photothermally actuates the resonator, while the reflection of a He-Ne laser ($\lambda = 632$ nm) from the cavity with the suspended membrane captures its motion. The reflection is measured by a photodetector (PD) and processed by a Vector Network Analyzer (VNA) and then converted to the response amplitude $|z_f|$ of the resonator in the frequency domain. Figure 4.1e shows the measured frequency response around the fundamental resonance (green points) and a fit to a harmonic oscillator model (black line), given by $|z_f| = \frac{A_{res}f_0^2}{Q\sqrt{(f_0^2-f^2)^2+(f_0 f/Q)^2}}$, where f_0 is resonance frequency, A_{res} is the vibration amplitude at resonance and Q is quality factor. Here, we extract $f_0 = 5.57$ MHz, $Q = 195.93$ and $A_{res} = 1.64$ V/V for device D1. We will now outline how the characteristics of the resonance frequency (f_0, Q and A_{res}) can be used to provide information about the temperature dependent properties of 2D material resonators, in particular near the buckling bifurcation.
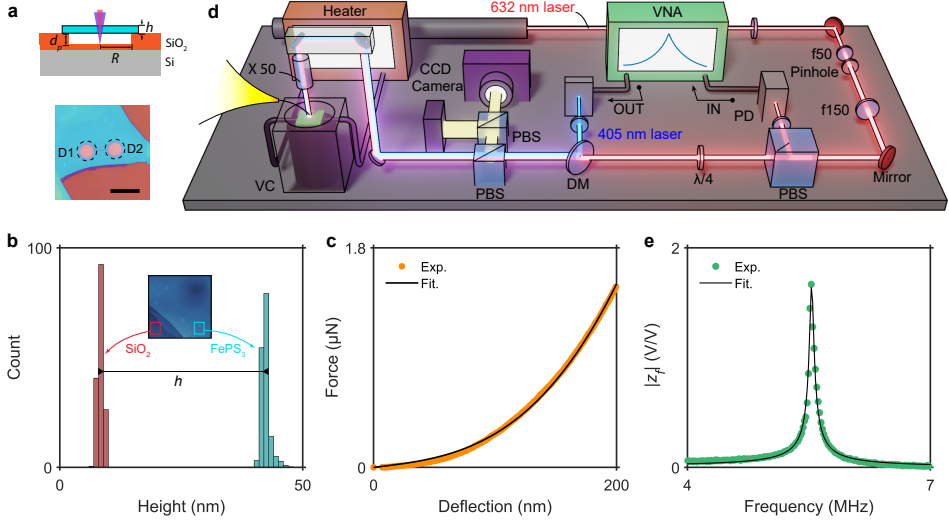
Figure 4.1: Characterization of FePS$_3$ resonator. **a** Top, cross-section of a FePS$_3$ membrane suspended on the substrate with etched cavities. Bottom, optical images of the fabricated devices D1 and D2. Scale bar is 15 μm. **b** Height histogram of the substrate (red), as well as FePS$_3$ membrane (cyan), measured by AFM. Insert, AFM scanning image on the boundary of FePS$_3$ flake. **c** AFM indentation results for device D1 (orange points), where the Young's modulus E of the membrane is extracted by fitting the measured force F to the cantilever deflection δ (black line). **d** Intereferometry setup, where the chip is fixed inside a vacuum chamber (VC). VNA, vector network analyzer; PBS, polarized beam splitter; PD, photo diode; DM, dichroic mirror. **e** Measured signal $|z_f|$ around fundamental resonance mode (green points), which is fitted with a harmonic oscillator model to extract the resonance frequency f_0, quality factor Q and the vibration amplitude A_{res} (black line).

4.3. RESULTS AND DISCUSSION

Figure 4.2a shows the measured $|z_f|$ as a function of actuation frequency and temperature (in the range from 300 to 316 K) for device D1. Interestingly, the resonance frequencies, including fundamental mode (indicated by the blue arrows) and second mode, first decrease and then increase as temperature increases, with a turning point at temperature T_t = 302 K (see Fig. 4.2b). Similarly, the measured vibration amplitude A_{res} and quality factor Q for device D1 also reach to their maximum at T_t (see Fig. 4.2c). These behaviors are also experimentally observed in devices D2 and D3 (see Appendix section 3). We attribute the turning of f_0 versus T to the mechanical buckling of the nanomechanical resonators under critical compressive loading, which has been reported before in carbon nanotube resonators [6] and arch MEMS devices [20]. In fact, the bulk thermal expansion coefficients (TEC), α_m, of the measured FePS$_3$ membranes in this work is much larger than the TEC α_{Si} of the Si/SiO$_2$ substrate. Hence, heating induces compressive displacement in the resonators and buckling is a natural consequence.

Due to the buckling, we cannot use the standard equation for the resonance frequency of a pre-tensioned plate or membrane for further analysis. Therefore, we use a mechanical buckling model for clamped circular plate, as illustrated in Fig. 4.2d. Using a Galerkin method from literature [21, 22], we obtain an expression of f_0 under boundary
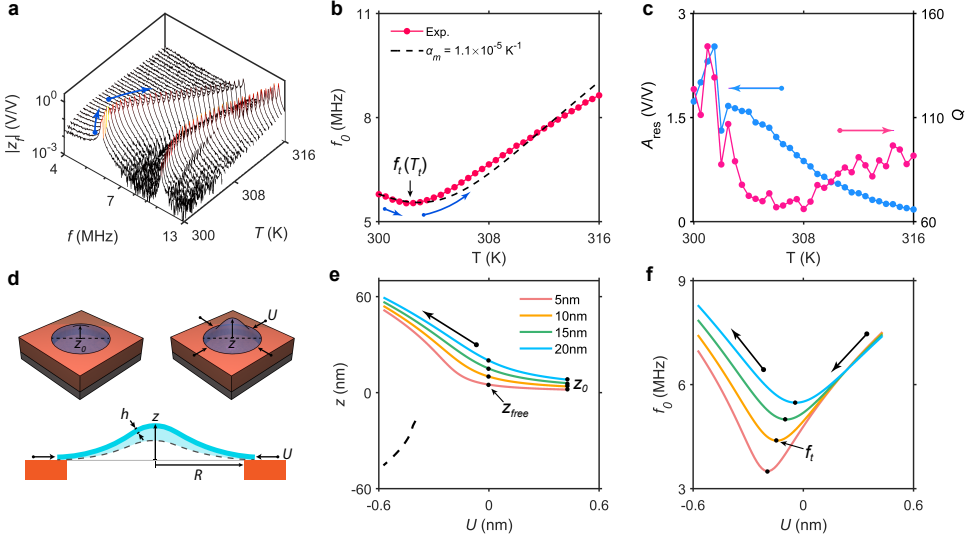
Figure 4.2: Thermally induced buckling in 2D nanomechanical resonator. **a** Mechanical response $|z_f|$ of device D1 as the function of frequency f and temperature T. The fundamental resonance frequency f_0 first decreases and then increases with increasing T (blue arrows). **b** f_0 versus T (red points). The minimum in f_0 is indicative of the temperature T_t at around 302 K. Drawn line, f_0 versus T fitted with the mechanical buckling model to the measurement, using $\alpha_m = 1.1 \times 10^{-5}$ K^{-1}. The deviation at high T indicates that α_m is T-dependent. **c** Vibration amplitude A_{res} at resonance and quality factor Q as a function of T for device D1, respectively. **d** Mechanical buckling illustration for a clamped circular membrane, where a boundary compressive displacement U causes a central deflection z of the membrane. **e** z versus U in the membrane estimated by Eq. 4.2. Lines, results under different values of free deflection z_{free} of the membrane. Dotted line, supercritical bifurcation at the critical buckling load when $z_{free} = 5$ nm. **f** f_0 of the resonator versus U. Black dots, resonance frequency f_t at the turning point.

compressive displacement:

$$f_0(T) = \frac{10.33h}{\pi d^2} \sqrt{\frac{E}{3\rho(1-\nu^2)}(1 + \beta(1-\nu^2)\frac{3z^2 - z_{free}^2}{h^2} + \frac{3}{8}(1+\nu)\frac{Ud}{h^2})}, \qquad (4.1)$$

where U is the thermally induced in-plane displacement of the plate, ρ is the mass density, $d = 2R$ is the diameter, z is the central deflection of the plate, z_{free} is the central deflection of free plate without loading (when $U = 0$), and $\beta = 0.52$ is a fitting factor as $\nu = 0.304$ (see Appendix section 1). Both U and z depend on temperature T. The details of derivation of Eq. 4.1 can be found in Appendix section 1. In contrast to the standard equation for the resonance frequency of a pre-bending plate [23], we now find that not only the bending rigidity determine $f_0(T)$, but also the thermally-induced boundary displacement U and the center deflection z of the membrane.

To find the relation between U and z, we consider a uniformly-clamped plate as depicted in Fig. 4.2d. By studying the static state of the plate using Gakerkin method (see

more details in Appendix section 1), we obtain an analytic solution:

$$\frac{32}{3}\left(1 - \frac{z_{free}}{z}\right) - 10.7\beta(1-v^2)\left(\frac{z_{free}^2 - z^2}{h^2}\right) + 4(1+v)\frac{Ud}{h^2} = 0. \tag{4.2}$$

Therefore, the change of central deflection z of the plate versus U as buckling happens can be extracted from Eq. 4.2. We further use COMSOL simulation method to obtain z and f_0 as the function of U, showing good agreements with the analytical solution obtained from Eqs. 4.1 and 4.2 (see Fig. 4.6). By substituting the parameters $R = 4$ μm, $E = 69.9$ GPa, $h = 33.9$ nm, $\rho = 3.375$ g/cm^3 and $v = 0.304$ into Eq. 4.2, we can evaluate z as a function of U for different z_{free}. As plotted in Fig. 4.2e, z gradually increases with increasing U. The dotted black line in Fig. 4.2e represents a supercritical bifurcation at the critical buckling load when $z_{free} = 5$ nm. This physically indicates an unstable equilibrium that the plate will either buckle up or down when it is slightly perturbed. For nonzero z_{free} in this work, the 2D membrane always buckles in the direction of its pre-deflection.

In order to investigate the effect of buckling on the resonance frequency f_0, we substitute the relation between z and U into Eq. 4.1. This results in a relation between f_0 and z_{free}, as plotted in Fig. 4.2f. When decreasing the displacement U by compression, f_0 reduces to a minimal value (the turning point) and then starts to increase. At this turning point, the minimum resonance frequency f_t of the resonator is reached (marked as dots in Fig. 4.2f). Both the experimental curves in Fig. 4.2a and the theoretical curves in Fig. 4.2f clearly show this frequency minimum, which we take as qualitative evidence for the occurrence of buckling in the 2D resonators.

Let us now quantify U and z as a function of T for device D1, using a model that follows the flow chart depicted in Fig. 4.3a. First, we need to determine the value of z_{free} in the mechanical buckling model. For this, we use the specific feature in the measured f_0 versus T data, which is $\frac{df_0}{dT}|_{T=T_t} = 0$ at the turning point (Fig. 4.2b). Assuming the Young's modulus of the membrane remains constant within the probed temperature range [24], z_{free} can be determined by f_t (see derivation in Appendix section 2). Here, using the parameters in Table 4.1 and the measured value of $f_t(T_t) = 5.53$ MHz, we extract $z_{free} = 20.6$ nm for device D1.

By substituting the obtained z_{free} into Eqs. 4.1 and 4.2, we further extract U and z as a function of T from the measured f_0 at each temperature for device D1. In Fig. 4.3b, we observe that the compressive displacement U becomes more than 10 times larger than its initial tensile value $U_0 = 0.073$ nm (Table 4.1) by heating the membrane by only 16 K. To validate the extracted $U(T)$, we determine the TEC α_m of the membrane. Using the TEC of the substrate α_{Si}, we can use the relation $\frac{1}{R}\frac{dU}{dT} = -(\alpha_m - \alpha_{Si})$ to determine α_m [17]. We thus fit this relation to the obtained ϵ as shown in Fig. 4.3c (orange line) and find α_m is approximately 1.1 to 0.2×10^{-5} K^{-1}, which is in good agreement with values reported in the literature for FePS$_3$ [25]. The fitting deviation for $f_0(T)$ in Fig. 4.2b is thus attributed to the temperature dependence of α_m of FePS$_3$, or the irregular deflection of the membrane as buckling happens.

To experimentally validate the extracted $z(T)$ from the buckling model in Fig. 4.3c, we use a white light interferometer to image the surface profile of the suspended FePS$_3$
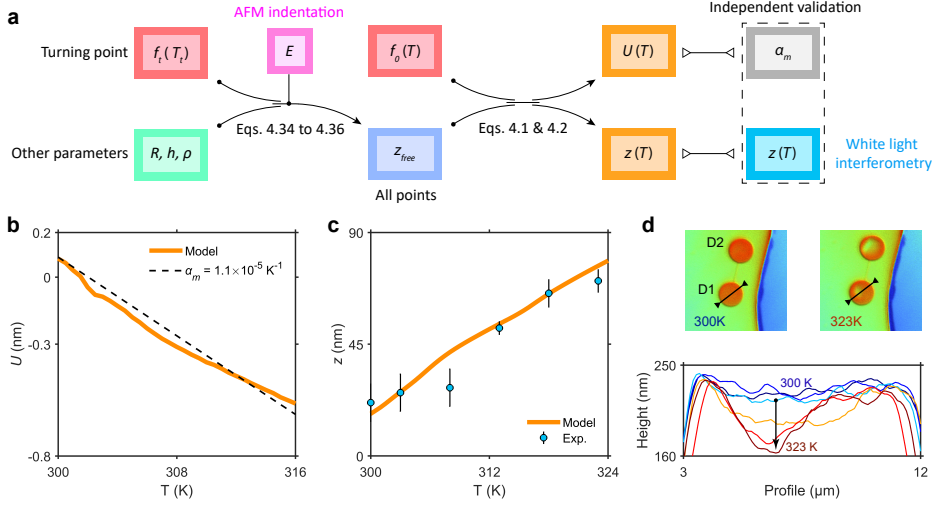
Figure 4.3: Change in boundary displacement and central deflection of device D1. **a** Flow chart of the mechanical buckling model, which allows to extract the boundary displacement U and central deflection z of the membranes as the function of temperature T. **b** U versus T. Orange line, the result obtained from mechanical buckling model; black lines, calculation with fixed values of TEC α_m. **c** z versus T. Orange line, the result obtained from mechanical buckling model; points, measurement by white light interferometry. **d** Top, images of FePS$_3$ flake under white light interferometry. Bottom, surface profile of the membrane as T increases (corresponding to the black arrow in top insert).

membranes as a function of temperature. As shown in Fig. 4.3d, we observe from the height profiles (black arrows, top panel) that the membrane deformation increases as T goes up (bottom panel). As a measure for $z(T)$, we take the difference between the maximum and minimum height for two height profiles and take the average value. As plotted in Fig. 4.3c, the extracted $z(T)$ (points) for device D1 quantitatively matches the estimated $z(T)$ (orange line), which confirms that device D1 exhibits mechanical buckling. In addition, the total strain in the FePS$_3$ membrane also changes from the initial tensile strain to a strong compressive strain. From the obtained $U_0 = 0.078$ nm and $z_{free} = 20.6$ nm, we extract the initial strain $\epsilon_0 = 1.84 \times 10^{-5}$ for device D1 using Eq. 4.27 and the relation $N_r = \frac{Eh\epsilon}{1-\nu}$. All obtained ϵ_0 for devices D1 to D3 are listed in Table 4.1.

We now focus on the vibration amplitude of the fundamental mode of the membrane. As shown in Fig. 4.2c, we observe a remarkable enhancement of up to 14× the vibration amplitude A_{res} at the turning point $T_t = 302$ K. This is attributed to the reduction of out-of-plane stiffness, $k_{eff} = m_{eff}(2\pi f_0)^2$, of the membrane near the buckling transition. Furthermore, we also find the thermally induced buckling in devices D2 and D3 during optomechanical measurements (see Appendix section 3). We quantify the frequency turning of these devices with the mechanical buckling model, and extract their z_0, ϵ_0 and ϵ_t as listed in Table 4.1. Similar to what was observed for device D1 (Fig. 4.2c), A_{res} for devices D2 and D3 also show more than 14 times enhancements near the buckling transition (see Fig. 4.10).

The implications of the observed phenomena extend beyond FePS$_3$ resonators. Even

for 2D materials with a negative TEC such as graphene, buckling might occur if it is cooled down and the initial tensile stress is low enough. A key assumption in Eqs. 4.1 and 4.2 is a uniform compressive force at the boundary of the membrane and a constant Young's modulus over the measured temperature range. In reality, inhomogeneities due to uneven adhesion between membrane and substrate could lead to multiple smaller corrugations and wrinkles superimposed in the membrane when buckling occurs. This potential limitation, which we did not observe for the devices studied in this work, deserves future study as the buckled mode shape as well as the Young's modulus depend on it [26, 27]. Possibly, the experimental quantification of the Young's modulus for each device with AFM, as we did in Fig. 4.2c, compensates for some of the effects of corrugations and wrinkles on the buckling bifurcation.

Despite the fact that the temperature-dependence of resonance frequency has been investigated in earlier works on 2D membranes [28–30], mechanical buckling has not been reported yet. It seems that one study on MoS_2 resonators might have almost reached the buckling point ($\frac{\mathrm{d}f_0}{\mathrm{d}T} \to 0$) at around 373 K [28]. In this chapter it was relatively straightforward to reach the buckling bifurcation due to the large TECs of the selected 2D materials. It is of interest to speculate on the ultimate limits of buckling induced resonance frequency decrease. As indicated in Fig. 4.2d, theoretically it might be possible to have the resonance frequency approaching zero for a deflection $z_{free} = 0$ nm. However, in practice it will be difficult to reach that point. Nevertheless, by making the membranes flatter and with low pre-stress, the zero resonance frequency might be approached, which allows for an extremely high tunability and therefore a high force, stress and temperature sensitivity of f_0 near the minimum f_t. For such flat and low stress membranes, we expect the bending rigidity of 2D materials to dominate the performance and resonance frequency versus temperature curve near the buckling bifurcation point.

Also from an application perspective, the thermally induced buckling in 2D nanomechanical resonators deserves further exploration. First, the frequency tuning with temperature is considerable. As shown in Fig. 4.4, we obtain a tunability, $\Delta f_0/(f_t \Delta T)$, more than 4.02 % K^{-1} for device D1, which is at least 2.3 times higher than reported in earlier studies [28, 29, 31]. The slope of frequency tuning for device D1 is $\Delta f_0/(\Delta T) =$ 194.3 kHz/K, which, when considering an accuracy of 1 kHz in determining f_0, results in a temperature resolution of 5.1 mK. This value is comparable to state-of-the-art temperature sensors [32] and thus highlights the application buckled 2D resonators as bolometer [33] and NEMS resonant infrared detector [34]. Furthermore, precise control over the buckling bifurcation can be obtained by tailoring the initial deflection of the membrane by applying, among others, electrostatic gating on the resonators [11], a gas pressure difference [35], or straining the resonators by MEMS actuators [36].

4.4. Conclusion

In summary, we reported the experimental observation of thermally-induced buckling in 2D nanomechanical resonators made of suspended $FePS_3$ membranes. Using an optomechanical method, we probed their dynamic responses as a function of temperature. A mechanical buckling model was developed to explain the observed large turning
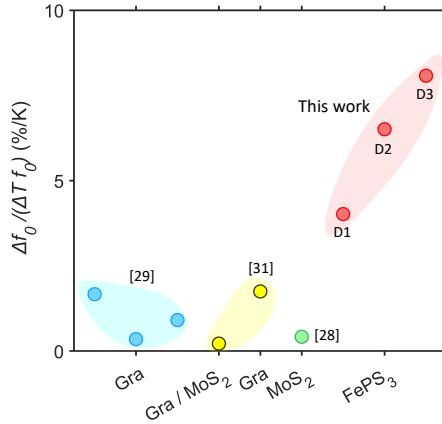
Figure 4.4: Frequency tunability by varying temperature for 2D nanomechanical resonators.

of the resonance frequency with temperature, which allows to determine the boundary compressive displacement and center deflection of the fabricated devices. Using white light interferometer, we independently validated the extracted deflection of the membrane versus temperature from buckling model. We found an enhancement of up to 14× vibration amplitude near buckling bifurcation, which we attributed to the decrease in out-of-plane stiffness of the membrane. The gained insight not only advances the fundamental understanding of buckling bifurcation membranes made of 2D materials, but also enables pathways for buckling-enhanced designs and applications such as temperature detectors, thermoelectric and NEMS devices.

4.5. METHODS

Sample Fabrication. A Si wafer with 285 nm dry SiO_2 is spin coated with positive e-beam resist and exposed by electron-beam lithography. Afterwards, the SiO_2 layer without protection is completely etched using CHF_3 and Ar plasma in a reactive ion etcher. The edges of cavities are examined to be well-defined by scanning electron microscopy (SEM) and AFM. After resist removal, $FePS_3$ nanoflakes are exfoliated by Scotch tape, and then separately transferred onto the substrate at room temperature through a deterministic dry stamping technique. Detailed descriptions of the $FePS_3$ crystal growth and characterization can be found in earlier works [37].

Laser Interferometry Setup. We present temperature-dependent optomechanical measurements in a laser interferometry setup [17]. The fabricated devices is fixed on a sample holder inside the vacuum chamber. A PID heater and a temperature sensor are connected with the sample holder, which allows to precisely monitor and control the temperature sweeping. A piezo-electric actuator below the sample holder is used to optimize the X-Y position of the sample to maintain both the blue and red laser in the center of the 2D resonators. We use a red and blue laser power of 0.9 and 0.13 mW respectively. Note we verified that the resonators vibrate in linear regime and the temperature raise due to self-heating is negligible [38].
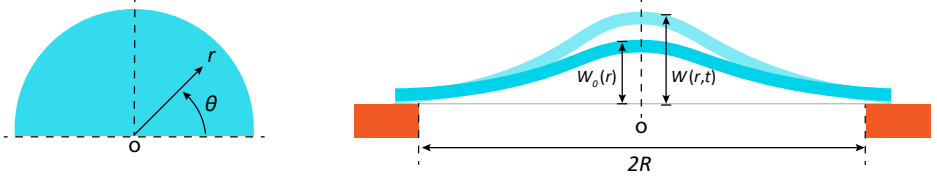
Figure 4.5: Schematic diagram of a clamped circular plate under buckling.

4.6. APPENDIX

4.6.1. MECHANICAL BUCKLING MODEL FOR CLAMPED CIRCULAR MEM-BRANES

BASIC EQUATION AND BOUNDARY CONDITIONS

Assume that a thin circular plate with radius R and thickness h, as shown in Fig. 4.5, undergoes axisymmetric non-linear bending vibrations under an uniformly distributed periodic lateral load $p\cos(\Omega t)$, where Ω is the excitation frequency in the range of the lower natural frequencies of the plate. Denoting the axisymmetric initial and total deflections by $W_0(r)$ and $W(r,t)$, respectively, and the stress function Φ in the r direction, we obtain the motion of the plate by means of the dynamic analog of the Marguerre equations as [21]:

$$\Phi_{,rr} + (1/r)\Phi_{,r} - (1/r^2)\Phi = -(Eh/2r)(W_{,r}^2 - W_{0,r}^2), \tag{4.3}$$

$$D\nabla^4(W - W_0) - N_r W_{,rr} - (1/r)N_\theta W_{,r} + \rho h W_{,tt} = p\cos\Omega t, \tag{4.4}$$

where

$$D = Eh^3/12(1 - \nu^2), \nabla^2 = \partial^2/\partial r^2 + (1/r)\partial/\partial r. \tag{4.5}$$

Here D is the flexural rigidity, E, ν and ρ are the Young's modulus, Poisson's ratio and mass density of the plate, respectively, and subscripts following a comma indicate derivative. The boundary conditions at $r = R$ are given as:

$$W - W_0 = (W - W_0)_{,r} = 0, \quad U = U_0 \quad \text{or} \quad \Phi_{,r} - (\nu/r)\Phi = (Eh/r)U_0, \tag{4.6}$$

where $U(r,t)$ is the displacement of the middle surface of the plate in the r direction, and U_0 is the initial displacement.

Here, the equations of motion (Eqs. 4.3 and 4.4), and the boundary conditions (Eq. 4.6), can be converted to:

$$\phi_{,rr} + (1/\zeta)\phi_{,\zeta} - (1/\zeta^2)\phi = -(1/2\zeta)(w_{,\zeta}^2 - w_{0,\zeta}^2), \tag{4.7}$$

$$L(w) \equiv c(\overline{\nabla})^4(w - w_0) + cw_{,\tau\tau} - (1/\zeta)(\phi w_{,\zeta})_{,\zeta} - \overline{p}\cos\omega\tau = 0, \tag{4.8}$$

$$w - w_0 = w_{,\zeta} - w_{0,\zeta} = 0 \quad \text{and} \quad \phi_{,\zeta} - \nu\phi = u_0 \, at \zeta = 1, \tag{4.9}$$

$$\overline{\nabla}^2 = \partial^2/\partial\zeta^2 + (1/\zeta)\partial/\partial\zeta. \tag{4.10}$$

With the notations:

$$\zeta = r/R, \quad (w, w_0) = (W, W_0)/h, \quad (u, u_0) = (U, U_0)R/h^2, \quad \phi = R\Phi/Eh^3,$$

$$\overline{p} = pR^4/Eh^4, \quad c = 1/12(1-v^2), \quad \Omega_0 = (1/R^2)\sqrt{D/\rho h}, \quad \omega = \Omega/\Omega_0, \quad \tau = \Omega_0 t. \quad (4.11)$$

GALERKIN METHOD

Assuming that both w_0 and w satisfy the clamped boundary conditions, one can put:

$$w_0(\zeta) = \sum_{m=1} a_m w_m(\zeta), \quad w(\zeta, \tau) = \sum_{m=1} b_m(\tau) w_m(\zeta), \quad m = 1, 2, 3, ..., \quad (4.12)$$

$$w_m(\zeta) = (1 - \zeta^2)^2 \zeta^{2(m-1)}. \quad (4.13)$$

In Eq. 4.12, the a_m are given constants while the b_m are unknown time functions. Substituting these expressions into Eq. 4.7 gives:

$$\phi_{,rr} + (1/\zeta)\phi_{,\zeta} - (1/\zeta^2)\phi = -(1/2\zeta)(w_{,\zeta}^2 - w_{0,\zeta}^2) = \sum_{k=1} A_k(\tau)\zeta^{2k-1}, \quad k = 1, 2, 3, ..., \quad (4.14)$$

For the determination of $b_m(\tau)$, we apply the Galerkin procedure to Eq. 4.8, which leads to the following conditions for each spatial function w_i:

$$\int_0^1 L(w) w_i(\zeta) \zeta \mathrm{d}\zeta = 0, \quad i = 1, 2, 3, ..., \quad (4.15)$$

Performing the integration gives:

$$\sum_{j=1} [M_{ij} b_{j,\tau\tau} + K_{ij}(b_j - a_j) - 12(1+v)u_o U_{ij} b_j] - \frac{1}{c} \sum_{j=1} \sum_{k=1} N_{ijk} b_j B_k = \frac{1}{c} Q_i \overline{p} \cos \omega\tau,$$

$$i, j, k = 1, 2, 3, ..., \quad (4.16)$$

where the notations are:

$$M_{ij} = \int_0^1 w_i w_j \zeta \mathrm{d}\zeta, \quad K_{ij} = \int_0^1 w_i(\overline{\nabla}^4 w_j)\zeta \mathrm{d}\zeta, \quad U_{ij} = \int_0^1 w_i(\zeta w_{j,\zeta})_{,\zeta} \mathrm{d}\zeta, \quad Q_i = \int_0^1 w_i \zeta \mathrm{d}\zeta,$$

$$N_{ijk} = \int_0^1 w_i \left[\left(\zeta^{2k} - \frac{2k+1-v}{1-v}\right) \zeta w_{j,\zeta} \right]_{,\zeta} \mathrm{d}\zeta, \quad B_k(\tau) = A_k(\tau)/4k(k+1). \quad (4.17)$$

The normalized stress in the radial direction can be expressed as:

$$\phi = \frac{u_0}{1-v}\zeta + \sum_{k=1} B_k \zeta \left(\zeta^{2k} - \frac{2k+1-v}{1-v}\right), \quad k = 1, 2, 3, ..., \quad (4.18)$$

NUMERICAL SOLUTION AND COMSOL SIMULATION

We can carry out the numerical solution of Galerkin method for the three degree of freedom system using the assumption:

$$w_0 = a_1 w_1(\zeta), \quad w = \sum_{m=1}^{3} b_m(\tau) w_m(\zeta), \quad (4.19)$$
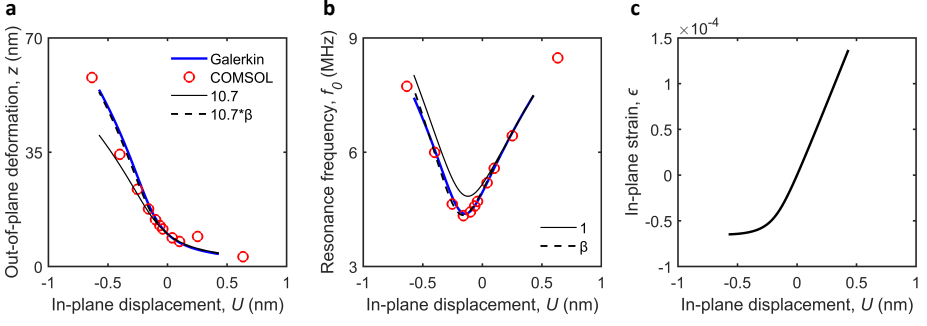
Figure 4.6: Solutions obtained from Galerkin method and COMSOL simulation. **a** Central deflection z versus in-plane displacement U of the plate. Red points, COMSOL simulation results. Blue line, Galerkin solution using three modes. Dash line, analytical solution of Eq. 4.22 without the calibration factor β. Dotted line, analytical solution of Eq. 4.22 with $\beta = 0.52$. **b** Fundamental resonance frequency f_0 versus U of the plate, under the corresponding conditions in **a**. **c** Relation between the average in-plane radial strain ϵ and U of the plate.

where a_1 represents the ratio of the maximum initial deflection to the plate thickness. For the static state, $b_{j,\tau\tau} = 0$ and $\overline{p} = 0$, we can thus extract the static maximum deflection at the center of the plate, $z = h \sum_{m=1}^{3} b_m$, by substituting Eq. 4.19 into Eq. 4.16. For the dynamic state, to determine the linear natural frequencies of the plate under the influence a_1 and an initial edge displacement u_0, we directly substitute Eq. 4.19 into Eq. 4.16 with $\overline{p} = 0$. By solving a set of three homogeneous equations (Eq. 4.16) in $b_j(\tau)$, we can finally obtain the natural frequencies ω_1^*, ω_2^*,..., of the plate. More details can be found in Ref [21].

Here we set the parameters of the circular plate as: $R = 4$ μm, $h = 33.9$ nm, $E = 69.6$ GPa, $v = 0.304$, $\rho = 3375$ kg/m^3, and the central deflection of the plate $z_{free} = a_1 h = 10$ nm (when $U = 0$). We plot the central deflection z and fundamental resonance frequency f_0 of the plate as the function of the in-plane displacement U, respectively, as shown in Fig. 4.6 (blue lines). Similar to our experimental observations, as the displacement varies from positive to negative values, z gradually increases due to the buckling ($z = z_{free}$ at $U = 0$), while f_0 first decreases and then increases again, with a lowest value at the turning point.

To further verify our solutions of static deformation and resonance frequency of buckled plate based on Galerkin method, we now introduce the simulation method using COSMOL, as shown in Fig. 4.7. Adopting the same parameters in COSMOL model as used in Galerkin equations above, we obtain the simulation results of both z and f_0 of the plate as the function of U, respectively, as shown in Fig. 4.6 (red points). We observe that the simulation results are matched well with the numerical solutions, where the existing deviations could probably because of the inaccuracy in the COMSOL simulation, such as coarse mesh size.

We further calculate the relation between the average radial strain ϵ and in-plane displacement U of the plate using Eq. 4.18, as plotted in Fig. 4.6c. We see ϵ is proportional to U in the pre-buckling regime, while the slope of ϵ versus U remarkably reduces in the
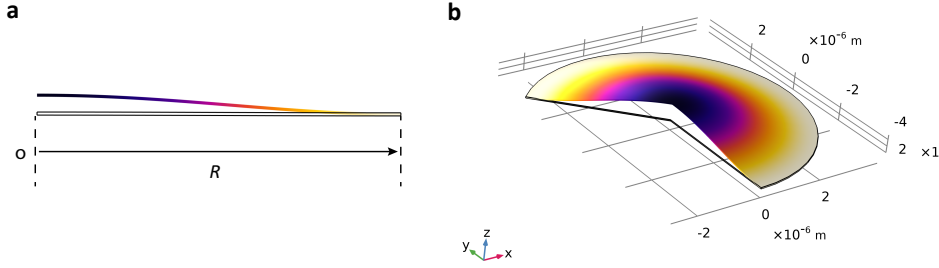
a

b

Figure 4.7: COMSOL model of a clamped circular plate under buckling.

post-buckling regime. This indicates that as buckling happens, the radial displacement will mainly convert to the deformation of the plate instead of in-plane strain.

Analytical solution of Galerkin method

We now extract the analytical solution of deformation $z(U)$ and fundamental resonance frequency $f_0(U)$ of Galerkin method by only considering the first mode for both static and dynamic states:

$$w_0 = a_1 w_1(\zeta), \quad w = b_1(\tau) w_1(\zeta). \tag{4.20}$$

Therefore, we can directly extract the values of notations in Eq. 4.17. For the static state, combining Eq. 4.20 with Eq. 4.16, we obtain:

$$\frac{32}{3}(b_1 - a_1) - 10.7(1 - v^2)b_1(a_1^2 - b_1^2) + 8(1 + v)b_1 u = 0. \tag{4.21}$$

Considering the notations in Eq. 4.11, we convert Eq. 4.21 to:

$$\frac{32}{3}\left(1 - \frac{z_{free}}{z}\right) - 10.7\beta(1 - v^2)\left(\frac{z_{free}^2 - z^2}{h^2}\right) + 8(1 + v)\frac{UR}{h^2} = 0. \tag{4.22}$$

Using the given parameters in Fig. 4.6, we thus can extract z as the function of U from Eq. 4.22, as plotted in Fig. 4.6a (dotted line). In Eq. 4.22, we add a factor β for calibrating the constant 10.7, since the second and three Gelerkin modes in Eq. 4.16 will soften the nonlinear component $b_j B_k$. As shown in Fig. 4.6a, by setting β as 0.52, we obtain a good agreement between the analytic solution and the Gelerkin solution considering all three modes. The fitting value of β will be discussed in the following.

For dynamic state, assume the dynamic mode as $b_1 + b_d$, we combine Eq. 4.20 with Eq. 4.16 and get:

$$-\frac{\lambda b_d}{10} + \frac{32}{3}(b_1 + b_d - a_1) - 10.7(1 - v^2)(b_1 + b_d)(a_1^2 - (b_1 + b_d)^2) + 8(1 + v)(b_1 + b_d)u = 0. \tag{4.23}$$

Ignoring the static components (as already solved in Eq. 4.21), Eq. 4.23 can be simplified as:

$$-\frac{\lambda b_d}{10} + \frac{32}{3}b_d - 10.7(1 - v^2)(b_d a_1^2 - 3b_1^2 b_d) + 8(1 + v)b_d u = 0. \tag{4.24}$$
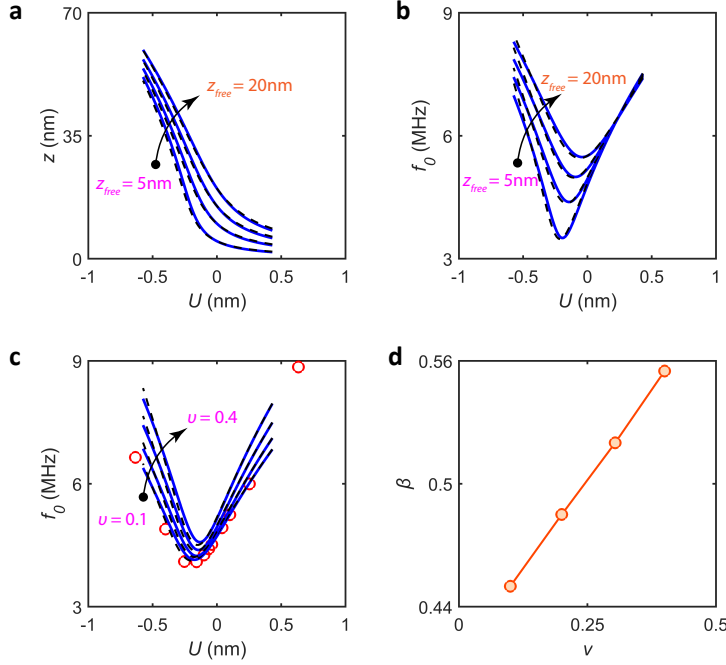
Figure 4.8: Discussion of variables in analytic solution. **a** and **b** Central deflection z and resonance frequency f_0 versus in-plane displacement U of the plate, as z_{free} increases from 5 to 20 nm, respectively. Blue lines, Galerkin solutions (three modes). Dotted lines, analytical solutions using $\beta = 0.52$. **c** f_0 versus U as the Poisson ratio v increases from 0.1 to 0.4. Red points, COMSOL simulation results when $v = 0.1$. **d** Values of the fitted β as a function of v, showing a linear relation.

We then adopt the normalization $b_d = 1$ and substitute the notations in Eq. 4.11 into Eq. 4.24:

$$\lambda = 10 \left[\frac{32}{3} - 10.7(1 - v^2) \frac{z_{free}^2 - 3z^2}{h^2} + 8(1 + v) \frac{UR}{h^2} \right]. \tag{4.25}$$

Therefore, we express the fundamental resonance frequency f_0 of the plate:

$$f_0 = \frac{\Omega_0}{2\pi} \sqrt{\lambda} = \frac{10.33h}{\pi d^2} \sqrt{\frac{E}{3\rho(1 - v^2)} \left(1 + \beta(1 - v^2) \frac{3z^2 - z_{free}^2}{h^2} + \frac{3}{4}(1 + v) \frac{UR}{h^2} \right)}. \tag{4.26}$$

Here, the calibration factor β is induced in Eq. 4.26. By adopting $\beta = 0.52$ in Eq. 4.26, we extract the result of f_0 versus U as shown in Fig. 4.6b (dotted line), which matches well with the Galerkin method and COMSOL simulation. In addition, Eq. 4.26 is comparable to the expression $f_0 = \frac{10.21h}{\pi d^2} \sqrt{\frac{E}{3\rho(1 - v^2)}}$ of the vibrated plate in the previous studies [23].

According to the expressions of N_{ijk} and B_k, we see the fitting factor β is only related to the Poisson ratio v of the material. In Figs. 4.8a and 4.8b, it is verified that when $v = 0.304$, $\beta = 0.52$ can be used for fitting the analytical solution under different values of
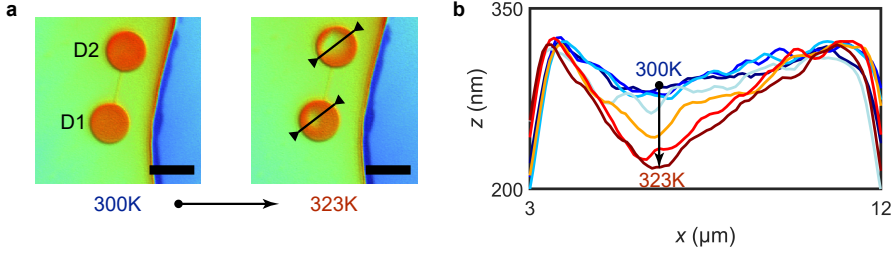
Figure 4.9: **a** Measurement results of FePS$_3$ nanoflake under white light interferometry. Left, 300 K; right, 323 K. Scale bar is 10 μm **b** Scanning of the surface profile of device D2 as temperature goes up from 300 K to 323 K, following the black line in **a**.

z_{free}. We then find that in order to obtain a good agreement between the analytical and Galerkin solutions, the fitting factor β follows the relation $\beta = 0.35\nu + 0.415$, as shown in Figs. 4.8c and 4.8d. As a result, when quantifying the buckling of resonators made up of other 2D materials, β can be estimated through this linear relation above.

Furthermore, we can extract the average radial tension on the plate by $N_r = \int_0^R \frac{\phi(r)}{r} \frac{Eh^3}{R^2} dr$. Substituting the normalized radial stress ϕ in Eq. 4.18, $a_1 = z_{free}/h$ and $b_1 = z/h$, we obtain:

$$N_r = \frac{Eh}{R^2}\left[\left(\frac{z^2 - z_{free}^2}{3} + UR\right)\frac{1}{1-\nu} - \frac{29}{105}(z^2 - z_{free}^2)\right]. \qquad (4.27)$$

Thus the boundary displacement U can be expressed as:

$$U = \frac{N_r R}{Eh}(1-\nu) - \frac{z^2 - z_{free}^2}{3R} - \frac{29(z^2 - z_{free}^2)}{105R}(1-\nu). \qquad (4.28)$$

Substituting Eq. 4.28 and the strain $\epsilon = \frac{N_r(1-\nu)}{Eh}$ back into Eq. 4.26, and using $\beta = 0.52$, we finally get:

$$f_0 = \frac{c_1}{2\pi R}\sqrt{\frac{E}{\rho(1-\nu^2)}\left[\epsilon(1+\nu) + \frac{c_{21}z^2 + c_{22}z_{free}^2}{R^2} + c_3\frac{h^2}{R^2}\right]}, \qquad (4.29)$$

where $c_1 = 2.58$, $c_{21} = 2.02 - 1.77\nu^2 + 0.25\nu$, $c_{22} = -0.98 + 0.73\nu^2 - 0.25\nu$ and $c_3 = \frac{4}{3}$.

Figure 4.9 shows the scanning results of FePS$_3$ devices D1 and D2 using white light interferometer. We observe that both of them buckle downwards as T increases from 300 K to 323 K (see Fig. 4.9a). T-dependent surface profile of devices D1 and D2 are shown in Figs. 3c and 4.9b, respectively. This also allows to extract the central deflection z of the membrane as the function of T. As depicted in Fig. 4.3e above, the measured values of $z(T)$ are comparable to the estimation from mechanical buckling model.

4.6.2. DETERMINING CENTRAL DEFLECTION OF 2D NANOMECHANICAL RESONATORS AT THE FREE STATE WITHOUT FORCE LOADING

We now explain how to extract the central deflection z_{free} of the plate when the displacement $U = 0$ from the measured f_0 versus T. As introduced in the main text, we use

one specific feature: at the turning point $T = T_t$, we have $\frac{\partial f_0}{\partial T}|_{T=T_t} = 0$. Firstly, we rewrite Eq. 4.26 as:

$$f_0^2(T) = \frac{1}{c_t}\left[1 + \beta(1-v^2)\frac{3z^2 - z_{free}^2}{h^2} + \frac{3}{4}(1+v)\frac{UR}{h^2}\right], \tag{4.30}$$

where the constant $1/c_t = (\frac{10.33h}{\pi d})^2 \frac{E}{3\rho(1-v^2)}$. From the condition at turning point above, we find that the derivative of Eq. 4.30 is expressed as:

$$\frac{\beta(1-v^2)}{h^2}6z_t\frac{\partial z}{\partial T} + \frac{3}{4}(1+v)\frac{R}{h^2}\frac{\partial U}{\partial z}\frac{\partial z}{\partial T} = 0, \tag{4.31}$$

and thus:

$$\frac{\partial U}{\partial z} = -8z_t\frac{\beta(1-v)}{R}, \tag{4.32}$$

where z_t is the central deflection of the plate at the turning point. Using the relation between z and U in Eq. 4.22, we then have:

$$\frac{\partial U}{\partial z} = \frac{h^2}{8(1+v)R}\left[-\frac{32}{3}\frac{z_{free}}{z_t^2} + 10.7\beta(1-v^2)\frac{2z_t}{h^2}\right]. \tag{4.33}$$

Substituting Eq. 4.33 into Eq. 4.32, and using $\beta = 0.52$, we extract:

$$z_t^3 = \frac{0.24z_{free}h^2}{1 - v^2}. \tag{4.34}$$

On the other hand, at the turning point, we can also rewrite Eq. 4.22 and Eq. 4.26 as:

$$\frac{32}{3}\left(1 - \frac{z_{free}}{z_t}\right) - 10.7\beta(1-v^2)\left(\frac{z_{free}^2 - z_t^2}{h^2}\right) + 8(1+v)\frac{U_tR}{h^2} = 0, \tag{4.35}$$

and

$$f_t(T = T_t) = \frac{10.33h}{\pi d^2}\sqrt{\frac{E}{3\rho(1-v^2)}\left(1 + \beta(1-v^2)\frac{3z_t^2 - z_{free}^2}{h^2} + \frac{3}{4}(1+v)\frac{U_tR}{h^2}\right)}, \tag{4.36}$$

where U_t represents the in-plane displacement of the plate at the turning point. Eq. 4.34 and Eq. 4.35 allow to express U_t as the function of z_{free}. Therefore, by substituting the obtained $z_t(z_{free})$ and $U_t(z_{free})$ into Eq. 4.36, we can finally determine that the measured frequency f_t at the turning point is only related to the free central deflection z_{free} of the plate.

4.6.3. RAW DATA OF OPTOMECHANICAL MEASUREMENTS FOR DEVICES D2 AND D3

Using optomechanical measurement, we also observe the thermally induced buckling on devices D2 and D3, respectively. As shown in Figs. 4.10a and 4.10c, the frequency tuning of these devices can be well explained with the buckling model for 2D resonators,
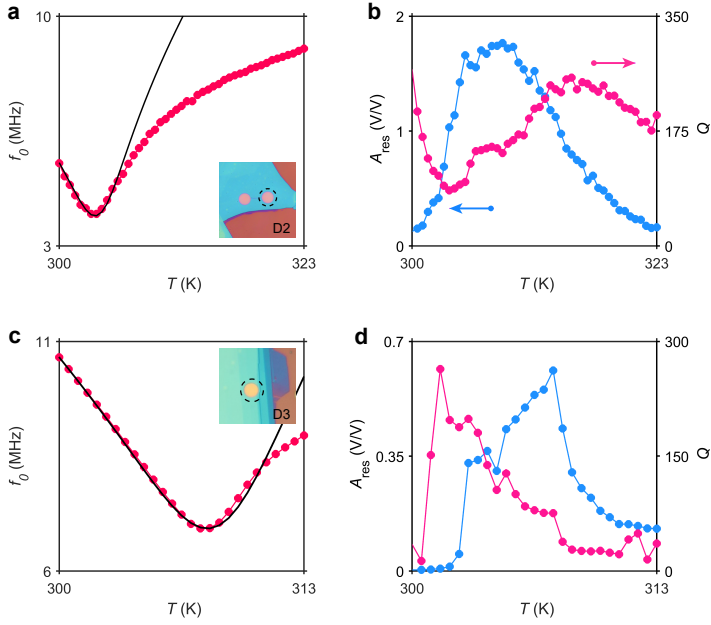
Figure 4.10: Optomechanical measurements on devices D2 and D3. **a** Points, measured resonance frequency f_0 versus temperature T for device D2; drawn line, f_0 estimated by Eqs. 1 and 2 using a TEC $\alpha_m = 2.1 \times 10^{-5}$. Inserts, optical images of device D2. **b** Measured vibration amplitude A_{res} and quality factor Q of the resonance peak versus T. **c** and **d** Corresponding results for device D3, where we adopt $\alpha_m = 1.5 \times 10^{-5}$ in **c**.
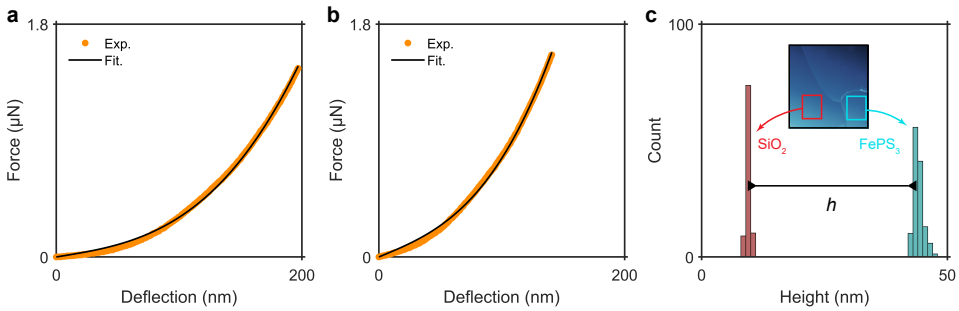
Figure 4.11: AFM measurements on devices D2 and D3. **a** and **b** AFM indentation results for device D2 and D3 (orange points), respectively, where the Young's modulus E of the membrane is extracted by fitting the measured force F to the cantilever deflection δ (black line). **c** Height histogram of the substrate (red), as well as FePS$_3$ membrane (cyan), measured by AFM. Insert, AFM scanning image on the boundary of FePS$_3$ flake.

where their extracted values of z_{free} and U_0 are listed in Table 4.1. The deviation between the measured and estimated $f_0(T)$ in device D2, especially at high T, suggests that α_m or E of the membrane is T-dependent. We also observe the enhancements of 14× and 47× vibration amplitude A_{res} near the buckling transition for devices D2 and D3, respectively, which are similar to what we found in device D1. In addition, the frequency tunability of these devices are about 6.51 % K^{-1} and 8.08 % K^{-1}, respectively, as plotted in Fig. 4.4. Therefore, we demonstrate that the force sensitivity and frequency tunability of 2D material resonators are commonly enhanced near the buckling bifurcation.

Furthermore, we also show the AFM measurement results for determining the Young's modulus of devices D2 and D3, as well as the thickness of device D3, as shown in Fig. 4.11. By fitting the applied force F versus AFM indentation δ, we extract the Young's modulus is equal to 70.3 GPa and 93.1 GPa for device D2 and D3, respectively. In addition, using tapping mode AFM, we extract a thickness h of 34.5 nm for device D3. These results are listed in Table 4.1, which are adopted to further investigate the buckling phenomena in 2D resonators.

BIBLIOGRAPHY

[1]N. Hu and R. Burgueño, "Buckling-induced smart applications: recent advances and trends", Smart Materials and Structures **24**, 063001 (2015).

[2]N. Lindahl, D. Midtvedt, J. Svensson, O. A. Nerushev, N. Lindvall, A. Isacsson, and E. E. Campbell, "Determination of the bending rigidity of graphene via electrostatic actuation of buckled membranes", Nano letters **12**, 3526–3531 (2012).

[3]P. Le Doussal and L. Radzihovsky, "Thermal buckling transition of crystalline membranes in a field", Physical Review Letters **127**, 015702 (2021).

[4]B. El Mansouri, L. M. Middelburg, R. H. Poelma, G. Q. Zhang, H. W. van Zeijl, J. Wei, H. Jiang, J. G. Vogel, and W. D. van Driel, "High-resolution mems inertial sensor combining large-displacement buckling behaviour with integrated capacitive readout", Microsystems & nanoengineering **5**, 1–14 (2019).

[5]S. Kim, J. Bunyan, P. F. Ferrari, A. Kanj, A. F. Vakakis, A. M. Van Der Zande, and S. Tawfick, "Buckling-mediated phase transitions in nano-electromechanical phononic waveguides", Nano letters **21**, 6416–6424 (2021).

[6]S. Rechnitz, T. Tabachnik, S. Shlafman, M. Shlafman, and Y. E. Yaish, "Dc signature of snap-through bistability in carbon nanotube mechanical resonators", Nano Letters **22**, 7304–7310 (2022).

[7]A. Kanj, P. F. Ferrari, A. M. van der Zande, A. F. Vakakis, and S. Tawfick, "Ultra-tuning of nonlinear drumhead mems resonators by electro-thermoelastic buckling", arXiv preprint arXiv:2210.06982 (2022).

[8]W. Zhang, H. Yan, Z. Peng, and G. Meng, "Electrostatic pull-in instability in mems/nems: a review", Sensors and Actuators A: Physical **214**, 187–218 (2014).

[9]R. L. Harne and K. Wang, "A review of the recent research on vibration energy harvesting via bistable systems", Smart materials and structures **22**, 023001 (2013).

[10] B. Xu, P. Zhang, J. Zhu, Z. Liu, A. Eichler, X.-Q. Zheng, J. Lee, A. Dash, S. More, S. Wu, et al., "Nanomechanical resonators: toward atomic scale", Acs Nano **16**, 15545–15585 (2022).

[11] P. G. Steeneken, R. J. Dolleman, D. Davidovikj, F. Alijani, and H. S. Van der Zant, "Dynamics of 2d material membranes", 2D Materials **8**, 042001 (2021).

[12] H. Liu, S. B. Basuvalingam, S. Lodha, A. A. Bol, H. S. van der Zant, P. G. Steeneken, and G. Verbiest, "Nanomechanical resonators fabricated by atomic layer deposition on suspended 2d materials", arXiv preprint arXiv:2212.08449 (2022).

[13] N. Iguiñiz, R. Frisenda, R. Bratschitsch, and A. Castellanos-Gomez, "Revisiting the buckling metrology method to determine the young's modulus of 2d materials", Advanced Materials **31**, 1807150 (2019).

[14] S. Kim, "Impact of the van der waals interface on the mechanics of 2d nanoelectromechanical systems", PhD thesis (University of Illinois at Urbana-Champaign, 2020).

[15] P. F. Ferrari, S. Kim, and A. M. Van Der Zande, "Dissipation from interlayer friction in graphene nanoelectromechanical resonators", Nano letters **21**, 8058–8065 (2021).

[16] A. Castellanos-Gomez, M. Poot, G. A. Steele, H. S. Van Der Zant, N. Agraıt, and G. Rubio-Bollinger, "Elastic properties of freely suspended mos2 nanosheets", Advanced materials **24**, 772–775 (2012).

[17] M. Šiškins, M. Lee, S. Mañas-Valero, E. Coronado, Y. M. Blanter, H. S. van der Zant, and P. G. Steeneken, "Magnetic and electronic phase transitions probed by nanomechanical resonators", Nature communications **11**, 2698 (2020).

[18] M. Šiškins, E. Sokolovskaya, M. Lee, S. Mañas-Valero, D. Davidovikj, H. S. Van Der Zant, and P. G. Steeneken, "Tunable strong coupling of mechanical resonance between spatially separated feps3 nanodrums", Nano letters **22**, 36–42 (2021).

[19] H. Liu, M. Lee, M. Šiškins, H. van der Zant, P. Steeneken, and G. Verbiest, "Tension tuning of sound and heat transport in graphene", arXiv preprint arXiv:2204.06877 (2022).

[20] A. Hajjaj, N. Jaber, S. Ilyas, F. Alfosail, and M. I. Younis, "Linear and nonlinear dynamics of micro and nano-resonators: review of recent advances", International Journal of Non-Linear Mechanics **119**, 103328 (2020).

[21] N. Yamaki, K. Otomo, and M. Chiba, "Non-linear vibrations of a clamped circular plate with initial deflection and initial edge displacement, part i: theory", Journal of sound and vibration **79**, 23–42 (1981).

[22] C. Kim and S. Dickinson, "The flexural vibration of slightly curved slender beams subject to axial end displacement", Journal of sound and vibration **104**, 170–175 (1986).

[23] A. Castellanos-Gomez, R. van Leeuwen, M. Buscema, H. S. van der Zant, G. A. Steele, and W. J. Venstra, "Single-layer mos2 mechanical resonators", Advanced Materials **25**, 6719–6723 (2013).

[24] Z.-D. Sha, Q.-X. Pei, Z. Ding, J.-W. Jiang, and Y.-W. Zhang, "Mechanical properties and fracture behavior of single-layer phosphorene at finite temperatures", Journal of Physics D: Applied Physics **48**, 395303 (2015).

4

[25] Y. Takano, N. Arai, A. Arai, Y. Takahashi, K. Takase, and K. Sekizawa, "Magnetic properties and specific heat of mps3 (m= mn, fe, zn)", Journal of Magnetism and Magnetic Materials **272**, E593–E595 (2004).

[26] L. Bonilla and M. Ruiz-Garcia, "Critical radius and temperature for buckling in graphene", Physical Review B **93**, 115407 (2016).

[27] R. J. Nicholl, H. J. Conley, N. V. Lavrik, I. Vlassiouk, Y. S. Puzyrev, V. P. Sreenivas, S. T. Pantelides, and K. I. Bolotin, "The effect of intrinsic crumpling on the mechanics of free-standing graphene", Nature communications **6**, 1–7 (2015).

[28] Z. Wang, R. Yang, and P. X.-L. Feng, "Thermal hysteresis controlled reconfigurable mos 2 nanomechanical resonators", Nanoscale **13**, 18089–18095 (2021).

[29] F. Ye, J. Lee, and P. X.-L. Feng, "Electrothermally tunable graphene resonators operating at very high temperature up to 1200 k", Nano Letters **18**, 1678–1685 (2018).

[30] D. Davidovikj, D. J. Groenendijk, A. M. R. Monteiro, A. Dijkhoff, D. Afanasiev, M. Šiškins, M. Lee, Y. Huang, E. van Heumen, H. van der Zant, et al., "Ultrathin complex oxide nanomechanical resonators", Communications Physics **3**, 163 (2020).

[31] T. Inoue, Y. Mochizuki, K. Takei, T. Arie, and S. Akita, "Tuning of the temperature dependence of the resonance frequency shift in atomically thin mechanical resonators with van der waals heterojunctions", 2D Materials **5**, 045022 (2018).

[32] *Lake shore ultra-low temperature rox™*, https://qd-uki.co.uk/lake-shore/temperature-sensors/ultra-low-temperature-rox/, March 16, 2023.

[33] A. Blaikie, D. Miller, and B. J. Alemán, "A fast and sensitive room-temperature graphene nanomechanical bolometer", Nature communications **10**, 4726 (2019).

[34] Z. Qian, Y. Hui, F. Liu, S. Kang, S. Kar, and M. Rinaldi, "Graphene–aluminum nitride nems resonant infrared detector", Microsystems & nanoengineering **2**, 1–7 (2016).

[35] A. Sarafraz, A. Givois, I. Roslon, H. Liu, H. Brahmi, G. Verbiest, P. G. Steeneken, and F. Alijani, "Dynamics of pressurized ultra-thin membranes", arXiv preprint arXiv:2212.05464 (2022).

[36] G. J. Verbiest, J. N. Kirchhof, J. Sonntag, M. Goldsche, T. Khodkov, and C. Stampfer, "Detecting ultrasound vibrations with graphene resonators", Nano letters **18**, 5132–5137 (2018).

[37] M. Ramos, F. Carrascoso, R. Frisenda, P. Gant, S. Mañas-Valero, D. L. Esteras, J. J. Baldoví, E. Coronado, A. Castellanos-Gomez, and M. R. Calvo, "Ultra-broad spectral photo-response in feps3 air-stable devices", npj 2D Materials and Applications **5**, 1–9 (2021).

[38] R. J. Dolleman, D. Lloyd, M. Lee, J. S. Bunch, H. S. Van Der Zant, and P. G. Steeneken, "Transient thermal characterization of suspended monolayer mos 2", Physical Review Materials **2**, 114008 (2018).

5

5

Optomechanical methodology for characterizing the thermal properties of 2D materials

Heat transport in two-dimensions is fundamentally different from that in three dimensions. As a consequence, the thermal properties of 2D materials are of great interest, both from scientific and application point of view. However, few techniques are available for accurate determination of these properties in ultrathin suspended membranes. Here, we present an optomechanical methodology for extracting the thermal expansion coefficient, specific heat and thermal conductivity of ultrathin membranes made of $2H\text{-}TaS_2$, $FePS_3$, polycrystalline silicon, MoS_2 and WSe_2. The obtained thermal properties are in good agreement with values reported in the literature for the same materials. Our work provides an optomechanical method for determining thermal properties of ultrathin suspended membranes, that are difficult to measure otherwise. It can does provide a route towards improving our understanding of heat transport in the 2D limit and facilitates engineering of 2D structures with dedicated thermal performance.

5.1. INTRODUCTION

Soon after the discovery of monolayer graphene, it was found that 2D materials have unique thermal properties, which open opportunities for heat control at the nanoscale [1–5]. Due to their ultrasmall thickness, thermal properties of 2D materials are dominated by surface scattering of acoustic phonons, which is highly sensitive to strain [6], grain size [7] and temperature [8], as well as material imperfections such as defects and impurities [9]. To understand and optimize heat transport in 2D materials, precise thermal characterization methods are of great importance.

So far, a variety of experimental techniques have been developed to characterize thermal transport in 2D materials, of which the transient micro-bridge method [10, 11] and the steady-state optothermal method based on Raman microscopy are most commonly used [12, 13]. However, the construction of a micro-bridge is complicated and thermal contact resistances can affect measurement results, while for Raman measurements, the probed temperature resolution is usually relatively small, leading to large error bars. These limitations undermine the accuracy of probing heat transport in 2D materials, causing large variations in the thermal material parameters reported in literature. For example, literature values for the thermal conductivity vary from 2000 to 5000 $\mathrm{Wm^{-1}K^{-1}}$ for suspended monolayer graphene [14].

In this chapter, we demonstrate an optomechanical non-contact method for measuring the thermal properties of nanomechanical resonators made of free-standing 2D materials. The presented methodology allows us to simultaneously extract the thermal expansion coefficient, the specific heat and the in-plane thermal conductivity of the material. It involves driving a suspended membrane using a power-modulated laser and measuring its time-dependent deflection with a second laser. Thus both the temperature-dependent mechanical fundamental resonance frequency of the membrane and characteristic thermal time constant at which the membrane cools down [15] are measured. A major advantage of the method is that no physical contact needs to be made to the membrane, such that its pristine properties are probed and no complex device fabrication is needed. Buckling effects are incorporated in the model to account for the induced compressive stress during temperature variations. Our results on 2H-TaS$_2$, FePS$_3$, polycrystalline silicon (Poly Si), MoS$_2$ and WSe$_2$ show good agreement with reported values in the literature.

5.2. FABRICATION AND METHODOLOGY

We fabricate 2D nanomechanical resonators by transferring 2D flakes over circular cavities with a depth of 285 nm and a radius R of 3 to 4 μm in a silicon (Si) substrate with a 285 nm thick silicon oxide (SiO$_2$) layer, as illustrated in Fig. 5.1a. The devices D1−D5 studied in this work are made of 2H-TaS$_2$, FePS$_3$, Poly Si, MoS$_2$ and WSe$_2$, respectively. By using tapping mode Atomic Force Microscope (AFM), we determine the thickness, h, of each membrane (see Table 5.1). All details about the device fabrication and thickness measurement can be found in Appendix section 1. To determine the Young's modulus E of each membrane, we use the AFM to indent the centre of suspended area with a force F while measuring the cantilever indentation δ [16]. The measured F versus δ, as depicted in Fig. 5.1b for device D1, is fitted with a model for point-force loading of a circular plate
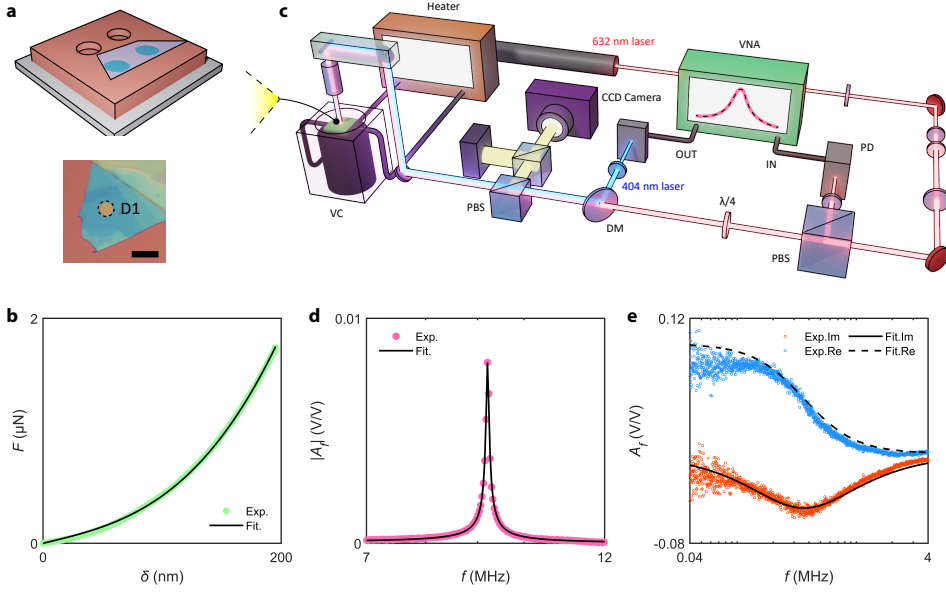
Figure 5.1: Sample characterization and experimental setup. **a** Top, schematic diagram of 2D nanomechanical resonators, composed of 2D flake suspended on the etched SiO_2/Si cavities; bottom, optical image of device D1 (2H-TaS$_2$). Scale bar is 5 μm. **b** AFM indentation results for device D1 (points), from which the Young's modulus E of the membrane is extracted by fitting the measured force F to the cantilever deflection δ (drawn line). **c** Laser interferometry setup used for the optomechanical measurement. The sample is mounted in a vacuum chamber (VC) with a pressure below 10^{-5} mbar. The reflected red laser is detected by the photodiode (PD) and input to the vector network analyzer (VNA). PBS, polarized beam splitter; DM, Dirac mirror. **d** Resonant peak of device D1 measured at MHz regime (points), which is fitted with a harmonic model (drawn line) to extract the resonance frequency f_0 of device D1. **e** Thermal signal measured at kHz regime, including imaginary (red points) and real (blue points) parts. The imaginary part is fitted with Eq. 5.1 (drawn lines) to obtain the thermal time constant τ of device D1.

given by $F = (\frac{16\pi D}{R^2}\delta) + n_0\pi\delta + Etq^3(\frac{\delta^3}{R^2})$, where $D = Eh^3/(12(1-v^2))$ is the bending rigidity of the membrane, v is Poisson ratio, $n_0 = Eh\epsilon_0/(1-v)$ is the initial tension in the membrane, and ϵ_0 is the prestrain. We extract $E = 108.45$ GPa and $\epsilon_0 = 6.75 \times 10^{-3}$ from the fit shown in Fig. 5.1b (drawn line), which are in good agreement with typical values found in literature for 2H-TaS$_2$ [17]. The obtained values of E for devices D2$-$D5 are listed in Table 5.1.

The setup for the optomechanical measurements [18, 19], is shown in Fig. 5.1c. A power-modulated diode laser ($\lambda = 405$ nm) photothermally actuates the resonator, while a constant He-Ne laser ($\lambda = 632$ nm), of which the reflected laser power depends on the position of the membrane, is used to detect the motion of the resonator. The power-modulation is supplied by a Vector Network Analyzer (VNA), which also analyzes the photodiode signal containing the reflected laser power and converts that to the response amplitude, A_f, of the resonator in the frequency domain. All measurements were done in vacuum at a pressure below 10^{-5} mbar. As shown in Fig. 5.1d, the amplitude A_f shows a clear fundamental resonance peak, which we fit with a harmonic oscillator model. For

Table 5.1: Characteristics of devices D1−D5, including radius R, thickness h, mass density ρ, Young's modulus E, atomic mass M, Poisson ratio v, Grüneisen parameter γ, as well as the obtained average TEC α_m, specific heat C_v and in-plane thermal conductivity k. The values of ρ, M, v and γ are taken from literature [17, 21–25].

	R (μm)	h (nm)	ρ (kgm^{-3})	E (GPa)	M (gmol^{-1})
D1 (2H-TaS$_2$)	4	23.2	6860	108.45	245
D2 (FePS$_3$)	4	33.9	3375	69.60	183
D3 (Poly Si)	4	24.0	2330	140.52	28
D4 (MoS$_2$)	3	4.8	5060	174.32	160
D5 (WSe$_2$)	3	5.5	9320	94.42	342

	v	γ	α_m ($\times 10^{-6}$ K^{-1})	C_v (Jmol^{-1}K^{-1})	k (Wm^{-1}K^{-1})
D1	0.35	2.13	6.96	42.0	8.6
D2	0.304	1.80	12.7	68.2	1.8
D3	0.22	0.45	3.10	20.7	5.3
D4	0.25	0.41	3.37	90.6	28.8
D5	0.19	0.79	7.63	53.8	11.0

device D1, we obtain a resonance frequency $f_0 = 9.53$ MHz and quality factor $Q = 160.31$. In addition, we find a maximum in the imaginary part of A_f at kHz frequencies (see Fig. 5.1e), which we attribute to the thermal expansion of the membrane that is delayed with respect to the increase in membrane temperature by the power-modulated laser [19, 20]. By solving the in-plane heat equation in membrane, the thermal signal can be expressed as:

$$A_f = \frac{A_{\text{th}}}{i2\pi f \tau + 1},$$ (5.1)

where A_{th} and τ are the thermal expansion amplitude and thermal time constant of the membrane, respectively. The red and blue laser powers are fixed at 0.9 and 0.13 mW respectively, to ensure linear vibration of the resonators with a negligible temperature raise of the membrane by self-heating [20]. We extract τ by fitting the measured imaginary part of A_f to Eq. 5.1 (see Fig. 5.1e). Here, we obtain the maximum of A_f at around 366.19 kHz for device D1, corresponding to $\tau = (2\pi \times 366.19 \text{ kHz})^{-1} = 434.62$ ns.

5.3. RESULTS

5.3.1. THERMALLY-INDUCED BUCKLING PHENOMENON

When changing the temperature, the thermal expansion coefficient (TEC) α_m of the membrane, which is higher than that of the silicon substrate α_{Si}, changes the in-plane displacement of the membrane from the boundary by a quantity U. This results in a re-markable change in the dynamics of 2D nanomechanical resonators, which can be used for probing the thermal properties [26, 27]. Therefore, we heat up the fabricated devices and investigate the dependence of resonance frequency f_0 on temperature T. As shown in Fig. 5.2a, we observe a decrease of f_0 with increasing T for device D1, which is in agreement with trends shown in literature [28] and can be attributed to a reduction
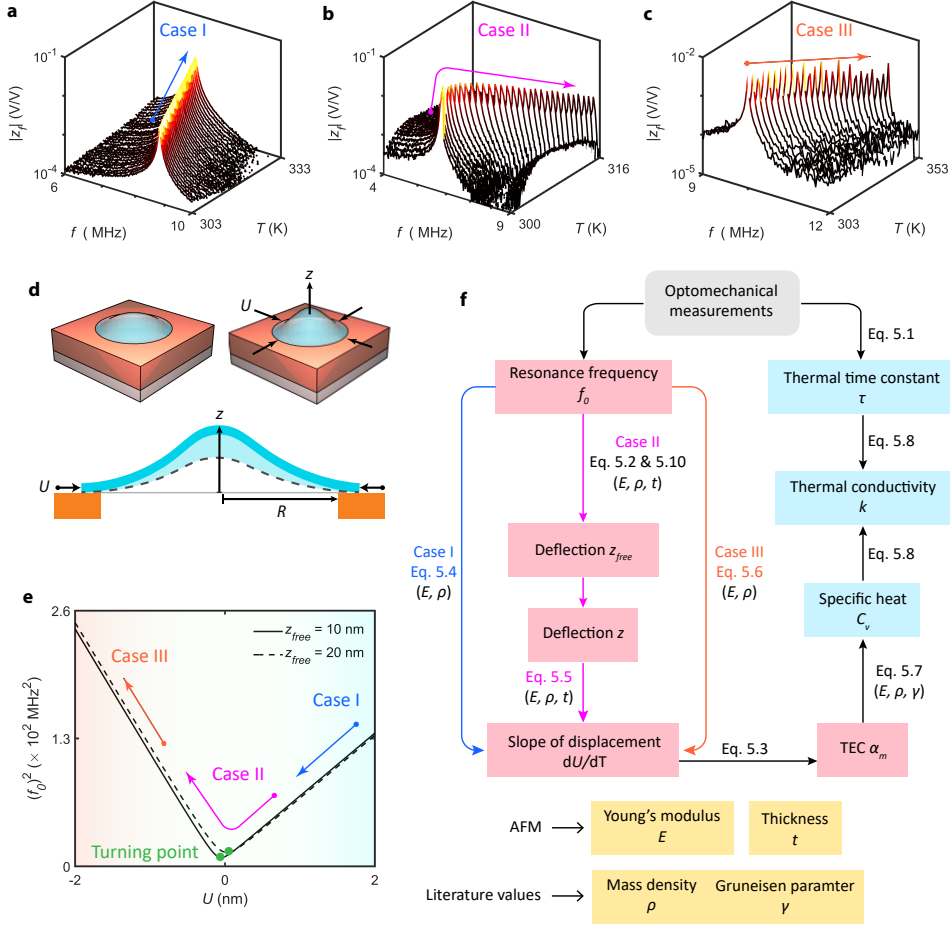
Figure 5.2: Optomechanical methodology for obtaining thermal properties. (a)-(c) Resonant peak measured as the function of temperature T for devices D1 to D3, corresponding to cases I to III, respectively. (d) Schematic diagram of the buckled device, where the central deflection z of the membrane increases as the boundary compression $\Delta \epsilon$ loaded. (e) Squared resonance frequency f_0^2 as the function of total strain ϵ in the membrane estimated by Eq. 5.2 and Eq. S1 under different z_0. f_0^2 first decreases and then increases again as ϵ varies from tensile to compressive stress, which is comparable to the measurement result for device D2. (f) The proposed procedure to determine thermal properties of 2D material membranes.

in strain when the material thermally expands. However, the results obtained for devices D2 and D3 are substantially different: as shown in Figs. 5.2b and 5.2c, we observe an initial decrease in f_0 with increasing T towards a minimum frequency (which we call the turning point), followed by a continuous increase. We attribute this to the thermally-induced buckling of the mechanical resonators as found in earlier studies [29–31], which is caused by the loaded compression since $\alpha_m > \alpha_{Si}$. Here, as depicted in Fig. 5.2d, the thermal expansion of the membrane causes a compressive displacement that triggers the membrane to buckle. We label the pre-buckling, the transition from pre- to post-buckling, and the post-buckling regions in Fig. 5.2e as cases I, II and III, respectively.

We use a Galerkin model for a clamped circular plate (details can be found in Chapter 4), to find an approximate analytical expression of the fundamental resonance frequency f_0 under thermally-induced buckling [32]:

$$f_0(T) = \frac{10.33h}{\pi d^2} \sqrt{\frac{E}{3\rho(1-v^2)}(1+\beta(1-v^2)\frac{3z^2 - z_{free}^2}{h^2} + \frac{3}{8}(1+v)\frac{Ud}{h^2})}, \qquad (5.2)$$

where d is the diameter of the plate, U is the thermally changed in-plane displacement from boundary, ρ is the mass density, z is the central deflection of the plate, z_{free} is the central deflection of the plate at free state when $U = 0$ (without loading), and β is a fitting factor related by the Poisson ratio v (see Fig. 4.8). Equation 5.2 shows that f_0 depends on the in-plane displacement $U(T)$ from boundary and the central deflection $z(T)$ of the membrane. The relation between $z(T)$ and $U(T)$ can be found in Appendix section 1 (Eq. 5.10). Following the literature [32] and Chapter 4, z_{free} can be extracted from the measured value of the fundamental resonance frequency at the turning point, f_t, using the built Galerkin model. By substituting $R = 4$ μm, $h = 23$ nm, $E = 108$ GPa, $\rho = 6860$ kg/m^3, $v = 0.35$ and $\beta = 0.54$ (determined by v) into Eq. 5.2 and Eq. S1, we obtain f_0^2 versus U as shown in Fig. 5.2e. For case I, f_0^2 decreases as U increases; while as buckling happens (cases II and III), z increases as U decreases, leading to an increase of f_0^2 since the components in Eq. 5.2 satisfy the condition $\beta(1-v^2)(3z(T)^2 - z_{free}^2) > |\frac{3}{8}(1+v)U(T)d|$. The estimation in Fig. 5.2e can thus account for all measured results of f_0 versus T for devices D1 to D3. In the following, we describe how to extract the slope of thermal-changed displacement U versus temperature $\frac{dU}{dT}$ for cases I to III, which is related to the TEC α_m of the membrane through [26]:

$$\frac{1}{R}\frac{dU}{dT} = -[\alpha_m(T) - \alpha_{Si}(T)]. \qquad (5.3)$$

CASE I: PRE-BUCKLING REGIME

For case I, the suspended membrane is nearly flat while the change of deflection z with increasing temperature T can be negligible. Therefore, assume $\frac{dz}{dT} = 0$, the derivative of Eq. 5.2 can be simplified as (see details in Appendix section 2):

$$\frac{df_0^2}{dT} = c_t \frac{dU}{dT}. \qquad (5.4)$$

where $c_t = \frac{13.34E}{\pi^2 d^3 \rho(1-v)}$. Therefore, in the pre-buckling regime, we can directly extract $\frac{dU}{dT}$ from the measured $\frac{df_0^2}{dT}$ using Eq. 5.4 (see the flow chart in Fig. 5.2f). Besides device D1,

we also show that devices D4 and D5 are in case I according to their measured f_0 versus T (see Appendix section 4).

CASE II: TRANSITION FROM PRE- TO POST-BUCKLING

For case II, Eq. 5.4 is not applicable anymore since $z(T)$ varies significantly with increasing temperature. We thus calculate the derivative of Eq. 5.2 (see Appendix section 2) and obtain:

$$\frac{\mathrm{d}f_0^2}{\mathrm{d}T} = c_t \left(1 - \frac{32}{\frac{16}{3(1-v^2)} \frac{z_{free}h^2}{z^3} + 10.7} \right) \frac{\mathrm{d}U}{\mathrm{d}T}, \tag{5.5}$$

As depicted in the flow chart of Fig. 5.2f, we first extract $z_{free} = 20.6$ nm for device D2 from the measured f_0 at the turning point using Eq. 5.2 and Eq. 5.2, as well as z versus T (see Fig. 4.3c). The obtained z_{free} and $z(T)$ are then substituted into Eq. 5.5 to extract $\frac{\mathrm{d}U}{\mathrm{d}T}$. The result of U versus T for device D2 shows the expected transition of displacement from tensile ($U > 0$) to compressive ($U < 0$), as plotted in Fig. 4.3b.

CASE III: POST-BUCKLING REGIME

For case III, Eq. 5.5 can be simplified as $z^3 \gg z_{free}h^2$, which results in:

$$\frac{\mathrm{d}f_0^2}{\mathrm{d}T} = -2c_t \frac{\mathrm{d}U}{\mathrm{d}T}. \tag{5.6}$$

Thus the result of $\frac{\mathrm{d}U}{\mathrm{d}T}$ for device D3 can be directly extracted from the measured f_0 versus T. The calculated curves in Fig. 5.2e also verify the linear relations given by Eq. 5.4 and Eq. 5.6.

5.3.2. EXTRACTING IN-PLANE THERMAL CONDUCTIVITY OF 2D MATERIALS

The flow chart depicted in Fig. 5.2f also shows how optomechanical measurements as a function of temperature enable a precise pathway for studying the thermal properties of 2D resonators. We first extract the TEC α_m of the membrane from the the results of $\frac{\mathrm{d}U}{\mathrm{d}T}$ for cases I to III, which are obtained from Eqs. 5.4 to 5.6, respectively, as discussed in the previous section. Then, we quantify the specific heat c_v of the membrane from its thermodynamic relation with α_m, which will be discussed in this section in more detail. Finally, from the solution of the 2D heat equation, we determine the in-plane thermal conductivity k of the membrane from the measured τ and the obtained c_v. In the following, we go step by step through this procedure for device D1.

Let us start with extracting the TEC α_m of the membrane. Since the in-plane displacement U originates from the boundary thermal expansion of the membrane, we can extract the TEC $\alpha_m(T)$ of the membrane from the obtained $\frac{\mathrm{d}U}{\mathrm{d}T}$ using Eq. 5.3, where the values of $\alpha_{Si}(T)$ are taken from literature [33]. The obtained α_m versus T for device D1 is shown in Fig. 5.3a (left).

In the second step, since the specific heat at constant volume is approximately equal to that at constant pressure for solid, we can directly extract the specific heat, C_v, of the membrane from the TEC α_m using the thermodynamic relation [25]:
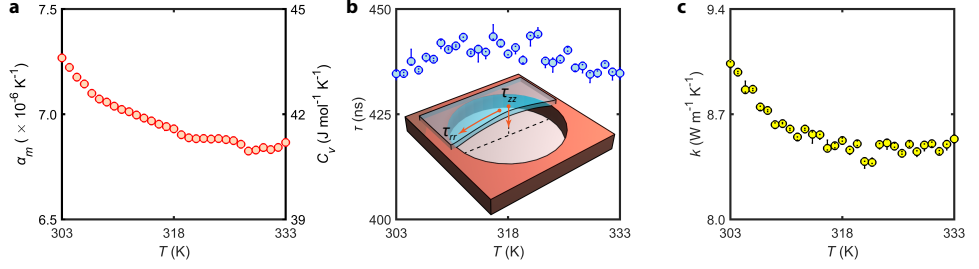
$$C_v = \frac{3\alpha_m K V_M}{\gamma \rho}, \tag{5.7}$$

Figure 5.3: Quantifying thermal characteristics of device D1. (a) Thermal expansion coefficient α_m and specific heat C_v of 2H-TaS$_2$ membrane versus temperature T. (b) Measured thermal time constant τ versus T. Insert, schematic diagram of heat transport in suspended 2D membrane. (c) In-plane thermal conductivity k versus T extract from Eq. 5.8 using the measured τ and the obtained C_v.

Table 5.2:   Comparison of different thermal conductivity measurement methods, including Ramana microscopy, Micro-bridge method and our optomechanics method, where the required temperature range is quantified by the studies of MoS$_2$ [10, 34, 35].

	Raman	Micro-bridge	Optomechanics
Required temperature range	50−100 K	10−50 K	< 10 K
Sample preparation	Easy	Difficult	Easy
Applicability to 2D materials	Applicable	Limited	Applicable

where $K = \frac{E}{3(1-2\nu)}$ is the bulk modulus, $V_M = M/\rho$ is the molar volume, M is the atomic mass, and γ is the Grüneisen parameter of the membrane taken from literature. These parameters are listed in Table 5.1 for the used materials. Using the obtained α_m, we extract C_v versus T for device D1, as plotted in Fig. 5.3a (right).

In the last step, we focus on the heat transport in 2D membranes. As shown in Fig. 5.3b, we experimentally observe that τ is between 434.6 and 444.0 ns in the probed T range for device D1. Considering the heat transport in a circular membrane, we solve the heat equation in the membrane with an appropriate initial temperature distribution and well-defined boundary conditions (see Appendix section 3), and obtain the thermal time constant based on the thermal properties of the membrane:

$$\tau^{-1} = \tau_{rr}^{-1} + \tau_{zz}^{-1} = \frac{k}{\rho c_v}\left(\frac{\mu^2}{R^2} + \frac{\pi^2}{4h^2}\right), \tag{5.8}$$

where τ_{rr} and τ_{zz} are the in-plane and out-of-plane thermal time constants of the membrane (see Fig. 5.3b, insert), respectively, $c_v = C_v/M$, $\mu^2 = 5$ is the in-plane diffusive constant (see Appendix section 3), and k is the thermal conductivity of the membrane. Due to the low h/R ratio for 2D materials, we find that $\tau_{zz} \ll \tau_{rr}$ and thus the extracted τ from our measurement is equal to τ_{rr}. By substituting the obtained C_v and the measured τ into Eq. 5.8, we extract $k = 8.6 \pm 0.3$ Wm^{-1}K^{-1} for device D1, as plotted in Fig. 5.3c.

The obtained in-plane thermal conductivity k for all devices D1−D5 are listed in Table 5.1, of which the raw data can be found in Fig. S6. For both 2H-TaS$_2$ (device D1) and FePS$_3$ (device D2), since relevant studies on their thermal properties are quite limited,
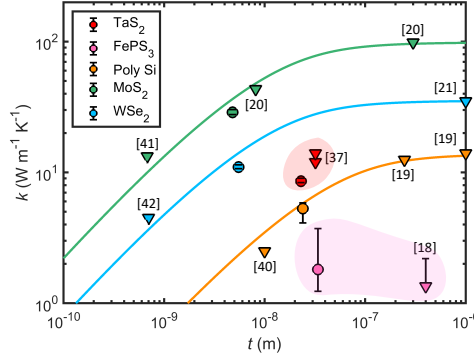
Figure 5.4: In-plane thermal conductivity k of 2D material membranes versus their thickness t. Circular points, the obtained k for devices D1−D5 in this work; triangle points, literature values; drawn lines, estimations of k versus t by Fuchs–Sondheimer model using Eq. 5.9.

we directly compare the obtained k with the values from the literature [21, 36] and observe good agreements (see Fig. 5.4). For Poly Si (device D3), MoS$_2$ (device D4) and WSe$_2$ (device D5), we observe that k depends on the membrane thickness h. We attribute this to a smaller mean free path (MFP) of phonons in thin membranes compared to their bulk counterparts [8]. To account for this effect, we use the Fuchs–Sondheimer model [23, 37] that evaluates thermal conductivity of 2D materials as a function of thickness:

$$\frac{k}{k_{\text{bulk}}} \approx 1 - \frac{3}{8}\frac{\Lambda_{\text{bulk}}}{h} + \frac{3}{2}\frac{\Lambda_{\text{bulk}}}{h}\int_1^\infty \left(\frac{1}{x^3} - \frac{1}{x^5}\right)e^{-\frac{h}{\Lambda_{\text{bulk}}}x}\mathrm{d}x, \qquad (5.9)$$

where k_{bulk} and Λ_{bulk} are the thermal conductivity and MFP of bulk, and x is a integration variable. The bulk thermal conductivities k_{bulk} for Poly Si, MoS$_2$ and WSe$_2$ are 13.8 Wm^{-1}K^{-1}, 98.5 Wm^{-1}K^{-1}, and 35.3 Wm^{-1}K^{-1}, respectively [22, 24, 38]. We find that the given k versus h, including our results and literature values [21–24, 36, 39–41], is well described by Eq. 5.9 as indicated by the fitted solid lines in Fig. 5.4 using Λ_{bulk} as fit parameter, obtaining 75 nm, 19 nm, and 19 nm for Poly Si, MoS$_2$ and WSe$_2$, respectively. These fitted values of Λ_{bulk} are also in good agreement with previously reported phonon MFPs [22, 42, 43], supporting the validity of employing Eq. 5.9 to predict the thickness dependent thermal conductivity of 2D materials.

5.4. DISCUSSION

Compared to other methods for determining the thermal conductivity of 2D materials, the optomechanical approach has several advantages, as summarized in Table 5.2. For the Raman microscopy method, since relatively large temperature changes are needed to resolve the resulting shift in Raman mode frequency, a very wide temperature range has to be measured to get an accurate slope χ_T of the Raman peak shift with temperature. For example, χ_T for MoS$_2$ is -0.013 cm^{-1}/K. Considering a limited resolution 0.25 cm^{-1} for a Raman microscope, a temperature increase of at least 20 K is required to obtain meaningful results [44]. In our measurements, we require only a narrow T range

to study the thermal transport (see Fig. 5.6). For the micro-bridge method, either thick crystals or stiff 2D materials like graphene are required to survive the complicated fabrication procedures including lithography and etching [1]. In contrast, for the presented contactless optomechanical method, one only needs to suspend membranes over cavities in a Si substrate, which is applicable for most 2D materials and can be done for any thickness.

Although we estimate the average MFP for bulk in Fig. 5.4, we note that the phonon MFP in 2D materials is highly related to the phonon dispersion relation, surface strain, crystal grain size, and temperature. These factors can be further studied using the presented optomechanical approach, which would help us to better understand the phonon scattering mechanisms in 2D materials. Moreover, our work suggests a new way to further investigate acoustic phonon transport in recently emerged 2D materials, such as phosphorene and MXenes with distinct thermal anisotropy [45, 46], as well as the magic-angle multilayer superconductor family [47]. It is also of interest to probe the dynamics of phonons across the interface in vdW heterostructures, so as to realize a coherent control of thermal transport across 2D interfaces [48, 49].

5.5. CONCLUSIONS

We demonstrated an optomechanical approach for probing the thermal transport in 2D nanomechanical resonators made of few-layer 2H-TaS$_2$, FePS$_3$, Poly Si, MoS$_2$, and WSe$_2$. We measured the resonance frequency and thermal time constant of the devices as a function of temperature, which are used to extract their thermal expansion coefficient, specific heat, as well as in-plane thermal conductivity. The obtained values of all these parameters (see Table 5.1) are in good agreement with values reported in the literature. Compared to other methods for characterizing the thermal properties of 2D materials, the presented contactless optomechanical approach requires a smaller temperature range, allows for easy sample fabrication, and is applicable to any 2D material. This work not only advances the fundamental understanding of phonon transport in 2D materials, but potentially also enables studies into the use of strain engineering and heterostructures for controlling heat flow in 2D materials.

5.6. APPENDIX

5.6.1. SAMPLE FABRICATION AND CHARACTERIZATION

A Si wafer with 285 nm dry SiO$_2$ is spin coated with positive e-beam resist and exposed by electron-beam lithography. Afterwards, the SiO$_2$ layer without protection is completely etched using CHF$_3$ and Ar plasma in a reactive ion etcher. The edges of cavities are examined to be well-defined by scanning electron microscopy (SEM) and AFM. After resist removal, 2D nanoflakes are exfoliated by Scotch tape, and then separately transferred onto the substrate at room temperature through a deterministic dry stamping technique. Using tapping mode atomic force microscopy (AFM), we measure the height difference between the membrane and the Si/SiO$_2$ substrate. As Fig. 5.5 shows, we find a membrane thickness t of 24.0 nm for device D3.
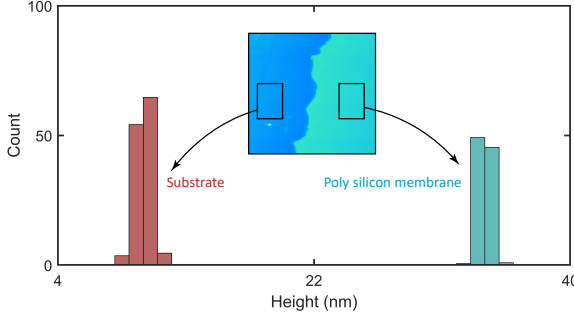
Figure 5.5: Height histogram of substrate (red), as well as Poly Si membrane (cyan), measured by tapping mode AFM. Insert, scanning image on the boundary of Poly Si membrane.

5.6.2. THERMALLY-INDUCED BUCKLING MODEL

In this Chapter, we observe different types of dynamic response in the measured devices $D1-D3$, attributed to the thermally-induced buckling in 2D nanomechanical resonators. Eq. 5.2 gives the expression of the resonance frequency $f_0(T)$ in buckled resonators. As discussed in Chapter 4, Eq. 5.2 can be solved by the relation between central deflection z of the membrane and compressive displacement U from the boundary:

$$\frac{32}{3}\left(1 - \frac{z_{free}}{z}\right) - 10.7\beta(1 - v^2)\left(\frac{z_{free}^2 - z^2}{h^2}\right) + 4(1 + v)\frac{Ud}{h^2} = 0, \qquad (5.10)$$

where U is the thermally induced in-plane displacement of the plate, ρ is the mass density, z is the central deflection of the plate, z_{free} is the central deflection of free plate without loading (when $U = 0$), and β is a fitting factor depends on v (see Chapter 4 Appendix). Therefore, using Eq. 5.10 and Eq. 5.2, we can extract $z_{free} = 20.6$ nm and $z(T)$ from the measured $f_0(T)$ for FePS$_3$ device D2, where more details can be found in Chapter 4.

For pre-buckling regime (case I), assume the deflection z nearly keeps constant, the only time-dependent parameter in Eq. 5.2 is $\Delta\epsilon$, which allows us to obtain the derivative $\frac{df_0^2}{dT} = c_t \frac{dU}{dT}$ for case I. For transition regime from pre- to post-buckling (case II), we first calculate the derivative of Eq. 5.10:

$$-\frac{dU}{dT} = \left[\frac{32}{3}\left(1 + \frac{z_{free}}{z^2}\right) + 10.7\beta(1 - v^2)\frac{2z}{h^2}\right]\frac{h^2}{4d(1 + v)}\frac{dz}{dT}. \qquad (5.11)$$

Therefore, by substituting Eq. 5.11 into the T-derivative of Eq. 5.2, we obtain Eq. 5.5. For post-buckling regime (case III), the thermally-induced buckling results in a large central deflection of the membrane, thus we assume $z_{free}h^2 \ll z^3$ and simplify Eq. 5.5 as $\frac{df_0^2}{dT} = c_t(1 - \frac{32}{10.7})\frac{dU}{dT} = -2c_t\frac{dU}{dT}$.

5.6.3. HEAT TRANSPORT MODEL

In this subsection, we explain how we derive thermal time constant τ with respect to the thermal properties of 2D membrane, as given in Eq. 5.8.

Consider the situation that a modulated-laser irradiates at the center of the suspended 2D membrane, the Fourier heat conduction equation in cylindrical coordinate for this problem can be written as:

$$\frac{\partial u}{\partial t} = \kappa \left(\frac{\partial^2 u}{\partial x^2} + \frac{1}{x} \frac{\partial u}{\partial x} + \frac{\partial^2 u}{\partial z^2} \right) + \frac{1}{c_p \rho} \frac{dQ}{dt} \quad \text{in} \quad 0 < z < z_t \quad 0 < x < r, \tag{5.12}$$

where $u(x, z, t)$ is time t-dependent temperature distribution in the membrane along with the radial x and perpendicular z directions, $\kappa = \frac{k}{c_p \rho}$ is thermal diffusivity, $\frac{dQ}{dt}$ is the absorbed heat energy per unit time per unit volume at the center of the membrane, c_p and k denote the specific heat and thermal conductivity of the membrane, respectively. Here we use the symbol z_t to represent the thickness of membrane, so as to distinguish it with time.

TRANSIENT STATE

We firstly discuss the transient state of heat transport in the membrane, corresponding to a laser pulse irradiates. As a result, Eq. 5.12 is rewritten as:

$$\frac{\partial u}{\partial t} = \kappa \left(\frac{\partial^2 u}{\partial x^2} + \frac{1}{x} \frac{\partial u}{\partial x} + \frac{\partial^2 u}{\partial z^2} \right) \quad \text{in} \quad 0 < z < z_t \quad 0 < x < r, \tag{5.13}$$

with the boundary conditions:

$$u = 0 \quad \text{at} \quad x = r, \quad u = 0 \quad \text{at} \quad z = 0 \quad \text{and} \quad \frac{\partial u}{\partial z} = 0 \quad \text{at} \quad z = z_t, \tag{5.14}$$

and the initial condition:

$$u = u_0(x, z) \quad \text{for} \quad t = 0 \quad \text{in} \quad 0 \le z \le z_t \quad \text{and} \quad 0 \le x \le r, \tag{5.15}$$

We adopt the Fourier method (separation of variables) to solve Eq. 5.13 combined by the boundary and initial conditions. Thus temperature distribution has a general expression as $u(x, z, t) = \psi(x)\chi(z)\Gamma(t)$, of which the independent cases, $\psi(x)$, $\chi(z)$ and $\Gamma(t)$ are separately given by:

$$\begin{cases} \frac{1}{\psi} \left(\frac{d^2 \psi}{dx^2} + \frac{1}{x} \frac{d\psi}{dx} \right) = -\eta^2, \quad \psi = 0 \quad \text{at} \quad x = r \\ \frac{1}{\chi} \frac{d^2 \chi}{dz^2} = -\gamma^2, \quad \chi = 0 \quad \text{at} \quad z = 0 \quad \text{and} \quad \frac{\partial \chi}{\partial z} = 0 \quad \text{at} \quad z = z_t \\ \frac{1}{\Gamma} \frac{d\Gamma}{dt} = -\lambda^2, \end{cases} \tag{5.16}$$

where the constants η, γ and λ are determined by solving the above equations combined with the corresponding conditions. We derive the eigenvalue solution of the first term in Eq. 5.16 as:

$$\psi_m(\eta_m, x) = J_0(\eta_m x) \quad , \quad m = 1, 2, 3, .., . \tag{5.17}$$

where η_m is the m-th root if the formula $J_0(\eta_m r) = 0$, e.g., $\eta_1 = \frac{2.4048}{r}$. Next, the solution of the second term in Eq. 5.16 is given as:

$$\chi_n(z) = a_n \sin \frac{(2n-1)\pi z}{2 z_t} \quad , \quad n = 1, 2, 3, ..., \tag{5.18}$$

where a_n is the constant of integration, $\gamma_n = \frac{(2n-1)\pi}{2z_t}$ is called the eigenvalues of the Sturm-Liouville problem. Then, the solution of the third term in Eq. 5.16 is given as:

$$\Gamma_{mn}(t) = b_{mn}e^{-\lambda_{mn}^2 t} \quad , \quad m = 1,2,3,..., \quad n = 1,2,3,..., \tag{5.19}$$

where b_{mn} is the constant of integration, $\lambda_{mn}^2 = \kappa(\eta_m^2 + \gamma_n^2)$. Totally, combine the solutions together, we have, from Eqs. 5.18 to 5.19:

$$u(x,z,t) = \sum_{m=1}^{\infty}\sum_{n=1}^{\infty} A_{mn} J_0(\eta_m x)(\sin\frac{(2n-1)\pi z}{2z_t})e^{-\lambda_{mn}^2 t}, \tag{5.20}$$

where the Fourier coefficient, A_{mn}, can be further extracted from the initial condition as [50]:

$$A_{mn} = \frac{\int_0^r \int_0^{z_t} x\psi_m(\eta_m,x)\chi_n(z)u_0(x,z)dzdx}{\int_0^r x\psi_m^2(\eta_m,x)dx \int_0^{z_t} \chi_n^2(z)dz}. \tag{5.21}$$

Finally, Eq. 5.20 and Eq. 5.21 are the derived solutions of the Heat Equation Eq.5.13 in the membrane, with the corresponding boundary conditions in Eq. 5.14.

Suppose the initial temperature distribution $u_0(x,z)$ in the membrane is constant, i.e. $u_0(x,z) = u_0$, we extract the series of Fourier coefficient as $A_{11} \approx 2.04u_0$, $A_{12} \approx 0.68u_0$, $A_{12} \approx 0.41u_0$, $A_{31} \approx -0.62u_0$...; on the other hand, the values of constant $\lambda_{11}^2 = \kappa(\eta_1^2 + \gamma_1^2)$, $\lambda_{12}^2 = \kappa(\eta_1^2 + \gamma_2^2)$,..., making the ratio $\frac{\lambda_{mn}^2}{\lambda_{11}^2} \gg 1$. This indicates that the first term in Eq. 5.20 dominates the sum of the rest of the terms, allows us to approximately express the temperature distribution as:

$$u(x,z,t) \approx 2.04u_0 J_0(\frac{2.4048x}{r})(\sin\frac{\pi z}{2z_t})e^{-\lambda_{11}^2 t}. \tag{5.22}$$

As a result, the thermal time constant of the membrane, extracted from λ_{11}^2, can be expressed as:

$$\tau_{rr} = \frac{1}{\kappa\eta_1^2} = \frac{r^2 c_p\rho}{5.78k}, \quad \tau_{zz} = \frac{1}{\kappa\gamma_1^2} = \frac{4z_t^2 c_p\rho}{\pi^2 k}, \tag{5.23}$$

where τ_{rr} and τ_{zz} represent the time constant along in-plane and across-plane directions, respectively. Note that the ratio $\frac{r}{z_t}$ is quite large in atomic-layer-thick 2D membrane, we thus have $\tau_{rr} \gg \tau_{zz}$.

QUASI-STEADY STATE

Define the temperature distributions of transient and quasi-steady as u_{trans} and u_{quasi}, respectively. It should be noticed that u_{trans} will be negligible as the time $t \to \infty$, since $e^{-\lambda_{11}^2 t} \to 0$ in Eq. 5.22. As a result, we only focus on u_{quasi} in the following and adopt $u = u_{quasi}$. In addition, to simplify discussion, we assume u is uniform in z- direction in 2D membrane, and the heat transport here in the quasi-steady case converts to 1D problem. Hence, Eq. 5.12 changes to:

$$\frac{\partial u}{\partial t} = \kappa\left(\frac{\partial^2 u}{\partial x^2} + \frac{1}{x}\frac{\partial u}{\partial x}\right) \quad \text{in} \quad 0 < z < z_t \quad 0 < x < r. \tag{5.24}$$
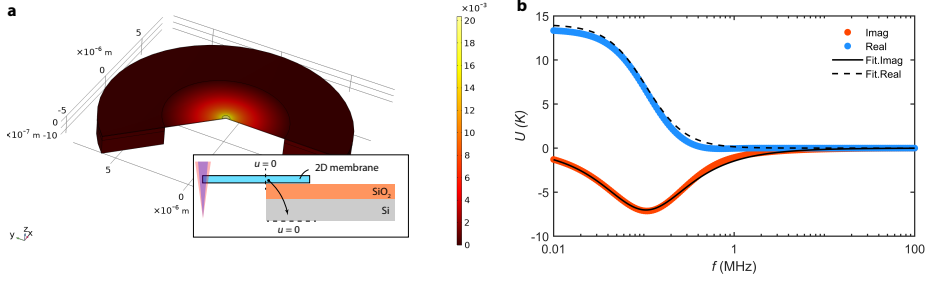
Figure 5.6: **a** 3D schematic diagram of 2D nanomechanical resonators in COMSOL simulation software. Insert, side view, where the boundary condition changes to the bottom of SiO_2/Si substrate. **b** Average temperature of the membrane as the function of heating rate f. Points, simulation results; lines, fitting by Eq. 5.1.

Due to the optothermal drive, we consider the oscillatory boundary conditions (along x-axis):

$$u = A\cos(\omega t) \quad \text{at} \quad x = 0 \quad \text{and} \quad u = 0 \quad \text{at} \quad x = r, \tag{5.25}$$

where A denotes the amplitude of temperature changing in membrane's center and ω is the modulating angular frequency of the laser. As $t \to \infty$, the solution of u will become periodic with ω, i.e. $u(x, t) = A(x)\cos(\omega t + \phi(x))$, where $A(x)$ and $\phi(x)$ are the amplitude and phase of the quasi-steady state, respectively. We rewrite $u(x, t)$ with complex form:

$$u(x, t) = \frac{1}{2}(U(x)e^{i\omega t} + U^*(x)e^{-i\omega t}), \tag{5.26}$$

where $A(x) = |U(x)|$ and $\phi(x) = \arctan\left(\frac{\text{Im}(U(x))}{\text{Re}(U(x))}\right)$. Substitute Eq. 5.26 back into Eq. 5.24, we obtain:

$$i\omega U(x)e^{i\omega t} - i\omega U^*(x)e^{-i\omega t} = \kappa\left(U''(x)e^{i\omega t} + U^{*''}(x)e^{-i\omega t} + \frac{1}{x}U'(x)e^{i\omega t} + \frac{1}{x}U^{*'}(x)e^{-i\omega t}\right). \tag{5.27}$$

Using the Lemma (zero sum of complex exponentials) condition, Eq. 5.27 can be simplified as:

$$i\omega U(x) - \kappa U''(x) - \frac{\kappa}{x}U'(x) = 0. \tag{5.28}$$

According to Eq. 5.28, now the problem becomes to solve the formula:

$$\frac{1}{U(x)}\left(U''(x) + \frac{1}{x}U'(x)\right) = -\left(\sqrt{\frac{\omega}{2\kappa}}(1-i)\right)^2, \tag{5.29}$$

with the boundary conditions:

$$U(0) = A \quad \text{and} \quad U(r) = 0. \tag{5.30}$$

Note that Eq. 5.29 has the same forms as the first terms of Eq.5.16 in transient case. Solving it gives:
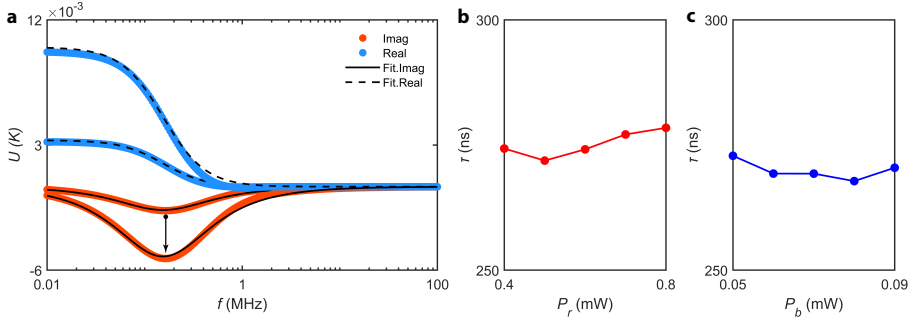
$$U(x) = c_1 J_0(mx) + c_2 Y_0(mx), \tag{5.31}$$

Figure 5.7: **a** COMSOL simulation results under different heating power. The amplitude of thermal signal increases as the heating power enhances from 1 to 3×10^{12} W m^{-3}, while its location is still fixed, indicating an unchanged thermal time constant τ. The measured τ for a MoS$_2$ sample as the function of **b** red and **c** blue laser powers, respectively.

where $m = \sqrt{\frac{\omega}{2\kappa}}(1-i)$. The constants c_1 and c_2 are determined by the boundary conditions Eq. 5.30 as:

$$c_1 = \frac{A J_0(mr)}{Y_0(0) J_0(mr) - Y_0(mr) J_0(0)} \quad \text{and} \quad c_2 = \frac{A Y_0(mr)}{J_0(0) Y_0(mr) - Y_0(0) J_0(mr)}. \tag{5.32}$$

Finally, the average temperature $\overline{U}$ in the membrane can be expressed as:

$$\overline{U} = \frac{1}{r} \int_0^r U(x) dx. \tag{5.33}$$

Note that $Y_0(x) \to \infty$ as $x \to 0$, we assign $Y_0(0)$ with a tiny Δ as $Y_0(\Delta)$, which then allows us to extract the effective and finite value of $\overline{U}$ integrated from Eq. 5.33.

To verify the accuracy of the built model at quasi-steady state, we extract $\overline{U}$ as the function of laser driving frequency f from Eq. 5.33. Assume $r = 4$ μm, $t = 31.4$ nm, $\rho = 3375$ kg m^{-3}, $c_p = 700$ J kg^{-1} K^{-1}, and $k = 5$ W m^{-1} K^{-1} for the membrane, we obtain $\tau = 1291.0$ ns, corresponding to a thermal diffusive constant $\mu^2 = 5.86$. This value is comparable to the obtained result of 5.78 at transient state.

COMSOL SIMULATION

We now calibrate the solution of heat equation using COMSOL simulation, as illustrated in Fig. 5.6a. We first fix the radius of laser spot as its realistic value $r_0 = 0.25$ μm. While for the boundary condition, $u|_{x=r} = 0$, considering the substrate, we change it to the bottom of Si (see the insert in Fig. 5.6a). The thicknesses of SiO$_2$ and Si layers are set at 285 nm and 1 μm, respectively, while the other parameters for the membrane, including r, t, ρ, c_p and k, are used the same values as given. We obtain the simulated temperature distribution of the membrane, as shown in Fig. 5.6b. By fitting Eq. 5.1 to simulation, we extract $\tau = 1506.9$ ns, corresponding to $\mu^2 = 5.02$. This value is thus adopted in Eq. 5.8, allowing us to estimate in-plane thermal conductivity of all fabricated devices.
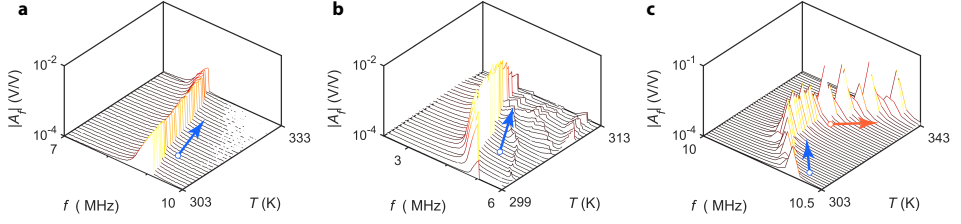
Figure 5.5: Measured resonance frequency f_0 as the function temperature T for **a** MoS_2 device D4, **b** WSe_2 device D5, as well as **c** another Poly Si device with buckling transition.
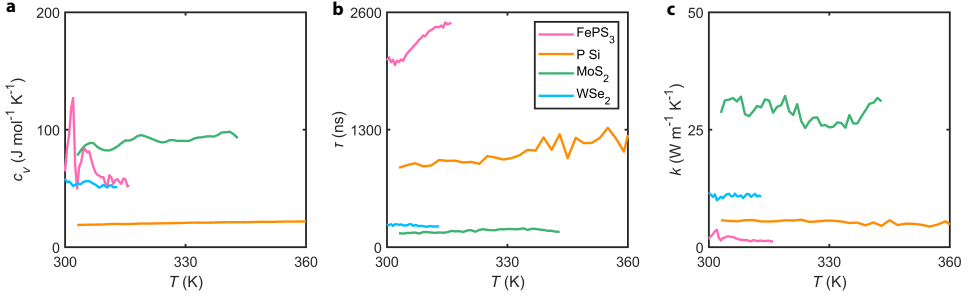

Figure 5.6: **a-c** Specific heat c_v, thermal time constant τ and in-plane thermal conductivity k as the function of T for the fabricated devices D2−D5, respectively.

DEPENDENCE ON LASER POWERS

Furthermore, we discuss the effect of laser powers on our optomechanical measurement, as depicted in Fig. 5.7. According to COMSOL simulation, we verify that the heating only plays a role on the amplitude of thermal signal, instead of its location which is related to τ (Fig. 5.7a). Next, we test MoS_2 device D4, and plot the extract τ as the function of red and blue laser powers, respectively (see Figs. 5.7a and 5.7b). As expected, the obtained τ nearly keep constant and are independent to both P_r and P_b. Therefore, we verify that the proposed optomechanical methodology does not need a laser calibration for determining the in-plane thermal conductivity of 2D materials.

5.6.4. RAW DATA OF OPTOMECHANICAL MEASUREMENTS

In Figs. 5.5a and 5.5b, we see that the measured f_0 decreases as T increases for devices D4 (MoS_2) and D5 (WSe_2). Therefore, both of them are in pre-buckling regime (case I), same as device D1 (2H-TaS_2). In addition, one could argue that the observed increase of f_0 with T for device D3 (Fig. 2c in the main text) is attributed to $\alpha_m < \alpha_{Si}$, instead of a post-buckling performance. As shown in Fig. 5.5c, we obtain the first decrease and then increase of f_0 with T increasing (case II) for another measured Poly Si device, which verify that $\alpha_m > \alpha_{Si}$ for Poly Si and the observed increase of f_0 in device D3 corresponds to the mechanical response in post-buckling regime. Figure. 5.6 shows the obtained specific heat c_v, the measured τ and the obtained in-plane thermal conductivity as the function of T for the fabricated devices D2−D5, respectively.

BIBLIOGRAPHY

[1] Y. Wang, N. Xu, D. Li, and J. Zhu, "Thermal properties of two dimensional layered materials", Advanced Functional Materials **27**, 1604134 (2017).

[2] R. Mas-Balleste, C. Gomez-Navarro, J. Gomez-Herrero, and F. Zamora, "2d materials: to graphene and beyond", Nanoscale **3**, 20–30 (2011).

[3] F. Wu, H. Tian, Y. Shen, Z.-Q. Zhu, Y. Liu, T. Hirtz, R. Wu, G. Gou, Y. Qiao, Y. Yang, et al., "High thermal conductivity 2d materials: from theory and engineering to applications", Advanced Materials Interfaces **9**, 2200409 (2022).

[4] X. Gu and R. Yang, "Phonon transport and thermal conductivity in two-dimensional materials", Annual review of heat transfer **19** (2016).

[5] E. Pop, V. Varshney, and A. K. Roy, "Thermal properties of graphene: fundamentals and applications", MRS bulletin **37**, 1273–1281 (2012).

[6] H. Liu, G. Qin, Y. Lin, and M. Hu, "Disparate strain dependent thermal conductivity of two-dimensional penta-structures", Nano letters **16**, 3831–3842 (2016).

[7] H. Ying, A. Moore, J. Cui, Y. Liu, D. Li, S. Han, Y. Yao, Z. Wang, L. Wang, and S. Chen, "Tailoring the thermal transport properties of monolayer hexagonal boron nitride by grain size engineering", 2D Materials **7**, 015031 (2019).

[8] Z. Luo, J. Maassen, Y. Deng, Y. Du, R. P. Garrelts, M. S. Lundstrom, P. D. Ye, and X. Xu, "Anisotropic in-plane thermal conductivity observed in few-layer black phosphorus", Nature communications **6**, 8572 (2015).

[9] X. Gu, Y. Wei, X. Yin, B. Li, and R. Yang, "Colloquium: phononic thermal properties of two-dimensional materials", Reviews of Modern Physics **90**, 041002 (2018).

[10] I. Jo, M. T. Pettes, E. Ou, W. Wu, and L. Shi, "Basal-plane thermal conductivity of few-layer molybdenum disulfide", Applied Physics Letters **104**, 201902 (2014).

[11] C. Wang, J. Guo, L. Dong, A. Aiyiti, X. Xu, and B. Li, "Superior thermal conductivity in suspended bilayer hexagonal boron nitride", Scientific reports **6**, 1–6 (2016).

[12] A. A. Balandin, S. Ghosh, W. Bao, I. Calizo, D. Teweldebrhan, F. Miao, and C. N. Lau, "Superior thermal conductivity of single-layer graphene", Nano letters **8**, 902–907 (2008).

[13] H. Zhou, J. Zhu, Z. Liu, Z. Yan, X. Fan, J. Lin, G. Wang, Q. Yan, T. Yu, P. M. Ajayan, et al., "High thermal conductivity of suspended few-layer hexagonal boron nitride sheets", Nano Research **7**, 1232–1240 (2014).

[14] D. L. Nika and A. A. Balandin, "Phonons and thermal transport in graphene and graphene-based materials", Rep. Prog. Phys. **80**, 036502 (2017).

[15] R. J. Dolleman, S. Houri, D. Davidovikj, S. J. Cartamil-Bueno, Y. M. Blanter, H. S. Van Der Zant, and P. G. Steeneken, "Optomechanics for thermal characterization of suspended graphene", Physical Review B **96**, 165421 (2017).

[16] A. Castellanos-Gomez, M. Poot, G. A. Steele, H. S. Van Der Zant, N. Agraıt, and G. Rubio-Bollinger, "Elastic properties of freely suspended mos2 nanosheets", Advanced materials **24**, 772–775 (2012).

5

[17] M. Lee, M. Šiškins, S. Mañas-Valero, E. Coronado, P. G. Steeneken, and H. S. van der Zant, "Study of charge density waves in suspended 2h-tas2 and 2h-tase2 by nanomechanical resonance", Applied Physics Letters **118**, 193105 (2021).

[18] M. Šiškins, E. Sokolovskaya, M. Lee, S. Mañas-Valero, D. Davidovikj, H. S. Van Der Zant, and P. G. Steeneken, "Tunable strong coupling of mechanical resonance between spatially separated feps3 nanodrums", Nano letters **22**, 36–42 (2021).

[19] H. Liu, M. Lee, M. Šiškins, H. van der Zant, P. Steeneken, and G. Verbiest, "Tension tuning of sound and heat transport in graphene", arXiv preprint arXiv:2204.06877 (2022).

[20] R. J. Dolleman, D. Lloyd, M. Lee, J. S. Bunch, H. S. Van Der Zant, and P. G. Steeneken, "Transient thermal characterization of suspended monolayer mos 2", Physical Review Materials **2**, 114008 (2018).

[21] F. Kargar, E. A. Coleman, S. Ghosh, J. Lee, M. J. Gomez, Y. Liu, A. S. Magana, Z. Barani, A. Mohammadzadeh, B. Debnath, et al., "Phonon and thermal properties of quasi-two-dimensional feps3 and mnps3 antiferromagnetic semiconductors", ACS nano **14**, 2424–2435 (2020).

[22] S. Uma, A. McConnell, M. Asheghi, K. Kurabayashi, and K. Goodson, "Temperature-dependent thermal conductivity of undoped polycrystalline silicon layers", International Journal of Thermophysics **22**, 605–616 (2001).

[23] J. J. Bae, H. Y. Jeong, G. H. Han, J. Kim, H. Kim, M. S. Kim, B. H. Moon, S. C. Lim, and Y. H. Lee, "Thickness-dependent in-plane thermal conductivity of suspended mos 2 grown by chemical vapor deposition", Nanoscale **9**, 2541–2547 (2017).

[24] S. Kumar and U. Schwingenschlogl, "Thermoelectric response of bulk and monolayer mose2 and wse2", Chemistry of Materials **27**, 1278–1284 (2015).

[25] M. Šiškins, M. Lee, S. Mañas-Valero, E. Coronado, Y. M. Blanter, H. S. van der Zant, and P. G. Steeneken, "Magnetic and electronic phase transitions probed by nanomechanical resonators", Nature communications **11**, 2698 (2020).

[26] F. Ye, J. Lee, and P. X.-L. Feng, "Electrothermally tunable graphene resonators operating at very high temperature up to 1200 k", Nano Letters **18**, 1678–1685 (2018).

[27] C.-H. Liu, I. S. Kim, and L. J. Lauhon, "Optical control of mechanical mode-coupling within a mos2 resonator in the strong-coupling regime", Nano letters **15**, 6727–6731 (2015).

[28] Z. Wang, R. Yang, and P. X.-L. Feng, "Thermal hysteresis controlled reconfigurable mos 2 nanomechanical resonators", Nanoscale **13**, 18089–18095 (2021).

[29] S. Kim, J. Bunyan, P. F. Ferrari, A. Kanj, A. F. Vakakis, A. M. Van Der Zande, and S. Tawfick, "Buckling-mediated phase transitions in nano-electromechanical phononic waveguides", Nano letters **21**, 6416–6424 (2021).

[30] S. Rechnitz, T. Tabachnik, S. Shlafman, M. Shlafman, and Y. E. Yaish, "Dc signature of snap-through bistability in carbon nanotube mechanical resonators", Nano Letters **22**, 7304–7310 (2022).

[31] A. Kanj, P. F. Ferrari, A. M. van der Zande, A. F. Vakakis, and S. Tawfick, "Ultra-tuning of nonlinear drumhead mems resonators by electro-thermoelastic buckling", arXiv preprint arXiv:2210.06982 (2022).

[32] H. Liu, G. Baglioni, C. B. Constant, H. S. van der Zant, P. G. Steeneken, and G. J. Verbiest, "Enhanced photothermal response near the buckling bifurcation in 2d nanomechanical resonators", arXiv preprint arXiv:2305.00712 (2023).

[33] Y. Okada and Y. Tokumaru, "Precise determination of lattice parameter and thermal expansion coefficient of silicon between 300 and 1500 k", Journal of applied physics **56**, 314–320 (1984).

[34] X. Zhang, D. Sun, Y. Li, G.-H. Lee, X. Cui, D. Chenet, Y. You, T. F. Heinz, and J. C. Hone, "Measurement of lateral and interfacial thermal conductivity of single-and bilayer mos2 and mose2 using refined optothermal raman technique", ACS applied materials & interfaces **7**, 25923–25929 (2015).

[35] S. Sahoo, A. P. Gaur, M. Ahmadi, M. J.-F. Guinel, and R. S. Katiyar, "Temperature-dependent raman studies and thermal conductivity of few-layer mos2", The Journal of Physical Chemistry C **117**, 9042–9047 (2013).

[36] O. Çakıroğlu, N. Mehmood, M. M. Çiçek, A. Aikebaier, H. R. Rasouli, E. Durgun, and T. S. Kasırga, "Thermal conductivity measurements in nanosheets via bolometric effect", 2D Materials **7**, 035003 (2020).

[37] E. H. Sondheimer, "The mean free path of electrons in metals", Advances in physics **50**, 499–537 (2001).

[38] J. Liu, G.-M. Choi, and D. G. Cahill, "Measurement of the anisotropic thermal conductivity of molybdenum disulfide by the time-resolved magneto-optic kerr effect", Journal of Applied Physics **116**, 233107 (2014).

[39] J. L. Braun, C. H. Baker, A. Giri, M. Elahi, K. Artyushkova, T. E. Beechem, P. M. Norris, Z. C. Leseman, J. T. Gaskins, and P. E. Hopkins, "Size effects on the thermal conductivity of amorphous silicon thin films", Physical Review B **93**, 140201 (2016).

[40] A. Arrighi, E. del Corro, D. N. Urrios, M. V. Costache, J. F. Sierra, K. Watanabe, T. Taniguchi, J. A. Garrido, S. O. Valenzuela, C. M. S. Torres, et al., "Heat dissipation in few-layer mos2 and mos2/hbn heterostructure", 2D Materials **9**, 015005 (2021).

[41] P. Norouzzadeh and D. J. Singh, "Thermal conductivity of single-layer wse2 by a stillinger–weber potential", Nanotechnology **28**, 075708 (2017).

[42] X. Liu, G. Zhang, Q.-X. Pei, and Y.-W. Zhang, "Phonon thermal conductivity of monolayer mos2 sheet and nanoribbons", Applied Physics Letters **103**, 133113 (2013).

[43] Q. Cui, F. Ceballos, N. Kumar, and H. Zhao, "Transient absorption microscopy of monolayer and bulk wse2", ACS nano **8**, 2970–2976 (2014).

[44] T. S. Kasırga, "Thermal conductivity measurements in 2d materials", in *Thermal conductivity measurements in atomically thin materials and devices* (Springer, 2020), pp. 11–27.

[45] G. Qin and M. Hu, "Thermal transport in phosphorene", Small **14**, 1702465 (2018).

[46] N. C. Frey, A. Bandyopadhyay, H. Kumar, B. Anasori, Y. Gogotsi, and V. B. Shenoy, "Surface-engineered mxenes: electric field control of magnetism and enhanced magnetic anisotropy", ACS nano **13**, 2831–2839 (2019).

5

[47] J. M. Park, Y. Cao, L.-Q. Xia, S. Sun, K. Watanabe, T. Taniguchi, and P. Jarillo-Herrero, "Robust superconductivity in magic-angle multilayer graphene family", Nature Materials **21**, 877–883 (2022).

[48] X. Wu and Q. Han, "Phonon thermal transport across multilayer graphene/hexagonal boron nitride van der waals heterostructures", ACS Applied Materials & Interfaces **13**, 32564–32578 (2021).

[49] W. Ren, Y. Ouyang, P. Jiang, C. Yu, J. He, and J. Chen, "The impact of interlayer rotation on thermal transport across graphene/hexagonal boron nitride van der waals heterostructure", Nano Letters **21**, 2634–2641 (2021).

[50] M. J. Hancock, "The 1-d heat equation", MIT OpenCourseWare. Accessed August **31**, 2018 (2006).

5

6

6

TUNING HEAT TRANSPORT IN GRAPHENE BY TENSION

Heat transport by acoustic phonons in 2D materials is fundamentally different from that in 3D crystals because the out-of-plane phonons propagate in a unique way that strongly depends on tension and bending rigidity. Here, using optomechanical techniques, we experimentally demonstrate that the heat transport time in freestanding graphene membranes is significantly higher than the theoretical prediction, and decreases by as much as 33 % due to an electrostatically induced tension of 0.07 N/m. Using phonon scattering and Debye models, we explain these observations by the tension-enhanced acoustic impedance match of flexural phonons at the boundary of the graphene membrane. Thus, we experimentally elucidate the tunability of phononic heat transport in 2D materials by tension, and open a route towards electronic devices and circuits for high-speed control of temperature at the nanoscale.

6.1. INTRODUCTION

Although in most bulk materials the propagation speed of different types of acoustic phonons is of similar magnitude, the situation is vastly different in 2D materials [1–5]. In these atomically thin materials, in-plane phonons have a constant propagation speed that is determined by the atomic bond stiffnesses, whereas out-of-plane flexural phonons, exhibit a frequency-dependent speed that is determined by both in-plane strain and bending rigidity [6–9], such that flexural and in-plane phonon velocities can differ by more than an order of magnitude. Initial studies suggested that flexural phonons provide the dominant pathway for heat transport and storage in 2D materials [10, 11], however it has been difficult to experimentally separate flexural and in-plane phonon contributions.

Evidence for the importance of speed differences on the phononic heat transport in 2D materials was provided by theoretical analysis [12] and by the experimental observation of two distinct thermal time constants in graphene membranes, of which the longest, τ, is a probe for studying heat transport by the relatively slow flexural phonons [13–16]. To understand heat propagation via these different in-plane and out-of-plane phononic channels in 2D materials, studies of the role of flexural phonons are essential. Yet, unlike the lattice thermal conductivity of 2D materials, which has been well characterized by Raman microscopy [17, 18], a microscopic picture of how the rate of heat transport is related to the properties of flexural phonons remains elusive, as it requires a methodology for measuring their effect on temperature variations in suspended 2D materials with nanosecond resolution.

In this chapter, we demonstrate that heat flow in graphene can be tuned by tension using an optothermomechanical method to experimentally characterize heat transport in graphene drum resonators with nanosecond resolution. We control the tension by an electrostatic force induced by a voltage V_g on a gate underneath the graphene drum. Using an optothermal drive, we actuate the graphene drum resonators [19]. From the mechanical resonance frequency $\omega_0/(2\pi)$ (>10 MHz) as a function of V_g, we determine the in-plane tension and effective mass of the drum and from the mechanical response at low frequencies (<1 MHz), we extract the thermal time constant τ of the resonators. To explain the observed tension-dependence of τ, we combine the Debye model for phononic heat transport with a boundary scattering model that describes acoustic phonon reflection and transmission at the edge of the graphene drum. From this analysis it follows that heat transport mainly depends on tension due to its effect on the acoustic impedance match between the flexural phonons on the suspended and supported part of membrane.

6.2. RESULTS AND DISCUSSION

Four graphene drum resonators, device D1−D4, are measured to study the effect of tension on heat transport, as shown in Figs. 6.1a and 6.1b. The surface profile measured by atomic force microscopy indicates an initial downward deflection of the membrane, resulting from sidewall adhesion at the edge of the membrane [20] (see Fig. 6.1c). We measure the motion of the resonators using the interferometer depicted in Fig. 6.1d. By exciting the membrane with a modulated blue laser, while interferometrically detect-

ing its motion, the frequency response of the devices is determined and used to characterize both the mechanical and thermal parameters of the devices. Figure. 6.1e shows the measured motion amplitude z_ω of device D1 at $V_g = 0\,\text{V}$ over the frequency range from 0.1 to 100 MHz. We extract $\omega_0/(2\pi)$ and quality factor Q of the device by fitting the measured data to a harmonic oscillator model (Fig. 6.1f). For device D1 this results in $\omega_0/(2\pi) = 25.49\,\text{MHz}$ and $Q = 43.25$. The average quality factor of the four devices at room temperature is $Q = 36.5 \pm 8.4$, which is comparable to literature values [21, 22]. Around 1 MHz, we observe an additional broad signal in the imaginary part of the frequency response (Fig. 6.1g). This signal is associated [19] with the frequency dependent optothermal force $F_{\text{th},\omega}$ on the resonator, because it is only present when driving the membrane optothermally. Following literature [13], far below mechanical resonance, the displacement $z_\omega = F_{\text{th},\omega}/k$ is proportional to the effective thermal expansion force $F_{\text{th},\omega}$ that is delayed with respect to the laser power $P(t) = P_{\text{ac}}e^{i\omega t}$ as a consequence of the time τ it takes to increase the membrane temperature by laser heating. As shown by the fits in Fig. 6.1g, the low-frequency z_ω is given by:

$$z_\omega = \frac{C_{\text{slow}}}{1 + i\omega\tau} + C_{\text{fast}}, \tag{6.1}$$

where C_{slow} and C_{fast} are the normalized thermal expansion amplitudes contributed from out-of-plane and in-plane phonons, respectively [13]. We extract these parameters by fitting Eq. 6.1 to the real and imaginary parts of the measured z_ω, as depicted in Fig. 6.1g. Here, the peak in the imaginary part of z_ω is located at 1.23 MHz, corresponding to $\tau = (2\pi \times 1.23\,\text{MHz})^{-1} = 129\,\text{ns}$. We checked the laser power dependence and verified that it has no significant effect on the measured value of τ (see Fig. 6.4).

By applying V_g on graphene drum resonators, we observe a clear change in both the measured $\omega_0/(2\pi)$ and τ (see Fig. 6.2). V_g generates an electrostatic force, pulling the drum down and thereby increasing tension. Figure. 6.2a shows plots of $\omega_0/(2\pi)$ against V_g for all devices from $-4\,\text{V}$ to $4\,\text{V}$. The typical W-shaped curves show both electrostatic softening and tension hardening, as often observed in electrostatic gate-tuning of graphene membranes [21]. The observed values of τ, of all above 75 ns, are significantly higher than the value of $\tau \approx 2\,\text{ns}$ obtained from the theoretical expression $\tau = r^2\rho_g c_p/(2k)$, that follows from solving the heat equation for a perfect circular graphene membrane [23] for typical values of specific heat c_p and thermal conductivity k. Interestingly, it is also shown here that τ reduces by as much as 33 % when the tension in the membrane is increased by V_g (Figs. 6.2b–6.2d). This n-dependent decrease in τ is unexpected from the heat equation, because recent studies show that c_p increases [24] while k decreases [25, 26] as the tension in graphene increases, from which one would expect τ to increase at higher n, precisely opposite to our experimental observations.

To shed light on the obtained large magnitude of τ and its negative dependence on V_g-induced tension in Figs. 6.2b–6.2e, we firstly quantify n in the drum. Following literature[21], we model $\omega_0/(2\pi)$ tuning of the drum resonator by continuum mechanics:

$$\omega_0(V_g) = \sqrt{\frac{1}{m_{\text{eff}}}\left[\frac{2\pi E t s_0}{1-v^2} + \frac{8\pi E t}{(1-v^2)r^2}z_g^2 - \frac{1}{2}\frac{\partial^2 C_g}{\partial z_g^2}V_g^2\right]}, \tag{6.2}$$

in which s_0 is the built-in strain, m_{eff} is the modal mass of the fundamental mode of the
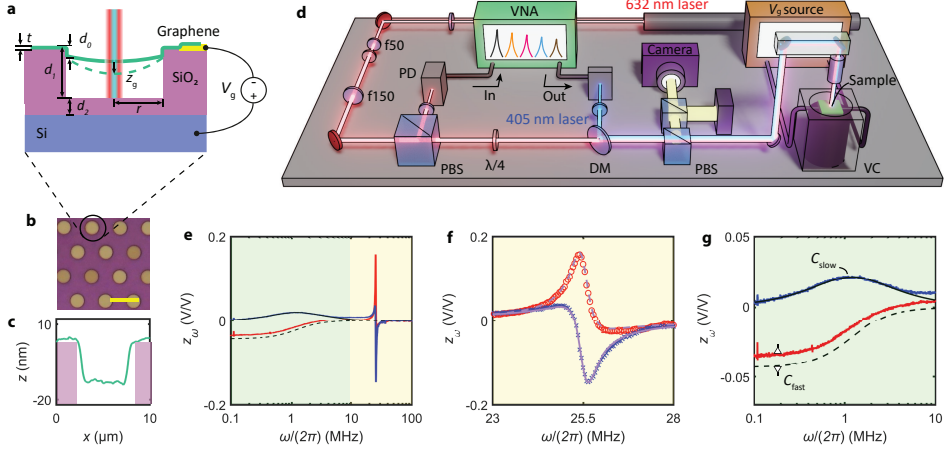
Figure 6.1: Graphene membrane characterization. **a** Schematic of a graphene drum of radius r over a cavity of depth d_1 in a SiO_2/Si substrate irradiated by lasers. The graphene has a sidewall of length d_0 into the cavity. The voltage V_g pulls the drum down by z_g, increasing its tension. **b** Optical image of the drums with a scale bar of $10\,\mu m$. **c** Atomic force microscope line trace over device D4 indicates a downward deformation of drum, originating kink at the boundary. Note the different units for x and z on the axis. **d** Interferometric setup. The sample is placed inside a vacuum chamber (VC). The blue (405 nm) laser is intensity modulated by a vector network analyzer (VNA) to actuate the resonator. Intensity variations of the reflected red (633 nm) laser caused by resonator motion, are measured by photodiode (PD) and recorded with the VNA. PBS: polarized beam splitter; DM: dichroic mirror. **e** Frequency response of device D1, including real (red) and imaginary (blue) parts of the motion z_ω. **f** Fits of $z_\omega/(2\pi)$ (lines) to Eq. 1 to obtain ω_0. **g** Fits of Eq. 1 to z_ω near the thermal peak (black solid and dashed lines) provide τ, C_{fast} and C_{slow} of the resonator.

Table 6.1: Characteristics of devices D1−D4: radius r (μm), effective gap g_0 (nm), pretension n_0 (N/m), effective mass m_{eff} ($\times 10^{-16}$kg), normalized areal density η, the second derivative of the capacitance with respect to the electrostatic deflection $\frac{\partial^2 C_g}{\partial z_g^2}$ (mF m^{-2}), bending rigidity κ (eV), and percentual energy absorption γ.

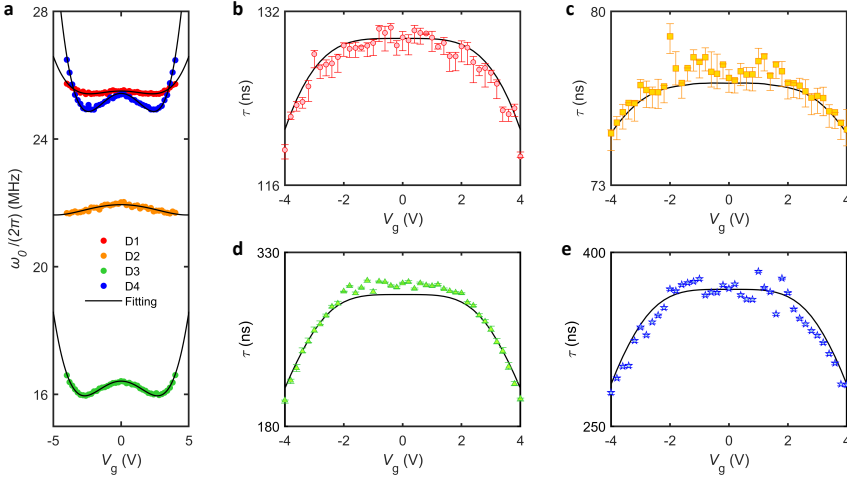| device	r	g_0	n_0	m_{eff}	η	$\frac{\partial^2 C_g}{\partial z_g^2}$	κ	γ
D1	2.5	212	0.24	0.50	19.40	6.56	3.8	8.18
D2	2.5	237	0.34	0.96	37.10	9.12	9.4	6.90
D3	5	227	0.21	1.06	10.36	34.75	2.2	3.26
D4	5	237	0.18	0.39	3.80	30.35	0.6	1.29

Figure 6.2: Tuning thermodynamic properties of graphene drum devices with gate voltage. **a** Solid dots: ω_0 versus V_g measured in devices D1–D4; drawn lines: fits based on Eq. 6.2. **b**–**e** Points: τ versus V_g measured in devices D1–D4, respectively; solid lines: fits to data using the Debye and scattering models; error bars are from the fits to the measured thermal signals as plotted in Fig. 6.1g.

circular membrane resonator with a theoretical value $m_{\text{eff,th}} = 0.271\pi r^2 \rho_g$ where ρ_g is the mass density of double-layer graphene, C_g is the capacitance between membrane and bottom gate, and the second derivative $\frac{\partial^2 C_g}{\partial z_g^2}$ quantifies the electrostatic softening. The 2D Young's modulus $Et \approx 175.39\,\text{N/m}$ in average and Poisson ratio $\nu = 0.16$ were determined via AFM indentation[27] (see Appendix section 1). The center deflection z_g can be expressed[28] as $\varepsilon_0 r^2 V_g^2/(8g_0^2 n_0)$, where $n_0 = Et s_0/(1-\nu)$ is the pretension, ε_0 is the permittivity of vacuum, and $g_0 = d_1 + d_2/\varepsilon_{\text{SiO2}} - d_0$ is the effective gap between the drum and the electrostatic gate. We fit the measured V_g dependence of ω_0 by Eq. 6.2 (black lines in Fig. 6.2a) to extract the fit parameters n_0, m_{eff} and $\frac{\partial^2 C_g}{\partial z^2}$ for each device, as listed in Table 6.1. The extracted initial tension n_0 for all devices ranges from 0.18 to 0.34 N/m, which corresponds to typical literature values reported for graphene membranes [21, 28–30]. The modal mass m_{eff} ranges from 0.39 to 1.06 $\times 10^{-16}$ kg, which is larger than the mass expected for double-layer graphene. This difference can be attributed to polymer residues left on or between the double-layer graphene after fabrication [29, 31]. The good quality of the fits with Eq. 6.2 in Fig. 6.2a (drawn lines) allows us to use the obtained fit parameters to extract the membrane deflection z_g at all V_g. By using the equation [21] $n = n_0(1 + 4z_g^2/r^2)$, we obtain the corresponding membrane tension $n(V_g)$.

Since the classical heat equation clearly does not suffice to account for the observed τ and its tension dependence, we now will use a phonon scattering model to assess the transient thermal conduction in the membrane [12]. This model assumes that the transport of the relevant flexural acoustic phonons is ballistic on the membrane, since their mean free paths are much longer than the radius r of the membrane [32–34]. Moreover, we neglect any heat transport through polymer residues left over after fabrication as its

thermal conductivity (0.2 W/mK) is much lower than that of graphene (> 1000 W/mK) [17, 35]. The kink at the membrane edge (Fig. 6.1c) is the main source of n-dependent phonon scattering [36] (see Fig. 6.5) and results in the following expression for τ:

$$\tau = \frac{r}{2c_z \sum_j \overline{w}_{1z \to 2j}}, j = l, t, z, \tag{6.3}$$

in which the transmission rate $\overline{w}_{1z \to 2j}$ is the probability that a flexural phonon on the suspended part of the graphene (subscript 1) is transmitted across the membrane edge and becomes a phonon of type j on the supported part of the graphene (subscript 2), where j can either be a flexural phonon ($j = z$), or a longitudinal or transverse in-plane phonon ($j = l, t$). $\overline{w}_{1z \to 2j}$ depends both on n and on the speed of sound c_z of flexural phonons (see Appendix section 2). Due to the scattering at the edge of the membrane, the calculated magnitude of $\overline{w}_{1z \to 2j}$ is much lower than 1, which results in a value of τ that is much larger than the value $\tau = r^2 \rho_g c_p / (2k)$ in the absence of scattering. This scattering is a kind of Kapitza thermal boundary resistance [37] and thus potentially accounts for the large value of τ observed in our fabricated graphene resonators (Figs. 6.2b−6.2e). The transmission rates for in-plane (LA and TA) phonons, $\overline{w}_{1l \to 2j}$ and $\overline{w}_{1t \to 2j}$, are much higher than $\overline{w}_{1z \to 2j}$, which results in a negligible contributions to τ in Eq. 6.3 (see Appendix section 2). Therefore, we only consider the incidence of flexural phonons in the scattering model.

Heat is transported by phonons of many different frequencies, while $\overline{w}_{1z \to 2j}$ depends on the speed of these phonons. Therefore, to analyze the effect of tension on heat transport, the dispersion relation for flexural phonons is needed, which is given [38] by $\omega_q = \sqrt{(\kappa q^4 + n q^2)/(\eta \rho_g)}$, where q is the wavenumber, κ is the bending rigidity of the membrane, and $\eta = m_{\text{eff}}/(0.271\pi r^2 \rho_g)$ is the normalized areal density of the membrane (listed in Table 6.1 for all devices). From this dispersion relation, the speed of sound for flexural phonons is found using $c_z = \frac{\partial \omega_q}{\partial q}$.

We now theoretically estimate the thermal time constant of graphene drum resonators. In practice, flexural phonons over a large frequency span, ranging up to the Debye frequency ω_{qd}, will contribute to τ. To account for this (see flow chart in Fig. 6.9a), we analyze the heat transport contribution for every q using the tension dependent phonon speed $c_z(\omega_q, n)$ and determine the thermal time constant for phonons of that wavenumber $\tau(\omega_q, n)$ using Eq. 6.3. Then, we use the Bose-Einstein distribution to determine the expected phonon energy density via the specific heat spectral density $C_{v,\omega}^z(\omega_q, n)$ of flexural phonons of a certain q (Debye model). The detailed expression of $C_{v,\omega}^z(\omega_q, n)$ can be found in Eq. 6.5. Finally, we take a weighted integral over the contributions of all flexural phonons to determine $\tau(n)$ using $1/\tau(n) = \int_0^{\omega_{qd}} C_{v,\omega}^z(\omega_q, n)/(C_v^z(n)\tau(\omega_q, n))d\omega_q$, where the total specific heat due to flexural phonons is determined using $C_v^z(n) = \int_0^{\omega_{qd}} C_{v,\omega}^z(\omega_q, n)d\omega_q$ [38, 39]. More details about the phononic scattering and Debye models can be found in Appendix sections 2 and 3.

The obtained function $\tau(n)$ is fit to the experimental data in Figs. 6.2b− 6.2e, obtaining good agreement between fit and experiments for all four devices, using κ as the only fit parameter. All other model parameters are determined independently from measurements. The fitted values of κ vary over a range from 0.6 to 9.4 eV, which is similar to
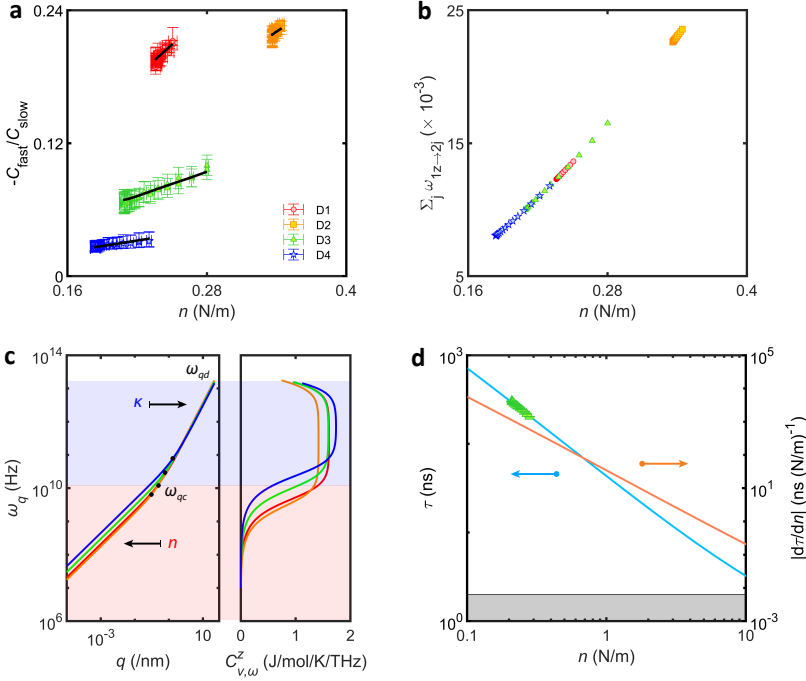
Figure 6.3: Analysis and experimental demonstration on tunable heat transport in graphene drum resonators. **a** Ratio of normalized thermal expansion amplitudes $|C_{\text{fast}}/C_{\text{slow}}|$ versus tension n. Points: the measurements; solid lines: the modelled estimates. **b** $\sum_j \overline{w}_{1z \to 2j}$ ($j = l, t, z$) of flexural phonons for devices D1−D4 as $c_z = 575\,\text{m/s}$, indicating the tension-enlarged impedance matching of acoustic phonons at the boundary of membrane. This tunability is the same for all-frequency phonons with different c_z. **c** Left panel: calculated $\omega_q(q)$ for devices D1−D4. $\omega_q(q)$ is dominated by n in ~MHz regime (red shadow) and dominated by κ in ~THz regime (blue shadow), respectively, while the cross-over frequency ω_{qc} is located at ~GHz regime. Right panel: $C_{v,\omega}^z$ for all devices. **d** Tunable τ with n varying from 0.1 to 10 N/m, using device D3 as an example. Green points: the measured τ versus n for device D3; blue line: estimated τ by the scattering model; red line, tension tunability $|d\tau/dn|$; grey region: the estimation of τ using $r^2 \rho_g c_p/(2k)$.

values reported in literature [40, 41]. Although the exact mechanism behind these bending rigidity variations remains unclear, we observe in Fig. 6.9b that κ increases with η of the membranes, potentially indicating that polymer residues do not only affect the mass of the membrane, but also play an important role in the heat transport by increasing the membrane's bending rigidity.

To analyze the main mechanism by which n can reduce τ in graphene resonator, we investigate three different ways: via $c_z(n, \omega_q)$, via $C_{v,\omega}^z(n, \omega_q)$, and via $\overline{w}_{1z \to 2z}$. Since n mainly affects the dispersion relation of low-frequency (MHz) phonons, the direct impact of n on τ via the first two paths is relatively small (see Fig. 6.10). Therefore, the observed decrease of τ in Figs. 6.2b−6.2e is mainly attributed to the n-induced increase in $\sum_j \overline{w}_{1z \to 2j}$, as plotted in Fig. 6.3b. Specifically, we see the wave amplitudes $|u_{2j}|$ of all three transmitted modes increase with n (Fig. 6.5b), indicating an enhanced impedance matching of acoustic phonons between the suspended and supported part of the mem-

brane.

Besides τ, the normalized thermal expansion amplitudes C_{fast} and C_{slow} in Eq. 6.1 can provide us with more information on the heat flow. We attribute the opposite signs of C_{fast} and C_{slow} in the measurements to the opposite signs of the Grüneisen parameters for the in-plane and out-of-plane phonon modes. Here we will use them to analyze the relative contributions of the in-plane and flexural phonons to the thermal expansion force [13], and also show that the tension dependence of these amplitudes C_{fast} and C_{slow} agrees well to the presented model. From the low frequency fits of z_ω (see Fig. 6.1g), we determine the tension dependence of C_{fast} and C_{slow} in Eq. 6.1. Because the thermal expansion amplitude is proportional to the temperature increase, the measured ratio $|C_{\text{fast}}/C_{\text{slow}}|$ is approximately proportional to the relative temperature increase of both phonon baths [13]. Qualitatively, the n-enhanced c_z will reduce the edge scattering rate according to Eq. 6.3, and therefore increases the cooling rate of the flexural phonon bath. As a consequence, the temperature increase of that phonon bath and C_{slow} decrease [7], which leads to an increase of the ratio $|C_{\text{fast}}/C_{\text{slow}}|$ with n as observed in Fig. 6.3a. Also shown in Fig. 6.3a (lines), our model also accurately captures the relation between n and $|C_{\text{fast}}/C_{\text{slow}}|$ for all devices (see more details in Appendix section 5).

We now turn to Fig. 6.3c to get more insight in the tension tuning mechanism of τ. For high-frequency (~THz) flexural phonons (blue shadow, Fig. 6.3c), κ dominates $\omega_q(q)$ for all devices D1−D4 (Fig. 6.3c, left panel), and thus $C_{v,\omega}^z(\omega_q)$ also shows significant device-to-device variations (Fig. 6.3c, right panel) which is responsible for the measured variations in τ. More details about how κ and η affect $\omega_q(q)$ and $C_{v,\omega}^z(\omega_q)$ can be found in Appendix section 4. On the other hand, for low-frequency (~MHz) flexural phonons (red shadow, Fig. 6.3c), the situation is completely different. The resonance frequency of the graphene membranes can be understood as a standing wave of flexural acoustic phonons and is thus proportional to the ratio $c_z \propto \sqrt{n/\eta}$ and the membrane radius, such that κ does not play an important role. c_z is thus fully determined by n and η, in line with experimental graphene resonators reported in the literature [21]. We estimate the cross-over frequency ω_{qc} where the phonon dispersion $\omega_q(q)$ makes the transition from tension n- dominated to κ- dominated regime, at around 84.8, 52.6, 174.4 and 422.7 GHz for devices D1−D4, respectively.

The measured parameters (listed in Table 6.1) allow us to model the phonon dispersion and specific heat spectral density in Fig. 6.3c over the wide frequency range from the MHz to the THz regime. Let us discuss how this results in the tunability of the heat transport using Fig. 6.3d. As n increases from 0.1 to 10 N/m, τ decreases from ~1 μs to less than 4 ns (blue line), while the tunability $|d\tau/dn|$ also decreases significantly (orange line). In such a wide tuning of n, the tunability of heat transport is attributed not only to the increase of the transmission rate $\overline{w}_{1z\to2j}$ of flexural phonons, but also to the increased speed of sound ($c_z \approx \sqrt{n/(\eta\rho_g)}$ for $n \gg \kappa q^2$) and the change of $C_{v,\omega}^z(n,\omega_q)$. The low τ (~2 ns at $n = 10$ N/m) under high tension is comparable to its value obtained from the heat equation $r^2\rho_g c_p/(2k)$, demonstrating that at high tension, the heat flow rate from the centre to the boundary of membrane [19, 22] (grey region, Fig. 6.3d) sets a lower limit on the acoustic phonon transport rate, whereas at low tension the boundary scattering determines the upper limit. Understanding these limits on the tension tunability of heat transport is important for proposed applications in the field of 2D phononics,

such as switchable thermal transistors, ultra-sensitive thermal logic gates, and reconfigurable phononic memories [42, 43].

6.3. Conclusion

To conclude, we measured the thermal time constant that governs nanosecond-scale heat transport in suspended graphene drums and presented experimental evidence for its tunability via gate-controlled in-plane tension. Using a Debye model that captures the scattering of acoustic phonons at the membrane edge, we present a microscopic picture of heat transport in suspended graphene membranes, where bending rigidity and tension dominate the flexural dispersion relation for THz and MHz frequency phonons, respectively. Tension is responsible for tuning the transmission rate of flexural phonons from the suspended to the supported part of the graphene. The gained insight not only advances our fundamental understanding of acoustic phonons in 2D materials, but also enables pathways for controlled and optimized thermal management in 2D-based phononic, thermoelectric, electronic and quantum devices, as well as in 2D sensing applications such as nanoelectromechanical system (NEMS).

6.4. Methods

Sample fabrication. We pattern circular cavities with a depth of 240 nm using reactive ion etching into a Si/SiO_2 chip. We pattern Ti/Au electrodes (5/60 nm) on the chip which are used to define the cavities. The cavity depth is less than the SiO_2 thickness of 285 nm to prevent an electrical short-circuit between the Si electrode and the suspended drums. We subsequently transfer large-scale CVD graphene over the cavities. This double-layer graphene is fabricated by stamping one monolayer CVD graphene on top of another one, where an extra layer of polymethyl methacrylate (PMMA) is attached on each graphene layer. During this process, polymer residues between the layer potentially affect the interlayer coupling. Finally, we remove the PMMA by annealing the devices for 30 min in a furnace at a pressure of 500 Torr, with a constant flow of 0.5 SLPM of an inert dry gas (Ar or N_2) at a temperature of 300 °C. The initial thickness of PMMA is 800 nm. Using the extracted effective mass of the membrane m_{eff} and the mass density of PMMA ($1180 \, \text{kg/m}^3$), we obtain the thicknesses of polymer residue about 6.7, 14.0, 2.9, 0.3 nm for devices D1−D4, respectively, which means most of the PMMA has been evaporated after annealing.

Optothermal drive. To measure ω_0, τ, C_{fast}, and C_{slow} in the graphene drums, we use an interferometer (red laser, $\lambda = 633$ nm) to detect their motion. An intensity modulated blue laser ($\lambda = 405$ nm) irradiates the suspended drum resulting in a periodic heat flux[22] to actuate it. The heat flux results in a motion of the drum due to the thermal expansion force. All measurements are performed at room temperature inside a vacuum chamber at 10^{-6} mbar. A vector network analyzer (VNA) modulates the intensity of a blue laser at frequency ω to optothermally actuate a resonator while it analyzes the resulting intensity modulation of the red laser caused by the mechanical response of the same resonator. The red and blue laser powers used are 1.20 and 0.13 mW respectively, where the resonators vibrate in the linear regime and the temperature increase due to self-heating was negligible[19]. We experimentally verified that the extracted thermal

time constant τ does not depend on the laser power (see Fig. 6.4).

Scattering model of acoustic phonons. We develop this model for scattering of phonons at the sidewall between the suspended and supported graphene to evaluate the thermal time constant τ. Due to phonon transmission across the graphene-support interface and strong interface-scattering of flexural modes, the mean free path of flexural phonons on supported graphene will be much reduced[44], thus we only assume the ballistic transport of acoustic phonons on domain 1. For incoming flexural phonons (defined as mode $1z$), the transmission rate $w_{1z \rightarrow 2j}(j = l, t, z)$ can be calculated as a function of the incident angle θ_{1z} (see Fig. 6.5b for details). Here, $c_l =21.6$ km/s and $c_t =16$ km/s are determined from the linear dispersion of in-plane phonons in graphene, using[45] Lame parameters $\lambda = 48$ J/m^2 $\mu = 144$ J/m^2. The total transmission coefficient $\overline{w}_{1z \rightarrow 2j}$ is then obtained by integrating $w_{1z \rightarrow 2j}$ over all incidence angles from $-\pi/2$ to $\pi/2$. We also assume kink angle $\beta = 90°$ at membrane edge. More details can be found in Appendix section 2.

6.5. APPENDIX

6.5.1. MECHANICAL CHARACTERIZATION OF GRAPHENE DRUM RESONATORS

We use indentation measurements with an atomic force microscope (AFM) to determine the 2D Young's modulus Et of the suspended graphene drums. This indentation measurement is modelled as a clamped circular membrane with central point loading. The relationship between the applied force F with the AFM cantilever and the resulting deformation δ is given by $F = n_0 \pi \delta + Et q^3 \delta^3 / r^2$, where $q = 1/(1.05 - 0.15v - 0.16v^2)$ is a geometrical factor with a Poisson's ratio $v = 0.16$ [46] and n_0 is the pretension in the membrane. We extract Et of our graphene devices through fitting the measured curves of F vs δ and obtain a mean Young's modulus $Et =175.39$ N/m [27]. We thus employ this value to estimate the surface tension of graphene resonators.

As described in Methods section, an optomechanical drive allows us to actuate the graphene resonators and measure their thermodynamic properties. For the detection of the motion of the graphene membranes, we use a red laser (λ=633 nm) with a power P_{dc} of 1.2 mW, whereas we use an intensity modulated blue laser (λ=405 nm) with a power P_{ac} of 0.13 mW. We sweep the frequency $\omega/2\pi$ of the intensity modulation from 100 kHz to 100 MHz. To correct for intrinsic phase shifts from the interferometric setup, we calibrate the measured signals on the VNA by pointing the blue laser directly onto the photodiode (see more details in [19]). This correction allows us to obtain the real and imaginary part of the membrane motion z_ω as shown in Figs. 6.1e−6.1g.

We verified that the thermal time constant τ is not related to the laser powers P_{ac} and P_{dc} in the previous derivation [19]. Here as expected, for our fabricated graphene resonators, τ nearly remains unchanged with P_{dc} and P_{ac} increasing, as shown in Figs. 6.4a and 6.4b, respectively. Therefore, the small change of laser powers caused by electrostatic deflection will not play a role on the tension-tuning τ. In addition, the thermal signal only occurs in case of optothermal drive rather than other kinds of actuation, such as electrostatic and piezo drive methods, indicating the unique thermodynamic mechanism behind the thermal signal we observed in measurements.
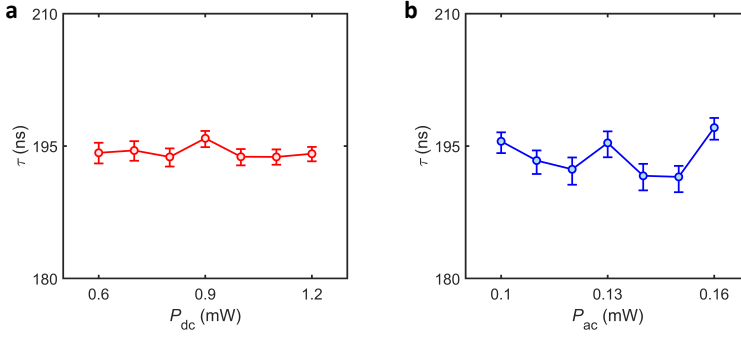
Figure 6.4: Optothermal measurements on graphene resonators as laser powers tuned. **a** Thermal time constant τ of graphene membrane versus red laser power P_{dc}, as blue laser power P_{ac} fixed at 0.13 mW. **b** τ versus P_{ac} as P_{dc} fixed at 1.1 mW. Inserts are the cross-section illustrations of the membrane when we tune P_{dc} and P_{ac}, separately.

6.5.2. SCATTERING MODEL FOR ACOUSTIC PHONONS

Since the measured τ (see Figs. 6.2b−6.2d) are much larger than the theoretically estimate of heat transport from the center of membrane to its boundary, we attribute this to the strong scattering of acoustic phonons at the kink, as illustrated in Fig. 6.5a. This scattering can be regarded as the Kapitza thermal boundary resistance between suspended and supported regions of graphene membrane. Domain 1 and domain 2 represent the suspended membrane and the sidewall, respectively. Using the Snell's law, and the continuities of deflection and stress, we can extract the transmission rate for the different phonon modes ($2j$, $j = l, t, z$) at specific incident angle θ of flexural phonons, given by

$$w_{1z \to 2j} = \frac{c_j |u_{2j}|^2 \mathrm{Re}(\cos\theta_{2j})}{c_z |u_{1z}|^2 \cos\theta_{1z}}, j = l, t, z \tag{6.4}$$

where $|u_{1z}|$ and $|u_{2j}|$ are wave amplitudes of modes $1z$ and $2j$, respectively. The relation between incoming angle θ_{1z} and outgoing angle θ_{2j} is determined by Snell's law as $\sin\theta_{2j} = c_{2j}/c_{1z} \sin\theta_{1z}$, where c_l =21.6 km/s, c_t =16 km/s, and the speed of flexural phonons c_z depends on tension n, bending rigidity κ and the normalized areal density η. Wave amplitudes $|u_{2j}|$ is related to $|u_{1z}|$, incoming angle θ_{1z} and tension n, as derived in ref. [36]. Fig. 6.5b plot $|u_{2z}|$ as a function of θ_{1z}, assume the incoming wave amplitude $|u_{1z}| = 1$, $c_z = 575$ m/s, and $\beta = 90°$. Here, the observed two transmission peaks emerge due to a resonant excitation of waves residing at the kink of membrane. Using the obtained $|u_{2j}|$ and Eq. 6.4, we further plot the transmission $\omega_{1z \to 2j}$ and reflection $\omega_{1z \to 1j'}$ possibilities over all θ as shown in Fig. 6.5c. It shows that that flexural phonons can only transmit across over the kink under the condition of $\theta < 0.055$.

Importantly, it should be noticed that $|u_{1z}|$ rapidly increase as tension n increases from 0.1 to 0.5 N/m (Fig. 6.5b). This leads to the increasing transmission rate $\overline{w}_{1z \to 2j}$ ($j = l, t, z$) with tension (Fig. 6.5d), where $\overline{w}_{1z \to 2j}$ is obtained by integrating $w_{1z \to 2j}$ over all incident angles from $-\pi/2$ to $\pi/2$. As a result, we verify that the induced tension will weaken the impedance mismatch of acoustic phonons at the boundary of graphene membrane, results in the observed decreasing τ in Figs. 6.2b−6.2e. On the other hand,
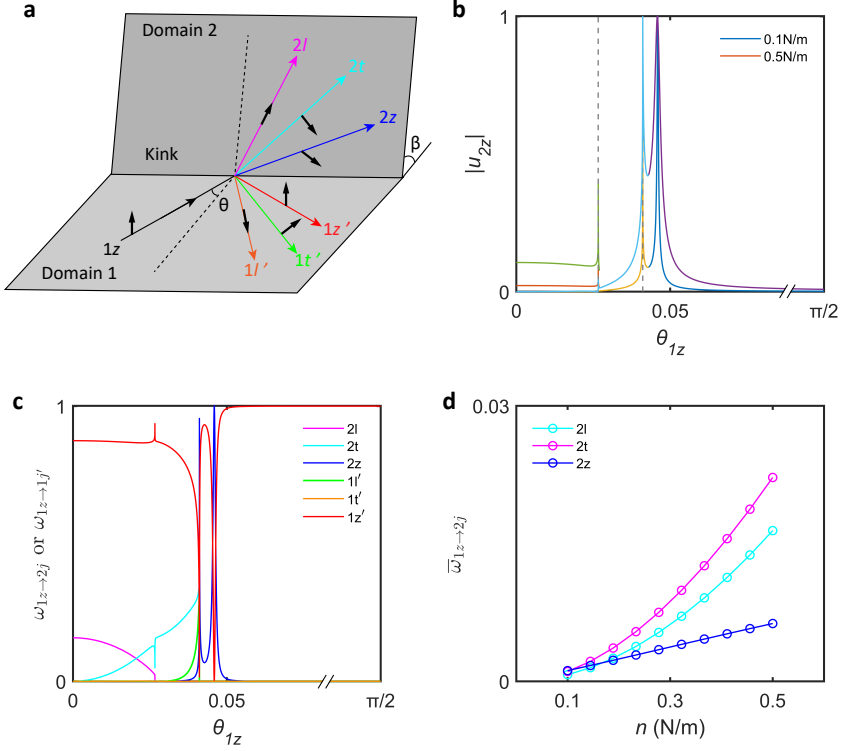
Figure 6.5: Phonons scattering at the boundary of graphene membrane. **a** Diagram of the scattering model for an incoming flexural phonon (mode $1z$) on the kink. Transmitted and reflected modes are denoted by ($2l$, $2t$, and $2z$) and ($1l'$, $1t'$, and $1z'$), respectively. **b** Wave amplitude $|u_{2z}|$ of the transmitted mode $2z$ in the condition of tension $n = 0.1\,\text{N/m}$ and $n = 0.5\,\text{N/m}$, respectively. Assume $c_z = 575\,\text{m/s}$. **c** Transmission $\omega_{1z \rightarrow 2j}$ and reflection $\omega_{1z \rightarrow 1j'}$ possibilities versus angle θ_{1z} of the incoming flexural phonon, computed by the full set of equations given in ref.[36]. Assume $n = 0.3\,\text{N/m}$ and $c_z = 575\,\text{m/s}$. **d** Transmission rates $\overline{w}_{1z \rightarrow 2j}$ ($j = l, t, z$) of flexural phonons versus n, fixing c_z at $575\,\text{m/s}$.
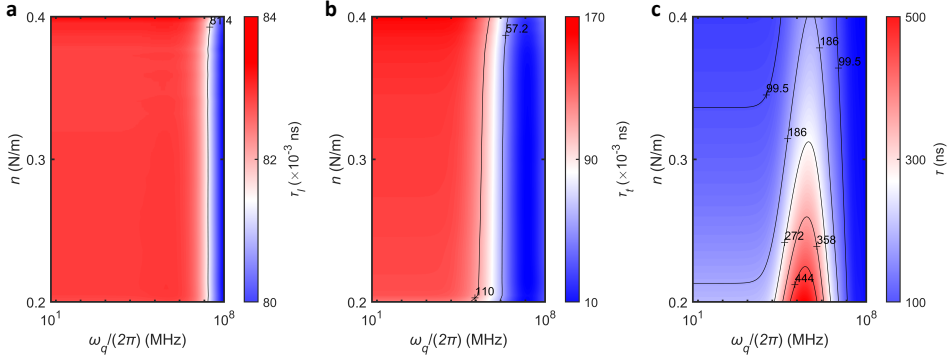
Figure 6.6: Thermal time constants of three types of acoustic phonons as functions of phonons frequency $\omega_q/(2\pi)$ and tension n. **a**−**c**, Results of $\tau_l(n,\omega_q)$, $\tau_t(n,\omega_q)$ and $\tau(n,\omega_q)$, respectively. In general, the magnitude of $\tau(n,\omega_q)$ is three order larger than that of $\tau_l(n,\omega_q)$ and $\tau_t(n,\omega_q)$, indicating the dominant contribution of flexural phonon on the thermal characterization in graphene. The calculated result in **c** is then weighted by the ω_q-dependent specific heat and obtain the total $\tau(n)$ in theory.

the amplitudes of $\overline{w}_{1z\rightarrow2j}$ are quite low (< 0.01), which apparently explains the large values of τ.

In Figs. 6.7a−6.7c, we calculate all transmission rates $\overline{w}_{1z\rightarrow2j}$ ($j = l, t, z$) as the functions of n and c_z. Besides $\overline{w}_{1z\rightarrow2z}$, we see $\overline{w}_{1z\rightarrow2l}$ and $\overline{w}_{1z\rightarrow2t}$ also increases with n as expected. Meanwhile, $w_{1z\rightarrow2z}$ also displays a positive dependence on c_z, meaning that high-speed (corresponds to high q) flexural phonons will be more easily to transmit across over the kink and leave the suspended membrane. By substituting $\overline{w}_{1z\rightarrow2j}$ into Eq. 6.2, we determine $\tau_l(n,\omega_q)$, $\tau_t(n,\omega_q)$ and $\tau(n,\omega_q)$ as shown in Figs. 6.6a to 6.6c, respectively. The speed c_z is ω_q-dependent given by $c_z = \frac{\partial \omega_q}{\partial q}$. Here, we adopt the radius $r = 5\,\mu$m and the bending rigidity $\kappa = 0.6$ eV. τ_l and τ_t are roughly three orders of magnitude lower than τ as expected, due to the much high values of $w_{1z\rightarrow2l}$ and $w_{1z\rightarrow2t}$ compared to $w_{1z\rightarrow2z}$ (see Fig. 6.7c).

Note that in Eq. 6.2 and Eq. 6.4, we only consider the incidence of ZA phonons to the kink and thus to determine the thermal time constant. This is because the contributions from in-plane (LA and TA) phonons to τ can be ignored compared to that from ZA phonons. Using the scattering model, we calculate the values of in-plane τ for graphene resonator D1. The results are 0.22 ns and 8.16×10^{-3} ns for LA and TA phonons, respectively, which are much lower than the measured τ as plotted in Fig. 6.2b. This is attributed to the higher speeds c_l and c_t compared to c_z, and the higher transmission coefficients $\overline{w}_{1l\rightarrow2j}$ and $\overline{w}_{1t\rightarrow2j}$ compared to $\overline{w}_{1z\rightarrow2j}$ as well. The negligible contribution from in-plane phonons show that flexural phonons dominate the phononic heat transport in graphene [10, 47].

6.5.3. DEBYE MODEL OF ACOUSTIC PHONONS

Acoustic phonons in graphene exhibit dispersion relations [48]. In-plane (LA and TA) phonons have a linear dispersion relation $\omega_q = c_j q$ ($j = l, t$) where q is the wavenumber (Fig. 6.8a, left panel). Following the previous theoretical and experimental works, we use
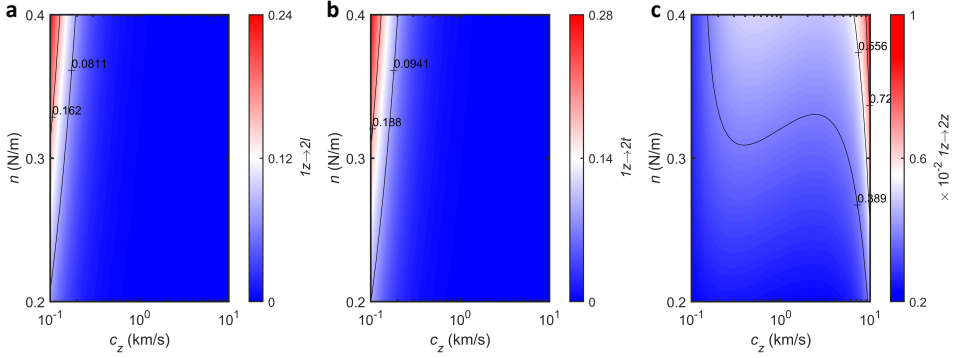
Figure 6.7: Transmission rates of three types of acoustic phonons as functions of sound speed c_z and tension n. **a−c**, Results of $\overline{w}_{1z \to 2l}$, $\overline{w}_{1z \to 2t}$ and $\overline{w}_{1z \to 2z}$, respectively.

$c_l =21.6$ km/s and $c_t =16$ km/s in our work [38, 49]. In contrast, flexural phonons have a nonlinear dispersion relation [50] expressed as $\omega_q = \sqrt{(\kappa q^4 + nq^2)/(\eta \rho_g)}$, where κ is the bending rigidity of the membrane, and η is the normalized areal density extracted from the effective mass of the membrane m_{eff} (obtained from the fits in Fig. 6.2a). The specific heat spectral density $C^z_{v,\omega}$ of flexural phonons in graphene is given by [38]:

$$C^j_{v,\omega} = k_B \left(\frac{\hbar \omega_q}{kT} \right)^2 \frac{e^{\hbar \omega_q / kT}}{\left(e^{\hbar \omega_q / kT} - 1 \right)^2} D\left(\omega_q \right), j = l, t, z \qquad (6.5)$$

where k_B is the Boltzmann constant, $\hbar$ is the Planck constant divided by 2π, $D(\omega_q)$ is the density of states for the given dispersion relations, and $T = 293.15$ K represents the room temperature. Using Eq. 6.5, we obtain the specific heat spectral densities $C^l_{v,\omega}$ and $C^l_{v,\omega}$ of in-plane phonons (see Fig. 6.8a, right panel), as well as $C^z_{v,\omega}$ under different η, κ and n as plotted in Fig. 6.3c (right panel). Here we demonstrate $C^l_{v,\omega}$ and $C^l_{v,\omega}$ are unchanged over all different devices owe to the linear dispersion of in-plane phonons.

In the flexural dispersion $\omega_q = \sqrt{(\kappa q^4 + nq^2)/(\eta \rho_g)}$, n dominates the low frequency (MHz) regime while κ dominates the high frequency (THz) regime. The point, where ω_q transit from n- domination to κ- domination, can be defined as the cross-over frequency ω_{qc} of dispersion (see Fig. 6.8b). Through intersecting $\omega_q = q\sqrt{n/(\eta \rho_g)}$ and $\omega_q = q^2 \sqrt{\kappa/(\eta \rho_g)}$, we can determine ω_{qc} for all devices D1−D4, which are located at 84.8, 52.6, 174.4 and 422.7 GHz, respectively (see Fig. 6.3c).

6.5.4. ANALYSIS OF TUNABLE THERMAL TRANSPORT

As depicted in Fig. 6.9a, there are three paths to affect τ in graphene resonator: via the speed of sound $c_z(n, \omega_q)$, via the specific heat spectral density $C^z_{v,\omega}(n, \omega_q)$, and via the transmission rate $\overline{w}_{1z \to 2z}$. According to the calculation on scattering and Debye models, the path through $\overline{w}_{1z \to 2z}$ dominates the tunable τ in our devices.

The extracted bending rigidity κ (Fig. 6.9b) is seen to increase with the normalized areal density η (as listed in Table 6.1). Since the devices are fabricated identically, we
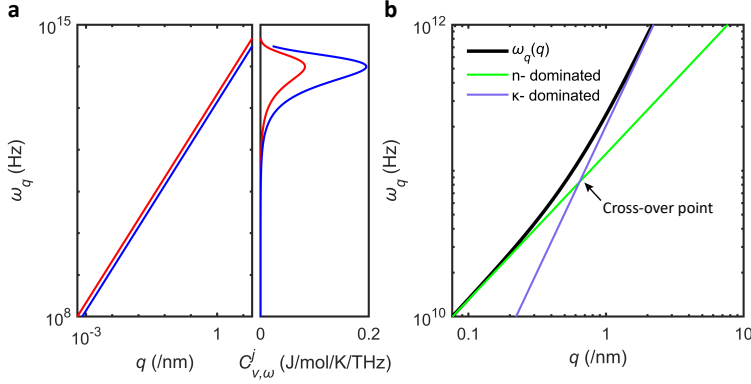
Figure 6.8: Dispersion relations of in-plane phonons. **a** Left panel: dispersion relations of in-plane phonons LA (red line) and TA (blue line); right panel: the corresponding specific heat spectral densities $C_{v,\omega}^l$ (red line) and $C_{v,\omega}^t$ (blue line). **b** Dispersion relation of flexural phonons for device D1 (black line), using the extracted tension $n = 0.25\,\text{N/m}$, bending rigidity $\kappa = 3.8\,\text{eV}$ and normalized areal density $\eta = 19.401$ from the main text. The cross-over frequency $\omega_{qc} = 84.8\,\text{GHz}$ shows the transition of dispersion relation from n- dominated regime to κ- dominated regime.
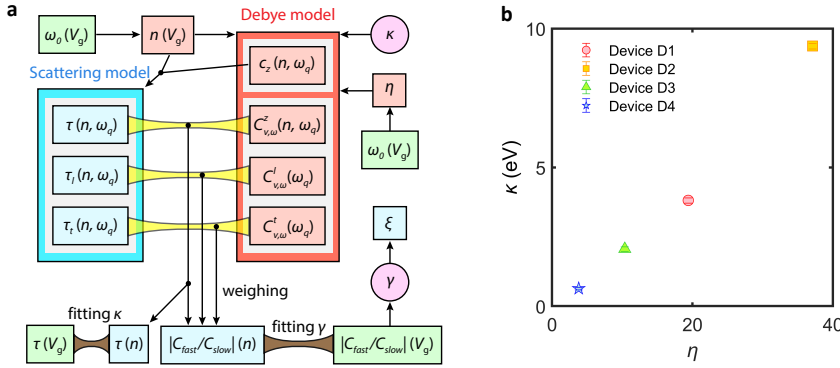
Figure 6.9: Roles of tension played on heat transport tuning. **a** Flow chart of the theoretical model to estimate the thermal time constant τ and the ratio of normalized thermal expansion amplitudes $|C_{\text{fast}}/C_{\text{slow}}|$. Green frames: measured parameters; pink frames: fitting parameters. From Debye model we obtain the phonon frequency ω_q- dependent speed c_z and specific heats C_v^z, C_v^l, C_v^t for phonons, which are used as weighing factors in the scattering model to evaluate τ and $|C_{\text{fast}}/C_{\text{slow}}|$ as a function of tension n. **b** Fitted bending rigidity κ of the membrane versus the normalized areal density η. These values of κ result in a good match between the modelled and measured τ for devices D1−D4 (drawn lines).

attribute these differences to variations in residues on and between the double CVD graphene layers. These residues affect acoustic phonon transport and the resulting forces on the graphene membrane in three different ways. First, residues decrease ξ, the relative optical power absorbed by flexural phonons (Fig. 6.12), and thus decrease their contribution to the thermal expansion amplitude of graphene [51] which is reflected in a reduction of $|C_{\text{fast}}/C_{\text{slow}}|$; second, the effective mass of the membrane, quantified by the normalized areal density η, increases which influences the flexural phonon dispersion, thus affecting τ; third, the bending rigidity κ increases with increasing η (Fig. 6.9b). For a bulk material, of uniform composition, the bending rigidity κ is expected to exhibit cubic scaling with thickness [52] and normalized mass η, however, if the interlayer shear interaction between the layers is weak, a more linear dependence is predicted to occur [53]. Since the data in Fig. 6.9b seems to be in between these two limiting cases, further study is needed to completely understand the observed relation between κ and η in our devices.

Let us now focus on the roles of κ, η and n played on the Debye scattering model. Assume $r = 5\,\mu$m, and the initial conditions of the discussed parameters are set as $\kappa = 0.6$ eV, $\eta = 10$, $n = 0.3$ N/m. We plot $\omega_q(q)$, c_z, $C_{v,\omega}^z$ and τ versus κ, η and n, respectively, as shown in Figs. 6.10a−l. Similar to what we have discussed on ω_q, it is clearly observed that n and κ dominate the MHz- and GHz- regimes, respectively, while η impacts both sides. More importantly, it should be noticed that the sensitivity of n on τ is extremely higher compared to that of κ and η (see Figs. 6.10a−l). This verifies again that the tunable heat transport we measured in graphene resonators is mainly attributed to the acoustic impedance matching at the edge of the membrane.

For each ω_q, the above calculation gives us the thermal time constant and the specific heat spectral density for all types of acoustic phonons at the given tension n. Following the definition of specific heat, we use a weighing relation:

$$1/\tau = \int_0^{\omega_{qd}} C_{v,\omega}^i(\omega_q)/(C_v^i \tau(\omega_q)) d\omega_q, \tag{6.6}$$

where $C_v^i = \int_0^{\omega_{qd}} C_{v,\omega}^i(\omega_q) d\omega_q$ is the total specific heat of a particular phonon type $i = l, t, z$, to separately obtain the weighted τ, τ_l and τ_t. In the flow chart depicted of Fig. 6.10a, κ is the only fitting parameter to match the theoretically estimated to the experimentally measured τ.

We further discuss the role of κ played on the tension-dependent tunable τ (Fig. 6.11). It shows that as κ goes up from 0.06 to 19 eV, the magnitude of τ is improved obviously. This is attributed to the improved contribution rate of high-frequency flexural phonons to the heat transport. In addition, we also observe the slope $|d\tau/dn|$ increases as κ increases, indicating a enlarged tunability on τ.

6.5.5. Thermal nonequilibrium of acoustic phonons

Characterizing thermal nonequilibrium among phonons in graphene has recently received a remarkable attention [2, 54, 55]. In this work, we consider the absolute ratio of normalized thermal expansion amplitudes $|C_{\text{fast}}/C_{\text{slow}}|$. According to the 2D heat equation [19], the thermal expansion amplitude is equal to $\alpha P_{\text{abs}} R$, where α and R is the thermal expansion coefficient and thermal resistance of acoustic phonons, and P_{abs} is

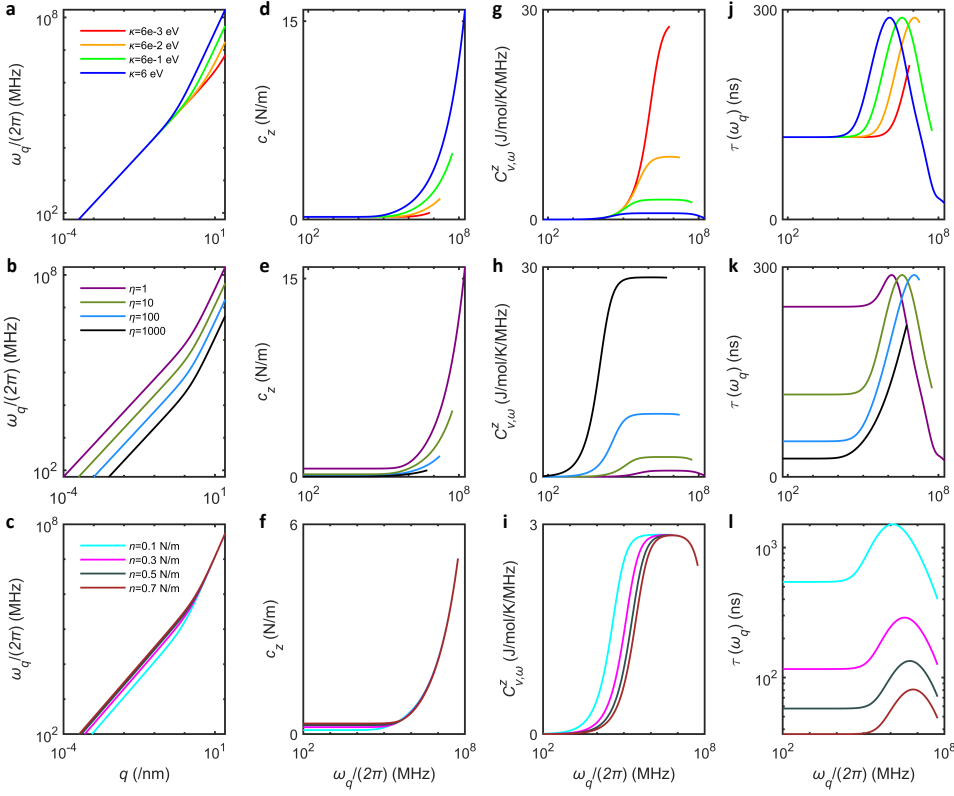Figure 6.10: Discussion for phononic scattering and Debye models. Four parameters of flexural acoustic phonons, including phonons frequency ω_q, speed of sound c_z, specific heat spectral density $C^z_{v,\omega}$ and thermal time constant τ are discussed with respect to bending rigidity κ, normalized areal density η and tension n. Initial settings are $\kappa = 0.6$ eV, $\eta = 10$, $n = 0.3$ N/m and $r = 5\,\mu$m.
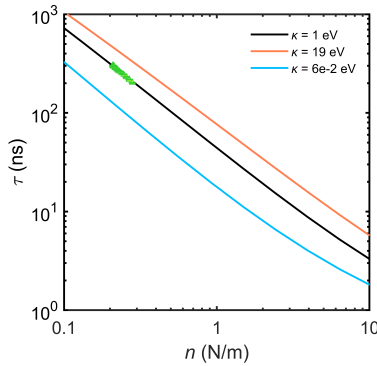

Figure 6.11: Influence of bending rigidity on the tension tuning of heat transport. Green points, the measured thermal time constant τ as a function of tension n for device D3 in the main manuscript; lines, estimated τ versus n under different values of κ.
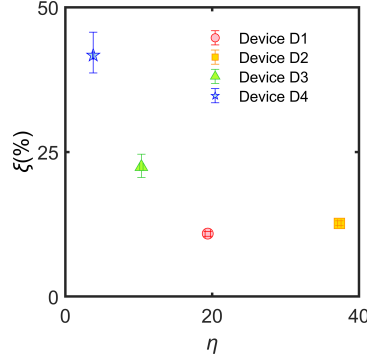
Figure 6.12: Percentual energy absorption ξ by flexural phonons as a function of η shows a strong decrease of ξ with increasing mass due to polymer residues.

the absorbed laser power by the phonons. Assume the values of α are equivalent for all acoustic phonons [56], using $\tau = RC_\nu$, we have $|C_{\text{fast}}/C_{\text{slow}}| = \gamma \frac{(\tau_l/C_\nu^l + \tau_t/C_\nu^t)}{\tau/C_\nu^z}$, where $\gamma = P_{\text{abs}}^{l,t}/P_{\text{abs}}^z$ represents the power absorption ratio between in-plane and flexural phonons. Through the fitting of γ, we obtain a good match between the computed and measured tension-dependence of $|C_{\text{fast}}/C_{\text{slow}}|$ for all devices (see Fig. 6.3a). using the expression $C_{\text{slow}} = \alpha R P_{\text{ac}}$, we also extract that the magnitude of C_{slow} is much smaller than 1 pm, which is negligible compared to the nm-scale deflection tuned by electrostatic force. Additionally, from γ, we can calculate the percentage ξ of optical power that is converted into flexural phonons, expressed as $\xi = P_{\text{abs}}^z/(P_{\text{abs}}^{l,t} + P_{\text{abs}}^z) \times 100\% = (1+\gamma)^{-1} \times 100\%$. As Fig. 6.12 shows, ξ rapidly decreases from 43.7% to less than 15% when the normalized areal density η increases.

Bibliography

[1] S. Chen, Q. Wu, C. Mishra, J. Kang, H. Zhang, K. Cho, W. Cai, A. A. Balandin, and R. S. Ruoff, "Thermal conductivity of isotopically modified graphene", Nature materials **11**, 203–207 (2012).

[2] R. Wang, H. Zobeiri, Y. Xie, X. Wang, X. Zhang, and Y. Yue, "Distinguishing optical and acoustic phonon temperatures and their energy coupling factor under photon excitation in nm 2d materials", Adv. Sci. **7**, 2000097 (2020).

[3] S. Lee, D. Broido, K. Esfarjani, and G. Chen, "Hydrodynamic phonon transport in suspended graphene", Nat. Commun. **6**, 1–10 (2015).

[4] A. Taheri, S. Pisana, and C. V. Singh, "Importance of quadratic dispersion in acoustic flexural phonons for thermal transport in two-dimensional materials", Phys. Rev. B **103**, 235426 (2021).

[5] A. Cepellotti, G. Fugallo, L. Paulatto, M. Lazzeri, F. Mauri, and N. Marzari, "Phonon hydrodynamics in two-dimensional materials", Nat. Commun. **6**, 1–7 (2015).

[6]E. Mariani and F. Von Oppen, "Flexural phonons in free-standing graphene", Phys. Rev. Lett. **100**, 076801 (2008).

[7]E. V. Castro, H. Ochoa, M. Katsnelson, R. Gorbachev, D. Elias, K. Novoselov, A. Geim, and F. Guinea, "Limits on charge carrier mobility in suspended graphene due to flexural phonons", Phys. Rev. Lett. **105**, 266601 (2010).

[8]N. Bonini, J. Garg, and N. Marzari, "Acoustic phonon lifetimes and thermal transport in free-standing and strained graphene", Nano letters **12**, 2673–2678 (2012).

[9]H. Tornatzky, R. Gillen, H. Uchiyama, and J. Maultzsch, "Phonon dispersion in MoS2", Phys. Rev. B **99**, 144309 (2019).

[10]L. Lindsay, D. Broido, and N. Mingo, "Flexural phonons and thermal transport in graphene", Physical Review B **82**, 115427 (2010).

[11]S. Sullivan, A. Vallabhaneni, I. Kholmanov, X. Ruan, J. Murthy, and L. Shi, "Optical generation and detection of local nonequilibrium phonons in suspended graphene", Nano lett. **17**, 2049–2056 (2017).

[12]A. K. Vallabhaneni, D. Singh, H. Bao, J. Murthy, and X. Ruan, "Reliability of raman measurements of thermal conductivity of single-layer graphene due to selective electron-phonon coupling: a first-principles study", Phys. Rev. B **93**, 125432 (2016).

[13]R. J. Dolleman, G. J. Verbiest, Y. M. Blanter, H. S. van der Zant, and P. G. Steeneken, "Nonequilibrium thermodynamics of acoustic phonons in suspended graphene", Phys. Rev. Res **2**, 012058 (2020).

[14]R. J. Dolleman, D. Lloyd, M. Lee, J. S. Bunch, H. S. Van Der Zant, and P. G. Steeneken, "Transient thermal characterization of suspended monolayer mos 2", Physical Review Materials **2**, 114008 (2018).

[15]C. Metzger, I. Favero, A. Ortlieb, and K. Karrai, "Optical self cooling of a deformable fabry-perot cavity in the classical limit", Physical Review B **78**, 035309 (2008).

[16]A. Blaikie, D. Miller, and B. J. Alemán, "A fast and sensitive room-temperature graphene nanomechanical bolometer", Nature communications **10**, 4726 (2019).

[17]D. Ghosh, I. Calizo, D. Teweldebrhan, E. P. Pokatilov, D. L. Nika, A. A. Balandin, W. Bao, F. Miao, and C. N. Lau, "Extremely high thermal conductivity of graphene: prospects for thermal management applications in nanoelectronic circuits", Appl. Phys. Lett. **92**, 151911 (2008).

[18]A. A. Balandin, S. Ghosh, W. Bao, I. Calizo, D. Teweldebrhan, F. Miao, and C. N. Lau, "Superior thermal conductivity of single-layer graphene", Nano letters **8**, 902–907 (2008).

[19]R. J. Dolleman, S. Houri, D. Davidovikj, S. J. Cartamil-Bueno, Y. M. Blanter, H. S. Van Der Zant, and P. G. Steeneken, "Optomechanics for thermal characterization of suspended graphene", Physical Review B **96**, 165421 (2017).

[20]J. S. Bunch, S. S. Verbridge, J. S. Alden, A. M. Van Der Zande, J. M. Parpia, H. G. Craighead, and P. L. McEuen, "Impermeable atomic membranes from graphene sheets", Nano lett. **8**, 2458–2462 (2008).

6

[21] C. Chen, S. Rosenblatt, K. I. Bolotin, W. Kalb, P. Kim, I. Kymissis, H. L. Stormer, T. F. Heinz, and J. Hone, "Performance of monolayer graphene nanomechanical resonators with electrical readout", Nature nanotechnology **4**, 861–867 (2009).

[22] R. J. Dolleman, D. Davidovikj, H. S. Van Der Zant, and P. G. Steeneken, "Amplitude calibration of 2d mechanical resonators by nonlinear optical transduction", Applied Physics Letters **111**, 253104 (2017).

[23] R. A. Barton, I. R. Storch, V. P. Adiga, R. Sakakibara, B. R. Cipriany, B. Ilic, S. P. Wang, P. Ong, P. L. McEuen, J. M. Parpia, et al., "Photothermal self-oscillation and laser cooling of graphene optomechanical systems", Nano lett. **12**, 4681–4686 (2012).

[24] K. Tada, T. Funatani, S. Konabe, K. Sasaoka, M. Ogawa, S. Souma, and T. Yamamoto, "Modulations of thermal properties of graphene by strain-induced phonon engineering", Jpn. J. Appl. Phys. **56**, 025102 (2017).

[25] M. Guo, Y. Qian, H. Qi, K. Bi, and Y. Chen, "Experimental measurements on the thermal conductivity of strained monolayer graphene", Carbon **157**, 185–190 (2020).

[26] Q. Liu and B. Xu, "Anomalous thermal transport of mechanically bent graphene: implications for thermal management in flexible electronics", ACS Appl. Nano Mater. (2022).

[27] M. Šiškins, M. Lee, D. Wehenkel, R. van Rijn, T. W. de Jong, J. R. Renshof, B. C. Hopman, W. S. Peters, D. Davidovikj, H. S. van der Zant, et al., "Sensitive capacitive pressure sensors based on graphene membrane arrays", Microsyst. Nanoeng. **6**, 1–9 (2020).

[28] P. Weber, J. Guttinger, I. Tsioutsios, D. E. Chang, and A. Bachtold, "Coupling graphene mechanical resonators to superconducting microwave cavities", Nano lett. **14**, 2854–2860 (2014).

[29] M. Will, M. Hamer, M. Muller, A. Noury, P. Weber, A. Bachtold, R. V. Gorbachev, C. Stampfer, and J. Guttinger, "High quality factor graphene-based two-dimensional heterostructure mechanical resonator", Nano letters **17**, 5950–5955 (2017).

[30] X. Zhang, K. Makles, L. Colombier, D. Metten, H. Majjad, P. Verlot, and S. Berciaud, "Dynamically-enhanced strain in atomically thin resonators", Nature Communications **11**, 5526 (2020).

[31] T. Miao, S. Yeom, P. Wang, B. Standley, and M. Bockrath, "Graphene nanoelectromechanical systems as stochastic-frequency oscillators", Nano lett. **14**, 2982–2987 (2014).

[32] H. Zhang, C. Hua, D. Ding, and A. J. Minnich, "Length dependent thermal conductivity measurements yield phonon mean free path spectra in nanostructures", Scientific Reports **5**, 9121 (2015).

[33] Y. Kuang, L. Lindsay, and B. Huang, "Unusual enhancement in intrinsic thermal conductivity of multilayer graphene by tensile strains", Nano letters **15**, 6121–6127 (2015).

[34] H. Gholivand and N. Donmezer, "Phonon mean free path in few layer graphene, hexagonal boron nitride, and composite bilayer h-bn/graphene", IEEE Transactions on Nanotechnology **16**, 752–758 (2017).

[35] W. Cai, A. L. Moore, Y. Zhu, X. Li, S. Chen, L. Shi, and R. S. Ruoff, "Thermal transport in suspended and supported monolayer graphene grown by chemical vapor deposition", Nano letters **10**, 1645–1651 (2010).

6

[36] R. J. Dolleman, Y. M. Blanter, H. S. van der Zant, P. G. Steeneken, and G. J. Verbiest, "Phonon scattering at kinks in suspended graphene", Phys. Rev. B **101**, 115411 (2020).

[37] R. Peterson and A. Anderson, "The kapitza thermal boundary resistance", J. Low Temp. Phys. **11**, 639–665 (1973).

[38] T. Nihira and T. Iwata, "Temperature dependence of lattice vibrations and analysis of the specific heat of graphite", Phys. Rev. B **68**, 134305 (2003).

[39] D. Singh, J. Y. Murthy, and T. S. Fisher, "Mechanism of thermal conductivity reduction in few-layer graphene", J. Appl. Phys. **110**, 044317 (2011).

[40] E. Han, J. Yu, E. Annevelink, J. Son, D. A. Kang, K. Watanabe, T. Taniguchi, E. Ertekin, P. Y. Huang, and A. M. van der Zande, "Ultrasoft slip-mediated bending in few-layer graphene", Nat. Mater. **19**, 305–309 (2020).

[41] Y. Wei, B. Wang, J. Wu, R. Yang, and M. L. Dunn, "Bending rigidity and gaussian bending stiffness of single-layered graphene", Nano lett. **13**, 26–30 (2013).

[42] M. Maldovan, "Sound and heat revolutions in phononics", Nature **503**, 209–217 (2013).

[43] A. A. Balandin, "Phononics of graphene and related materials", ACS nano **14**, 5170–5178 (2020).

[44] J. H. Seol, I. Jo, A. L. Moore, L. Lindsay, Z. H. Aitken, M. T. Pettes, X. Li, Z. Yao, R. Huang, D. Broido, et al., "Two-dimensional phonon transport in supported graphene", Science **328**, 213–216 (2010).

[45] J. Atalaya, A. Isacsson, and J. M. Kinaret, "Continuum elastic modeling of graphene resonators", Nano lett. **8**, 4196–4200 (2008).

[46] G. Lopez-Polın, C. Gomez-Navarro, V. Parente, F. Guinea, M. I. Katsnelson, F. Perez-Murano, and J. Gomez-Herrero, "Increasing the elastic modulus of graphene by controlled defect creation", Nature Physics **11**, 26–31 (2015).

[47] L. Lindsay, D. Broido, and N. Mingo, "Flexural phonons and thermal transport in multilayer graphene and graphite", Phys. Rev. B **83**, 235428 (2011).

[48] D. L. Nika and A. A. Balandin, "Phonons and thermal transport in graphene and graphene-based materials", Rep. Prog. Phys. **80**, 036502 (2017).

[49] X. Cong, Q.-Q. Li, X. Zhang, M.-L. Lin, J.-B. Wu, X.-L. Liu, P. Venezuela, and P.-H. Tan, "Probing the acoustic phonon dispersion and sound velocity of graphene by raman spectroscopy", Carbon **149**, 19–24 (2019).

[50] T. Gunst, K. Kaasbjerg, and M. Brandbyge, "Flexural-phonon scattering induced by electrostatic gating in graphene", Physical Review Letters **118**, 046601 (2017).

[51] E. Mercado, J. Anaya, and M. Kuball, "Impact of polymer residue level on the in-plane thermal conductivity of suspended large-area graphene sheets", ACS Appl. Mater. Interfaces **13**, 17910–17919 (2021).

[52] N. Lindahl, D. Midtvedt, J. Svensson, O. A. Nerushev, N. Lindvall, A. Isacsson, and E. E. Campbell, "Determination of the bending rigidity of graphene via electrostatic actuation of buckled membranes", Nano letters **12**, 3526–3531 (2012).

6

[53]G. Wang, Z. Dai, J. Xiao, S. Feng, C. Weng, L. Liu, Z. Xu, R. Huang, and Z. Zhang, "Bending of multilayer van der Waals materials", Physical Review Letters **123**, 116101 (2019).

[54]N. Hunter, N. Azam, H. Zobeiri, N. Van Velson, M. Mahjouri-Samani, and X. Wang, "Interface thermal resistance between monolayer wse2 and sio2: raman probing with consideration of optical–acoustic phonon nonequilibrium", Adv. Mater. Interfaces, 2102059 (2022).

[55]H. Zobeiri, N. Hunter, R. Wang, T. Wang, and X. Wang, "Direct characterization of thermal nonequilibrium between optical and acoustic phonons in graphene paper under photon excitation", Advanced Science **8**, 2004712 (2021).

[56]N. Yang, C. Li, and Y. Tang, "Effects of chirality and stacking on the thermal expansion effects of graphene", Mater. Res. Express **7**, 115001 (2020).

6

7

7

DETERMINING THERMAL INTERFACE CONDUCTANCE BETWEEN TWO 2D MATERIALS BY OPTOMECHANICS

For the development of nanoscale electronics and photonics based on 2D van der Waals (vdW) technology, energy dissipation at 2D interfaces is a significant issue. This causes high power densities during devices operation, which in turn limits their performance. To shed light into fundamental aspects of this challenge, in this chapter, we report a novel approach for characterizing the heat transport in pure $FePS_3$ and WSe_2 membranes, as well as their stacked heterostructure. Using optothermal actuation, we measure their resonance frequency and thermal time constant as a function of temperature. These allow us to extract a thermal interface conductance of 2.73 ± 1.71 $MWm^{-2}K^{-1}$ in the $FePS_3/WSe_2$ heterostructure, which is comparable to the reported values obtained from Raman microscopy. This work opens the door for efficient thermal management at nanoscale and offers significant new insights into energy dissipation in 2D vdW devices.

7.1. Introduction

Advances in 2D heterostructure offer great opportunities for next-generation electronic, photonic and thermoelectric applications at nanoscale, including field-effect transistors, quantum cascade lasers, photonic bandgap crystals and light emitters [1, 2]. However, low thermal interface conductance in 2D heterostructures, due to the presence of phonons-state mismatch by van der Waals interaction, limits the heat transport and results in large thermal isolation, causing significant restrictions on device performance. Therefore, characterizing thermal interface conductance is of importance to optimize heat transport in 2D heterogeneous devices, which provides a pathway toward well-cooled, high-performance functional nanodevices and efficient thermal management in nanosystems.

In this section, different from the commonly adopted technique based on Raman thermometry [3–5], we employ an optothermal approach for determining the thermal interface conductance, G, between two different 2D materials that are stacked in a double-layer heterostructure. Three resonators are fabricated by the Scotch tape method, including pure $FePS_3$ and WSe_2 devices, as well as a $FePS_3/WSe_2$ heterostructure device. Optomechanical measurement has been done to obtain their resonance frequency f_0 and thermal time constant τ as a function of temperature. By using a COMSOL model, we extract the thermal interface conductance of a $FePS_3/WSe_2$ heterostructure device, from its measured τ and the obtained specific heat and thermal conductivity for both pure $FePS_3$ and WSe_2 membranes.

7.2. Results and discussion

7.2.1. Laser interferometry of heterostructure resonators

To prepare the proposed heterostructure resonators, WSe_2 and $FePS_3$ nanoflakes are mechanically exfoliated by Scotch tape, and then transferred and suspended over cavities with a radius of $r = 3$ μm, as shown in Fig. 7.1a. Three types of membranes are formed: pure WSe_2 membranes (like device D2), pure $FePS_3$ membranes (D1) and $FePS_3/WSe_2$ heterostructures (D3). The overlapped region of two flakes forms the heterostructure. After fabrication, we use AFM to characterize the thickness and Young's modulus of the suspended 2D membranes. Here, we obtain $t_1 = 34.5$ nm and $E_1 = 93.1$ GPa for pure $FePS_3$, while $t_2 = 8.6$ nm and $E_2 = 98.3$ GPa for pure WSe_2 membrane. The heat transport in $FePS_3/WSe_2$ heterostructure can be captured by a thermal model, as shown in Fig. 7.1b. In order to determine the thermal conductance at the interface, we adopt an optomechanical approach together with COMSOL finite element simulation: first, resonance frequency f_0 and thermal time constant τ of the pure devices D1 and D2 are measured as a function of temperature T; accordingly, the specific heat c_p and thermal conductivity k for both pure membranes can be extracted using the theory introduced in Chapter. 5; then, we input these results into a double-layer COSMOL model, where the heat transport is simulated to estimate τ under different G; finally, by adjusting G such that the tau from the model matches the measured τ, we extract the thermal conductance G for heterostructure device D3.

Figures 7.1c and 7.1d show the results of optomechanical measurements for all devices D1−D3. Note that the observed minimum in f_0 versus T curve for device D1 is
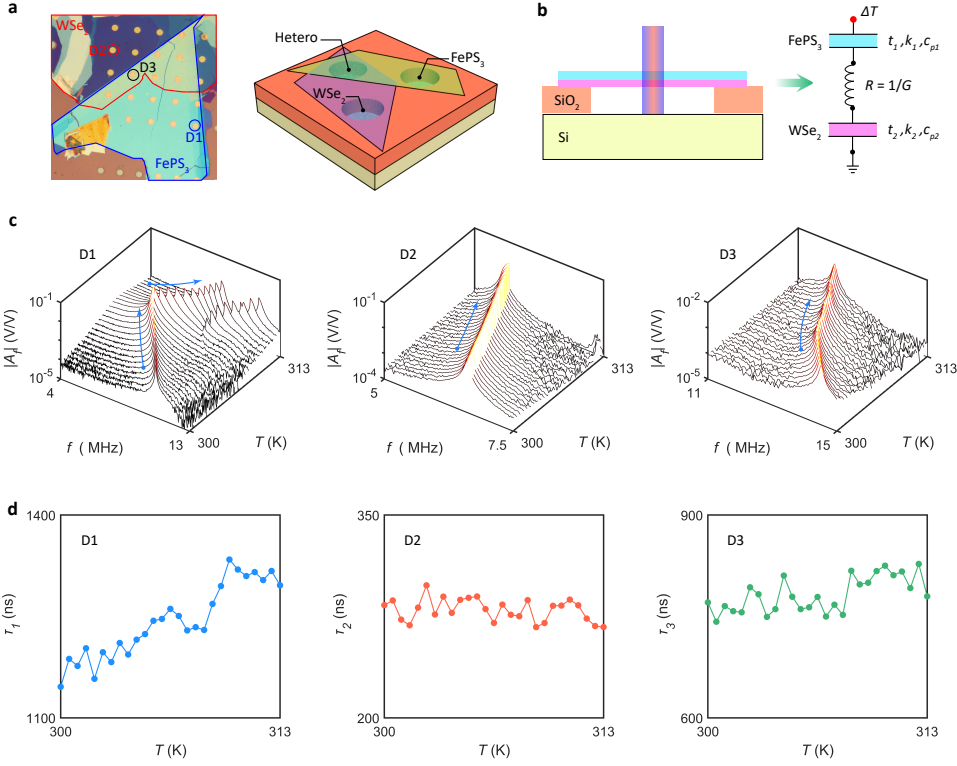
Figure 7.1: Temperature-dependent optomechanical measurements on 2D resonators. **a** Optical image (top view) and the 3D schematic of the devices. D1, pure FePS$_3$ device; D2, pure WSe$_2$ device; D3, FePS$_3$/WSe$_2$ heterostructure device. **b** Left, cross-section view of the heterostructure; right, equivalent thermal model correspondingly. **c** Measured resonance peak for devices D1−D3 as temperature T increases. **d** Thermal time constant τ as the function of T for devices D1−D3, extracted from the fits to the measured thermal signal.

attributed to the thermally-induced buckling bifurcation (see Chapter 4). The experimental values of τ for heterostructure device D3 ($\sim$ 780 ns) is between those of device D1 ($\sim$ 1250 ns) and device D2 ($\sim$ 280 ns). Using the measured $\tau(T)$ and the slope $\frac{df_0^2}{dT}$, we extract c_{p1} = 775.1 ± 30.4 Jkg^{-1}K^{-1} and k_1 = 3.9 ± 0.5 Wm^{-1}K^{-1} for FePS$_3$, as well as c_{p2} = 102.2 ± 4.5 Jkg^{-1}K^{-1} and k_2 = 7.0 ± 0.2 Wm^{-1}K^{-1} for WSe$_2$, respectively. All of the extracted values above are comparable to values reported in the literature [6–9].

7.2.2. DETERMINING THERMAL INTERFACE CONDUCTANCE

After characterizing the thermal properties for pure membranes, we now move on to the thermal interface conductance in heterostructure G. As shown in Fig. 7.2a, we build a double-layer model in COMSOL to simulate the heat transport in heterostructure, where a thermal contact, with interface conductance G, is set at the interface. More details of the model can be found in Appendix. The thermal properties (c_p and k) of top and bottom layers in the model are set with the values obtained for pure FePS$_3$ and WSe$_2$
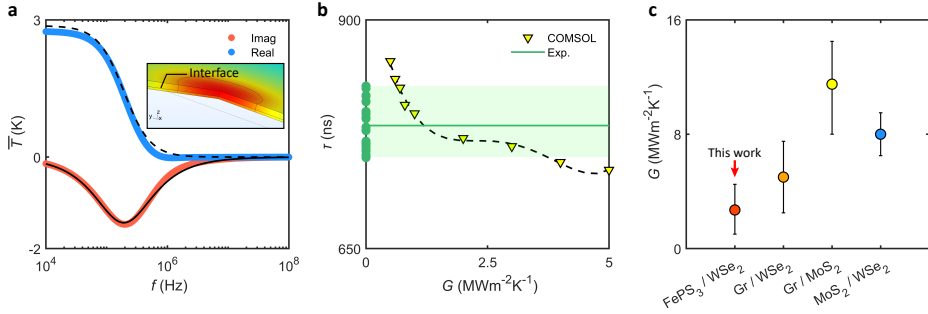
Figure 7.2: Determining thermal interface conductance in FePS$_3$/WSe$_2$ heterostructure. **a** Comsol simulation of the volume averaged ac temperature modulation $\overline{T}$ of the membrane, when optothermally heated by a power modulated laser in its center. Blue line, real part; red line, imaginary part; insert, diagram of COMSOL model. Boudary heat source is setting as 100 Wm^{-2}. **b** Yellow points, thermal time constant τ versus thermal interface conductance G simulated by COMSOL. Green points, the measured τ_3 for heterostructure device D3. **c** Extracted G of FePS$_3$/WSe$_2$ interface in this work and reported results for other kinds of 2D interfaces from [3].

membranes, respectively. Assume a thermal interface conductance $G = 1$ MWm^{-2}K^{-1}, we simulate the heat transport in heterostructure and obtain its volume-average temperature modulation amplitude T as a function of he frequency f of a power modulated laser, as shown in Fig. 7.2a. This result is then fitted with the thermal equation (Eq. 2.9 in Chapter. 2), giving us a thermal time constant $\tau_3 = 797.66$ ns for heterostructure.

Using COMSOL simulation, we then extract the relation between G and τ_3 for FePS$_3$/WSe$_2$ heterostructure, as plotted in Fig. 7.2b (yellow dots). We find that τ_3 gradually decreases as G increases, indicating the heat transport will be affected more by the bottom WSe$_2$ layer in case of a better heat conduction between the layers. Thus, using the measured τ_3 (green points in Fig. 7.2b), we extract $G = 2.73 \pm 1.71$ MWm^{-2}K^{-1} for heterostructure device D3. Compared to the reported results for monolayer graphene, MoS$_2$ and WSe$_2$ interfaces [3], our obtained G is a little bit smaller (Fig. 7.2c). This could be attributed to a larger mismatch of acoustic phonons between the FePS$_3$ and WSe$_2$ membrane, or the contamination such as polymer residues induced by fabrication. In addition, we assume that the thermal properties of each layer in the heterostructure device D3 is equivalent to their pure counterparts (devices D1 and D2), which, in case of lateral variations in the material properties, could cause errors in the estimations of G.

Our proposed method is suitable for studying other kinds of 2D interfaces, and since it is performed on suspended membranes, has the advantage of excluding the influence of substrate on the propagation of heat carriers in 2D materials. Additionally, large T-measuring range is required to achieve a recognizable detection for the Raman shift $\Delta\chi_T$ of 2D materials. By contrast, optomechanical measurement is done with a T-accuracy of 1 K, which provides a much more precise and sensitive platform for characterizing the thermal transport in 2D materials.

It has been verified that the heat flow across the 2D interfaces is dominated by the overlapping phonon density of states (PDOS) of flexural phonons [3]. As a result, it is of interest to further quantify the acoustic mismatch between the FePS$_3$ and WSe$_2$ by PDOS

calculations, to analyze the cause of thermal interface conductance from its underlining physical essence. Additionally, it is worth to explore the thermal interface conductance in anisotropic 2D materials such as black phosphorus, which could provide a strategy for guiding heat in desired directions.

7.3. CONCLUSION

In conclusion, we fabricated a $FePS_3/WSe_2$ heterostructure resonator and presented a method to determine its thermal interface conductance by optothermomechanical means. Independent optomechanical measurements have been done firstly on pure $FePS_3$ and WSe_2 membranes to extract their thermal properties, which are then imported into a built double-layer model in COMSOL. The simulation result allows us to extract the thermal interface conductance $G = 2.73 \pm 1.71$ MWm^{-2}K^{-1} for heterostructure device from its measured thermal time constant, showing a good agreement with the reported values from literature. Our methodology could elucidate the fundamental heat transport through the vdW heterostructure and benefit the thermal management and optimization at nanoscale.

7.4. APPENDIX

7.4.1. HEAT TRANSPORT IN DOUBLE-LAYER CIRCULAR PLATE

For a double-layer circular plate under cylindrical coordinates, as depicted in Fig. 7.3, the homogeneous of heat conduction equations are given as:

$$\begin{cases} \frac{\partial T_1}{\partial t} = \kappa_1 \left(\frac{\partial^2 T_1}{\partial x^2} + \frac{1}{r} \frac{\partial T_1}{\partial x} + \frac{\partial^2 T_1}{\partial z^2} \right), & \text{in} \quad 0 < z < z_1 \quad 0 < x < r, \\ \frac{\partial T_2}{\partial t} = \kappa_2 \left(\frac{\partial^2 T_2}{\partial x^2} + \frac{1}{x} \frac{\partial T_2}{\partial x} + \frac{\partial^2 T_2}{\partial z^2} \right), & \text{in} \quad z_1 < z < z_2 \quad 0 < x < r, \end{cases} \tag{7.1}$$

where we use the heights z_1 and z_2 to define the thickness of the membranes, $\kappa_1 = \frac{k_1}{c_{p_1} \rho_1}$ and $\kappa_2 = \frac{k_2}{c_{p_2} \rho_2}$ represent the thermal diffusivity, k, c_p and ρ are the thermal conductivity, specific heat and mass density of the membrane, respectively. To obtain the distributions of temperature T_1 and T_2, we combine Eq. 7.1 with the boundary and initial conditions:

$$\begin{cases} T_1 = 0, & \text{at} \quad x = r, \\ T_1 = 0, & \text{at} \quad z = 0, \\ T_2 = 0, & \text{at} \quad x = r, \\ -k_1 \frac{\partial T_1}{\partial z} = G(T_1 - T_2), & \text{at} \quad z = z_1 \\ k_1 \frac{\partial T_1}{\partial z} = k_2 \frac{\partial T_2}{\partial z}, & \text{at} \quad z = z_1, \\ \frac{\partial T_2}{\partial z} = 0, & \text{at} \quad z = z_2, \end{cases} \tag{7.2}$$

where G is the thermal interface conductance.

In the following, we employ the commonly used method, separation variables, to solve T_1 and T_2:

$$\begin{cases} T_1(r, z, t) = \psi(r) Z_1(z) \Gamma(t), \\ T_2(r, z, t) = \psi(r) Z_2(z) \Gamma(t). \end{cases} \tag{7.3}$$
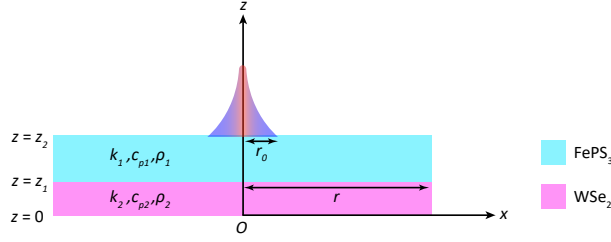
Figure 7.3: Illustration of double-layer circular plate.

Combining the boundary and initial conditions in Eq. 7.2, the general solutions for Eq. 7.3 are:

$$
\begin{cases}
T_1(r,z,t) = \sum_{m=1}^{\infty}\sum_{n=1}^{\infty} A_{mn} J_0(\eta_m r)\sin(\gamma_n z)e^{-\lambda_{mn}^2 t}, \\
T_2(r,z,t) = \sum_{m=1}^{\infty}\sum_{n=1}^{\infty} B_{mn} J_0(\eta_m r)[\cos(\mu_n z)+\tan(\mu_n z_2)\sin(\mu_n z)]e^{-\lambda_{mn}^2 t},
\end{cases}
\tag{7.4}
$$

where $m = 1,2,3,...$ and $n = 1,2,3,...$ are the m-th and n-th eigenvalues values, A_{mn} and B_{mn} are integration parameters. γ_n and μ_n can be determined by the relations $\lambda_{mn}^2 = \kappa_1(\eta_m^2 + \gamma_n^2) = \kappa_2(\eta_m^2 + \mu_n^2)$ and

$$
\begin{vmatrix}
\kappa_1\gamma_n\cos(\gamma_n z_1)+G\sin(\gamma_n z_1) & -G\cos(\mu_n z_1) & -G\sin(\mu_n z_1) \\
\kappa_1\gamma_n\cos(\gamma_n z_1) & \kappa_2\mu_n\sin(\mu_n z_1) & -\kappa_2\mu_n\cos(\mu_n z_1) \\
0 & \sin(\mu_n z_2) & -\cos(\mu_n z_2)
\end{vmatrix} = 0.
\tag{7.5}
$$

Similar to the derivations in Appendix of Chapter 5, the thermal time constant τ of the double-layer structure here can be expressed by $\tau = 1/\lambda_{mn}^2$. Thus from Eq, 7.5 we know that τ is related to the thermal diffusivity and thickness of both top and bottom membrane, as well as the interface conductance G.

7.4.2. COMSOL SIMULATION FOR HEAT TRANSPORT

Although T_1 and T_2 in Eq. 7.4 can be solved with the form of Green's functions in previous study [10], it is complicated to obtain the analytical solution for λ_{mn}^2, much less considering the size of laser spot r_0 is smaller than r, and the existing Si substrate in realistic case. Therefore, we adopt COMSOL simulation method to estimate τ in heterostructure device, as shown in Fig. 7.4.

For structural parameters, we set $r = 3$ μm, $r_0 = 0.25$ μm, $t_1 = 34.5$ nm, $t_2 = 8.6$ nm, $\rho_1 = 3375$ kgm^{-3} and $\rho_2 = 9320$ kgm^{-3}. The independent optomechanical measurements on pure FePS$_3$ and WSe$_2$ membranes give us $c_{p1} = 775.1$ Jkg^{-1}K^{-1}, $k_1 = 3.9$ Wm^{-1}K^{-1}, $c_{p2} = 102.2$ Jkg^{-1}K^{-1} and $k_2 = 7.0$ Wm^{-1}K^{-1}. The initial and boundary conditions of heat transport in Eq. 7.2 are also set in this model. To simulate the modulated laser irradiation on the membrane, we use a boundary heat source on the upper surface of FePS$_3$ layer (with a radius of r_0) and add a harmonic perturbation. As a result, by varying G from from 0.5 to 5 MWm^{-2}K^{-1}, we obtain the relation between τ and G as plotted in Fig. 7.2b.
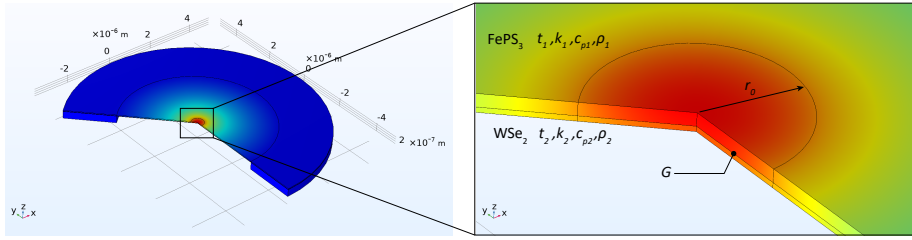
Figure 7.4: COMSOL model for simulating heat transport in a double-layer circular membrane.
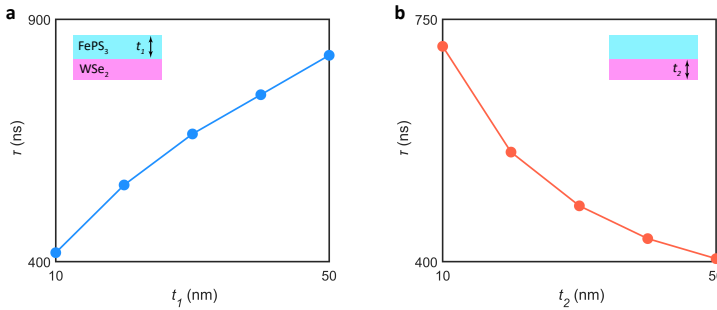

Figure 7.5: COMSOL model for simulating heat transport in a double-layer circular membrane.

As we know from Eq. 7.5, thermal time constant τ of heterostructure is not only related to G, but also highly depends on the thicknesses of both top and bottom layers, t_1 and t_2. Therefore, by fixing $G = 1\ \mathrm{MWm^{-2}K^{-1}}$, we further discuss the influence of t_1 and t_2 on the heat transport through simulation, as shown in Fig. 7.5. When fixing $t_2 = 20$ nm and tuning t_1 from 10 to 50 nm, τ_3 gradually increases from 418.62 to 825.70 ns; when fixing $t_1 = 20$ nm and tuning t_2 from 10 to 50 nm, τ_3 gradually decreases from 710.92 to 404.41 ns. Note that for pure $FePS_3$ and WSe_2 membranes, the measured $\tau_1 \approx 1250$ ns and $\tau_2 \approx 280$ ns. Therefore, we conclude that the increase of thickness of one layer will cause it to contribute more to the heat transport in the heterostructure, as expected.

BIBLIOGRAPHY

[1] L. Zhang, Y. Zhong, X. Qian, Q. Song, J. Zhou, L. Li, L. Guo, G. Chen, and E. N. Wang, "Toward optimal heat transfer of 2d–3d heterostructures via van der waals binding effects", ACS Applied Materials & Interfaces **13**, 46055–46064 (2021).

[2] A. Arrighi, E. del Corro, D. N. Urrios, M. V. Costache, J. F. Sierra, K. Watanabe, T. Taniguchi, J. A. Garrido, S. O. Valenzuela, C. M. S. Torres, et al., "Heat dissipation in few-layer mos2 and mos2/hbn heterostructure", 2D Materials **9**, 015005 (2021).

[3] S. Vaziri, E. Yalon, M. Muñoz Rojo, S. V. Suryavanshi, H. Zhang, C. J. McClellan, C. S. Bailey, K. K. Smithe, A. J. Gabourie, V. Chen, et al., "Ultrahigh thermal isolation across

heterogeneously layered two-dimensional materials", Science advances **5**, eaax1325 (2019).

[4]A. Behranginia, Z. Hemmat, A. K. Majee, C. J. Foss, P. Yasaei, Z. Aksamija, and A. Salehi-Khojin, "Power dissipation of wse2 field-effect transistors probed by low-frequency raman thermometry", ACS applied materials & interfaces **10**, 24892–24898 (2018).

[5]E. Yalon, C. J. McClellan, K. K. Smithe, M. Muñoz Rojo, R. L. Xu, S. V. Suryavanshi, A. J. Gabourie, C. M. Neumann, F. Xiong, A. B. Farimani, et al., "Energy dissipation in monolayer mos2 electronics", Nano letters **17**, 3429–3433 (2017).

[6]F. Kargar, E. A. Coleman, S. Ghosh, J. Lee, M. J. Gomez, Y. Liu, A. S. Magana, Z. Barani, A. Mohammadzadeh, B. Debnath, et al., "Phonon and thermal properties of quasi-two-dimensional feps3 and mnps3 antiferromagnetic semiconductors", ACS nano **14**, 2424–2435 (2020).

[7]Y. Takano, N. Arai, A. Arai, Y. Takahashi, K. Takase, and K. Sekizawa, "Magnetic properties and specific heat of mps3 (m= mn, fe, zn)", Journal of Magnetism and Magnetic Materials **272**, E593–E595 (2004).

[8]W.-X. Zhou and K.-Q. Chen, "First-principles determination of ultralow thermal conductivity of monolayer wse2", Scientific reports **5**, 1–8 (2015).

[9]S. Kumar and U. Schwingenschlogl, "Thermoelectric response of bulk and monolayer mose2 and wse2", Chemistry of Materials **27**, 1278–1284 (2015).

[10]Y. Sun, J. Ma, S. Liu, and J. Yang, "Analytical solution of transient heat conduction in a bi-layered circular plate irradiated by laser pulse", Canadian Journal of Physics **95**, 322–330 (2017).

7

8

8

CONCLUSION

In this thesis, by focusing on the mechanics and thermodynamics of suspended 2D membranes, we investigated a wide variety of topics, including fabrication techniques, mechanical phenomena, heat transport and energy dissipation. This concluding chapter summarizes the key results from individual chapters and gives a perspective on future works.

THIS thesis gives an overview of experimental study on the mechanics and thermo-dynamics of nanomechanical resonators composed of 2D materials. The research outline, as depicted in Fig. 8.1, is in-line with the author's scientific research progression in the past four years.

8.1. INTRODUCTION AND METHODOLOGY

In Chapter 1, We began by giving an introduction on the excellent characteristics of 2D materials, as well as the fundamental performance and applications of 2D nanomechanical resonators, which, at the very beginning, elucidated the background and motivation of this thesis.

In Chapter 2, we first outlined the process for suspending 2D membranes on the etched Si substrate to fabricate nanomechanmical resonators. Afterwards, various of typical techniques that characterize the fundamental properties of 2D membranes were discussed, including AFM (tapping/contact modes), Raman microscopy and white light interferometry. Then, emphasis was given to introducing the laser interferometry setup, which was commonly used to probe the mechanical and thermodynamic properties of manufactured devices in this thesis. We also introduced the basis for how to tune the mechanical resonance frequency of 2D nanomechanmical resonators.

8.2. MECHANICS: NOVEL TECHNIQUE AND PHENOMENA

During the transfer and fabrication of 2D nanomechanical resonators, we already faced the restrictions arisen from the Scotch tape approach such as irregularly structural deformations and residue contamination, especially when making multilayer heterostructure devices. In Chapter 3, aiming at a more efficient and reliable technical route, we realized a pathway for high-quality MoS_2/graphene resonators using the atomic layer deposition (ALD) method. More importantly, our fabricated heterostructure devices showed a lower energy dissipation at the interface, compared to their exfoliated counterparts, making them promising for atomically thin tunable resonators and 2D sensors.

The large and sensitive tunability of dynamic properties makes 2D nanomechanical resonators promising candidates for sensing applications. However, during the demonstration of thermal tuning in $FePS_3$ resonators, we observed an unexpected minimum in the resonance frequency versus temperature curve, which is significantly different from previous studies. In Chapter 4, we focused on this new discovery and described it in details through a built mechanical buckling model. The change of surface strain and central deflection of the membrane were characterized as a function of temperature. This phenomenon was also observed in $2H\text{-}TaS_2$ and WSe_2 resonators. Furthermore, we found that the amplitudes of both thermal expansion and resonance were remarkably enhanced near the buckling bifurcation point, which is attributed to the low out-of-plane stiffness of the membrane.

8.3. THERMODYNAMICS: PRECISE PROBE AND MODULATION

We then moved on to the thermodynamics of suspended 2D membrane. The laser in-terferometry setup provides a precise platform to probe the phononic heat transport

8

with nanosecond resolution. In Chapter 5, we proposed an optomechanical methodology for characterizing the thermodynamic properties of 2D membranes, including the thermal expansion coefficient, specific heat and thermal conductivity. To achieve this, we measured the resonance frequency and thermal time constant of the membrane as a function of temperature. Our work shows comparable results compared to previous first-principle studies and Raman measurements.

To our surprise, the aforementioned approach utterly failed to work with the best-known 2D material, graphene. In Chapter 6, a two-order-higher magnitude of thermal time constant was tested in double-layer graphene resonators. Instead of the phononic transport in the membrane, we accounted for these experimental observations by the strong phonons scattering at the boundary of membrane between the supported and suspended part. This scattering turned out to be highly correlated with the surface tension in the membrane. As a result, by applying tension using electrostatic deflection, we realized a ~ 33% decrease of heat transport in graphene resonators.

8.4. Outlook

As discussed above, the link between mechanics and thermodynamics has already been established by optomechanical measurement on 2D nanomechanical resonators. This motivated us to investigate additional mechanisms and phenomena in suspended 2D membranes that have not been thoroughly studied. In Chapter 7, we concentrated on the thermal transport in 2D heterostructure. Optomechanical measurement was presented combined by COMSOL simulation, which allows us to characterize the thermal conductance at 2D interface.

Additionally, there are still many directions and topics that are worthwhile to be done. In terms of dynamic phenomena, besides the studied buckling, mode coupling, particularly the coupling of various resonators, still needs to progress. Such coupling effects can lead to rich physics in 2D nanomechanical resonators. Using optomechanical measurement, it is worth to study the control of energy between modes through phononic heat transport. With regard to material performance, a basic assumption in this thesis is that the mechanics and thermodynamics of 2D membranes are anisotropic. Considering that many 2D materials, like As_2S_3 and black phosphorus (BP), exhibit large in-plane isotropy, it is of interest to explore their phononic transport, buckling bifurcation and thermoelastic damping along different lattice axis.

In the manufacture and integration of 2D-based NEMS, it is still challenging to fabricate these suspended devices at large scale. ALD technique, as already demonstrated the strong adaptability for multi-layer and uniform nanofabrication, would be ideal for making ultra-large NEMS with low energy dissipation. Additionally, the semiconductor devices based on 2D vdW bilayer structures might greatly benefit from the accurate thickness control of the ALD approach. For advanced sensing applications, we proved that the amplitudes of thermal expansion and resonance of suspended 2D membrane will be significantly enlarged near buckling bifurcation. This could open up opportunities for the realization of ultra-sensitive sensors that rely on buckled 2D resonators.

In 2D materials industry, the route toward novel characteristics and advanced applications is always accompanied by difficulties and challenges. How to stabilize the performance of 2D NEMS so as to achieve their repeatability? Where is the upper limit
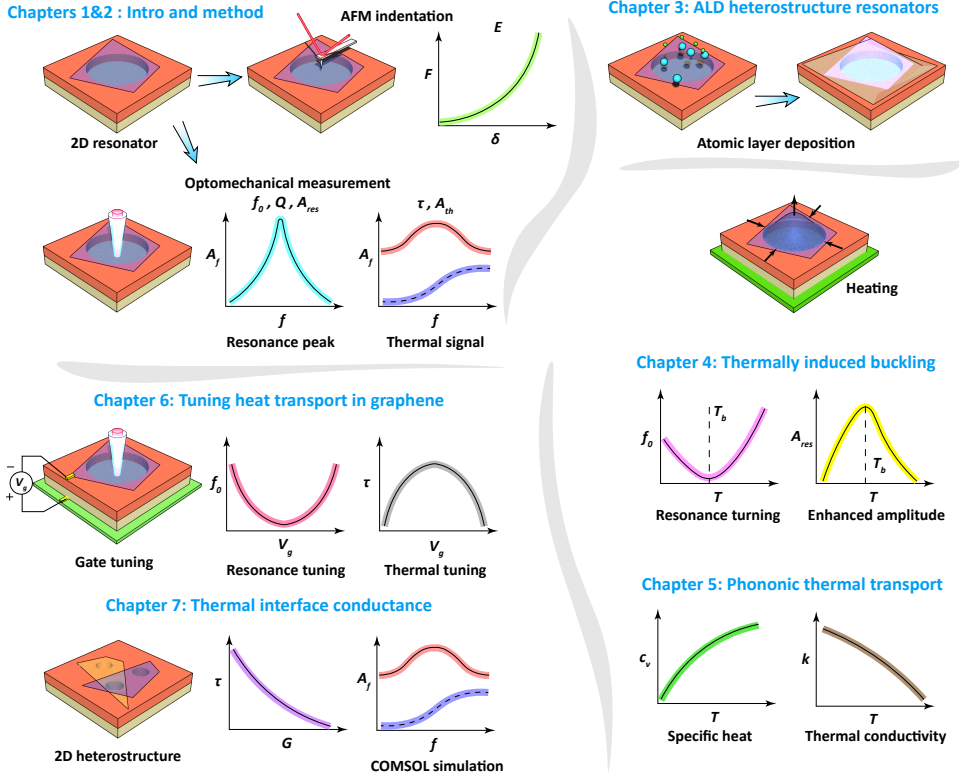
Figure 8.1: Research outline of this thesis.

8

of 2D sensors performance? How to realize large-scale fabrication with considerable yields for semiconductor manufacturing? Is it possible to push 2D resonators to mechanical qubits for storing and processing quantum information? Can we achieve room-temperature superconductor in twisted graphene or vdW heterostructures? Keeping in mind that it takes almost 30 years for carbon fibers to go from laboratory to aircraft and aerospace industries, we do believe, at the milestone of graphene's coming 20th birthday, that the explosive industrial applications of 2D materials will come soon. With the encouraging achievements over the past two decades and the promising opportunities in front of us, let's keep going!

ACKNOWLEDGEMENTS

Time has passed so quickly; although my journey here at TU Delft is coming to the end, it feels like I just started yesterday. Honestly, these past four years have been quite challenging for me—being far from my hometown and family, adapting to a different culture and environment, and dealing with the COVID-19 pandemic... However, I do have had an unforgettable experience here. Not only because the expanding knowledge on 2D material world, but also the privilege of getting to know many kind and excellent people. They have offered me their selfless help during this significant period, and consequently, I am enthusiastic about expressing my gratitude to everyone I have encountered in this acknowledgment.

First and foremost, I would like to express my heartfelt gratitude to my exceptional promotors, who have guided me in exploring the wonders of the 2D world and provided unwavering support and encouragement. **Gerard**, I am at a loss for words to adequately convey my gratitude to you. You are a diligent, proactive, and brilliant supervisor, as well as a masterful soccer player. You are always ready to reply my emails whenever early morning or late night, summer or Christmas holidays. The most valuable thing I have gleaned from you is not just about 2D materials, but about maintaining rigor, pragmatism, and objectivity in research. I firmly believe that I will uphold this approach in my future scientific career in China. Best wishes with your family and your multiple projects. Looking forward to come back one day and celebrate for Prof. Verbiest.

Peter, you are an outstanding leader and that's why our DMN group has grown stronger in such a short period. Thank you once again for granting me this invaluable opportunity to pursue my PhD here. Your exceptional ability to identify issues in theoretical models and experiments, coupled with your unique perspectives and analyses, have been truly enlightening. One particularly memorable instance was when I was grappling with background noise around ENIGMA, you just took out your phone, opened a sensor app and we squatted on the ground to pinpoint the noise source. I aspire to follow in your footsteps, even twenty years from now-to become a scientist who is continually curious about knowledge and deeply passionate about research.

I would like to extend my heartfelt gratitude to all the committee members for dedicating their valuable time to read my thesis. **Herre**, I thoroughly enjoyed conducting various experiments in your laboratories. The comfort of the sofa outside was an added bonus, which might explain why you often found me napping there. Thank you for providing such conducive conditions and offering valuable suggestions for our publications! **Yaroslav**, whenever our colleagues at TNW encountered theoretical problems, you were always the first person we thought of discussing with and seeking help from. I appreciate the discussion with you on energy dissipation and buckling effects of 2D nanomechanical resonators, and it has greatly benefited my works. **Saurabh**, it was a truly impressive experience to collaborate with you during your visit to TU Delft. Thank

you for sharing your extensive knowledge about field-effect transistors and engaging in enlightening brainstorming sessions! Upon my return to China, I have decided to pursue related research and eagerly look forward to future collaborations and discussions with you. **Ageeth**, thank you for helping us with ALD material samples during the lockdown time. I am delighted that our collaborative paper was eventually published online. I wish you achieve more remarkable achievement at the University of Michigan. **Professor Bolotin**, it was a pleasure to meet you at the IWEPNM winter school and share the exhilarating experience of skiing on the snowy mountains. Our discussions on 2D material resonators and acoustic phonons, along with the insights gained from speaking with you and your PhDs, Yuefeng and Jan, have inspired me immensely. Thank you for accepting the role of being on the committee.

To my paranimfs, **Ruben** and **Zichao**. Ruben, a.k.a. ultrasound AFM master, thanks for sharing so many funny stories and dutch jokes (especially about French people) during coffee break and lunch time! There are always endless topics every time we chat. Honestly, I still wonder how you beat me once on basketball court, you do have a secret training at home right? Anyway, I will definitely join your defense online next year and all best wishes for your soccer team and your academic career. Zichao, when I saw your CV, I promised Peter that you will be an excellent PhD. Yes you are! I should admit that you are the best soccer player among all Delft Chinese PhDs (as far as I know), after all, you are the seed player in your primary school team. Keep going, I am 120 % percent sure you will have a very successful PhD.

Since my daily life was traveling between TNW and 3mE buildings, I would like to start from my colleagues at Quantum Nanoscience (QN). **Martin**, the god of clean room, you are an enthusiastic, independent, and outstanding scientist! Thanks for your advice and help at the beginning of my PhD. I wish you would make more and more achievements in your postdoctoral career at Munich! **Makars**, if I were to predict which of my colleague would gain the Nobel Prize, the first person I think of is you. You work diligently and always have novel ideas. Keep in touch and look forward to the big news from you! **Maurits**, you are a rigorous and independent thinking researcher. Thanks for all academic discussion about buckling and thermoelastic damping. I wish you seccess with your research and obtain nice publications! **Roberto**, you are such a humor guy but also a clean room master. Every time when you showed me your designed Graphene microphone, I wonder how can you achieve such complicated fabrication recipes in CR. Thanks for recommending so many nice restaurants in Napoli. Next time let me show you great Chinese food in my hometown. Finally, **Gabriele**, my close friend, the Pizza you made is definitely the best Pizza I have eaten all over the world! I am really missing our coffee break at QN and the pingpong games. Hope you will enjoy your life with families and friends.

Let me now go back to PME department. First, I would like to thanks all other PIs in DMN group. **Farbod**, our nonlinear dynamic authority, it is my honor to collaborate with you on several papers. I am very admire very much on your comprehensive abilities, such as the piano performance at Christmas event, and the best teacher prizes for three years continuously. Look forward to meet you around West Lake in the near future! **Sabina**, our Nature's Rising Star, we are all impressed with what you've achieved in such a few years! You are the target for our young PhDs to learn from. Thanks very much for

your kind words on my DMN talk every time. **Richard**, one secret for sharing is that I really like the Lego models on your desk-sometimes I paid more attention on them than what's Gerard saying. Best wishes for your very cool satellite project. **Wouter**, although our connection is not a lot, from your setup in Optical lab, besides Enigma, I can still imagine you must have many cool ideas.

Then, it comes to my DMN colleagues whom I have spent with during the hard covid period. **Ata**, a.k.a. Emotional chef & Old cow, my League of Legend teammate, how many sins have we experienced in the past few years!? From my inner heart, I am really glad to see that you are enjoying your life at Delft now, and I do believe you will become a successful guy whatever you are doing. For our bet, I will definitely pay you 200€if I get married within two years, however, it is only covered in your journey fee, so please come to China and let's have fun! **Xianfeng**, another old cow (maybe not now), I still remember the moment five years ago, when I added your Wechat and asked whether Peter have available position for PhDs, thanks for that. Now, we define the way 'push pingpong ball to the diagonal and let people rush' as Xianfeng style. Best wishes for your postdoc in Singapore and Let's make big news together in China! **Irek**, my funny roommate at Mechiel de Ruyterweg, here is the answer for your question: the way to control points is exchanging the racket from left to right hand, but of course, I will change it back when 10:10 so that I can still win the game. Anyway, best wishes for your CellSound company and let the world hear your sound. **Ali**, we almost have two publications there together! Thanks for building the entire theoretical models and proving them with experimental data. Hope you will have a wonderful life in Netherlands with your family. **Abhilash**, you know, I can rapidly judge whether you are in the office based on your perfume-sometime directly told Farbod you are not when he is searching for you. Thanks for sharing so many funny stories during lunch time! Hope one day you will become the leader of ASML research. **Martin (Robin)**, you are the loudest postdoc in the world! I was wondering if you can be the source that produces ultrasound for your setup. Very happy to see you start as PI this year in France, I wish you become a huge guy in AFM field.

Mingxing, a.k.a. 'Dalao'(huge guy in academia), I wonder have you ever tried being in clean room 24/7? You are such a hard-working researcher with infinite idea and energy. Good luck with your business, crude, Bitcoins, and stocks in Dastardaq Market. **Andrea**, you are a responsible and creative person, and I have the feeling that you are whether working in clean room or on the way to there. I really like our conversations inside the optical lab and besides coffee machine. **Matthijs**, thanks for sharing your objective point of view on different international hot spots during lunch, hope everything goes well in Finland! **Satadal**, we started the work with Gerard almost at the same moment, till now you have already built a competitive company! Your broad knowledge base on culture, traffic and tourism over different countries helped me a lot when traveling around EU. **Tomas**, thanks a lot for the training of Polytec vibrometer, it really helped me understand the dynamics of my graphene drums. Thanks for organising a lot afterwork activities, and I still remember your house warming and our cycling to Kinderdijk. **Doon Hoon**, it is funny that we often meet each other in the library during weekends. Thanks for giving me the training in Kavli clean room and providing me with your fabricated chips. Hope you would achieve your willing and become a professor in the future!

There are also many new and energetic PhDs in our DMN group. **Xiliang**, just take

144 ACKNOWLEDGEMENTS

CURRICULUM VITÆ

Hanqing LIU

05-01-1995   Born in Rizhao, Shandong, China.

EDUCATION

2009–2012   High School
              Rizhao No.1 Middle School of Shandong
              Rizhao, China

2012–2016   Undergraduate in Applied Physics
              National University of Defense Technology, Changsha, China
              Thesis: Adaptive Energy Selective Metamaterial Using Phase
                            Transition V_2O_5 (Best Bachelor Thesis, NUDT)
              Promotor: Prof. dr. Peiguo Liu

2016–2018   Master in Electronic Science and Technology
              National University of Defense Technology, Changsha, China
              Thesis: Functional Photoelectric Devices Based on Multi-
                            layer Graphene Stacks (Excellent Master Thesis, Mil-
                            itary)
              Promotor: Prof. dr. Peiguo Liu

2019–2023   PhD in Precision and Microsystems Engineering
              Delft University of Technology, Delft, The Netherlands
              Thesis: Mechanics and Thermodynamics of Suspended 2D
                            Membranes
              Promotor: Prof. dr. Peter G. Steeneken
              Copromotor: dr. Gerard J. Verbiest

LIST OF PUBLICATIONS

─────────────────As First author─────────────────

7. **Hanqing Liu**, Peter G. Steeneken and Gerard J. Verbiest, *Thermoelastic damping in 2D nanomechanical resonators*, in preparation.

6. **Hanqing Liu**, Abin Varghese, Saurabh Lodha, Herre S.J. van der Zant, Peter G. Steeneken and Gerard J. Verbiest, *Determining thermal interface conductance between two 2D materials by optomechanics*, in preparation.

5. Peiguo Liu* and **Hanqing Liu***, *Electromagetic protection strategy using adaptive energy selective mechanism*, published on: The Innovation, 4, 100513 (2023).

4. **Hanqing Liu**, Hatem Brahmi, Carla Boix-Constant, Herre S.J. van der Zant, Peter G. Steeneken and Gerard J. Verbiest, *Characterizing thermal transport in two-dimensional materials using optomechanics*, To be submitted.

3. **Hanqing Liu**, Gabriele Baglioni, Carla Boix-Constant, Herre S.J. van der Zant, Peter G. Steeneken and Gerard J. Verbiest, *Enhanced sensitivity and tunability of thermomechanical resonance near the buckling bifurcation*, preprint online: arXiv:2305.00712 (2023), Revision.

2. **Hanqing Liu**, Saravana B. Basuvalingam, Saurabh Lodha, Ageeth A. Bol, Herre S.J. van der Zant, Peter G. Steeneken and Gerard J. Verbiest, *Nanomechanical resonators fabricated by atomic layer deposition on suspended 2D materials*, published on: 2D materials, 10, 045023 (2023).

1. **Hanqing Liu**, Martin Lee, Makars Siskins, Herre S.J. van der Zant, Peter G. Steeneken and Gerard J. Verbiest, *Tension tuning of sound and heat transport in graphene*, published on: Physical Review B, 108, L081401 (2023).

─────────────────As coauthor─────────────────

4. Ali Sarafraz, **Hanqing Liu**, Marko Spasenovic, Sten Vollebregt, Tomas M. Garcia, Peter G. Steeneken, Farbod Alijani and Gerard J. Verbiest, *Stress distribution quantification in ultra-large graphene membrane through mode shape imaging*, to be submitted.

3. Hadi Arjmandi-Tash, Roshan Prasad, **Hanqing Liu**, Gerard J. Verbiest, Peter G. Steeneken and Farbod Alijan, *Enhancing elastic stiffness of graphene via crumple creation*, in preparation.

2. Gabriele Baglioni, Roberto Pezone, Sten Vollebregt, Katarina Cvetanovic Zobenica, Marko Spasenovic, Dejan Todorovic, **Hanqing Liu**, Gerard J. Verbiest, Herre S.J. van der Zant, Peter G. Steeneken, *Ultra-sensitive graphene membranes for microphone applications*, published on: Nanoscale, 15, 6343-6352 (2023).

─────────────────────────────────

*These two authors contributed equally.

1. Ali Sarafraz, Arthur Givois, Irek Roslon, **Hanqing Liu**, Hatem Brahmi, Gerard J. Verbiest, Peter G. Steeneken and Farbod Alijani, *Dynamics of pressurized ultra-thin membranes*, preprint online: Nonlinear Dynamics, 111, 14751–14761 (2023).

————————————————————Other works————————————————————

7. Chenxi Liu, Peiguo Liu, Cheng Yang, Yue Lin and **Hanqing Liu**, *Analogue of dual-controlled electromagnetically induced transparency based on a graphene metamaterial*, published on: Carbon, 142, 354-362 (2019).

6. N Hu, Fengling Wu, Lian Bian, **Hanqing Liu** and Peiguo Liu, *Dual broadband absorber based on graphene metamaterial in the terahertz range*, published on: Optical Materials Express, 8, 3899-3909 (2018).

5. **Hanqing Liu**, Peiguo Liu, Lian Bian, Chenxi Liu and Qihui Zhou, *Electro-optic modulator side-coupled with a photonic crystal nanobeam loaded graphene/Al_2O_3 multilayer stack*, published on: Optical Materials Express, 8, 761-774 (2018).

4. **Hanqing Liu**, Jianfeng Tan, Peiguo Liu, Lian Bian and Song Zha, *Tunable coupled-resonator-induced transparency in a photonic crystal system based on a multilayer-insulator graphene stack*, published on: Materials, 11, 2042 (2018).

3. **Hanqing Liu**, Song Zha, Peiguo Liu, Xiaotian Zhou and Lian Bian, *Perfect absorption in 1D photonic crystal nanobeam embedded with graphene/Al_2O_3 multilayer stack*, published on: Superlattices and Microstructures, 117, 429-436 (2018).

2. **Hanqing Liu**, Peiguo Liu, Lian Bian, Chenxi Liu, Qihui Zhou and Yanfei Dong, *Electrically tunable switching based on photonic-crystal waveguide loaded graphene stacks*, published on: Optics Communications, 410, 565-570 (2018).

1. **Hanqing Liu**, Peiguo Liu, Lian Bian, Chenxi Liu, Qihui Zhou and Yuwei Chen, *Electrically tunable terahertz metamaterials based on graphene stacks array*, published on: Superlattices and Microstructures, 112, 470-479 (2017).